Wielding Focused Ultrasound Induced Sterile Inflammation: A Double-Edged Sword in Cancer and the CNS

A Dissertation

Presented to the faculty of the School of Engineering and Applied Science
in partial fulfillment of the requirements for the degree of

Doctor of Philosophy

By Alexander S. Mathew
May 2021

Dissertation Advisor
Richard J. Price, Ph.D.

Department of Biomedical Engineering

University of Virginia

Table of Contents

Acknowledgements

This work would not have been possible without a mountain of support from a host of advisors, colleagues, friends, and family. I first thank my research advisor, Dr. Richard Price. From my first interview with him in 2016 to our most recent email exchange, Dr. Price has constantly encouraged scientific curiosity and put his students first. Thank you so much for your scientific wisdom, professional guidance, and friendship over these last few years. I have benefited immeasurably from your advocacy, and hope to emulate your example of servant leadership one day. I am grateful to our collaborators and members of my thesis committee. To Dr. Tim Bullock, thank you for your continuous mentorship, immunology expertise, and many thought provoking discussions throughout my graduate career. To Dr. Kevin Janes, thank you for challenging me to think in new ways about systems biology and science in general. QBR is still the best class I have ever taken, and I continue to recommend it to all new BME students. To Dr. Patrick Dillon, thank you for allowing me to contribute to your trial research and to shadow your clinical work. To Dr. Sepideh Dolatshahi, thank you for your support as a member of my thesis committee and continuous mentorship in systems immunology.

I am indebted to my colleagues in the Price lab, many of whom have made substantial contributions to the projects presented here. I'd especially like to thank Andrew Thim for his scientific insights, dry sense of humor, and unwavering willingness to help with experiments. From building FUSSY, to talking about video games, and complaining about science, you made the grad school experience way more fun than it should have been. To Katie Gorick, thank you for your friendship, and allowing me to benefit from your BBB opening expertise and knowledge, without which half of this dissertation would not exist. Thank you so much to our lab manager Dr. Ji Song, who made every lab day significantly easier and more pleasant. Thank you to the rest of my grad student colleagues, including Brian Mead, Colleen Curley, Natasha Sheybani, Delaney Fischer, Tor Breza, Mark Schwartz, Anna Debski, Lydia Petricca, and Kathy Nowak, as well as our amazing undergrads, for creating an engaging, collaborative, entertaining, and meme-worthy lab culture. #PLS. I am also grateful to a long list of UVa staff, including members of the UVa MSTP, BME department, GATC, BTRF, RHC, and bioinformatics core.

Finally I must thank my family and friends. To my parents, Denise and Mammen, and my sister Susan, thank you for your lifelong support and encouragement. I wouldn't have gotten far without it. To my wife Lara, my in-laws Joy, Burkhard, and Noaa, and basically-brother Dave, thank you all for being incredible friends. I am truly lucky to know such a supportive, kind group of people.

Abstract

Focused ultrasound (FUS) is an exciting medical technology capable of inducing diverse therapeutic bioeffects applicable to a wide array of diseases. Often performed under image guidance, FUS generates acoustic waves outside the body and orients them to converge in diseased tissue without affecting surrounding healthy tissue. The ability of FUS to precisely ablate pathologic regions without the need for ionizing radiation has already garnered clinical utilization for treatment of uterine fibroids, bone metastases, and essential tremor. Research efforts have recently shifted to the investigation of more advanced applications of FUS, including immunomodulation and disruption of the blood brain barrier. We applied data-driven approaches to investigate each of these, generating actionable mechanistic insights toward accelerating clinical adoption of FUS as a precision medicine.

Immunotherapies have revolutionized cancer therapy in the last decade, empowering patients' own immune systems to recognize and destroy tumor cells. However the success of these therapies is highly variable, dependent on the baseline immunologic cooperativity of the tumor microenvironment (TME). FUS thermal ablation (FUSTA) may provide an opportunity to sensitize immunologically "cold" tumors, increasing the proportion of patients who could benefit from immunotherapy. In addition to clinical utility as a tumor debulking therapy, a growing body of evidence has shown FUSTA generates pro-inflammatory signatures in the TME. Attempts to leverage these effects for enhancement of immunological tumor control have been mostly unsuccessful, in part due to an incomplete knowledge of how FUSTA interfaces with the TME. Here, used high throughput transcriptomic and immunophenotypic profiling to reveal pro- and anti-tumor mechanisms induced by FUSTA in a model of aggressive melanoma. These insights enabled design of novel FUSTA-drug combinations capable of significantly delaying tumor growth. We identified similarly nuanced immunomodulatory impacts in the first clinical trial to combine FUSTA with immunotherapy in breast cancer patients. These were then directly contrasted against a parallel study of the same immunotherapy when paired with high-dose conformal radiation therapy in solid human malignancies. Ultimately, we conclude that maximizing the immunogenicity of FUSTA will require pharmacological blockade of concomitant tissue repair mechanisms.

The blood brain barrier (BBB), a specialized vasculature unique to the central nervous system (CNS), remains one of the most significant neuropharmacological obstacles. Pulsed, low-intensity FUS in conjunction with systemically administered microbubbles (MBs) can transiently disrupt the BBB, facilitating localized delivery of therapeutics to the brain. FUS-mediated BBB disruption (BBBD) has been shown to enhance accumulation of chemotherapies, genes, neural

stem cells, and antibodies in the brain, therapeutics normally too large to bypass the BBB. As this technology rapidly approaches clinical maturity, it is becoming increasingly important to understand the cellular consequences of perturbing the BBB, a protective physiological structure crucial to maintaining homeostasis in the CNS. Herein, we perform investigations of the nature of the parenchymal response to BBBD, as well as its experimental determinants. We first describe how anesthesia, used in all preclinical FUS BBBD studies, influences local reactivity and signaling networks following BBBD. Next, we investigate how FUS acoustic pressure affects gene delivery and transcription in distinct cell populations of the CNS. Finally, we identify the relative power of MB activation and contrast enhancement measured during FUS BBBD to predict transcript expression in the hours following treatment. Together these studies provide fundamental knowledge concerning the biological response to BBBD, with clear safety and therapeutically relevant implications.

Chapter 1: Introduction

1.1 Focused Ultrasound – State of the Art

Focused Ultrasound (FUS) is a rapidly evolving therapeutic technology with the potential to augment treatment of many diseases, spanning from Alzheimer's to melanoma. Like a magnifying glass focusing sunlight, FUS concentrates acoustic energy generated outside the body to a small volume in target tissue, producing therapeutic bioeffects. FUS offers several clinically attractive advantages compared to other forms of focal therapy (e.g. radiation, microwave, cryotherapy, photodynamic therapy). Specifically, FUS is truly noninvasive (unlike cryotherapy or microwave therapy), highly targetable (with up to millimeter precision), capable of reaching deep tissues (unlike light-based therapies), and non-ionizing which enables repeated treatment (unlike radiotherapy). Treatments are often performed under ultrasound or MRI-guidance for enhanced precision and treatment monitoring. Further, administration of FUS is extraordinarily diverse, enabling tunable induction of bioeffects including tissue ablation, hyperthermia, neuromodulation, immunomodulation, clot/stone fragmentation, and drug delivery. In this chapter, we will discuss the evolution of biomedical FUS, two emerging FUS applications, and the necessary steps to bring them to patient bedsides.

The advent of modern FUS research is a testament to the accumulated contributions of physicists, biologists, physicians, and engineers spanning well over a century. In 1880, French scientists Jacques and Pierre Curie became the first to demonstrate piezoelectricity, the physical property of some materials to produce electricity in response to mechanical stimuli (1). Importantly, leveraging a proof from mathematician Gabriel Lippmann (2), the Curie brothers soon showed that this phenomenon is reversible (3). The so-called converse piezoelectric effect, by which an electric field applied to a piezoelectric element generates mechanical vibration, is the guiding principle underlying many modern technologies, including all ultrasonic transducers. Johannes Gruetzmacher designed the first focused transducer in 1935 by adding a concave quartz surface to a piezoelectric generator (4). Biomedical applications of FUS were first investigated in the 1940's by John Lynn and colleagues, who demonstrated successful ablation of bovine liver (5). William and Francis Fry, often called the "Fathers" of FUS, along with many other pioneers, would continue to make significant advances throughout the latter half of the 20th century, applying FUS to noninvasively ablate diseased brain tissue in the context of Parkinson's Disease and cancer (6–9). In parallel, significant technological developments in FUS instrumentation (e.g. phased array transducers) and imaging modalities (e.g. MRI) made therapeutic applications increasingly feasible (10–13). In the 1990's, Kullervo Hynynen and colleagues proposed applying FUS under MRI guidance (14), now commonly known as MRgFUS,

and later used this technique to demonstrate that low intensity FUS combined with systemically administered microbubbles enables the reversible opening of the blood brain barrier (15). Since these milestones, FUS research has experienced exponential growth. A Google Scholar strict search for “focused ultrasound” returned 6270 manuscripts published in 2020 alone, compared to 1440 in 2005, and just 110 in 1990. According to the most recent “State of the Field” report from the FUS Foundation, FUS is being evaluated for its potential to treat 136 distinct pathologies. In 2019, over 60,000 patients were treated across 585 treatment sites throughout the world. Built on the foundation laid by countless scientists over many decades, FUS appears poised to experience a biomedical golden age.

The most well studied and clinically mature application of FUS is thermal ablation (FUSTA). In this regimen, high intensity continuous or semi-continuous pressure waves are targeted to pathological tissue. Acoustic absorption of these waves leads to rapid local increases in temperature beyond 60 °C and near-instant coagulative necrosis, with minimal damage to surrounding tissue. The ability to concentrate individual sonications to grain-of-rice sized volumes, paired with image guidance, enables precise cellular destruction. Real-time ablation monitoring may be performed utilizing MR or ultrasound-based thermography. These technical advances translate to proven clinical benefits, significantly reducing anesthesia, cosmetic, side effect, and financial burden compared to surgery (16–22). Consequently, FUSTA has garnered increasing oncological and neurological adoption. The vast majority of all clinical-stage FUS trials and FDA approved FUS applications are for thermal ablation of various solid tumors (e.g. prostate malignancies, uterine fibroids, bone metastases) or brain pathologies (e.g. essential tremor). Despite this progress, FUSTA is still in its early stages of clinical use. Further studies will be required to establish long-term clinical benefits and side-effects compared to first-line therapies.

In recent decades, FUS research has shifted to exploration of FUS regimens beyond thermal ablation. According to data compiled by the FUS Foundation, there are currently over four times as many research sites investigating alternative FUS applications and biological effects as there are for FUSTA. Hyperthermia, a sub-lethal form of thermal FUS, can be used to locally modulate cellular stress (23), radiosensitivity (24), or drug release (25–27). Histotripsy leverages high-intensity short-duration pulses to generate “cavitation clouds” that mechanically fractionate tissue with even sharper margins and less off-target heating than FUSTA (28, 29). Pulsed ultrasound has been shown to stimulate or repress activity of neurons in the brain, leading to multiple neuromodulation studies (30–34). Systemic administration of microbubbles can be used in combination with FUS to induce local tissue destruction (high-intensity) or enhance drug delivery to tissues of interest (low-intensity), including across the blood-brain barrier (BBB).

Finally, common to many of these regimens and FUSTA is an emerging appreciation for the role of sterile inflammatory responses induced by therapy (35–37). The prospect of locally inducible inflammation could find significant use in a number of pathologies, especially cancer. In aggregate, these alternative FUS protocols represent extraordinary therapeutic potential. We will review two of these, namely FUS immunomodulation and FUS BBB disruption, in greater detail, and discuss the approaches necessary to facilitate clinical adoption.

1.2 Immunomodulation with Focused Ultrasound Thermal Ablation

In 2011, Weinberg and Hanahan published an update to their seminal “Hallmarks of Cancer” (38), originally a set of six organizing biological themes common to most if not all malignancies (39). Two new hallmarks of cancer proposed in the update included “Avoiding immune destruction” and “Tumor-promoting inflammation”. These additions reflect an increasing recognition for the critical roles the immune system plays in both tumor surveillance and tumorigenesis. Viewing cancer through a lens of dysregulated immunology has enabled pivotal scientific breakthroughs that are rapidly shifting therapeutic paradigms (40). In this section, we will review cancer immunology, followed by a discussion of challenges facing the field and the potential for FUSTA to overcome them.

The dynamic set of interactions that occur between the host immune system and cancer cells as they progress from precancerous to malignant are jointly referred to as immunoediting (41). Immunoediting occurs in 3 steps, the first of which is “elimination”. During the elimination phase, the immune system is functioning to effectively locate, identify, and destroy abnormal host cells, followed by the establishment of immunological memory against similar aberrant cells. As with most immune processes, elimination involves a series of interactions between immune cells, soluble factors, and cytokines from both innate and adaptive immune compartments. Innate immune cells serve as the first line of defense against cancer cell proliferation. Neoantigens, abnormal proteins such as those derived from mutations in the exons of cancer cells, can be recognized and engulfed by phagocytic cells such as neutrophils or macrophages. Natural Killer (NK) cells secrete cell-destroying enzymes upon recognition of any nucleated cell with abnormal expression of major histocompatibility complex (MHC) class I. While these innate immune cells are proficient in the prompt local destruction of precancerous cells in the elimination phase, it is ultimately the adaptive immune compartment that is required for the establishment of systemic anti-cancer immunity. Adaptive immune cells are highly specialized, each possessing a unique receptor that recognizes a unique non-self antigen. When naïve lymphocytes bind to their cognate antigen (such as a tumor neoantigen) they undergo rapid proliferation and differentiation into

pools of effector and memory cells. The primary cells facilitating adaptive immunity are T cells and B cells, each with distinct activation and effector mechanisms. T cells bind processed antigen fragments that are displayed via MHC. Professional antigen presenting cells (APCs), such as dendritic cells (DCs), phagocytose foreign entities, displaying processed antigen to CD4+ T cells via MHC class II. Effector CD4+ T cells are known as T helper cells, whose function is to license activity of other cytotoxic immune cells against a specific threat via secretion of cytokines such as IFN-γ. CD8+ T cells specifically interact with cancer cells displaying mutant cognate epitopes via MHC class I. Effector CD8+ T cells, called cytotoxic T cells, release enzymes such as perforin and granzyme to directly induce cell death of the target cell. Cytotoxic T cells are thought to be the most potent mediators of anti-tumor immunity (42). Unlike T cells, B cells bind their cognate antigen as it exists natively expressed extracellularly of a cancer cell or microbe. Upon antigen binding and stimulatory signals from helper T-cells, naïve B cells differentiate into antibody-secreting effector cells called plasma cells. Antibodies, essentially secreted B cell receptors, bind to target antigens, neutralize them, and facilitate their destruction via the complement cascade. Activated T and B cells may also differentiate into memory cells. Memory lymphocytes persist for years and lower the antigenic threshold required to activate a targeted immune response, effectively providing the host with long-term protection against similar future threats.

A crucial component of healthy tumor elimination is immunoregulation, a system of limiting mechanisms that ensure the specificity, proportionality, and resolution of immune targeting to minimize damage to healthy host tissue. A classic example is the co-stimulation required for CD4+ T cell activation. Binding of the CD4+ T cell receptor to MHC class II on APCs is insufficient for activation alone. A second interaction between CD28 on the T cell and B7, a membrane protein upregulated in mature APCs, is required to induce T cell proliferation. In fact, naïve T cells that bind MHC in the absence of co-stimulation can become anergic, a process called peripheral tolerance. Even activated T cells that do receive appropriate co-stimulation soon begin expressing the immune checkpoint CTLA-4, a receptor with significantly higher affinity for B7 than CD28, leading to termination of co-stimulation and prevention of an excessive immune response. In addition to internal regulation mechanisms in effector cells, there exist myeloid and lymphoid cells with dedicated immunosuppressive functions. M2 macrophages, for example, are powerful mediators of inflammation resolution, secreting a variety of immunosuppressive cytokines and growth factors that inactivate cytotoxic activity and promote tissue repair. In the adaptive compartment, regulatory T cells (T-regs) also secrete immunosuppressive cytokines and express ligands that restrain the activation of effector T cells, such as CTLA-4 (43). Nearly all immune

cells have been shown to contribute to angiogenesis and vascular remodeling, both of which are required for tumor progression (44).

Oncogenic disruption of the coordinated actions of immunosurveilance and immunoregulation begins during the second phase of immunoediting, known as equilibrium (41). During this state, cancer cells lay dormant, avoiding immune recognition but still constrained from rapidly proliferating or metastasizing. Little is known about the precise mechanisms by which this occurs, but it is thought that general genomic instability combined with selective immune pressures induced during the elimination phase produce genetic or epigenetic modifications that alter antigenicity or antigen presentation via MHC class I (45, 46). Equilibrium may last many years before progression to escape (47).

Clinically detectable tumors represent progression to the escape phase, where they have accumulated enough immunologically relevant adaptations to simultaneously evade immune detection and commandeer immunoregulatory mechanisms for their own growth and metastasis. The extent and nature of immune escape varies substantially between and even within tumor types, often involving both innate and adaptive dysregulation. Cells with mutations in MHC presentation machinery can evade surveilling NK or CD8+ T cells (48, 49). Many tumors upregulate immune checkpoint molecules such as CTLA-4 to interfere with appropriate co-stimulation (50). PD-L1, another immune checkpoint frequently overexpressed by tumors, is capable of inducing exhaustion, anergy, or apoptosis in effector T cells (50).

It is important to note that the escape phase is not characterized by a lack of inflammation, but rather a lack of *appropriate* inflammation. Indeed tumors are often densely infiltrated with leukocytes, sometimes likened to a wound that never heals (51). Tumoral secretion of high levels of cytokines including TGF-β, IL-1, IL-4, IL-6, and IL-10 elicit excessive recruitment and activation of immunosuppressive myeloid cells and T-regs (52). Pro-tumor myeloid cells such as M2 macrophages and myeloid derived suppressor cells (MDSCs) are innate immune cells ideally suited to creating a permissive tumor microenvironment (53, 54). In addition to suppressing cytotoxic functions, such cells secrete a variety of growth factors, angiogenic molecules, and matrix metalloproteinases (MMPs) that enable the tumor to grow and metastasize (52). High levels of pro-tumor myeloid cells are almost invariably correlated to poorer prognostic outcomes across a number of tumor types (55–60).

Targeting the mechanisms of immunoediting has unleashed a powerful new type of cancer treatment: immunotherapy (40, 52). This growing class of small molecules, vaccines, monoclonal antibodies, and cell-based therapies are intended to activate a patient's own immune system against malignancy. Among the most well studied and successful immunotherapies are the

checkpoint inhibitors anti CTLA-4 and anti-PD1. This category of monoclonal antibodies target the immunoregulatory mechanisms hijacked by cancer cells that prevent anti-tumor T-cell activation. Blockage of CTLA-4 is thought to both limit competition for B7 during co-stimulation of effector T cells and attenuate the immunosuppressive effects of regulatory T cells (61). Similarly, anti-PD1 targets the tolerogenic program induced by PD1 on effector T cells (62). FDA approved formulations of anti-CTLA4 (e.g. Ipilimumab) and anti-PD1 (e.g. Nivolumab, Pembrolizumab) have seen remarkable clinical success in many tumor types including melanoma (63–65), non-small cell lung carcinoma (NSCLC) (66, 67), colorectal cancer (68, 69), and renal cell carcinoma (RCC) (70). Combination of ipilimumab and nivolumab has led to synergistic therapeutic benefit in several clinical trials, rapidly becoming first line therapy for metastatic melanoma and certain metastatic NSCLC subtypes (71–74). Checkpoint inhibitors can elicit durable responses in some patients even after cessation of treatment, suggesting establishment of systemic immunity (75).

Still, two significant challenges are preventing widespread implementation of immunotherapy. First, clinical efficacy is highly dependent on the nature of the tumor microenvironment (TME). For example, in a recent clinical trial of nivolumab combined with the indoleamine-pyrrole 2,3-dioxygenase 1 (IDO1) inhibitor epacadostat in solid tumors, patient response was 71% in PD-L1 positive patients and only 29% in PD-L1 negative patients (76). Indeed, in the case of checkpoint inhibition, patient response varies drastically across tumor types, critically dependent on the presence of preexisting intratumoral T-cells, and/or neo-antigens. Even in tumors with sufficient T cell infiltration, the effects of checkpoint blockade can be nullified by overwhelming immunosuppressive myeloid and T-regulatory cell signaling (77). A second major hurdle for immunotherapy is toxicity from off target immune activation. Immunotherapeutic doses required to induce durable responses lead to severe (grade 3 or 4) autoimmune side effects in as many as 13% of patients (75, 78). To expand the immunotherapy-responsive population and reduce the dose required to achieve durable responses, development of adjuvant approaches that increase immunogenicity while reducing tumor-supporting inflammation is necessary.

FUSTA may be uniquely positioned to meet this need. In addition to effective tumor ablation, recent preclinical (79–86) and clinical (87–95) evidence suggests FUSTA is capable of eliciting immune responses in the TME. The mechanism(s) of this induced immunity are unclear. Several studies show FUSTA elicits the release of damage associated molecular patterns (DAMPs), such as heat shock protein 70 (HSP70), into the TME (93, 96). DAMPs are endogenously expressed danger signals that elicit sterile inflammation by binding to pattern recognition receptors (PRRs), activating many pathways also engaged by pathogens. Others

propose FUSTA stimulates the release of tumor antigens, increasing their availability to DCs for acquisition, trafficking to tumor-draining lymph nodes, and presentation to tumor-specific T-cells (90, 93, 97, 98). FUSTA treated tumor lysate has been shown to enhance activation of effector T-cells when given as a tumor vaccine or loaded onto injected DCs compared to untreated tumor lysate in models of hepatocellular carcinoma (99, 100). Other studies have shown local release of cytokines such as TNF-α and IFN-γ, and increased recruitment of various immune cells after FUSTA (90, 98). These promising investigations have generated interest in the ability of FUSTA to simultaneously establish primary and systemic tumor growth control, the so-called abscopal effect. Significant effort is also underway to test whether FUSTA can sensitize immunologically "cold" tumors to immunotherapy (85, 101). The prospect of locally targeted, non-invasive induction of tumor immunogenicity and responsiveness to immunotherapy represents an exciting therapeutic opportunity, though considerable translational hurdles remain.

1.3 Crossing the Blood Brain Barrier with Focused Ultrasound

The blood-brain barrier (BBB) is essential to maintaining homeostasis in the central nervous system (CNS). The BBB describes a specialized vasculature, consisting of nonfenestrated endothelium, pericytes, astrocytic processes, microglia, and basement membrane working in concert to precisely permit nutrient transport while protecting against toxins and pathogens. However, the BBB also presents a significant neuropharmacological obstacle, preventing 98% of small-molecule therapeutics and nearly 100% of large-molecule therapeutics from accessing the CNS (102). Significant efforts have focused on strategies to bypass or disrupt the BBB. Methods to bypass the BBB, including intracranial injection and intracerebroventricular infusion, require surgical intervention and thus carry significant risk. Chemical methods to disrupt the BBB, such as mannitol, cause global BBB disruption and lead to considerable neurotoxicity.

Focused ultrasound (FUS) following IV infusion of microbubbles (MB) is a promising approach for BBB disruption (BBBD) (103–105). In this technique, ultrasound waves produced extracorporeally pass through the skull and cause MB circulating in a targeted region of the brain to oscillate. These oscillations disrupt BBB tight junctions and enhance transport of molecules into the brain parenchyma. FUS induced BBBD is an attractive alternative to surgical and chemical methods as it is targeted, non-invasive, and repeatable. Many therapies normally restricted by the BBB have been successfully delivered with FUS + MB, including antibodies (106–108), chemotherapeutics (109–111), neural stem cells (112, 113), and genes (114–116).

BBBD with FUS is reversible and may be applied in a manner that yields little to no histological damage after repeated treatment (104, 117, 118). However, recent molecular profiling

studies have demonstrated that, under certain conditions, FUS induced BBBD can lead to increased expression of pro-inflammatory cytokines, homing receptors, and damage associated molecular patterns (DAMPs) as well as increased systemic macrophage accumulation (119). These findings are consistent with sterile inflammation (SI), an innate immune response normally triggered by traumatic brain injury or ischemia. The potential for FUS to induce local SI has sparked discussion of the cellular implications of FUS, both where additional inflammation may be desirable (such as cancer or Alzheimer's) or undesirable (such as multiple sclerosis or stroke) (120–123).

Two distinct methods exist for monitoring BBBD treatments: magnetic resonance imaging (MRI) and passive cavitation detection (PCD). Modern FUS devices are commonly registered with MRI scanners to precisely target sonications. After systemic administration of an MR contrast agent such as gadolinium, BBBD with FUS can be confirmed by visualization of contrast enhancement in T1-weighted MR images of the targeted regions. The extent of barrier disruption may be estimated by ratiometrically comparing contrast enhancement of the treated region with its pretreatment or contralateral counterpart. Alternatively, a more quantitative measure of barrier permeability may be obtained by performing dynamic contrast enhanced (DCE) MRI (124). In this method, a bolus of contrast agent is intravenously injected followed by serial MRI scanning as the contrast agent circulates. Ktrans, the rate constant of gadolinium efflux from the vasculature to the extravascular extracellular space, is determined voxel-wise by nonlinear least squares fitting of the convolution of the concentration of contrast agent in plasma with a single exponential impulse response function. While DCE-MRI is more quantitative than simple ratiometric imaging, it is also requires significantly more experimental and computational effort, making it impractical clinically.

The second method for monitoring BBBD experiments is PCD, sometimes called acoustic emissions monitoring. This technique utilizes a listening hydrophone positioned outside the skull, often embedded directly in the FUS transducer, to record pressure waves produced by MB oscillating in response to FUS. Steady oscillation of MB, called stable cavitation, imparts the mechanical forces on vessel walls needed to disrupt the BBB and produces concomitant peaks at harmonics (2f, 3f, 4f, f = operating frequency of the treatment transducer), the sub harmonic (0.5f), and ultra-harmonics (1.5f, 2.5f, 3.5f) in the Fourier domain. Meanwhile, unstable oscillation and violent collapse of MB, called inertial cavitation, can damage neuronal tissue and produce concomitant broadband signal (in-between harmonics) in the Fourier domain. Unlike MRI-based methods, PCD can be performed in real time to monitor FUS treatments. It has been proposed to

incorporate PCD-based feedback control into BBBD systems to minimize cavitation damage to the brain (125, 126).

Given the general applicability of noninvasively delivering new therapeutics to the brain, it is not surprising that FUS BBBD has been preclinically validated across diverse pathologies. In rodent models of glioma, FUS BBBD has led to enhanced efficacy and delivery of chemotherapies including doxorubicin (127–129) and carboplatin (130, 131). Recent work from our lab demonstrated a significant survival advantage for glioma bearing mice treated with the immunotherapeutic antibody αCD47 after FUS BBBD (132). Delivery of antibodies across the BBB also demonstrated reduced plaque burden and increased neurogenesis in models of Alzheimer's disease (133, 134). Research from our lab and others have shown FUS-enhanced gene therapy reduces functional deficits in multiple models of Parkinson's disease (135, 136). Additionally, the potential for FUS BBBD to be therapeutic even in the absence of drugs is an active area of investigation (109, 121, 137).

1.4 Translational Challenges Facing Non-Ablative FUS Applications in the Age of Precision Medicine

Immunomodulation and BBBD with FUS are promising therapeutic applications. Though they are technically distinct modalities, we argue the current challenges and knowledge gaps faced by each are fundamentally similar. Clinical development of both therapies is comparable, each having only been evaluated in a handful of phase I clinical trials. Research of both is highly interdisciplinary, requiring expertise in engineering (acoustics, imaging, electronics, signal processing), complex biological microenvironments (tumors, blood brain barrier), and medical translation (disease-specific pathogeneses, practical feasibility, potential side effects). We further argue both must be evaluated through the lens of precision medicine, that is, the modern trend toward adapting therapy to the specific pathology of a specific patient to enhance outcomes and minimize unnecessary toxicity. In this section we will review open questions for FUS immunomodulation and BBBD, and propose innovative approaches needed to answer them.

While cancer immunomodulation with FUSTA in combination with immunotherapy is theoretically appealing, optimal implementation has not been achieved. In a preclinical investigation of the efficacy of FUSTA immunotherapy combination strategies, Silvestrini et al. concluded that synergistic benefits of FUSTA-immunotherapy are crucially dependent on timing of administration and identity of immunotherapeutics (85). Recent work from our lab highlights that targeting tumor-specific immunosuppressive mechanisms may also be necessary to reap the benefits of FUSTA immunogenicity (138). We identify two barriers to effective design of FUSTA-

immunotherapy combinations. First, the molecular mechanisms of FUSTA-induced immunomodulation are poorly understood, inhibiting rational selection of pharmacological synergists. As discussed previously, reported immune responses to FUSTA include i) heat shock protein (HSP) production inducing enhanced antigen presentation (90, 93, 97, 98), ii) increased immunostimulatory molecules including TNF-α, IFN-γ, and IL-12 (90, 98), iii) reduced pro-tumor molecules including IL-10 (90), and iv) increased infiltration of dendritic cells (DCs), CD4+ T-cells, CD8+ T-cells, and natural killer cells (83, 98, 139, 140). However, it is still unclear which, if any, of these are dominant drivers of FUSTA-induced antitumor immunity. Second, there is a limited appreciation of the nature and extent to which adaptive resistance mechanisms develop in response to FUSTA. It is well known that cancer cells develop resistance to radiotherapy, chemotherapy, and immunotherapy (72, 141–147). Knowledge of these mechanisms in the context of FUSTA is of special importance to clinicians and the development of FUSTA-immunotherapy strategies.

BBBD with FUS faces parallel knowledge gaps. First is an incomplete understanding of precisely how FUS-activated MB enhance BBB permeability. While the prevailing theory is that MB oscillation induces mechanical forces that disrupt tight junction organization, recent evidence suggest a significant role for active transcellular transport (148, 149). Second, aside from delivery mechanisms, the impact of FUS BBBD on the CNS landscape is also unclear (138). Recent reports of sterile inflammation (SI) caused by FUS-activated MB have raised concerns over its feasibility for repeated clinical application. Studies have demonstrated this response can last for at least 24 h after a single sonication, and is dependent on MB dose and FUS pressure (119, 150–152). Proposed causes for this response include damage due to direct and indirect acoustic forces on the neurovascular unit, ischemia reperfusion injury due to FUS-induced vasospasm, and leakage of blood into the brain parenchyma (119, 150–152). However, transient SI can provide beneficial effects in certain disease contexts with respect to clearance and regeneration (153). Indeed, this may be the primary mechanism by which FUS promotes Aβ plaque clearance in models of Alzheimer's disease (154). Similarly, neurogenesis observed after FUS may be attributable to tissue repair mechanisms preceded by SI (155, 156). Thus, a more complete understanding of how FUS BBBD affects the CNS and the dependence of these effects on experimental parameters are required to facilitate clinical utilization.

We propose the complex challenges facing translation of both immunomodulation and BBBD with FUS must be addressed by proportionally advanced methods. Because FUS simultaneously affects parenchyma, stroma, microvasculature, and lymphatics, the ensuing cascade of bioeffects has proven difficult to deconvolve with conventional biological assays.

Application of high throughput, single cell, and bioinformatics analyses of FUS-treated tissue will enable holistic interrogation of the effects of immunomodulation or BBBD on the tissue microenvironment. Importantly, a systems-level approach permits evaluation of undesirable effects induced by therapy. Biomedical investigations are susceptible to valuing experiments that validate a positive therapeutic effect over a potential toxicity. We anticipate immunomodulation and BBBD with FUS are not impervious to this susceptibility, and therefore propose unbiased approaches like RNA-sequencing as a countermeasure.

Ultimately, we argue immunomodulation and BBBD must be studied as precision medicines. Compared to simple tissue ablation, they are significantly more sophisticated techniques that generate local bioeffects tunable to the patient's disease and adjuvant pharmacological therapy. Leveraging these intricate relationships to maximize patient benefit while minimizing toxicity will require data-science driven investigations, consistent with the paradigm of precision medicine. Successful application of this approach is demonstrated herein. In Chapter 2, we use high throughput transcriptomic and single cell approaches to identify mechanisms of immunogenicity and immunosuppression induced by FUSTA in murine melanoma. We then leverage these insights to design new FUSTA-immunotherapy strategies capable of enhancing tumor growth control. In Chapter 3, we perform bioinformatics analyses of FUSTA in combination with pembrolizumab in phase I clinical trials. We contextualize these results by comparing immunological signatures against those generated by high dose radiation conformal therapy (HDCRT) combined with pembrolizumab. In Chapter 4, we investigate the effect of anesthesia on FUS BBBD, enumerating its potential to differentially affect metabolism, platelet activity, tissue repair, and signaling pathways. In Chapter 5, we use single cell RNA-sequencing to interrogate how the distribution of transfected brain-resident cell populations and their transcriptomes are affected by peak-negative pressure after FUS BBBD. Finally, in Chapter 6, we identify gene sets significantly correlated with measures of FUS BBBD, including contrast enhancement and PCD. Together, this body of work demonstrates clear benefits of data-science approaches to emerging FUS applications, and contributes significant novel insights that will help establish FUS immunomodulation and BBBD as precision therapies capable of improving patient health.

Chapter 2: Tuning Immune Mechanisms Induced by Focused Ultrasound Thermal Ablation Enhances Control of Murine Melanoma

Alexander S. Mathew, E. Andrew Thim, Alexandra R. Witter, Christopher J. Margraf, Ji Song, Lydia E. Petricca, Awndre E. Gamache, Natalie E. Johns, Timothy N.J. Bullock, and Richard J. Price.

2.1 Abstract

Focused ultrasound thermal ablation (FUSTA) is a completely non-invasive energy deposition technology capable of thermally coagulating solid tumors. Promising preclinical and clinical studies suggest that FUSTA can also generate immunostimulatory signatures in the tumor microenvironment (TME), which could promote resistance to recurrence, as well as sensitize refractory tumors to immunotherapy. To more completely delineate, contextualize, and leverage these signatures, we performed transcriptomic and immunophenotypic profiling of the TME at distinct intervals following FUSTA in an aggressive murine melanoma model. Bioinformatics analyses revealed that FUSTA triggers a dynamic cascade of pro- and anti- tumor immune mechanisms, consistent with sterile inflammation and wound healing. Flow cytometry analyses of conventional dendritic cell (cDC) subsets showed that FUSTA enhances tumor specific antigen acquisition in tumor draining lymph nodes, but not the activation signals required for maturation and activation of effector T cells. Leveraging these mechanistic insights, we determined that combination of αCTLA-4 and αCSF1R with FUSTA improves responses in distant melanomas compared to either therapy alone. Protein level validations of RNA-sequencing data proved that FUSTA activates inflamamsomes in the TME. Blockage of the NLRP3 inflammasome with a small molecule inhibitor extended the duration of tumoristasis after FUSTA, suggesting that pyroptosis and IL-1β release may accelerate tumor regrowth after ablative therapy. Together, this work details novel immunogenic and immunosuppressive reactions to FUSTA, and how the balance between the two can be pharmacologically weighted to synergistically promote systemic anti-tumor immunity.

2.2 Introduction

Melanoma incidence is increasing faster than any other form of cancer (157). Metastatic malignant melanoma (MMM) has an especially dismal prognosis, with a median survival of 5.3 months (158). Like other cancers, MMM has adapted multiple mechanisms to evade immune recognition, including upregulation of immunosuppressive molecules such as PD-L1, PD-L2, VEGF, and TGF-β, increased recruitment of tumor associated macrophages (TAMs), and induction of T-cell exhaustion (159). The advent of immunotherapeutics that block these mechanisms, such as the checkpoint inhibitors pembrolizumab and ipilimumab, has offered exciting therapeutic potential in MMM treatment (160, 161). These therapies can restore normal immunosurveilance mechanisms, leading to durable anti-tumor responses even after cessation of treatment. However, the clinical response to immunotherapy is highly dependent on the nature of the tumor microenvironment (TME). Intratumoral PD-L1 expression (162), CD8+ T cell density (163), and mutational load (164), for example, positively predict response to checkpoint inhibition in melanoma, while myeloid cell infiltration (165, 166) and beta catenin (167) expression are correlated with immunotherapy resistance. Strategies capable of reconditioning immunologically subdued tumors offer the promise of extending the benefits of immunotherapy to significantly more melanoma patients.

Focused ultrasound thermal ablation (FUSTA) represents notable potential in this capacity. This non-invasive modality directs conforming acoustic waves to small focal spot in pathological tissue, causing rapid coagulative necrosis, while tissue outside of the focus remains largely unaffected. FUS may be coupled to MRI or diagnostic ultrasound for targeting and treatment monitoring, and is an attractive therapeutic alternative to surgery or radiation for the reduction of solid tumors. In addition, FUSTA offers the distinct advantage over radiation in that it is non-ionizing, enabling repeated treatment. Preclinical and clinical evaluations suggest FUSTA can produce an immunologically favorable TME. FUSTA has been reported to elicit i) heat shock protein (HSP) production inducing enhanced antigen presentation (90, 93, 97, 98), ii) expression of immunostimulatory molecules including TNF-α, IFN-γ, and IL-12 (90, 98), iii) reduced pro-tumor molecules including IL-10 (90), and iv) increased infiltration of dendritic cells (DCs), CD4+ T-cells, CD8+ T-cells, and natural killer cells (83, 98, 139, 140). These promising signatures have generated interest in the ability of FUSTA to simultaneously establish primary and systemic tumor growth control (otherwise known as the abscopal effect), or sensitize immunologically “cold” tumors to immunotherapy.

The potential of using FUSTA to increase tumor visibility to the host immune system has yet to be fully realized, which we attribute to an incomplete understanding of precisely how

ablation perturbs the immune landscape of the TME. It is still unclear which, if any, of the FUSTA-induced immune signatures reported thus far are dominant drivers of antitumor immunity. The possibility for FUSTA to upregulate tumor-permissive immune or stromal responses in the TME remains severely underexplored. Further, there is a limited appreciation of the nature and extent to which adaptive resistance mechanisms develop in response to FUSTA. It is well known that cancer cells develop resistance to radiotherapy, chemotherapy, and immunotherapy (72, 141–147). Herein, we implement high throughput transcriptomic and single cell immunophenotypic approaches to serially profile the evolution of the immune response to FUSTA in an aggressive melanoma model. We identify temporal modulation of both anti- and pro-tumor mechanisms by FUSTA and assess their implications on conventional dendritic cell (cDC) antigen acquisition and maturity. These insights facilitate rational selection of immunotherapeutics that increase the likelihood of response in distant tumors when paired with FUSTA. Finally, we demonstrate that FUSTA triggers the assembly of the inflammasome in tumor cells, the blockage of which further delays regrowth of ablated tumors. Together, this work shows FUSTA generates a complex cascade of both immunogenic and immunosuppressive responses in the TME, and that pharmacological polarization of these responses is a viable strategy for improving immune recognition of refractory tumors.

2.3 Results

2.3.1 Serial RNA-sequencing of FUSTA Treated B16F10 Tumors

A custom ultrasound-guided focused ultrasound system was used to deliver FUSTA treatments to tumor bearing mice (**Figure 2.1A**). An integrated user interface facilitated control of FUS electronics, diagnostic US imaging, treatment planning, and 3D stage control. FUSTA was administered to flank tumors in a bidirectional raster scan with 2 mm spacing between individual 0.5 mm-diameter ablation sites (**Figure 2.1B**). To evaluate the effects of FUSTA on tumor growth dynamics, we treated mice bearing flank B16F10 tumors with FUSTA or sham and monitored tumor volume until mice met euthanasia criteria (**Figure 2.1C**). Though FUSTA was transiently tumoristatic, tumors began to rapidly regrow approximately 3 days after FUSTA treatment.

To assess how the tumor microenvironment (TME) reacts to FUSTA through time, we performed serial RNA-sequencing at 8 h, 24 h, 72 h, and 168 h after treatment to reflect acute, subacute, regrowth initiation, and exponential regrowth phases respectively (**Figure 2.2**). Differential gene expression (DGE) was computed at each time point relative to time-matched shams, to account for confounders such as baseline temporal tumor evolution, reactivity to anesthesia, tumor site preparation, degassed water bath exposure, and tissue harvest batch effects. DGE was marked 8 h post FUSTA, with significant upregulation of heat shock proteins (HSPs) and cytokines (**Figure 2.2A**). Notably, expression of the melanocyte transcript tyrosinase (*Tyr*) was significantly downregulated acutely after FUSTA. Of the 27 genes significantly (p-adjusted < 0.05) differentially expressed at 24 h, we highlight residual upregulation of HSPs and cytokines, along with downregulation of the transcripts for the cell surface proteins *Scara5* and *Ly6a* (**Figure 2.2B**). Interestingly, most of the transcripts significantly affected 72 h post FUSTA were upregulated, and included macrophage associated markers such as *Lyz2*, *Mpeg1*, and *Csf1r* (**Figure 2.2C**). By contrast, the majority of genes differentially regulated at 168 h post FUSTA were downregulated and included MHC class I genes *H2-K1* and *H2-D1* (**Figure 2.2D**).

Next, we performed gene set enrichment analysis at each time point to interrogate relative regulation of biological processes after FUSTA, followed by leading edge analyses to enumerate the contributory genes. Pathways associated with sterile inflammation such as chemokine activity, myeloid leukocyte migration, and IL-1 secretion were enriched or trending toward enrichment during the first 3 days of FUSTA treatment, followed by net repression at day 7 (**Figure 2.2E**). Engagement of pathways associated with initiation of an adaptive immune response, including MHC class I antigen processing and presentation, T cell migration, and type I interferon signaling were enriched at 8 h and 72 h, but repressed at 24 and 168 h post FUSTA (**Figure 2.2F**). We observed consistent over representation of genes associated with tissue remodeling including

wound healing, connective tissue development, and angiogenesis at all post FUSTA timepoints (**Figure 2.2G**). We observed temporally variable regulation of several miscellaneous cellular homeostatic pathways (**Figure 2.2H**). Oxidative stress and cellular division were generally discordant, with the latter repressed for the first 3 days after FUSTA and significantly enriched at 7 days.

2.3.2 FUSTA Induces Myeloid Predominance in the TME and Accumulation of Tumor Antigen in Lymph Node-Resident Dendritic Cells

We performed cell type deconvolution (168) on RNA-seq data to estimate the abundance of immune cell subsets in the TME at different times after FUSTA or sham treatment (**Figure 2.3A**). The absolute score, representing the total immune transcriptional content in the TME, was trending toward increase over sham at 8 h post FUSTA ($p = 0.19$), trending toward decrease at 24 h post FUSTA ($p = 0.18$), and significantly decreased at 168 h post FUSTA ($p = 0.01$). The total abundance of myeloid cells, including neutrophils, M2 macrophages, and activated mast cells were increased during the 3 days following FUSTA but decreased at 7 days. The average abundance of resting dendritic cells (DCs) was increased at all timepoints except 24 h, at which it was significantly decreased. Significant changes in the lymphoid compartment after FUSTA included an increase in naïve CD4+ T cell abundance at 24 h and a decrease in plasma cells at 168 h. The average CD8+ T cell abundance was decreased relative to time-matched shams at 24 h and beyond.

The significant depletion of resting DC signatures at 24 h led us to hypothesize that FUSTA enhances trafficking of tumor resident DCs to the tumor draining lymph nodes (TDLNs). To test this hypothesis, we treated mice bearing B16F1-ZsGreen-OVA tumors with FUSTA or sham, and harvested tumors and TDLNs for flow cytometry 24 h later (**Figure 2.3B**). We utilized a gating strategy capable of separating conventional DCs (cDCs) into cDC1 (CD8α+) and cDC2 (CD11b+) lineages, and analyzed both populations for acquisition of ZsGreen and metrics of antigen maturation, including percentage positivity of CD86 and mean fluorescence intensity (MFI) of MHC class II. Intratumoral CD11b+ DCs exhibited no change in ZsGreen acquisition, and significant decreases in both metrics of maturation 24 h post FUSTA. Maturation metrics in TDLN CD11b+ DCs were also significantly decreased, though nearly 4 fold more were positive for tumor antigen. The percentage of intratumoral CD8α+ DCs positive for ZsGreen or CD86 was significantly decreased 24 h after FUSTA, though their expression of MHC class II was trending toward increase. TDLN CD8α+ DCs were significantly more likely to be positive for ZsGreen after

FUSTA compared to sham, though they did not exhibit any significant changes in maturation metrics.

2.3.3 Combinatorial Administration of αCTLA-4 and αCSF1R Increases Likelihood of Abscopal Response after FUSTA

Transcriptomic and immunophenotypic profiling suggested that while FUSTA triggers sterile inflammatory mechanisms in the TME, they are not potent enough to activate anti-tumor immunity and/or are counteracted by a concomitant myeloid wound healing response. Therefore, we wondered whether pharmacological enhancement of co-stimulation via αCTLA-4 paired with blockade of tumor permissive myeloid cells via αCSF1R would effectively reorient the immune response to FUSTA toward improved tumor-specific recognition, destruction, and memory. To test this hypothesis, we established bilateral B16F10 tumors and treated mice with immunotherapy (ITx = αCTLA-4 on day -6, -3, and 0 + αCSF1R on day 0, 3, and 6) or control IgG combined with unilateral FUSTA or sham treatment (**Figure 2.4A**). We then monitored ipsilateral and contralateral tumor growth daily (**Figure 2.4B**), classifying tumors < 200 mm^3 in volume more than 7 days after FUSTA as responders. FUSTA + ITx elicited a larger proportion of ipsilateral and contralateral responders than either FUSTA or ITx alone (**Figure 2.4C**).

2.3.4 FUSTA Triggers Inflammasome Assembly, the Blockage of Which Delays Tumor Regrowth

We carefully examined GSEA results to identify specific signaling networks activated by FUSTA that may be contributing to the accumulation of tumor promoting myeloid signatures in the TME. Genes associated with the interrelated pathways of IL-1β production and inflammasome signaling were significantly enriched 8 h post FUSTA (**Figure 2.5A and 2.5B**). Expression of many HSPs, which can act as damage associated molecular patterns (DAMPs) in the initiation of inflammasome signaling, was markedly increased 8 h post FUSTA, with *Hspa1b* and *Hspb1* persisting at 24 h (**Figure 2.5C**). Through a combination of leading edge analysis and manual curation, we identified consistent upregulation of genes spanning the entire inflammasome pathway 8 h post FUSTA (**Figure 2.5D**). Significantly induced genes upstream of the inflammasome include the aforementioned HSPs, as well as *Il33*, *P2rx7, Cd14*, and *Txnip*. *Nlrp3*, the gene encoding the core protein of the NLRP3 inflammasome itself, was significantly upregulated at 8 h, along with a trending increase in *Casp1* expression. Downstream of

inflammasome activation, *Il1b*, *Il1r1*, *Il1rl1,* and *Il18rap* were all significantly upregulated 8 h post FUSTA.

To verify our transcriptional results, we performed immunohistochemical staining for HSP70 in B16F10 tumors acutely after FUSTA treatment. These mice were also pretreated with vehicle or MCC950, a small molecule inhibitor of NLRP3 inflammasome assembly (169). HSP70+ staining was observed after FUSTA whether mice were pretreated with vehicle or MCC950 (**Figure 2.6A**). We next interrogated inflammasome assembly via quantification of apoptosis-associated speck-like protein containing a CARD (ASC) specks by immunofluorescence (**Figure 2.6B**). FUSTA induced a significant increase in the number of intratumoral ASC specks compared to sham, the magnitude of which was partially abrogated by pretreatment with MCC950 (**Figure 2.6C**). To test whether FUSTA-induced inflammasome assembly was attributable to the tumor cells themselves or tumor-resident host cells, we repeated these studies in NLRP3 knockout mice bearing WT B16F10 tumors. Neither FUSTA-induced HSP70 expression nor ASC speck formation were affected by knockout of host NLRP3 (**Figure 2.S1**), implying that FUSTA elicited speck formation occurs predominantly in tumor rather than host cells. Finally, we wondered whether pretreatment with MCC950 would affect tumor growth dynamics following FUSTA treatment. Remarkably, administration of a single dose of MCC950 with FUSTA extended the average duration of tumoristasis compared to FUSTA alone, and achieved a complete tumor regression in one mouse (**Figure 2.6D**).

2.4 Discussion

FUSTA is a promising tool for simultaneous tumor debulking and immunological priming. The latter function has not yet been optimized in refractory tumor models, in part due to insufficient detail on immunologically relevant reactions and adaptations to FUSTA. In the current study, we serially profiled the evolution of the melanoma TME during distinct phases of reaction to FUSTA. The unbiased, high throughout, and temporal nature of these analyses enabled identification of immunostimulatory and immunosuppressive adaptations within the TME, as well as potential resistance mechanisms to FUSTA. αCTLA-4 and αCSF1R, specifically selected to synergize with these mechanisms, increased the likelihood of distant responses in the highly aggressive B16F10 melanoma model after FUSTA. We also demonstrated that FUSTA acutely activates the inflammasome, which possibly contributes to undesirable myeloid responses observed in the days following treatment. Preemptive blockage of this pathway extended the duration of growth control following FUSTA, highlighting a novel strategy for therapeutic enhancement of this exciting technology.

Thermal ablation is the most clinically mature application of focused ultrasound, already garnering FDA approval for the non-invasive volume reduction of uterine fibroids, osteoid osteomas, and prostate cancer. Its application is also highly diverse, with infinite permutations of parameters (frequency, duty cycle, intensity, treatment density, scanning pattern, etc.) falling under the umbrella of “FUSTA”. Important prior work has shown that these parameters are immunologically relevant. For example, increased spacing between adjacent sonications has been directly correlated to immunogenicity, hypothetically due to reduced neoantigen denaturation and preservation of danger signals in the peripheral “transition zone” surrounding directly coagulated tissue (83). To maximize immunostimulatory potential while still maintaining clinical relevance, we implemented the sparsest ablation scan that still reliably controlled tumor growth (2 mm lateral spacing between 0.5 mm wide treatment foci). The tumor growth profile following FUSTA with these parameters then suggested the 4 time points of interest for RNA-seq. During the acute (8 h) and subacute (24 h) phases, tumor was maximally controlled and likely undergoing the strongest immunomodulatory stimuli. Tumor regrowth generally began around day 3, and returned to exponential growth around day 7.

The most marked DGE was observed 8 h post FUSTA, with 1439 genes significantly up or downregulated. These genes were largely associated with a sterile inflammatory response, characterized by the upregulation of DAMPs (*Hspa1a, Hspa1b, Cryab)*, cytokines (*Cxcl3, Il1b*, *Cxcl5*) and oxidative stress markers (*Jun, Fos, Ptgs2*). FUSTA upregulated many genes that create favorable environment for engagement of adaptive immune mechanisms, such as

proteasomes *Psmd7, Psmb8,* and *Psmd1* which contribute to antigen processing and presentation via MHC class I (170). Increased antigen availability is thought to be one of the most potent mediators of immunogenicity by FUSTA (93, 99, 140), which our data supports. The upregulation of type I interferon-associated genes (*Egr1, Oasl, Irf6*) along with cytokines chemotactic for T cells (*Ccl2, Cxcl10, Ccl3*) are encouraging findings for the activation and recruitment of lymphoid effectors.

The physiological function of sterile inflammatory signaling is the preservation of host tissue after an insult such as FUSTA. As such, we also observed significant upregulation of transcripts associated with wound healing, which generally contributes to a tumor permissive microenvironment (171). *Il33*, for example, was significantly upregulated 8 h post FUSTA. This cytokine is closely tied to Th2 immune responses, wound healing, and generally poorer outcomes across a number of tumor types (172–174). *Il6,* another powerful pro-tumor cytokine generally associated with poor prognosis (175, 176), was also upregulated acutely after FUSTA, in agreement with previous results (177). These cytokines generally increase the recruitment of tumor promoting immune cells such as neutrophils, tumor associated macrophages, myeloid derived suppressor cells (MDSCs), and mast cells to the TME. Cell type deconvolution demonstrated trending increases in neutrophils, activated mast cells, and M2 macrophages in the 3 days post FUSTA. Consideration of these tumor permissive phenomena will be crucial to translation of FUSTA, as they likely blunt many of the desired immunogenic mechanisms.

At 24 h post FUSTA, differential gene expression was significantly attenuated. Though residual HSP and cytokine upregulation was still observed, GSEA revealed that the net effect on the TME was a repression of gene sets associated with adaptive immunity. mRNA expression of the extracellular matrix remodeling enzyme *Timp1*, which is correlated with poor prognosis in a number of cancers, was one of the few genes significantly upregulated at 24 h post FUSTA (178–180). *Tgfb1* and *Tgfbi,* critical regulators of the wound healing response were also identified by leading edge analysis as contributory genes induced at this subacute timepoint. Angiogenesis and connective tissue development pathways maintained their significant enrichment at 24 h. Together, these data suggest that the anti-tumor immune phenotype of FUSTA is relatively short-lived, possibly overwhelmed by the persistence of wound healing mechanisms.

In our hands, the shift from tumoristasis to tumor regrowth occurs approximately 3 days after FUSTA in the highly aggressive B16F10 model. RNA-sequencing performed at this timepoint was highly consistent with a pro-growth TME, as evidenced by the significant upregulation of growth factor associated transcripts (*Tgfbi, Egfr*), matrix remodeling factors (*Mmp2, Col14a1*), and tumor associated macrophage markers (*Csf1r, Lyz2, Mpeg1*). However, expression of

immunogenic transcripts associated with antigen presentation (*Cd36, Fcerg1, Psmb9*), T cell migration (*Cxcl16, Ccr2, Myo1g*), and interferon signaling (*Irf1, Irf5, Irf8*) were also enriched at this time point. These data suggest the immune landscape of the TME is still characterized by a complex mixture of pro- and anti-inflammatory reactions 3 days after FUSTA.

Many B16F10 tumors treated with our FUSTA regimen return to exponential growth around 7 days after treatment. Though relatively few genes were significantly differentially expressed compared to time-matched controls, GSEA revealed a common phenotype of immune suppression. Both innate and adaptive immune pathways were significantly repressed at 168 h, further supported by a significant reduction in absolute immune representation by cell type deconvolution. The repression of wound healing responses, combined with enrichment of cell division, connective tissue development, and angiogenesis pathways suggest that the TME becomes highly permissive 7 days after FUSTA, consistent with the resolution phase of inflammation. Fascinatingly, *H2-D1* and *H2-K1*, the two classical murine MHC class I genes, were two of the very few genes significantly downregulated 168 h post FUSTA. Modification of MHC class I expression is a well-known consequence of cancer immunoediting (181–183), and may represent a novel resistance mechanism acquired by tumors surviving the selective pressure imposed by FUSTA.

Past studies have shown FUSTA enhances neoantigen availability for acquisition by antigen presenting cells (APCs) and enhances maturation of DCs (93, 99, 140). The significant reduction in intratumoral resting DC signatures at 24 h post FUSTA despite no differences in activated DC populations led us to investigate the relationship between tumor antigen and DCs more precisely. We probed Cd11b+ and CD8a+ conventional DCs (cDCs) for their acquisition of fluorescent antigen (ZsGreen) and maturation status (via CD86 expression and intensity of MHC class II expression). Intratumoral metrics of tumor antigen acquisition and DC maturation were generally decreased or unchanged 24 h post FUSTA, in alignment with the deconvolution data. These results suggest that either activated cDCs are trafficking away from the tumor or a predominance of tolerogenic signals in the TME are hindering DC activation. While cDC maturation was unchanged in the tumor draining lymph nodes (TDLNs) 24 h after FUSTA, the fraction of cDCs positive for tumor antigen was 4 times higher for both subtypes with strong statistical significance. Together, these data suggest FUSTA may enhance direct drainage of tumor antigen to the lymph nodes but not deliver appropriate signals for costimulation and activation.

Aggregating our findings from serial transcriptomic and immunophenotypic profiling revealed two principle barriers hindering the immunostimulatory potential of FUSTA - 1) a myeloid

driven wound healing response and 2) insufficient DC co-stimulation of tumor-specific T cells. We theorized that αCSF1R and αCTLA-4 would target these respective barriers. αCSF1R depletes tumor associated macrophage accumulation in the TME and has been shown to increase the proportion of CD8+ T cells in several tumor types (184–186). αCTLA-4 is a well-known checkpoint inhibitor thought to improve anti-tumor immunity by minimizing competition for CD86 during co-stimulation, and limiting regulatory T cell activation (187). αCSF1R is not effective in the B16F10 model (188) and αCTLA4 only slows B16F10 tumor growth if given very early after inoculation (189). The promising performance of these antibodies when combined with FUSTA represents a clinically actionable strategy for immunologically cold tumors.

We are the first to our knowledge to show that FUSTA elicits the activation of the inflammasome. This hypothesis was first generated given the consistent upregulation of DAMPs post FUSTA, along with key transcripts upstream and downstream of the inflammasome, including *Il1b*. We also report significant upregulation of *Nlrp3,* consistent with a recent study of FUSTA in a breast cancer model (177). Pyroptosis, a form of immunogenic cell death facilitated by inflammasome signaling, has also been reported as a consequence of radiation therapy (190) and certain chemotherapies (191–194). The primary product of pyroptosis is the release of interleukin 1 beta, a potent cytokine chemotactic for myeloid cells and generally associated with poor prognosis (195, 196). Blockage of inflammasome signaling via the small molecule NLRP3 inhibitor MCC950 has been shown to improve outcomes in head and neck squamous cell carcinoma due to reduced recruitment of MDSCs and TAMs (197). We hypothesize that the extension of tumor growth control observed by administration of MCC950 immediately prior to FUSTA attenuates the wound healing response induced by pyroptosis while preserving the immunogenic release of tumor antigen and DAMPs. Though pyroptosis generally occurs in immune cells, the fact that ASC speck formation was inhibited in WT mice pretreated with MCC950, but not NLRP3 knockout mice further suggest that the inflammasome is predominantly induced in tumor cells after FUSTA.

This work supports an emerging paradigm of modulating the innate immune response to FUSTA. A recent study from our group demonstrated that pharmacological depletion of MDSCs with gemcitabine in murine breast cancer facilitated T-cell mediated immune control via FUSTA (138). Silvestrini et al. combined the checkpoint inhibitor αPD1 with the TLR9 agonist CpG in a FUSTA-priming protocol capable of controlling distant tumors in a syngeneic model of epithelial cancer (85). Priming tumors with αCTLA-4 prior to FUSTA to maximize antigen presentation while controlling pro-tumor myeloid responses with αCSF1R after ablation is another clinically feasible approach presented herein. Alternatively, preemptively targeting of specific molecular signaling

pathways upstream of FUSTA-induced myeloid recruitment, such as inflammasome activation, could be employed with even fewer off-target side effects.

We acknowledge several limitations within this work. First, RNA-sequencing only provides transcript-level data which may not correlate with protein (198–201). Further, bulk sequencing of whole tumor cannot distinguish expression changes from alterations in cell-type distributions. The B16-ZsGreen-OVA cell line, which we used to track tumor antigen, is inherently more immunogenic than the B16F10 cell line, and therefore may exhibit distinct temporal and qualitative responses to FUSTA. The flow cytometry studies were performed in female C57BL/6 mice, while RNA-sequencing studies were performed in male C57BL/6 mice, which may limit direct comparisons between the two. Finally, we note that the tumors treated with +/- FUSTA +/- MCC950 were harvested at 4 h, while those extracted from WT vs NLRP3 KO mice treated +/- FUSTA were harvested at 8 h.

To summarize, we performed serial transcriptomic and immunophenotypic profiling to track the evolution of the melanoma microenvironment in response to FUSTA. Though clear immunostimulatory mechanisms were identifiable at early time points, the most durable induced processes were associated with a myeloid-driven wound healing response. Evaluation of cDC subsets revealed that while FUSTA enhances the availability of tumor-specific antigen in TDLNs, it does not contribute to their maturation. Combinatorial immunotherapy designed to target immune tolerance mechanisms induced by FUSTA effectively skewed the immune response toward systemic immune control. Similarly, preemptive targeting of the NLRP3 inflammasome via MCC950 extended the duration of FUSTA primary growth control, presumably due to the upstream inhibition of pro-tumor inflammation. Thus, this body of work contributes novel mechanistic insights and clinically actionable strategies likely to improve melanoma patient outcomes. Future investigations should evaluate the potential of these the therapeutic combinations to engage the adaptive immune system, as well as their generalizability to other immunologically subdued tumor types.

2.5 Materials and Methods

2.5.1 Animals

8-10 week old male C57BL/6 mice obtained from Charles River were used for all *in vivo* studies unless otherwise specified. Male NLRP3 KO mice (B6.129S6-*Nlrp3*^{tm1Bhk}/J, Jackson Laboratory) were generously provided by the laboratory of Dr. John Lukens (University of Virginia). All mice were maintained on a 12/12 h light/dark cycle and given food and water *ad libitum.* All animal experiments were approved by the Animal Care and Use Committee at the University of Virginia and conformed to the National Institutes of Health regulations for the use of animals in research.

2.5.2 Tumor inoculation

Mice were anesthetized via intraperitoneal injection of ketamine (50–70 mg/kg; Zoetis) and dexmedetomidine (0.25–0.5 mg/kg, Zoetis) in 0.9% sterile saline and placed on a heating pad. Inoculation sites were prepared by depilating right flanks for unilateral studies, or both flanks for bilateral studies followed by application of alcohol scrubs. 5E4 B16F10 cells or 4E5 B16F1-ZsGreen-cOVA cells suspended in 100 µL cold D-PBS were injected subcutaneously over 30 seconds in the right flanks. For bilateral studies, an additional 2E4 B16F10 cells were injected subcutaneously on the left flank. After leaving mice undisturbed for at least 30 minutes, anesthesia was reversed by subcutaneous administration of Antisedan. Tumor volume was monitored by digital calipers, computed as length x width x width/2. On the first days of FUSTA or drug administration, mice were randomly assigned to groups such that average group volumes matched.

2.5.3 Focused Ultrasound Thermal Ablation

FUSTA treatments were applied using a custom built ultrasound-guided FUS system. Briefly, this system features a 64 mm diameter single element focused transducer (H-101, Sonic Concepts) orthogonally registered to an 8 MHz linear ultrasound imaging array (15L8, Siemens). The FUS transducer was connected to an amplifier (1040L, Electronics & Innovation, Ltd.) and controlled by a function generator (AFG3052C, Tektronix). A custom MATLAB (Mathworks) interface integrated real time control of US imaging, stage motion, and FUS parameters.

After anesthetization and tumor depilation, mice were placed inside a holder connected to a 3-D motorized stage system (8MT175-100XYZ, Standa Ltd.). The mice were then lowered into a water bath containing 37 °C degassed water such that the tumor was fully submerged and

positioned at the intersection of FUS and imaging transducer beam paths. Based on US image guidance, sonications were applied in a 2D grid pattern covering the whole tumor, with the following parameters for individual sonications: frequency = 3.3 MHz, duty cycle = 100%, acoustic power = 12 W, sonication duration = 10 s, spacing between sonications = 2 mm. Two grids separated by 1 – 2 mm in the Z axis were applied. For sham treatments, mice were anesthetized and placed in the same water bath without FUS treatment for approximately 5 minutes. After treatment, anesthesia was reversed by subcutaneous Antisedan administration.

2.5.4 MCC950 Administration

For MCC950 studies, MCC950 (Invivogen) was dissolved in sterile DMSO to a concentration of 3 mg/mL. One hour prior to FUSTA or sham treatment, mice were administered 100 µL MCC950 solution (300 µg MCC950) or DMSO vehicle via intraperitoneal injection.

2.5.5 Immunotherapy Administration

For immunotherapy studies, mice were given control IgG (250 µg IP, clone 2A3, Bio X Cell) on days -6, -3, 0, 3, and 6 or a combination of anti-CTLA4 (250 µg IP, clone 9D9, Bio X Cell) dissolved in 100 µL sterile PBS on days -6, -3, and 0 and anti-CSF1R (250 µg IP, clone AFS98, Bio X Cell) on days 0, 3, and 6. Day 0 represents day of FUSTA treatment.

2.5.6 Flow Cytometry

24 h after FUSTA, tumors and lymph nodes (axillary + brachial) were harvested for immediate flow cytometry processing. Tissues were mechanically homogenized and filtered through a 100 µm Nitex nylon filter (Genessee) to create single cell suspensions. A Lymphoprep™ (STEMCELL Technologies) density gradient was applied to tumors according to the manufacturer's instructions to isolate mononuclear cells. Tumor and lymph node suspensions were washed in PBS, pelleted by centrifugation, and resuspended in 150 µL PBS for staining. Staining steps were performed with minimal sample exposure to light. Live/dead Aqua staining (Invitrogen) was performed followed by incubation at 4 °C for 30 minutes. Blocking was performed by 15 minutes of incubation anti-mouse CD16/32 (Life Technologies) at 4 °C. Cells were pelleted and suspended in 100 µL antibody mix in FACS buffer with 2% normal mouse serum (Fischer) followed by incubation at 4 °C for 30 minutes.

The following antibodies/dilutions were used for surface marker staining F4/80 (1:500) - PerCp/Cy5.5 (Biolegend), CD8 (1:1000) - PE(eBioScience), Ly6C (1:2000) - PE Dazzle594,

(Biolegend), CD11c (1:1000) - PE Cy7(eBioScience), CD103 (1:500) - APC(eBioScience), CD11b (1:1000) - AF700(Biolegend), CD45 (1:200) - Super Bright 780 (eBioscience),
CD3 (1:500) – eFluor450 (eBioscience) or CD19 (1:500) - eFlour450 (eBioscience), MHC II (1:200) - BV605 (Biolegend), CD86 (1:500) - BV650 (Biolegend), Live/Dead (1:1000) - Aqua, (Invitrogen).

Flow cytometry was performed using either CytoFLEX (Beckman Coulter Life Sciences) or an Attune NxT (ThermoFischer Scientific) flow cytometer followed by analysis in FlowJo software (TreeStar). A sample gating strategy for quantification of ZsGreen in cDC1 and cDC2 lineages is provided in Figure S2.

2.5.7 RNA-Sequencing and Analysis

8 h, 24 h, 72 h and 168 h after FUSTA or sham treatment, mice were euthanized via an overdose of pentobarbital sodium and phenytoin sodium. Immediately following euthanasia, the tumors were harvested, placed in RNAlater (Qiagen), and stored at −80°C. RNA extraction was performed using the RNeasy Mini Kit (Qiagen). mRNA was isolated using the NEBNext Poly(A) mRNA Magnetic Isolation Module (New England Biolabs) followed by library preparation using the NEBNext Ultra II Directional RNA Library Prep Kit for Illumina (New England Biolabs). Sequencing was performed using a NextSeq 500 (Illumina, San Diego, California) at a target depth of 25 million 2 × 75 bp paired end reads per sample. Reads were quasi-mapped to the murine genome (mm10 assembly) and quantified at the transcript level using Salmon v0.11.2 (202) followed by summary to the gene level using tximport v1.18.0 (203). Differential gene expression and principle components analysis was performed with DESeq2 v1.30.1 (204). Gene set enrichment analysis was performed with the GO Biological Processes (205, 206) and Reactome (207) gene sets from MSigDB (208) using FGSEA v1.16.0 (209) run with 100,000 permutations. Cell-type deconvolution was performed by inputting TPM normalized counts mapped from the mm10 genome to the hg38 genome into the CIBERSORTx webtool (https://cibersortx.stanford.edu/) in absolute mode with B-mode batch correction and the LM22 signature matrix (168).

2.5.8 Immunohistochemistry

Either 4 h (MCC950 studies) or 8 h (NLRP3 KO studies) after FUSTA, mice were euthanized via an overdose of pentobarbital sodium and phenytoin sodium. Tumors were harvested, placed in 10% neutral-buffered formaldehyde for 48 hours, embedded in paraffin, and

sectioned 150 µm apart. 5 µm thick tissue sections were deparaffinized using EZ Prep solution (Ventana). A heat-induced antigen retrieval protocol set for 64 min was carried out using Cell Conditioner 1 (Ventana).

For HSP70 staining, immunohistochemistry was performed on a robotic platform (Ventana discover Ultra Staining Module, Ventana). Endogenous peroxidases were blocked with peroxidase inhibitor (CM1) for 8 min before incubating the section with HSP70 antibody (ab181606, Abcam) at 1:100 dilution for 60 min at room temperature. Antigen-antibody complex was then detected using the DISC. OmniMap anti-rabbit multimer RUO detection system and DISCOVERY ChromoMap DAB Kit (Ventana). Slides were counterstained with hematoxylin, followed by dehydration, clearing, and mounting for assessment. Sections were imaged with a 2.5X objective on an Axioskop light microscope (Zeiss) equipped with a PROGRES GRYPAX microscope camera (Jenoptik, Germany).

For immunofluorescence, sections then were first treated with TrueBlack® Lipofuscin Autofluorescence Quencher (23007, Biotium) for 35 seconds. Blocking was carried out with 5% NGS for 1 hour at room temperature, followed by incubation with rabbit anti-Asc pAb (AG-25B-0006, AdipoGen, 1:400) overnight at 4 °C. Sections then were labeled with Alexa Fluor 555 goat anti-rabbit IgG (H+L) (A-21428, ThermoFisher, 1:500) for 1 hour at room temperature. Sections were mounted with ProLong™ Diamond Antifade Mountant with DAPI (P36971, ThermoFisher). Sections were imaged using an LSM 880 confocal microscope (Zeiss). Nuclei (DAPI) were visualized by excitation at 405 nm and emission in a 145 nm band centered at 483 nm. ASC staining (Alexa 555) was visualized by excitation at 561 nm and emission in a 54 nm band centered at 589 nm. Using a 63x oil immersion objective (Zeiss), 12 bit-images were obtained after performing a Z-stack and performing a maximum intensity projection. 2 sections separated by 150 µm were imaged per tumor, with 3 images from randomly selected regions obtained per section. A custom MATLAB (Mathworks) program was developed to quantify ASC specks. Briefly, this program utilized a built-in function based on the Circular Hough Transform algorithm to identify circular objects in the ASC channel using an adaptive edge threshold with radii between 1 µm and 2 µm. ASC specks counts were averaged across all 6 images obtained from each tumor to obtain a final speck count.

2.6 Acknowledgements

We kindly thank the lab of Dr. John Lukens for providing the NLRP3 KO mice. We thank the University of Virginia Genome Analysis and Technology Core for assistance with RNA-sequencing sample processing. We also thank the University of Virginia Biorepository and Tissue Research Facility for assistance with HSP70 staining.

2.7 Figures

Figure 2.1

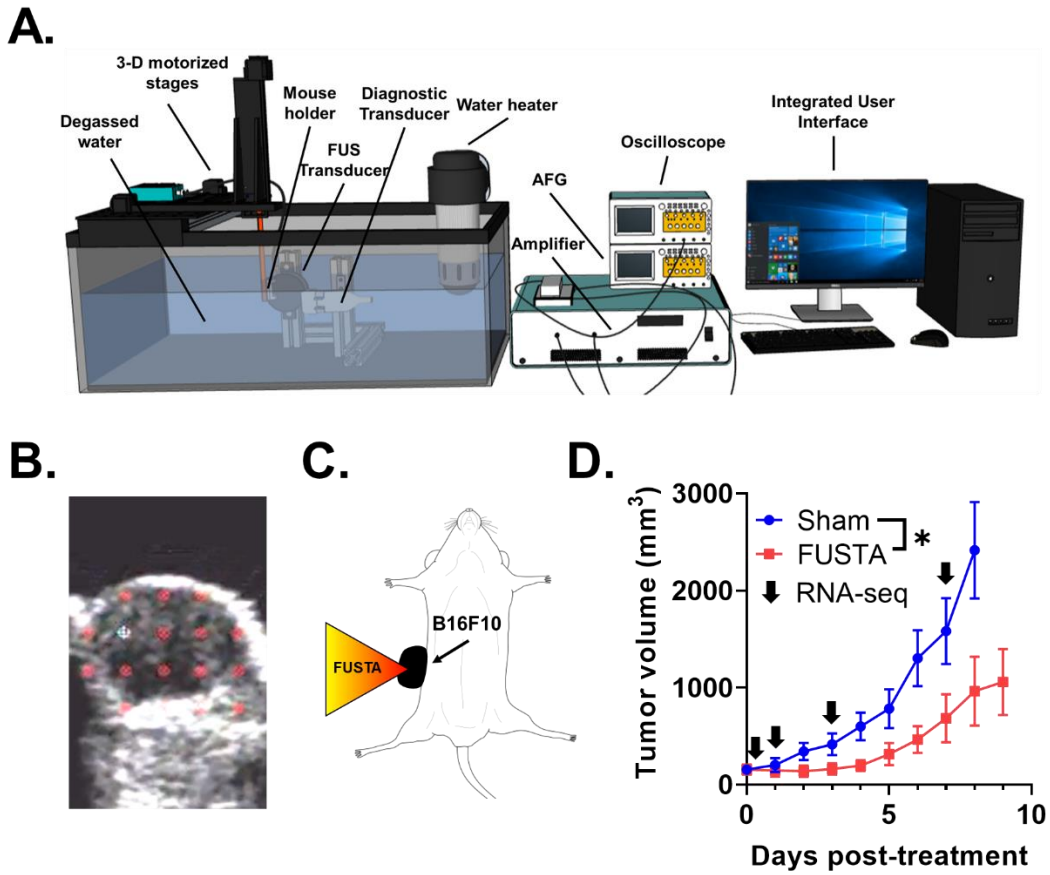

Figure 2.1. Overview of FUSTA Application. (A) Custom ultrasound-guided focused ultrasound system used for FUSTA application. Anesthetized mice were attached to a holder fastened to a 3D motorized stage system. Tumors were submerged in degassed water and oriented at the focal intersection of orthogonally registered diagnostic and therapeutic ultrasonic transducers. Control of real-time Imaging, treatment planning, stage motion, and treatment parameters were integrated in a single user interface. Rendering made with SketchUp software. (B) Sample B16F10 flank tumor on diagnostic ultrasound with an overlaid sparse-scan treatment grid. (C) Schematic of FUSTA application in a unilateral B16F10 flank tumor model. (D) Mean +/- SEM tumor volume of sham or FUSTA treated mice. *$p < 0.05$. Significance assessed by fitting a mixed effects model via restricted maximum likelihood and testing the fixed effect of treatment. Arrows indicate times at which both sham and FUSTA treated tumors were harvested for RNA-sequencing.

Figure 2.2

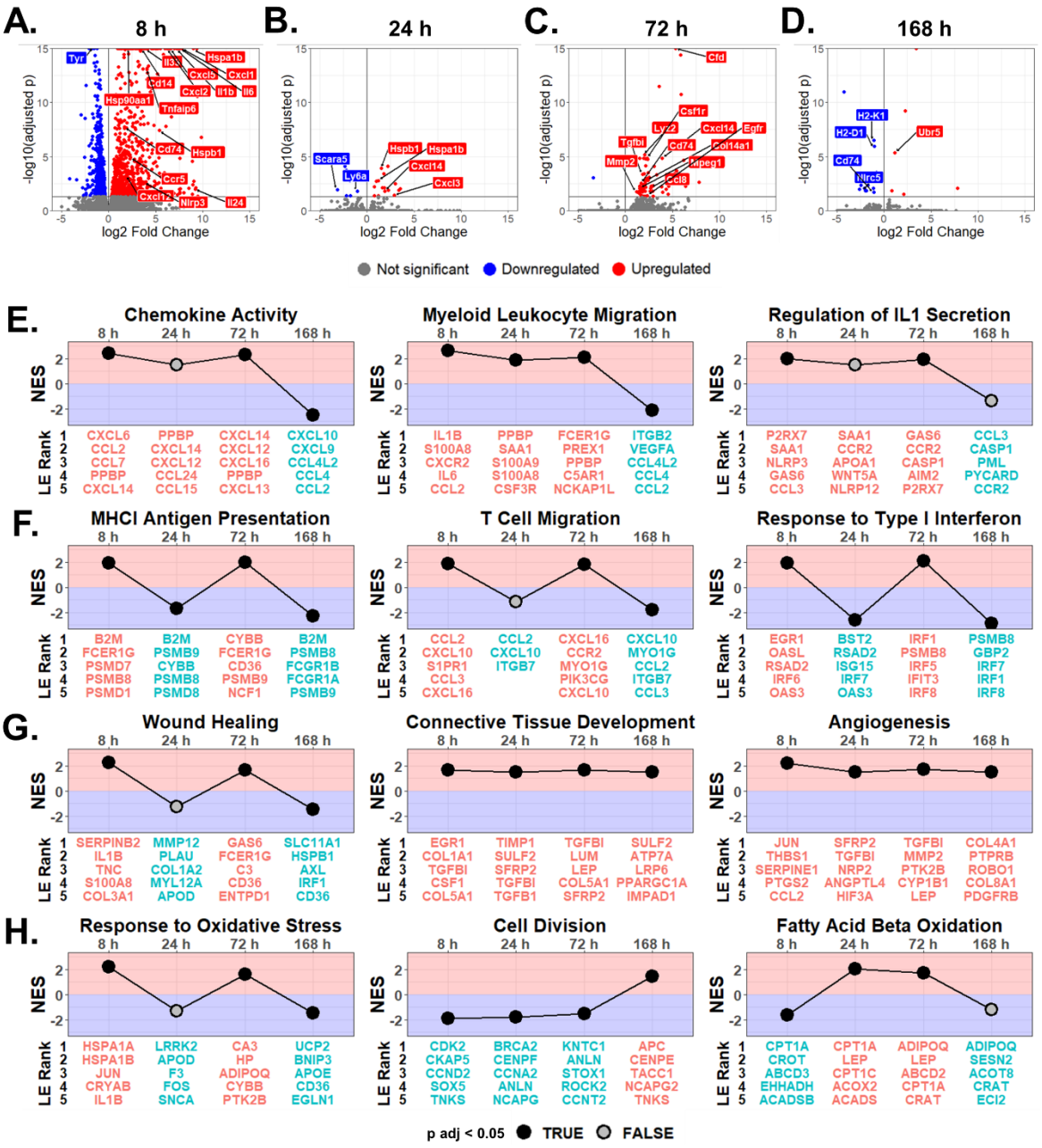

Figure 2.2: FUSTA Triggers Immunogenic and Immunosuppressive Transcriptional Signatures in the Melanoma TME. (A-D) Volcano plots showing differential gene expression in FUSTA treated samples relative to time-matched shams obtained 8 h (A), 24 h (B), 72 h (C), or 168 h (D) after treatment. Each dot represents a gene, color coded by the significance of its relative expression. Genes of interest are annotated. (E-H) Normalized enrichment scores (NES) for selected pathways assessed at each post-FUSTA timepoint. The fill of each dot corresponds to the significance of the NES. Leading edge transcripts contributing to enrichment (red text) or repression (blue text) are shown in order of rank below each corresponding timepoint. Selected families of pathways include sterile inflammation (E), adaptive immune stimuli (F), wound healing responses (G), and miscellaneous (H).

Figure 2.3

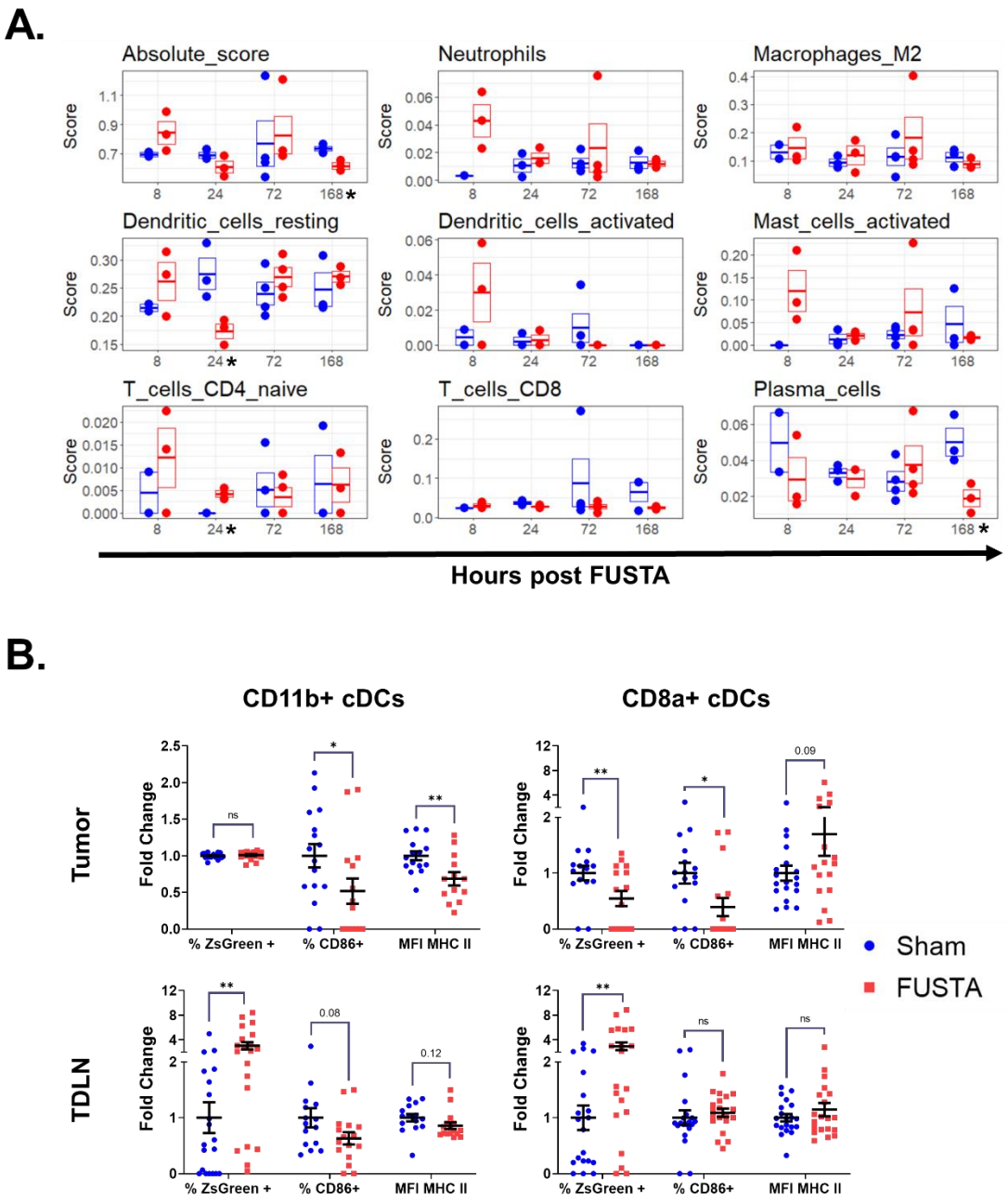

Figure 2.3: FUSTA Influences Temporal Evolution of Leukocyte Infiltration in the TME and Enhances Acquisition of Tumor Specific Antigen in the Draining Lymph Node. (A) Abundance of selected leukocyte populations inferred via cell type deconvolution. Individual dots represent single transcriptomes and overlaid box plots represent group mean +/- SD. (B) Fold change in conventional dendritic cell (cDC) metrics of antigen acquisition and maturation relative to sham mean. Results are the aggregate of 4 independent studies. Overlaid bars represent mean +/- SEM. cDCs were analyzed from either tumor (top) or tumor draining lymph nodes (bottom) and categorized by CD11b+, CD8a- (left) or CD11b-, CD8a+ (right). *p < 0.05. Significance was assessed by t-test.

Figure 2.4

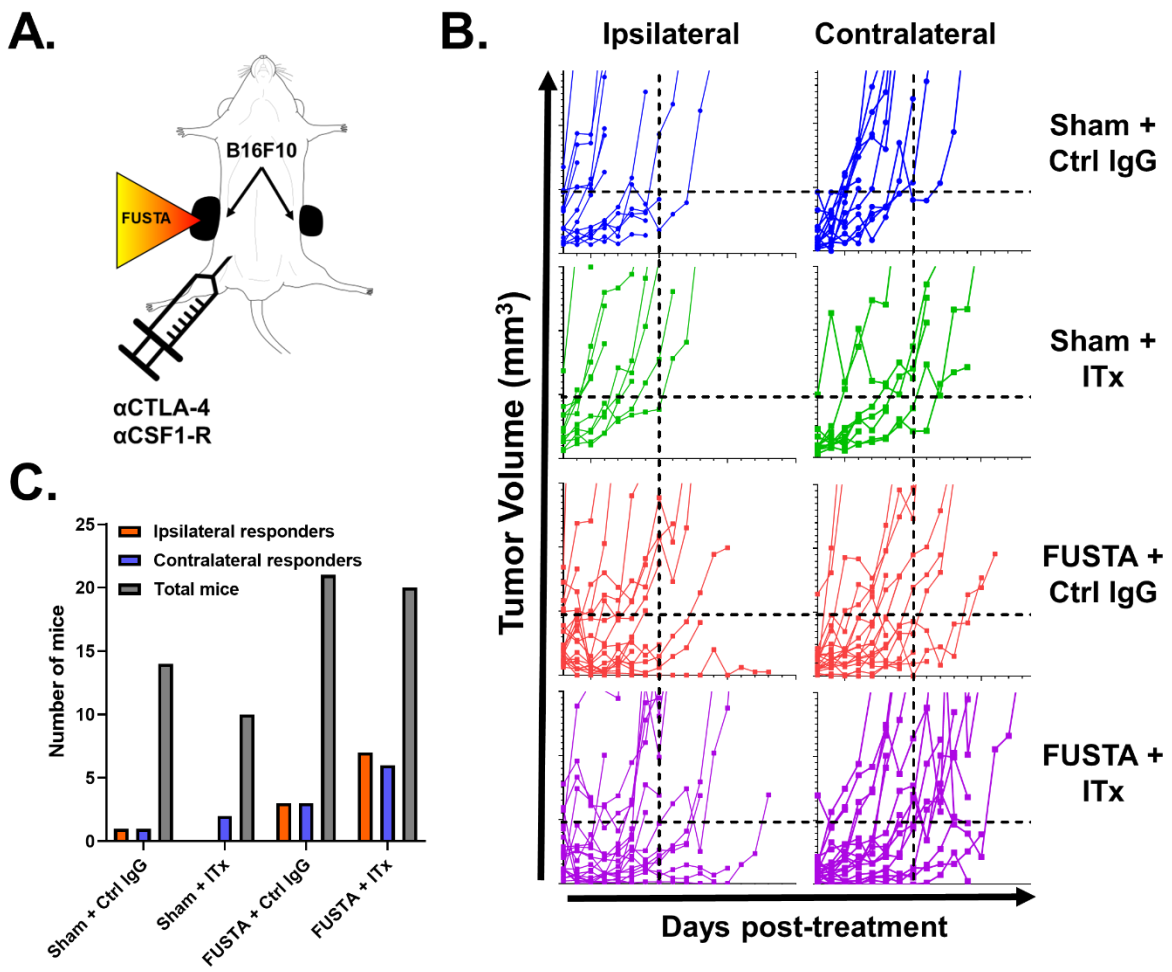

Figure 2.4: Combinatorial Administration of αCTLA-4 and αCSF1R Increases Likelihood of Abscopal Response after FUSTA. (A) Schematic of bilateral B16F10 tumor model. Right flank tumors were treated with sham or FUSTA. Immunotherapeutic antibodies or control IgG were administered intraperitoneally on days -6, -3, 0, 3, and 6 relative to FUSTA. (B) Individual ipsilateral and contralateral growth curves for mice treated with +/- FUSTA +/- immunotherapy. The lower right quadrant of each set of dashed lines represents the zone of response, characterized by temporal survival greater than 7 days after FUSTA and tumor volume below 200 mm^3. (C) Quantification of ipsilateral and contralateral responders from each treatment group, alongside the total number of treated mice.

Figure 2.5

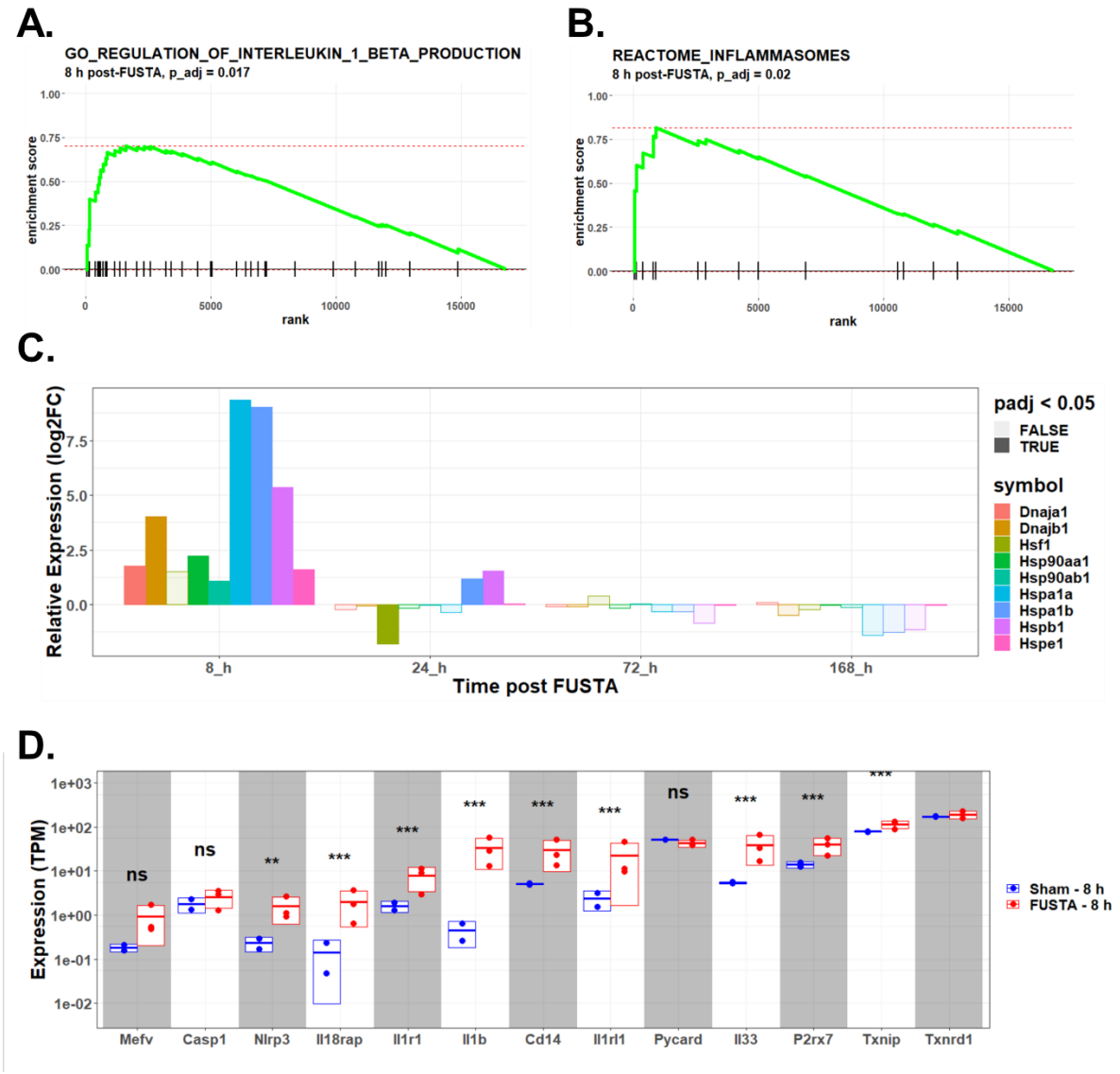

Figure 2.5: FUSTA Upregulates Transcriptional Signatures Indicative of Pyroptosis Induction in the TME. (A-B) Enrichment plots for the "REGULATION OF INTERLEULIN 1 BETA PRODUCTION" pathway from the Gene Ontology Biological Processes gene sets (A) and "INFLAMMASOMES" pathway from the Reactome gene sets at 8 h post FUSTA. (C) Fold change in expression of selected heat shock protein transcripts in tumors harvested each post FUSTA timepoint compared to time-matched shams. Transparency corresponds to significance of adjusted p values. (D) Depth and length normalized expression values (TPM) for selected transcripts in sham (blue) or FUSTA (red) treated tumors harvested 8 h after treatment. Box plots represent mean +/- SD. *p <0.05, **p < 0.01, ***p < 0.001. Significance assessed by Wald test after correction for multiple comparisons using the Benjamini and Hochberg method.

Figure 2.6

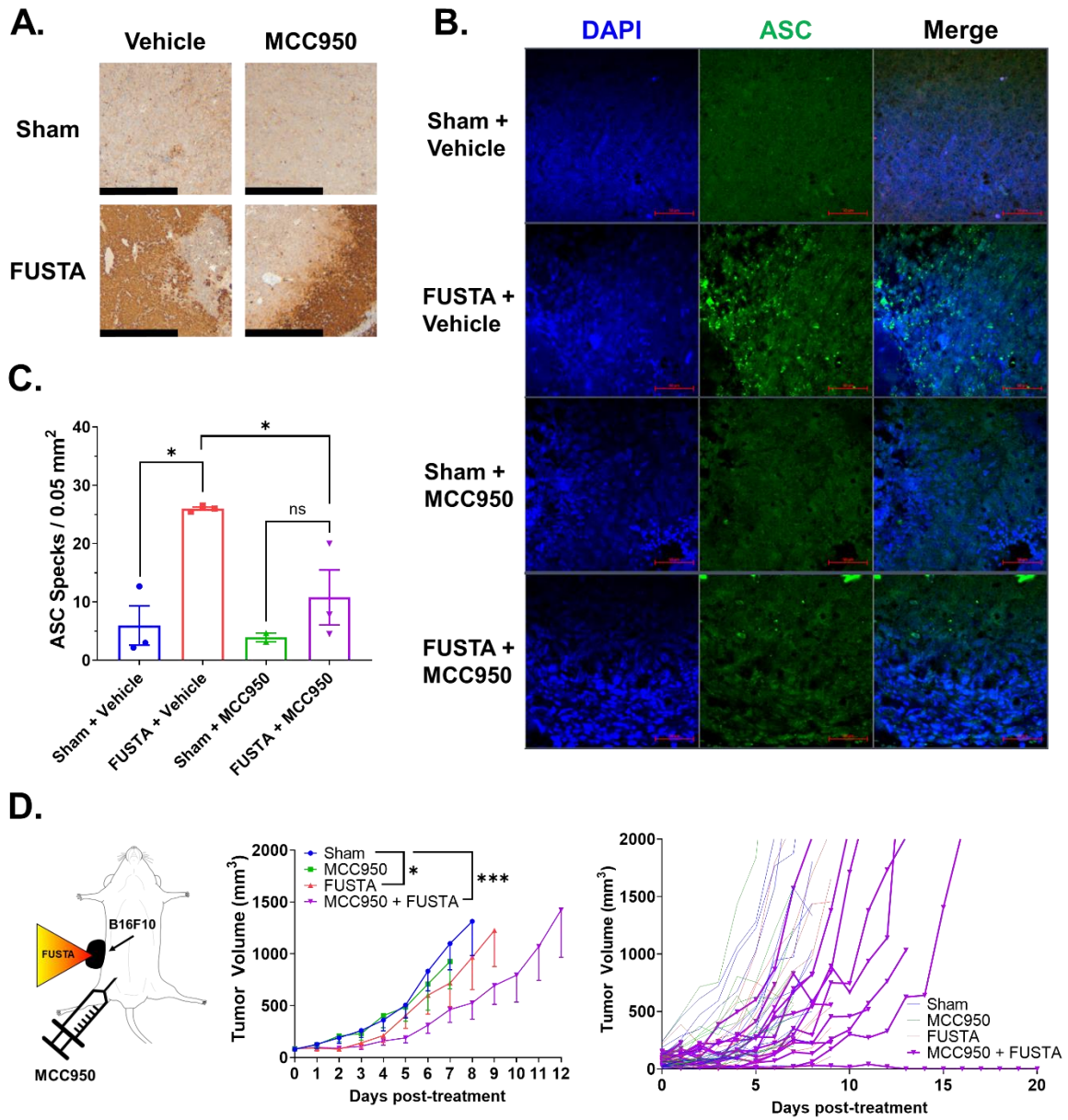

Figure 2.6: FUSTA Triggers Inflammasome Assembly, the Blockage of Which Extends Tumoristasis. (A) Representative brightfield images of HSP70 staining from tumor sections after treatment with sham (top) or FUSTA (bottom) and vehicle (left) or MCC950 (right). Scale bars measure 500 µm. (B) Representative immunofluorescence images of cellular nuclei (blue) and ASC (green) staining from tumor sections after treatment with +/- FUSTA +/- MCC950. Scale bars measure 50 µm. (C) Quantification of average ASC speck density. Bars represent mean +/- SEM. *p<0.05. Significance assessed by ordinary one-way ANOVA followed by Tukey's multiple comparison test. (D) Schematic (left), average tumor growth curves (middle), and individual growth curves (right) for treatment of mice with +/- FUSTA +/- MCC950. Error bars represents SEM. *p<0.05. Significance assessed by fitting a mixed effects model via restricted maximum likelihood and testing the fixed effect of treatment, followed by Tukey's multiple comparison correction.

Figure 2.S1

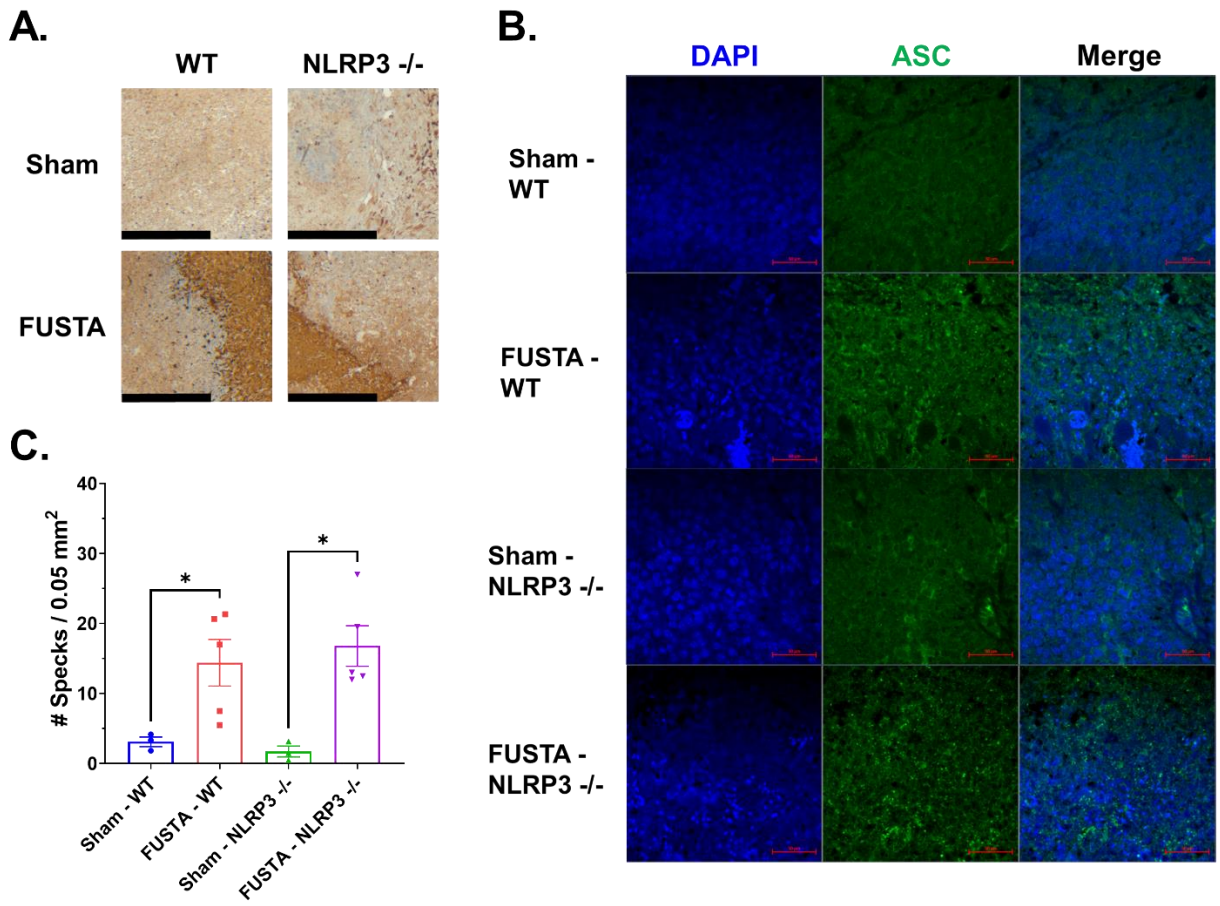

Figure 2.S1: FUSTA Inflammasome Assembly is Not Affected by host NLRP3 Knockout. (A) Representative brightfield images of HSP70 staining from tumor sections after treatment with sham (top) or FUSTA (bottom) in WT (left) or NLRP3 KO (right) backgrounds. Scale bars measure 500 µm. (B) Representative immunofluorescence images of cellular nuclei (blue) and ASC (green) staining from tumor sections after treatment with +/- FUSTA +/- NLRP3 KO. Scale bars measure 50 µm. (C) Quantification of average ASC speck density. Bars represent mean +/- SEM. *p<0.05. Significance assessed by ordinary one-way ANOVA followed by Tukey's multiple comparison test.

Figure 2.S2

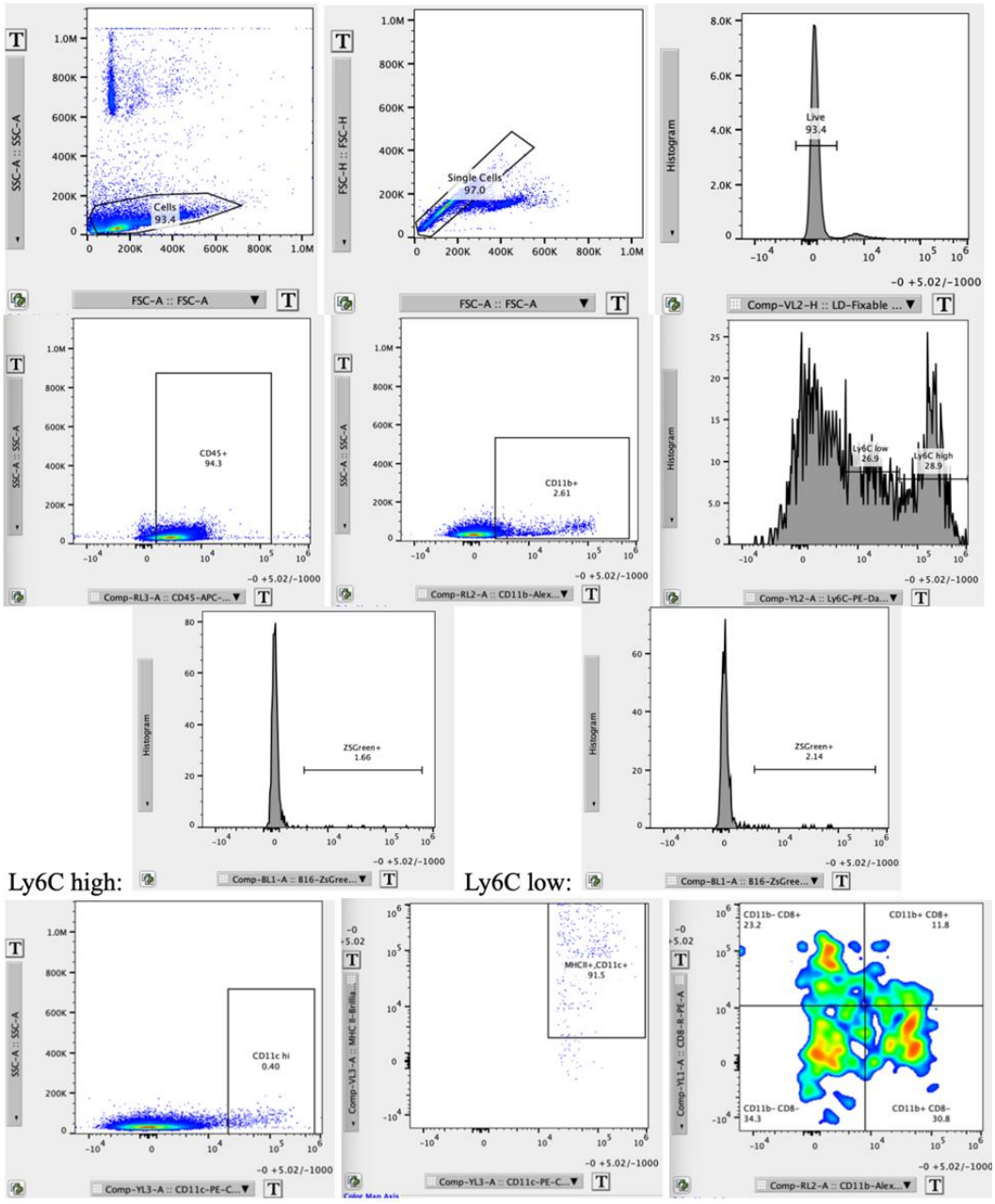

Figure 2.S2: Gating strategy to identify cDC1 and cDC populations. Representative flow gating strategy for a lymph node extracted from a B16F1-ZsGreen-OVA tumor bearing mouse. The first row of flow panels represents gating to identify live single cells. The second row demonstrates isolation of Ly6C low vs high CD45+ Cd11b+ cells followed by quantification of ZsGreen in each population in the third row. The fourth row shows gating to isolate cDCs (Cd11c hi, MHCII+) and differentiate cDC1 (CD8α+, CD11b-) and cDC2 (CD11b+, CD8α-).

Chapter 3: High-Dose Conformal Radiation Therapy Versus Focused Ultrasound Thermal Ablation: The Relative Potential of Focal Therapies to Sensitize Human Tumors to Pembrolizumab

Alexander S. Mathew, Christopher K. Luminais, Gina R. Petroni, Kimberly A. Chianese-Bullock, James M. Larner, Patrick M. Dillon, Timothy N.J. Bullock, and Richard J. Price

3.1 Abstract

Immunotherapies have revolutionized cancer treatment, but only offer durable benefit to a minority of patients with compatible tumor immune contexture. Adjuvant strategies that reshape immunologically subdued tumors toward increased susceptibility to immunotherapy may extend the reach of these exciting agents. Focal therapies, such as high-dose conformal radiation therapy (HDCRT) and high intensity focused ultrasound thermal ablation (FUSTA), are well positioned to act as immunotherapy sensitizers, as they have been shown to noninvasively enhance immunogenicity in the TME. Here, we incorporate data from two phase I clinical trials into a parallelized bioinformatics pipeline to test transcriptome-wide consequences of pembrolizumab (pembro) in combination with either HDCRT or FUSTA in solid human tumors. These analyses suggest a net immunosuppressive effect of HDCRT that is most effectively attenuated by pretreatment or coincident treatment with pembro. Meanwhile, analysis of FUSTA treated tumors suggests that the ablated region produces more immunogenic signatures than the periablated region, possibly due to more potent activation of immunogenic cell death. Inter-trial comparisons revealed both focal therapies increased myeloid representation in the TME. These findings have provocative implications for optimizing immunotherapy sensitization with focal technologies, and justify larger clinical investigations of both HDCRT and FUSTA as immunoadjuvants.

3.2 Introduction

Cancer is the 2nd leading cause of death worldwide, in part due to the frequent emergence of oncogenic defense mechanisms against immune surveillance (210–215). Immunotherapeutic agents that target these defenses and are capable of generating systemic anti-tumor responses show great promise toward improving patient survival (216–223). However, the clinical response frequency of immunotherapy remains low and critically dependent on the presence of T-cells in the tumor microenvironment (TME). Thus, there is a need to expand the responding population by developing strategies that synergize with immunotherapies via dampening immunosuppression and promoting lymphocyte infiltration.

Focal therapies hold considerable potential in meeting this need. These minimally invasive, targeted technologies elicit localized destruction of tumor using various types of energy deposition. Parallel investigations have demonstrated the capacity of radiation therapy (224–226), focused ultrasound (79–86), microwave ablation (227–229), photodynamic therapy (230–233), cryoablation (234–236), and radiofrequency ablation (237–239) to alter immunogenicity in the TME. In some cases, focal treatment of a primary lesion generated a systemic anti-tumor immune response powerful enough to control distant metastases, a phenomenon known as the abscopal effect (240–243). There is now significant interest in optimizing administration of focal therapy to increase the probability of an abscopal effect and/or sensitize otherwise refractory tumors to immunotherapy (85, 227, 231, 233, 236, 238). Indeed using a single technology to simultaneously debulk primary malignancies and generate durable anti-tumor immunity with minimal damage to healthy tissue represents a highly attractive clinical model.

High-dose conformal radiation therapy (HDCRT) and high intensity focused ultrasound thermal ablation (FUSTA) are among the most promising focal therapies currently under investigation for their ability to convert tumors from immunologically “cold” to “hot”. Compared to other energy deposition technologies, both HDCRT and FUSTA have the clinical advantages of being truly non-invasive, highly adaptable to the 3-dimensional structure of the tumor, and able to reach deep tissue structures. FUSTA offers the additional benefit of being non-ionizing, enabling the possibility of more repeated treatments. Though radiation therapy is certainly more clinically mature than FUS for tumor debulking, both therapies are in early stages of development with respect to their immunomodulatory potential. HDCRT and FUSTA effect cytotoxicity via divergent mechanisms (heat ablation vs DNA damage), yet both are hypothesized to elicit immunogenic cell death (ICD), as evidenced by translocation of calreticulin to the cell surface (244, 245). Preclinical studies of both therapies have reported increases in intratumoral expression of cytokines and damage associated molecular patterns (DAMPs), as well as the availability of tumor

neoantigens after treatment (79, 180, 226, 246, 247). These pro-inflammatory changes to the TME cooperatively increase the visibility of tumor to the immune system, enhancing tumor-specific antigen acquisition and presentation by dendritic cells (DCs) after HDCRT (79, 180, 226, 246, 247) or FUSTA (90, 93, 97, 98). Tumor lysate extracted from HDCRT (248, 249) or FUSTA (99, 100) treated tumors are more effective tumor vaccines than untreated lysate. Other studies have shown increases in tumor infiltrating lymphocytes (TILs) after FUSTA in models of breast cancer (84), or after HDCRT in models of prostate cancer (250).

Currently, neither HDCRT nor FUSTA are immunogenic enough to consistently establish systemic anti-tumor immunity by themselves, spawning new investigations of their potential to augment intratumoral sensitivity to checkpoint inhibitors (CIs). A number of preclinical studies have demonstrated abscopal responses after radiation therapy (RT) in combination with CIs such as anti-CTLA4 or anti-PD1 (251–254). Early phase clinical trials of melanoma, non-small cell lung carcinoma (NSCLC), among others, demonstrated promising response rates in patients treated with RT combined with ipilimumab (anti-CTLA-4) (255). However, in a large trial of metastatic prostate cancer, there was no significant difference in overall survival in men receiving ipilimumab vs placebo after palliative RT (255). The dosing schema seem to be crucial to the success of RT + CI, with studies demonstrating RT should be given before anti-PD1 and delivered in fractions (rather than a single dose) to maximize abscopal responses (256). Though fewer studies combining FUSTA with CI exist, preliminary studies suggest abscopal responses in the context of murine breast cancer are maximized when immunomodulatory agents (in this case anti-PD1 combined with CpG) are given ahead of FUSTA rather than coincidentally (85).

Given the developmental parallelisms of these two focal therapies as immunomodulators, a clinically relevant unknown is their relative efficacy in sensitizing tumors to CI. Herein, we utilize bioinformatics approaches to analyze and compare immunological consequences of two clinical trials combining pembrolizumab (pembro) with either HDCRT or FUSTA. The first trial, "HDCRT Plus Pembrolizumab in Advanced Malignancies" (AM001, NCT02987166), tests the effects of 3 distinct sequences of HDCRT and pembro in various solid tumors. The second trial, "Focused Ultrasound and Pembrolizumab in Metastatic Breast Cancer" (BR48, NCT03237572), tests two sequences of FUSTA and pembro in metastatic breast cancers of any receptor status. Identical processing of pre- and post-treatment samples from both trials enables us to perform side-by-side comparative assessments including differential gene expression, gene set enrichment analysis, cell-type deconvolution, and T-cell receptor profiling. These analyses yield new insights into the intratumoral consequences of each combination therapy, and represent the first direct comparison of HDCRT vs FUSTA in combination with CI in humans.

3.3 Results

3.3.1 Overview of AM001 and BR48 Trial Design and Transcriptional Profiling

"HDCRT Plus Pembrolizumab in Advanced Malignancies" (AM001, NCT02987166) and "Focused Ultrasound and Pembrolizumab in Metastatic Breast Cancer" (BR48, NCT03237572) are Phase I clinical trials sponsored by the University of Virginia. The goals of both trials are to test the safety and T-cell infiltration profiles induced by focal therapy in combination with the PD-1 inhibitor, pembrolizumab (pembro) in solid tumors. AM001 contains 3 arms, which compare different sequences of administration of high-dose conformal radiation therapy (HDCRT) and pembro in patients with advanced solid tumor malignancy for which palliative radiation is recommended. Meanwhile, BR48 contains 2 arms, comparing sequences of administration of high intensity focused ultrasound thermal ablation (FUSTA) and pembro in patients with metastatic or unresectable breast cancer (any receptor status). Included as secondary objectives for both trials are gene expression analyses of pre- and post- treatment biopsies to further characterize the immunological impact of each therapy. BR48 biopsies included ablated and periablated samples, enabling comparative analysis of tumor directly coagulated by FUS vs surrounding tumor experiencing sub-lethal effects. Overviews of the first 43 days of each trial, during which biopsies were extracted for gene expression analyses, are provided in **Figure 3.1A**. Per the trial designs, BR48 contained exclusively breast tumors while each arm of AM001 contained varying mixtures of solid malignancies (**Figure 3.1B**).

To identify sources of transcriptome variability within and between trials, we performed principle components analyses (PCA) on variance-stabilizing-transformed counts obtained from each of the 63 total sequenced samples (**Figure 3.2A**). Global variability in gene expression was primarily explained by tumor type, with local clustering largely driven by inter-patient heterogeneity. No significant clustering attributable to sequencing batch, biopsy time point, or treatment condition were identified. All subsequent analyses testing effects of therapy are paired, comparing differences in post vs pre-treatment on a per-patient basis. Implementation of this approach for differential gene expression (DGE) analysis, while additionally blocking for sequencing batch effects, enabled successful identification of 100's to 1000's of differentially expressed genes (DEGs) as a function of treatment condition within each trial (**Figure 3.2B**). We note that because BR48 has yet to reach full accrual, we remain blinded to patient arm assignment. Therefore, all BR48 analyses are arm-agnostic, representing unifying effects induced by FUSTA with or without pembrolizumab.

3.3.2 Treatment Sequence Affects Induction of Immune Checkpoints after Pembrolizumab, but not Induction of DNA Damage Response Transcripts after HDCRT

With respect to AM001, we wondered whether the individual effects of HDCRT and pembro on gene expression were consistent across arms, or were dependent on the order of administration. A careful examination of differentially regulated transcripts across all arms and time points revealed that HDCRT (Arm A: day 1, Arm B: day 22, Arm C: day 1) consistently upregulated transcripts associated with DNA damage responses regardless of whether pembro had been administered previously or jointly. Specifically, expression of *BAX, CDKN1A,* and *DDB2* were upregulated in nearly all patients after administration of HDCRT across all 3 arms (**Figure 3.3A**). In contrast, response to pembro seemed to be adversely affected by previous treatment with HDCRT. Expression of the immune checkpoints *IDO1* and *TNFSF9* (the gene coding for 4-1BBL) was only significantly increased after pembro in Arm A and Arm B (**Figure 3.3B**). We observed a similar trend for expression of *CXCL11*, an interferon gamma-induced cytokine chemotactic for activated T-cells, amongst others. Expression of these immunomodulatory transcripts was blunted in tumors previously treated with HDCRT.

To test whether genes differentially expressed as a function of time and treatment arm were enriched for specific biological processes, we performed gene set enrichment analysis (GSEA). Consistent with the trends in immunomodulatory transcript expression, GSEA revealed the strongest enrichment for immunity associated pathways, such as GO T CELL ACTIVATION only in Arm A and Arm B (**Figure 3.3C**). Interestingly, both HDCRT and pembro enriched gene sets associated with extracellular matrix development, such as GO COLLAGEN CONTAINING EXTRACELLULAR MATRIX (**Figure 3.3D**).

3.3.3 Sequencing and Pretreatment Gene Expression Profiles May Predict Clinical Course after Administration of HDCRT and pembro

In AM001, overall survival (OS) was greatest in Arm B, followed by Arm A, followed by Arm C with median survival times of 500 days, 427 days, and 238 days on study respectively (**Figure 3.4A**). These differences were not statistically significant. Median times to disease progression were 50 days, 84 days, and 74 days on study for Arms A, B, and C respectively (**Figure 3.4B**). Arm B maintained the longest period of 100% progression free survival (72 days), and the patient with the strongest response with at least 1072 days of progression free survival (PFS). Comparison of PFS by log rank test returned a p-value of 0.078.

We next wondered whether pretreatment gene expression profiles predicted clinical response to any combination of HDCRT and pembro. To test this, we pooled pretreatment

transcriptomes across trial arms and constructed a Cox regression model for each gene, comparing its relative expression against patient PFS. Surprisingly, we identified patients with above average pretreatment expression of *TREX1* and *FKBPL* exhibited significantly longer PFS than patients with below average pretreatment expression (**Figure 3.4C and 3.4D**).

3.3.4 Ablated and Periablated Breast Tumors Exhibit Enhanced but Distinct Immunogenicity Signatures after FUSTA

To identify gene sets significantly enriched and repressed after FUSTA in BR48, we performed DGE followed by GSEA for ablated and periablated samples relative to matched pre-treatment samples. Though the number of genes significantly differentially expressed was greater in ablated vs periablated regions compared to pretreatment (**Figure 3.2B**), the identities of the associated biological processes significantly enriched by each were similar (**Figure 3.5A**). Immunogenic pathways enriched in both ablated and periablated regions were associated with innate and adaptive immune responses, including cytokine production, antigen processing, and T cell activation. These pathways were more strongly enriched in terms of normalized enrichment score (NES) and adjusted p-value for ablated samples compared to periablated counterparts. Complement activation, however, was significantly repressed in the periablated region. Both regions were also enriched for genes associated with wound healing and extracellular matrix remodeling, for which periablated region exhibiting stronger NES and adjusted p values. Both regions downregulated gene sets associated with DNA replication.

Using leading edge analysis (LEA), we examined the identities and extent of similarity of genes contributing to pathway modulation in ablated and periablated regions after FUSTA. Transcripts encoding classic cytotoxic proteins involved in innate defense were upregulated in both periablated regions (**Figure 3.5B**). These included *DEFA1* (more than 30 fold upregulated in ablated tissue), *GZMB,* and *PRF1*. Of the extensive cytokine expression induced in both regions, only *CCL7* was more strongly induced in the periablated region than in the ablated region (**Figure 3.5C**). Fascinatingly, we noted significant enrichment of the inflammasome cascade, consistent with data reported in Chapter 2 (**Figure 3.5D**). In the ablated tissue for example, we observed significant upregulation of *CASP1* and *GSDMD*, both of which are principle mediators of pyroptosis. Expression of transcripts associated with T cell activation was strongest in the ablated region, with the exception of *CD81* which was more significantly upregulated in periablated regions (**Figure 3.5E**). Expression of transcripts associated with TGF-β signaling were more discordant between ablated or periablated regions (**Figure 3.5F**). LEA revealed marked upregulation of *FOS, TGFB1I1,* and *ADAMTSL2* in periablated regions but not ablated

regions. Finally we examined genes downregulated in both regions associated with repression of DNA replication pathways (**Figure 3.5G**). We note the nearly-6-fold-downregulation of *POLA1* in ablated regions.

3.3.5 Comparison of Immunologic Gene Signatures in AM001 vs BR48

After analysis of AM001 and BR48 individually, we next sought to compare the nature and extent of immunologic gene signatures across trials. First, we compared the significance of enrichment or repression of biological pathways across trials and conditions (**Figure 3.6**). We organized selected pathways into 5 themes, including adaptive immunity, cytokine production, innate immunity, miscellaneous, and wound healing. There existed considerable overlap in the identities and significance of pathways across all 5 themes between AM001 and BR48. The contrasts from AM001 representing the overall effect of combination therapy (the day 43 vs day 1 comparisons) for Arm A and Arm B were most similar to both ablated and periablated signatures in BR48. Some notable deviations include the repression of B cell receptor signaling and complement activation in periablated regions, which are more similar to the acute effect of HDCRT observed in Arm C in AM001. Mitochondrial gene expression and oxidative phosphorylation were also repressed in BR48 contrasts, but upregulated in some AM001 contrasts. Finally, we note that fibroblast proliferation pathways were not significantly modulated in BR48, but significantly enriched in multiple AM001 contrasts.

To evaluate the differential effects of HDCRT, pembro, and FUSTA on immune cell composition in the tumor microenvironment, we performed cell type deconvolution (CTD) on length and depth normalized transcript counts. Linear correlation between IHC counts of CD8+ T cells and CTD estimates of CD8 abundance was positive but noisy, with $R = 0.47$ and $R^2 = 0.22$ (**Figure 3.7A**). Despite heterogeneity in tumor types assigned to each arm of AM001 and BR48, distributions of immune cells were generally similar, with most tumors predominantly infiltrated by M0 or M2 macrophages (**Figure 3.7B**). The relative abundance of M2 macrophages was significantly increased after HDCRT in arms B and C (**Figure 3.7C**). Meanwhile, in BR48, neutrophils were significantly enriched in the periablated region after FUSTA (**Figure 3.7D**). The only significant change in Arm A of AM001 was a relative increase in abundance of activated mast cells (**Figure 3.7E**). While no significant abundance alterations in CD8+ T cells were detected (**Figure 3.7F**), we note a trending increase after pembro in AM001 Arm B ($p = 0.12$), and trending decreases after radiation in AM001 Arm B ($p = 0.06$), after radiation in AM001 Arm C ($p = 0.06$), and in the BR48 periablated region ($p = 0.11$). Other proportion shifts in the adaptive immune compartment include decreases in resting CD4+ memory T cells in both BR48 regions (**Figure**

3.7G), and decreases in follicular helper T-cells after HDCRT in AM001 Arm B and after FUSTA in the periablated region (**Figure 3.7H**). To further investigate the nature of T cell infiltration, we analyzed T-cell receptor alpha and beta chains. Though we were able to detect many unique *TRA* and *TRB* clones, we did not detect any trial-specific changes in their abundance or clonality (**Figure 3.S1**).

3.4 Discussion

Though sensitization of refractory tumors to immunotherapies, such as CI, with focal therapies is an appealing clinical paradigm, fundamental knowledge gaps and practical implementation challenges still remain. Biological ramifications of combination therapy on the TME, type of focal therapy technology that maximizes synergy, and temporal sequence of administration are all still unclear in the context of human malignancy. To address these hurdles, we jointly analyzed paired transcriptional data from two clinical trials combining pembro with either HDCRT (AM001) or FUSTA (BR48), generating new insights about the effect of focal therapy in combination with CI both within and between trials. Broadly considered, HDCRT and pembro appeared to have opposite immunostimulatory influences on the TME alone, and positive net synergy only when pembro was administered first or coincidentally. In BR48, both ablated and periablated tumor volumes were enriched for pro-inflammatory gene sets, though the effect was more marked in the ablated region. Families of biological processes over-represented in both trials were surprisingly similar, with the most immunogenic contrasts from each inducing pathways associated with cytokine production and T cell activation. Immune cell type abundance estimates varied by trial and treatment arm, with significant alterations in relative proportions of specific myeloid and lymphoid effectors.

The first goal of this study was to evaluate the transcriptional signatures modulated by focal therapy and CI within each trial individually. Arms A, B, and C from AM001 each contained a pre-treatment biopsy, a day 22 biopsy (21 days after the first intervention of HDCRT+pembro, pembro alone, or HDCRT alone respectively), and a day 43 biopsy (21 days after the second intervention of no treatment, HDCRT alone, or pembro alone respectively), enabling 3 contrasts within each arm. We examined differentially expressed genes (DEGs) with the intent of determining whether the effects of HDCRT monotherapy were augmented if performed after pembro and vice versa. HDCRT elicited robust relative increases in the expression of well-known radiation response genes, including *BAX, CDKN1A,* and *DDB2* regardless of the treatment arm, suggesting coincident or prior pembro administration does not affect the ability of HDCRT to disrupt the cell-cycle in the TME (257–259). HDCRT also induced arm-independent upregulation of genes associated with a wound healing response such as *COL11A1*, *TIMP1*, *MMP2*, and *ADAMTS9*. Modified wound healing responses and fibrosis after radiation have been described before, and are associated with poor prognostic outcomes due to their connection with increased accumulation of pro-tumor macrophages and fibroblasts (260–264). While the net effect (day 43 vs day 1) of combination therapy in all 3 arms was significant enrichment for the GO COLLAGEN CONTAINING ECM pathway, the normalized enrichment scores were the strongest when HDCRT

was given first, and weakest when pembro was given first. On the other hand, the immunostimulatory potential of pembro was dependent on past exposure to HDCRT. Upregulation of *IDO1, TNFSF9, and CXCL11* was observed only in arms A and B, but not arm C 3 weeks after pembro administration. *IDO1* codes for indoleamine 2,3-dioxygenase 1, a metabolic mediator of peripheral tolerance known to impede T cell division (265). *TNFSF9* encodes the ligand for 4-1BB, an important co-stimulatory receptor expressed by activated T-cells. Upregulation of checkpoint molecules such as these is a known consequence of pembro therapy, and a positive indicator of successful establishment of a T-cell driven anti-tumor response in the TME (265). This response is further confirmed by *CXCL11,* a cytokine induced by interferon gamma chemotactic for T-cells. Lack of expression of these markers after pembro administration in Arm C indicates a potential negative synergy, in which the desirable immune effects of pembro are blunted by previous HDCRT treatment.

In an attempt to identify pretreatment gene signatures that predicted PFS in AM001, we performed Cox regression analysis. Paradoxically, we observed high pretreatment expression levels of *TREX1* was significantly correlated with longer PFS. High doses of radiation have been shown to activate *TREX1,* a DNA exonuclease that blunts the cyclic GMP-AMP Synthase (cGAS)-Stimulator of Interferon Genes (STING) pathway and its ability to mediate radiation induced immunogenicity (265). As its name suggests, cGAS-STING facilitates a phosphorylation cascade resulting in interferon-β synthesis, and agonists of this pathway have been tested as immunoadjuvants (266). It is possible the positive prognostication of high *TREX1* in AM001 reflects saturation or uncoupling of its inhibitory function in these patient' tumors, enabling HDCRT and pembro to induce a more effective immune response than in patients with inducible *TREX1*. The positive correlation of *FKBPL* expression with PFS was also interesting, as this gene's downregulation has been implicated as a mechanism of radioresistance (267), while its overexpression has been shown to be cytotoxic *in vitro* (268). Together, these data implicate *FKBPL* as a useful predictive biomarker for sensitivity to HDCRT + pembro.

We next examined the effects of recent FUSTA on the TME, remaining agnostic to prior pembro status due to incomplete trial accrual. In BR48, biopsies were obtained in both ablated and periablated regions, to test the hypothesis that the most immunogenic effects of FUSTA are generated in a "transition zone" beyond the central area of thermal coagulation (245). Surprisingly, though both regions were enriched for genes associated with diverse inflammatory pathways, the effects were strongest in the ablated regions. LEA suggested the stronger inflammatory signals in the ablated region are attributable to more concentrated ICD signatures, as evidenced by significant upregulation of important inflammasome genes (*CASP1, NLRC4, GSDMD*) and

cytotoxic enzymes (*GZMB, PRF1*) that were much more weakly induced in the periablated region. These data are in close alignment with those presented in Chapter 2, which implicate NLRP3 inflammasome activation by FUSTA in murine melanomas. Interestingly, the periablated region was also associated with stronger signatures of wound healing than the ablated region. Together, these results suggest that the ICD induced by direct ablation may elicit a stronger anti-tumor immune response than the sub-lethal stress response induced in the periablated region, contradicting previous hypotheses (37, 269).

The second major goal of this study was to compare immunologically relevant signatures between trials to identify which of HDCRT or FUSTA is the stronger sensitizer to pembro. We first examined normalized GSEA scores. Ablated and periablated regions from BR48 were most similar to post-pembro timepoints from all arms of AM001, with less similarity to the post-HDCRT timepoints (such as d43 vs d22 in Arm B, or d22 vs d1 in Arm C). Generally speaking, however, the nature of pathways engaged and repressed in both arms were similar, highlighting the parallel effects these focal therapies likely have in modulating the immune landscape of the TME. Both therapies are capable of generating an innate immune response, simultaneously enriching anti-tumor gene sets (such as interferons and T-cell activation markers) and pro-tumor gene sets (such as wound healing pathways), while inducing signatures of general cell stress as evidence by stunted metabolic and DNA replication gene expression.

CTD revealed notable trial-specific effects on immune cell representation in the TME. M2 macrophages were be consistently increased by irradiation in AM001, consistent with previous studies (270–272). HDCRT seemed to simultaneously elicit trending decreases in CD8 T cells, further suggesting the therapy may contribute to a net immunosuppressive TME. Activated mast cells, proposed to be involved in post-RT fibrosis (273–275), were also observed in AM001 arm A. Pembro generally had the opposite effect of HDCRT, leading to trending increases in CD8 T cell representation at the cost of M2 macrophage abundance. This effect was strongest in Arm B, suggesting that prior or even concomitant HDCRT may blunt this effect. Rather than M2 macrophages, neutrophils were enriched in the periablated region after FUSTA. This result is also in agreement with our CTD findings presented in Chapter 2. Further, FUSTA seemed to induce downregulations in CD4 and follicular helper T cell populations in the TME. Together, these data suggest HDCRT and FUSTA may influence distinct populations of immune cells, but both trend toward myeloid enrichment and lymphoid depletion which are classically associated with poorer prognosis (165, 166). These data further support evidence from our lab and others that counteracting the myeloid response to the sterile inflammatory responses induced by focal therapy are necessary to appropriately polarize the TME toward CI sensitization (85, 138, 177).

Though significant steps were taken to facilitate comparison within and between AM001 and BR48, we acknowledge limitations to our approach. Both studies were phase I trials designed to test safety, and therefore not sufficiently powered to detect arm-specific differences while appropriately controlling for other confounders. Consequently, variability with respect to tumor type, patient demographics, and past treatment status could not be explicitly accounted for in the randomization process or negative binomial modelling framework for DGE. Notable differences between the trials themselves include distinct inclusion/exclusion criteria and asynchronous permutations of focal therapy + pembro sequencing between arms. Further, we were not able to disaggregate BR48 data by arm, as the trial was still ongoing at the time of writing this manuscript. Finally, we acknowledge that the majority of analyses are transcriptional only, and therefore suffer from potential incongruence with protein expression. All conclusions presented should be considered exploratory only, and not be used to directly inform clinical practice.

In summary, this work represents the first comparative analysis of the effects of HDCRT and FUSTA in combination with pembro on human tumors. Our results identify key transcripts, gene sets, and immune subtypes regulated as functions of the sequence and nature of focal therapy administration in combination with pembro, reinforcing the need to optimize immunoadjuvant + CI approaches. We identify that both focal therapies induce a complex mixture of pro and anti-tumor effects, the balance of which may need to be adjusted by additional pharmacological agents to produce the ideal microenvironment for tumor rejection. Finally, our survival analyses demonstrated the utility of pre-treatment screening and stratification based on gene expression, and suggested new mechanisms of response vs non-response in patients receiving focal therapy-IC combinations. Larger clinical studies directly comparing the two focal therapies will be needed to validate the hypotheses generated herein, and dissect the relative potential of HDCRT vs FUSTA to sensitize tumors to pembro.

3.5 Materials and Methods

3.5.1 Clinical Trials Overview

AM001 (NCT02987166) is a phase I randomized clinical trial designed to test the safety of the sequences of HDCRT and pembro. 21 patients with histologically or cytologically proven advanced solid tumors for which palliative radiation was recommended were randomized to 3 treatment arms with various sequences of HDCRT (24 Gy over 3 fractions) and pembro (200 mg). In Arm A, HDCRT was given on day 1 with pembro given on days 1, 43, 64, and 85. In Arm B, HDCRT was given on day 22, with pembro given on day 1, 43, 64, and 85. In Arm C, HDCRT was given on day 1, with pembro given on days 22, 43, 64, and 85. Biopsies intended for gene expression analysis were performed on the HDCRT-targeted lesions immediately prior to day 1 treatment, and post-treatment on days 22 and 43.

BR48 (NCT03237572) is a phase I randomized clinical trial designed to test the safety of sequences of FUSTA and pembro. 7 patients with histologically confirmed metastatic or unresectable breast cancer with at least one accessible lesion in the breast/chest wall/axilla were randomized to two treatment arms with various sequences of FUSTA (45 W acoustic power, up to 50% ablation volume) and pembro (200 mg). In both arms, patients received FUSTA on day 15 and pembro on days 22, 43, and 64 with one cohort of patients receiving an additional priming dose of pembro on day 1. Biopsies intended for gene expression analysis were performed on the FUSTA-targeted lesions immediately prior to day 1 treatment, and post-treatment on day 22.

Both AM001 and BR48 were approved by the UVA Institutional Review Board for Health Sciences Research (UVA IRB-HSR). Written consent was obtained from all subjects.

3.5.2 Bulk RNA Sequencing and analysis

Biopsies obtained from both trials were stored in Trizol and processed identically. Total RNA extraction was performed using the RNeasy Mini Kit (Qiagen). mRNA was isolated using the NEBNext Poly(A) mRNA Magnetic Isolation Module (New England Biolabs, Ipswich, Massachusetts) followed by library preparation using the NEBNext Ultra II Directional RNA Library Prep Kit for Illumina (New England Biolabs). Sequencing was performed using a NextSeq 500 (Illumina, San Diego, California) at a target depth of 33.3 million 2 x 75 bp paired end reads per sample.

Reads were quasi-mapped to the human genome (hg38 assembly) and quantified at the transcript level using Salmon v0.11.2 (202) followed by summary to the gene level using tximport v1.18.0 (203). Differential gene expression and principle components analysis was performed with DESeq2 v1.30.1 (204). Model designs included covariates for sequencing batch, patient ID,

and treatment condition (Arms A, B, and C at time points d1, d22, and d43 for AM001; pretreatment, periablated, and ablated for BR48). A single surrogate variable was included to estimate processing artifacts using SVA 3.38.0 (276). Gene set enrichment analysis was performed with the GO Biological Processes (205, 206) gene sets from MSigDB (208) using FGSEA v1.16.0 (209) run with 100,000 permutations. Survival analysis, visualization, and parallelization were performed using survival v3.1-12 (277), survminer v0.4.9 (278), and RegParallel v1.8.9 (279) respectively. CTD was performed by inputting TPM normalized counts to the CIBERSORTx webtool (https://cibersortx.stanford.edu/) in absolute mode with B-mode batch correction (168). TCR analyses were performed using MiXCR v3.0.13 with default settings (280). TCR clonality was computed by taking the complement of the normalized Shannon-Wiener diversity index for both T cell receptor α and T cell receptor β clones. All other plots were generated using ggplot2 unless otherwise specified (281).

3.6 Acknowledgements

We are grateful to Dr. Kevin Janes for useful advice with respect to data interpretation. We thank the University of Virginia Genome Analysis and Technology Core for assistance with RNA-sequencing sample processing.

3.7 Figures

Figure 3.1

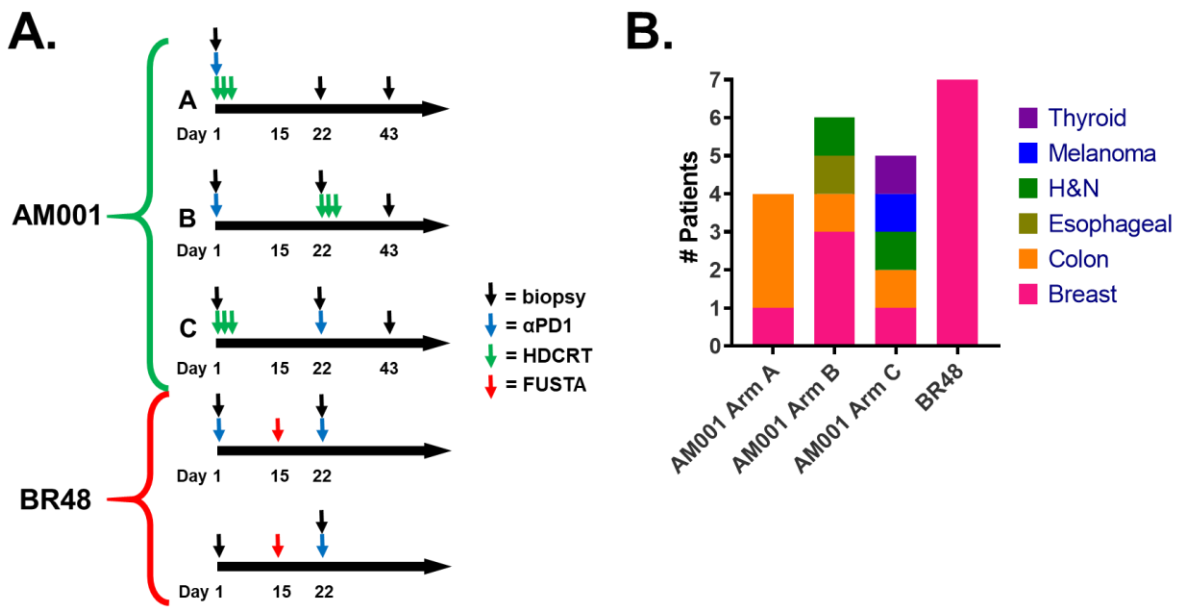

Figure 3.1: Overview of AM001 and BR48 Trial Designs. (A) Timeline of administration of focal therapies and pembrolizumab (αPD1) in each treatment arm of AM001 (top) or BR48 (bottom). The timelines only present information relevant to biopsies studied within the scope of this study. Pembrolizumab continues to be given on and after day 43 in both trials, but biopsies for gene expression were only obtained until day 43 in AM001 and day 22 in BR48. Arm identifiers are shown to the left of the timelines for AM001, and remain unknown for BR48 until the trial has fully accrued. (B) Distribution of primary tumor types analyzed for gene expression.

Figure 3.2

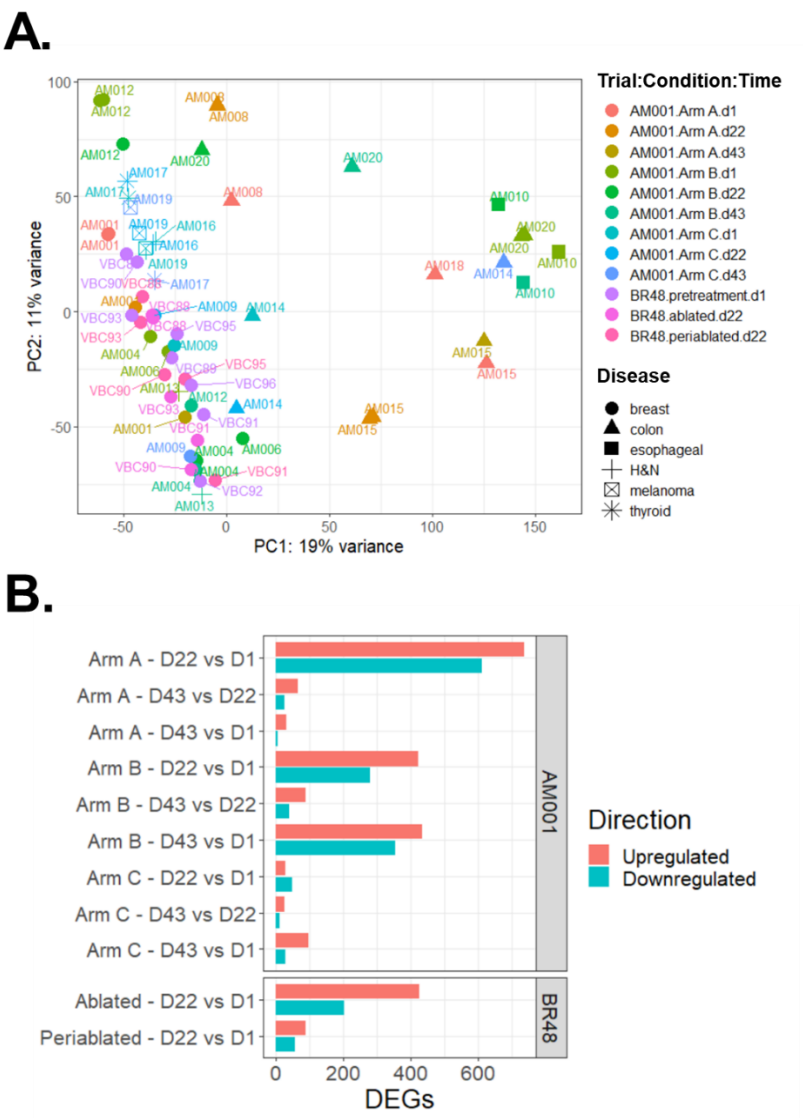

Figure 3.2: Overview of AM001 and BR48 RNA-Sequencing. (A) Principle components analysis of RNA-seq transcript counts after variance stabilizing transformation. Each point represents a single sample, color coded according to combination of trial, condition, and time point. Shapes represent primary disease type. (B) Number of significantly (p adjusted < 0.05) differentially expressed genes (DEGs) for each condition within each trial, separated according to up or downregulation.

Figure 3.3:

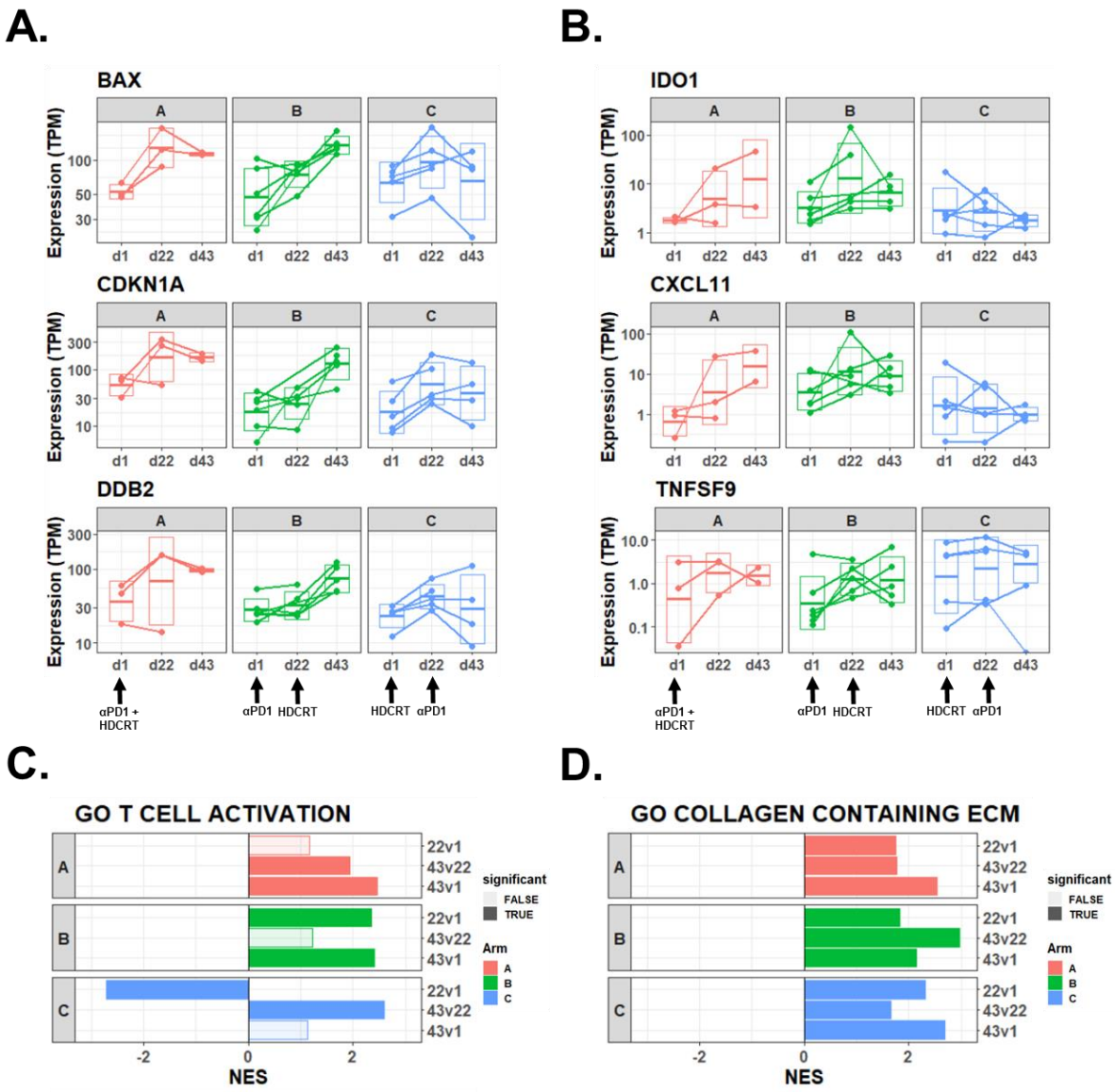

Figure 3.3: Sequencing Affects Induction of Immune Checkpoints after Pembro, but not Induction of DNA Damage Response Transcripts after HDCRT. (A and B) Transcripts per million (TPM) normalized counts of selected DNA damage response transcripts (A) or proinflammatory transcripts (B) grouped by treatment arm and time point. Samples are connected by patient ID. Cross bars correspond to mean +/- SD. Arrows below the plots indicate administration of therapeutics for each arm for reference. (C and D) Normalized enrichment scores for the GO T CELL ACTIVATION pathway (C) or the GO COLLAGEN CONTAINING EXTRACELLULAR MATRIX pathway (D). Bars are grouped according to time contrasts within arms. Opacity indicates p adjusted < 0.05.

Figure 3.4

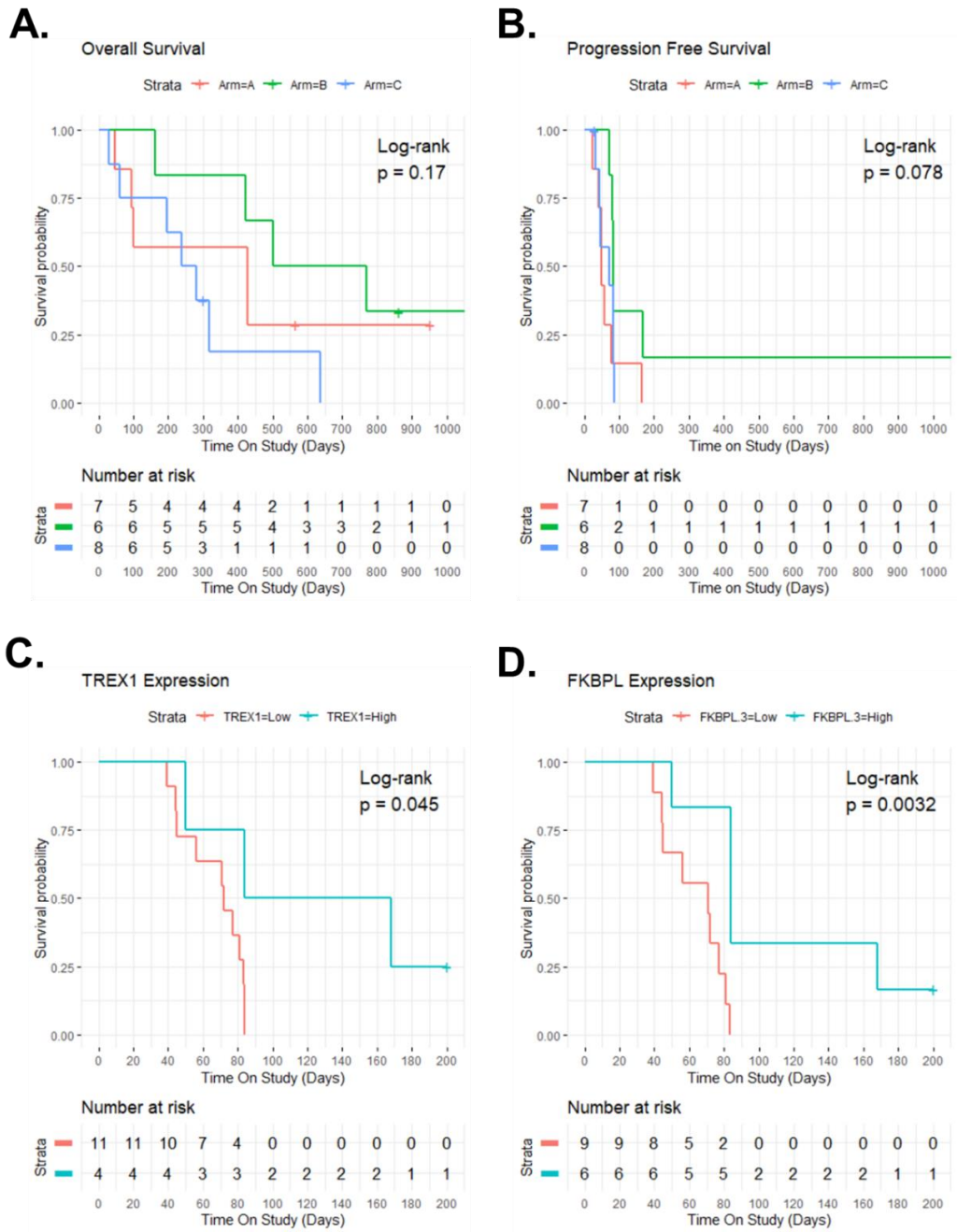

Figure 3.4: Sequencing and Pretreatment Gene Expression Profiles May Predict Clinical Course after Administration of HDCRT and pembro. (A) Kaplan-Meier curve for overall survival measured from the time of trial start, grouped by treatment arm. (B) Kaplan-Meier curve for progression free survival measured from the time of trial start, grouped by treatment arm. PFS is determined as the time to first observation of radiologic progression of disease in or out of the HDCRT field. (C-D) Kaplan-Meier curves for PFS, grouped by expression of *TREX1* (C) or *FKBPL* (D)

Figure 3.5

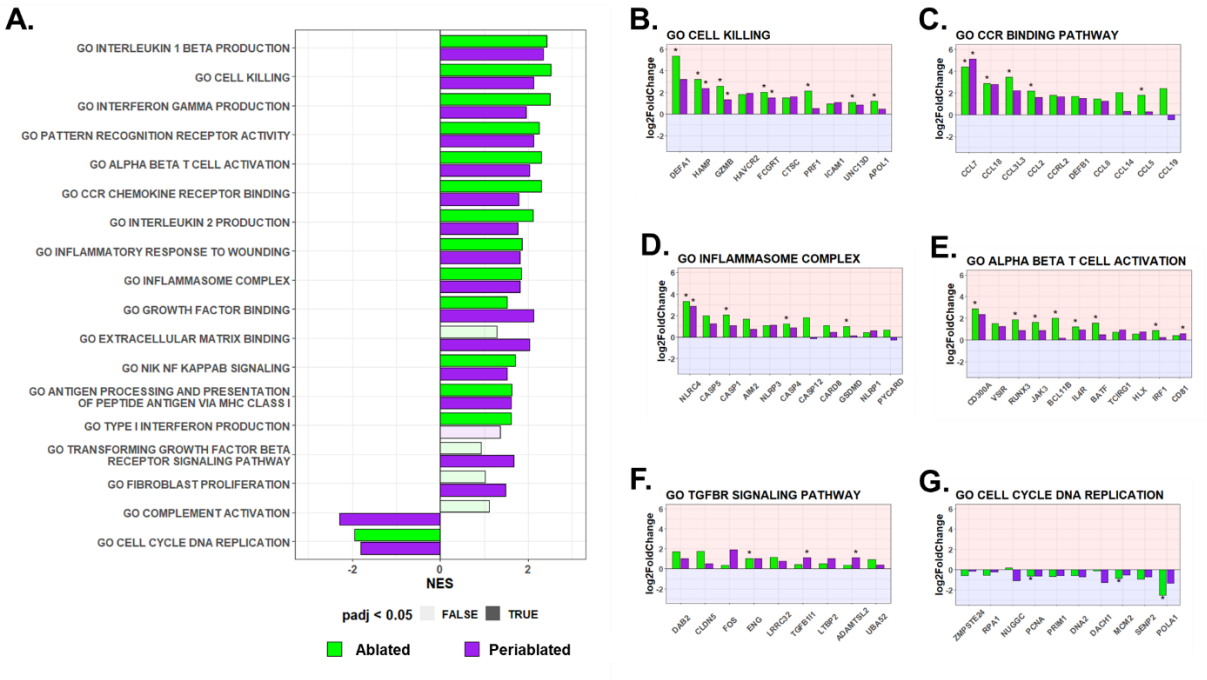

Figure 3.5: Ablated and Periablated Breast Tumors Exhibit Enhanced but Distinct Immunogenicity Signatures after FUSTA. (A) Normalized enrichment scores for selected pathways modulated in BR48, grouped according to ablated vs pretreatment (green) or periablated vs pretreatment (purple). Opacity indicates p adjusted < 0.05. (B-G) Log2Fold change in expression relative to pretreatment for the top 5 – 10 transcripts from ablated and periablated leading edges for enrichment of GO CELL KILLING (B), GO CCR BINDING PATHWAY (C), GO INFLAMMASOME COMPLEX (D), GO ALPHA BETA T CELL ACTIVATION (E), GO TGFBR SIGNALING PATHWAY (F), and GO CELL CYCLE DNA REPLICATION (G). * indicates p-adjusted < 0.05.

Figure 3.6

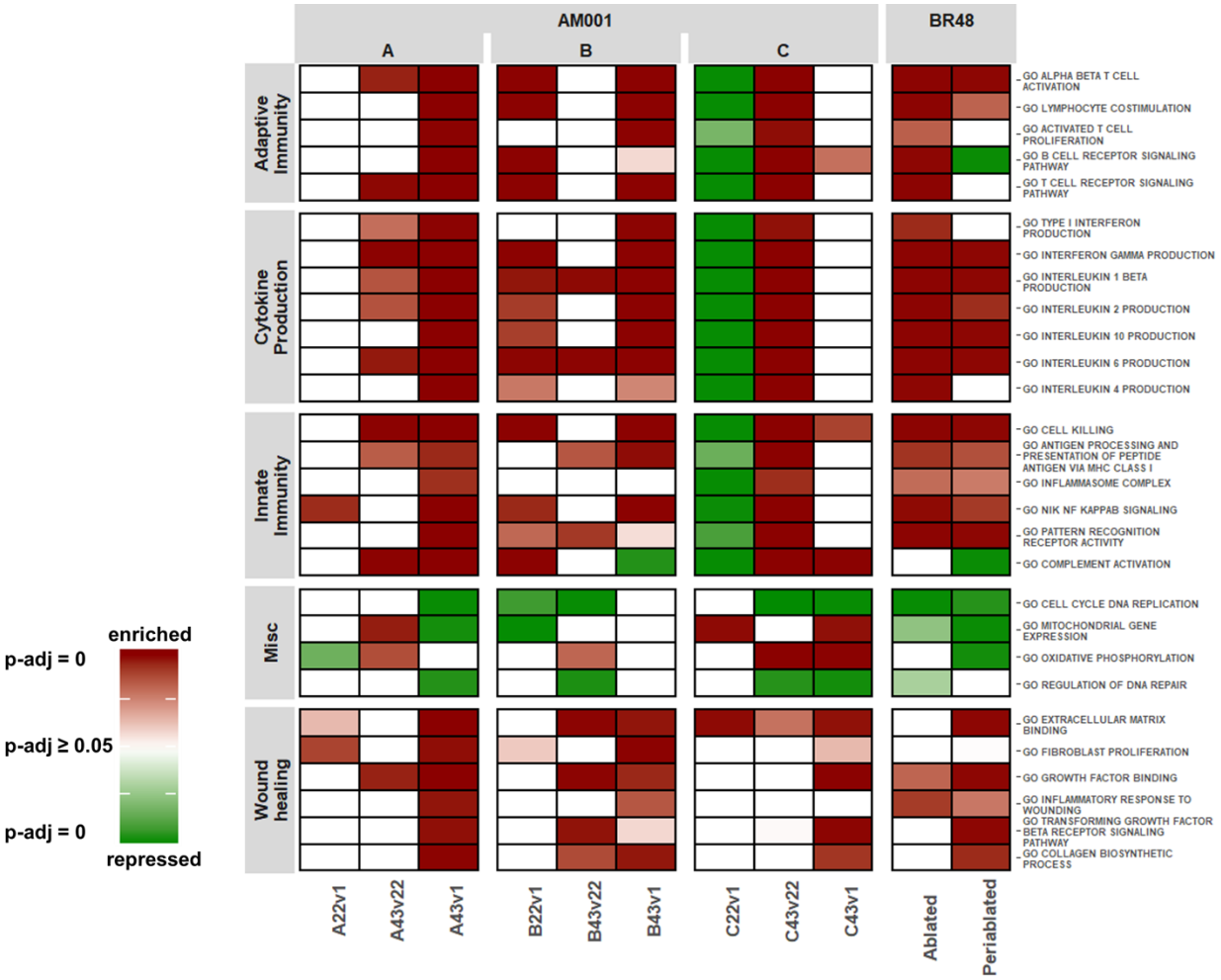

Figure 3.6: Comparison of Biological Theme Representation in AM001 vs BR48. Heatmap showing significance of repression (green) or enrichment (red) of pathways (rows) associated with adaptive immunity, cytokine production, innate immunity, miscellaneous, and wound healing for conditions within each trial (columns). Full opacity corresponds to an adjusted-p-value of 0, while full transparency corresponds to an adjusted p-value **≥** 0.05.

Figure 3.7

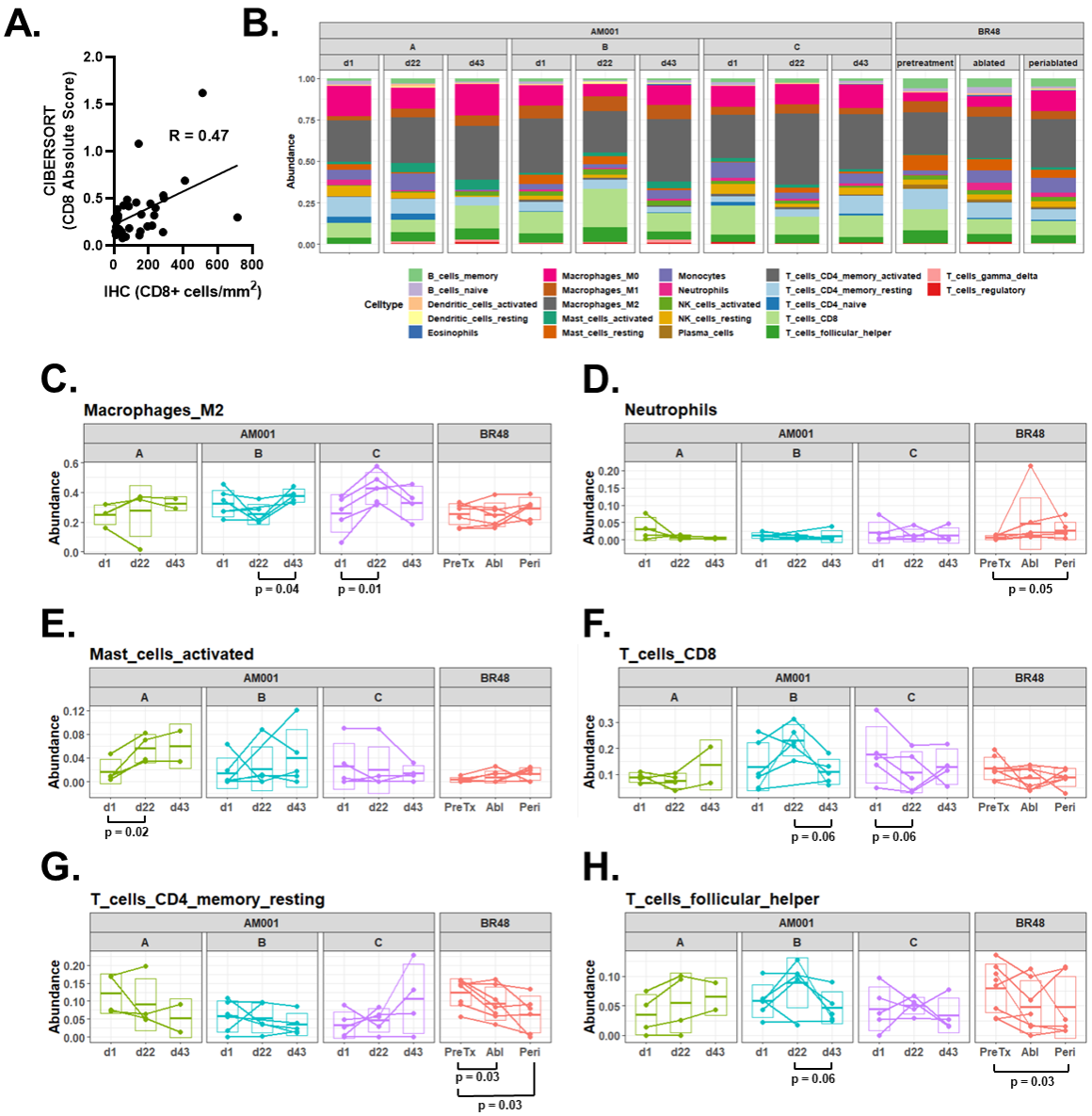

Figure 3.7: Digital Flow Cytometry in AM001 vs BR48. (A) Correlation between patient-matched absolute CD8 abundance as measured by CIBERSORT and CD8+ T cell counts measured by a pathologist on stained tissue sections. (B) Stacked bar plots of average abundances of all 22 cell types grouped by trial and treatment condition. (C-H) Normalized abundance estimates for M2 macrophages (C), neutrophils (D), activated mast cells (E), CD8 T cells (F), memory resting CD4 T cells (G), and follicular helper T cells (H). Points are connected according to patient ID. Cross bars correspond to mean +/- SD. P values were determined by paired t tests.

Figure 3.S1

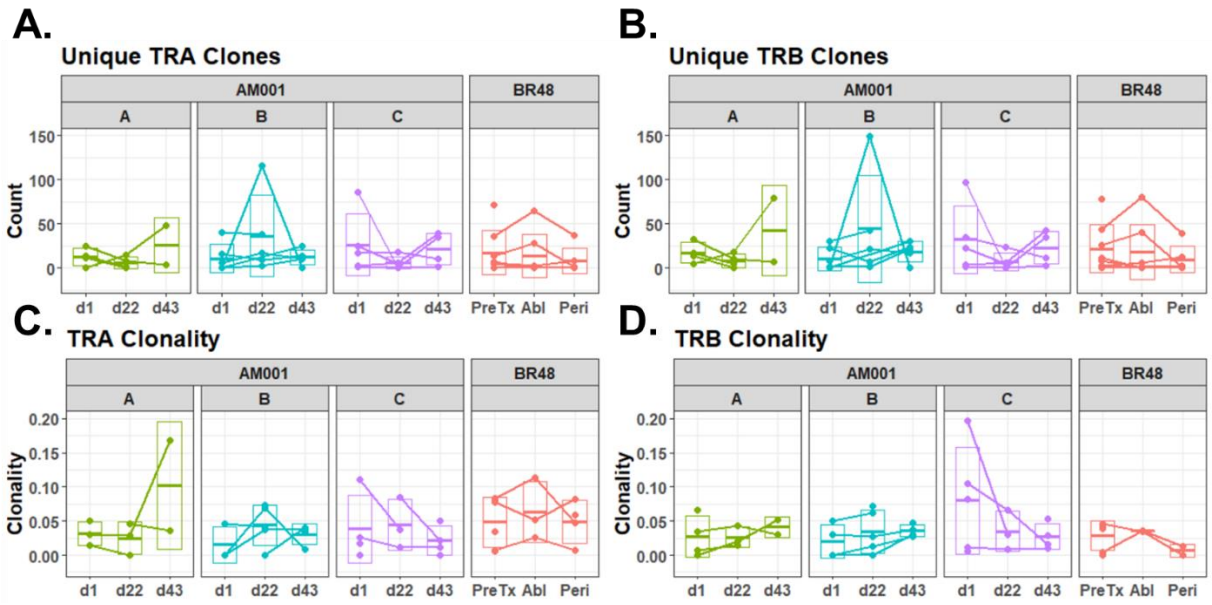

Figure 3.S1: Combinations of pembro and FUSTA or HDCRT do not significantly alter numbers or clonality of T cell receptors. (A-B) Counts of unique T cell receptor alpha (TRA) chains (A) or T cell receptor beta (TRB) chains (B) grouped by trial and treatment condition. Connected points represent the same patient. (C-D) Clonality of TRA populations (C), and TRB populations (D), as measured by the complement of the normalized Shannon-Weiner diversity index, grouped by trial and treatment condition. Connected points represent the same patient.

Chapter 4: Transcriptomic Response of Brain Tissue to Focused Ultrasound-Mediated Blood-Brain Barrier Disruption Depends Strongly on Anesthesia

Alexander S. Mathew, Catherine M. Gorick, E. Andrew Thim, William J. Garrison, Alexander L. Klibanov, Grady W. Miller, Natasha D. Sheybani, and Richard J. Price

*This chapter is adapted from:

Mathew, Alexander S., et al. "Transcriptomic response of brain tissue to focused ultrasound-mediated blood–brain barrier disruption depends strongly on anesthesia." *Bioengineering & Translational Medicine* (2020): e10198.

Abbreviations:

An	Anesthesia
BBB	Blood Brain Barrier
BBBD	Blood Brain Barrier Disruption
CNS	Central Nervous System
DAMP	Damage Associated Molecular Pattern
DGE	Differential Gene Expression
FUS	Focused Ultrasound
GO	Gene Ontology
GSEA	Gene Set Enrichment Analysis
H&E	Hematoxylin and Eosin
Iso	Isoflurane
Iso-FUS	Isoflurane anesthesia with Focused Ultrasound treatment
KD	Ketamine/Dexmedetomidine
KD-FUS	Ketamine/Dexmedetomidine anesthesia with Focused Ultrasound treatment
LEA	Leading Edge Analysis
MB	Microbubbles
MRgFUS	Magnetic Resonance-guided Focused Ultrasound
NES	Normalized Enrichment Score
PCA	Principal Components Analysis
PNP	Peak-Negative Pressure
QC	Quality Control
RBC	Red Blood Cell
RIN	RNA Integrity Number
SI	Sterile Inflammation

4.1 Abstract

Focused ultrasound (FUS) mediated blood brain barrier disruption (BBBD) targets the delivery of systemically-administered therapeutics to the central nervous system (CNS). Pre-clinical investigations of BBBD have been performed on different anesthetic backgrounds; however, the influence of the choice of anesthetic on the molecular response to BBBD is unknown, despite its potential to critically affect interpretation of experimental therapeutic outcomes. Here, using bulk RNA sequencing, we comprehensively examined the transcriptomic response of both normal brain tissue and brain tissue exposed to FUS-induced BBBD in mice anesthetized with either isoflurane with medical air (Iso) or ketamine/dexmedetomidine (KD). In normal murine brain tissue, Iso alone elicited minimal differential gene expression (DGE) and repressed pathways associated with neuronal signaling. KD alone, however, led to massive DGE and enrichment of pathways associated with protein synthesis. In brain tissue exposed to BBBD (1 MHz, 0.5 Hz pulse repetition frequency, 0.4 MPa peak-negative pressure), we systematically evaluated the relative effects of anesthesia, microbubbles, and FUS on the transcriptome. Of particular interest, we observed that gene sets associated with sterile inflammatory responses and cell-cell junctional activity were induced by BBBD, regardless of the choice of anesthesia. Meanwhile, gene sets associated with metabolism, platelet activity, tissue repair, and signaling pathways, were differentially affected by BBBD, with a strong dependence on the anesthetic. We conclude that the underlying transcriptomic response to FUS-mediated BBBD may be powerfully influenced by anesthesia. These findings raise considerations for the translation of FUS-BBBD delivery approaches that impact, in particular, metabolism, tissue repair, and intracellular signaling.

4.2 Introduction

The blood-brain barrier (BBB) is essential to maintaining homeostasis in the central nervous system (CNS). The BBB describes a specialized vasculature, consisting of nonfenestrated endothelium, pericytes, astrocytic processes, microglia, and basement membrane working in concert to precisely permit nutrient transport while protecting against toxins and pathogens. However, the BBB also presents a significant neuropharmacological obstacle, preventing 98% of small-molecule therapeutics and nearly 100% of large-molecule therapeutics from accessing the CNS (102). Significant efforts have focused on strategies to bypass or disrupt the BBB. Methods to bypass the BBB, including intracranial injection and intracerebroventricular infusion, require surgical intervention and thus carry significant risk. Chemical methods to disrupt the BBB, such as mannitol, cause global BBB disruption and lead to considerable neurotoxicity.

Focused ultrasound (FUS) following IV infusion of microbubbles (MB) is a promising approach for BBB disruption (BBBD) (103–105). In this technique, ultrasound waves produced extracorporeally pass through the skull and cause MB circulating in a targeted region of the brain to oscillate. These oscillations disrupt BBB tight junctions and enhance transport of molecules into the brain parenchyma. FUS induced BBBD is an attractive alternative to surgical and chemical methods as it is targeted, non-invasive, and repeatable. Many therapies normally restricted by the BBB have been successfully delivered with FUS + MB, including antibodies (106–108), chemotherapeutics (109–111), neural stem cells (112, 113), and genes (114–116).

BBBD with FUS is reversible and may be applied in a manner that yields little to no histological damage after repeated treatment (104, 117, 118). However, recent molecular profiling studies have demonstrated that, under certain conditions, FUS induced BBBD can lead to increased expression of pro-inflammatory cytokines, homing receptors, and damage associated molecular patterns (DAMPs) as well as increased systemic macrophage accumulation (119). These findings are consistent with sterile inflammation (SI), an innate immune response. The potential for FUS to induce local SI has sparked discussion of the cellular implications of FUS, both where additional inflammation may be desirable (such as cancer or Alzheimer's) or undesirable (such as multiple sclerosis or stroke) (120–123). Transcriptomic studies have shown that FUS induced SI is proportional to both microbubble dose and FUS acoustic pressure (150, 151). At pressures capable of reliably opening the BBB, as measured by MR contrast enhancement, we previously observed upregulation of proinflammatory transcripts (such as Ccl3, Ccl12, Ccl4, and GFAP) and pathways at 6 h post-FUS, trending toward resolution at 24 h post-FUS, consistent with previous studies (119, 150, 152). Recent work has demonstrated the extent of post-FUS SI can be modulated by administration of dexamethasone (282). Still, knowledge of

the contributions of FUS experimental parameters to the SI response as well as non-inflammatory effects on the brain parenchyma remain limited.

One such parameter is general anesthesia. Anesthetic protocols, ubiquitous in preclinical FUS BBBD studies, distinctly impact the circulation time of MB and the extent of FUS-induced vascular damage (283, 284). Common anesthetics vary widely in their effects on the CNS, differentially affecting cerebral vasculature, neuronal signaling, inflammation, and metabolism (285–287). Indeed, a review of the FUS BBBD literature (**Table 4.S1**) highlights considerable diversity in anesthetic protocols used in pre-clinical studies of experimental therapeutic efficacy, with isoflurane and ketamine being the most commonly chosen agents. We hypothesize that anesthetics differentially alter the underlying reactivity of the brain parenchyma when FUS is applied, which may produce anesthesia-dependent synergies and conflicts with respect to SI, drug metabolism, or neuronal damage. Herein, we test this hypothesis by detailing the cumulative transcriptome level and pathway level impacts of anesthesia, MB, and FUS on the brain parenchyma.

4.3 Results

4.3.1 Characterization of FUS-Induced BBBD and Passive Cavitation Analysis

Mice were anesthetized with either isoflurane in medical air (Iso) or ketamine/dexmedetomidine (KD) and treated with Magnetic Resonance-guided Focused Ultrasound (MRgFUS) targeted to the right or left striatum (n = 4 per group). Contrast-enhanced MRIs (**Figure 4.1A**), collected before and after treatment, revealed enhanced signal in mice anesthetized with Iso compared to KD (**Figure 4.1B and 4.1C**). To evaluate MB activity, we analyzed acoustic emissions data obtained from a listening hydrophone embedded in the therapeutic transducer. No significant differences in harmonic emissions (i.e. 2^{nd}, 3^{rd}, 4^{th} harmonics) or broadband emissions (< 10 MHz) were found between Iso and KD (**Figure 4.1D**).

4.3.2 Transcriptomic Variation is Driven Primarily by KD and Secondarily by FUS BBBD

Bulk RNA sequencing was performed on mRNA extracted 6 h post-FUS from the treated region of each brain treated with MRgFUS shown in **Figure 4.1**. Brains extracted from naïve mice, mice treated with each anesthetic alone, and mice treated with each anesthetic and MB were also sequenced 6 h after treatment (n = 3 per group). After read alignment and QC, principal components analysis (PCA) was performed on transformed transcript counts from each sample to assess global differences between treatment conditions (**Figure 4.2A**). Interestingly, the first principal component segregated samples by whether they received KD, with Iso-treated mice clustering more closely to the naïve controls. FUS-treated mice formed a distinct cluster only in the KD treated mice. Similar results were obtained when hierarchical clustering was performed on inter-sample Euclidian distances computed between samples based on their transcript counts (**Figure 4.2B**). With the exception of one sample, the first branch point of the dendrogram separated samples by KD status, while the second and third branch points distinguished samples by FUS treatment.

4.3.3 Overview of Differential Gene Expression and Gene Set Enrichment Analyses

To evaluate relative transcriptomic differences between conditions, differential gene expression contrasts were computed for all 21 unique combinations of the 7 conditions evaluated (**Figure 4.2C**). KD alone produced the most profound effect on the transcriptome, with over 3000 genes significantly differentially regulated (p-adjusted < 0.05) compared to naïve brain. Regardless of the anesthetic background, FUS and MB produced moderate (on the order of hundreds of differentially expressed genes) and negligible (< 9 differentially expressed genes) effects on gene expression respectively. Iso alone had a marginal effect on the transcriptome,

only significantly changing the expression of 26 genes. Next, we performed gene set enrichment analysis (GSEA) to identify biological processes consistent with genes differentially expressed within each contrast (**Figure 4.2D**). GSEA was performed using the Gene Ontology (GO) Biological Pathways database, wherein each "GO" term represents a collection of genes associated with a particular biological phenomenon. Surprisingly, Iso alone affected more biological pathways than KD, despite KD affecting considerably more genes. The addition of MB changed relatively few biological pathways. FUS had the strongest effect on biological pathways on both anesthetic backgrounds, inducing more pathways than it repressed.

4.3.4 Anesthetics Differentially Affect the Transcriptome of Normal Brain Tissue

The relative transcriptional impact of Iso and KD on the mouse striatum was marked, with Iso significantly changing expression of 26 genes compared to the 3,291 significantly changed by KD (**Figure 4.3A**). Iso alone induced a traditional anesthetic transcriptional program of repression of neuronal activity (**Figure 4.3B**). KD, however, had a minimal effect on these pathways, instead enriching for steps of protein synthesis and targeting (**Figure 4.3C**). These trends persisted upon addition of MB or FUS. To assess the effect of anesthesia on neuroinflammation, we examined GO processes related to inflammation differentially changed by Iso or KD alone (**Figure 4.3D**). Both anesthetics enriched the CCR Chemokine Receptor Binding pathway, while only Iso induced the Leukocyte Migration pathway. The addition of FUS+MB led to further activation of both inflammatory pathways. Iso alone also had a unique effect on development pathways, downregulating neuronal development (likely due to repressing neuronal signaling) and upregulating development of glial cells, oligodendrocytes, and vasculature (**Figure 4.3E**). In general, addition of MB or MB+FUS led to loss of significance of these pathways. To identify which transcripts contributed to the enrichment or repression of particular pathways, we performed leading edge analysis (LEA). Pecam1 (CD31) was identified as the most significant gene driving the enrichment of the CCR Chemokine Receptor Binding, Leukocyte Migration, and Vasculature Development pathways. Indeed, Pecam1 is one of the few genes induced by Iso with an adjusted p-value less than 0.05.

4.3.5 Anesthetics Differentially Affect the Transcriptome of Brain Tissue Exposed to FUS BBBD

We next sought to compare gene expression changes induced by FUS BBBD when performed under Iso (Iso-FUS) vs KD (KD-FUS). First, we evaluated the extent and overlap of differentially expressed genes (**Figure 4.4A**) and differentially regulated pathways (**Figure 4.4B**),

controlling for changes due to anesthesia + MB alone. While more genes were differentially regulated by KD-FUS, more gene sets were significantly enriched/repressed by Iso-FUS. Interestingly, despite minimal intersection of transcript identities between the two BBBD conditions, 41% of the pathways significantly induced by KD-FUS were also significantly induced by Iso-FUS. Second, we identified 6 categories of biological pathways consistently changed by Iso-FUS, KD-FUS, or both (**Figure 4.4C**). Regardless of the anesthetic background, FUS led to enrichment of genes involved in endothelial cell activity, including pathways associated with cell-cell adhesion and angiogenesis. Iso-FUS induced these pathways more significantly, and additionally led to the expression of genes associated with leukocyte adhesion. Similarly, both FUS conditions led to activation of many inflammation pathways, with the breadth and depth of these responses substantially enhanced in the Iso-FUS condition. Notably, the MHC class I and MHC class II antigen processing and presentation pathways were only upregulated when comparing KD-FUS treated mice to naïve controls. We found the most significant divergence between Iso-FUS and KD-FUS when comparing metabolic pathways. Iso-FUS led to repression of broad and specific metabolic programs while several of these were enriched by KD-FUS. Consistent with significant inflammation and endothelial activation, platelet activity was enhanced by Iso-FUS, while these pathways were relatively unchanged by KD-FUS. Gene sets associated with tissue repair were enriched by FUS under both anesthetics and those associated with neurogenesis were additionally upregulated by KD-FUS only. Signaling pathways engaged by FUS treatment independent of anesthesia included VEGFR signaling, Wnt signaling, and the NF-κB signaling pathway. STAT, SAPK, dopamine, and integrin signaling were further enriched only in Iso-FUS contrasts.

To further compare the effect of anesthesia on FUS BBBD, we performed leading edge analysis (LEA) on selected gene sets enriched by both Iso-FUS and KD-FUS. Comparing transcripts in the LEA of the (Iso + MB + FUS)/(Iso + MB) contrast against those in LEA of the (KD + MB + FUS)/(KD + MB) contrast for the same pathway allows us to address whether FUS is achieving the same “end” (pathway enrichment) by similar “means” (transcript regulation) on different anesthetic backgrounds. We performed comparative LEA on gene sets associated with cell-cell junctions and inflammation, as these were the most consistently induced by both Iso-FUS and KD-FUS. Out of the 173 genes in the Cell Junction Organization gene set (GO:0034330), Iso-FUS and KD-FUS enriched 48 and 50 respectively (**Figure 4.4D**). 19 transcripts were found in the leading edge of both anesthetics including Cdh5 (VE-Cadherin), Vcl, and Flt1. While all 3 of these transcripts were significantly upregulated by KD-FUS across multiple contrasts, only Cdh5 was significantly upregulated by FUS under Iso. Notably, when compared to naïve controls

alone, KD alone significantly downregulated Flt1 and KD + MB led to a trending decrease (p-adj = 0.06).

We next compared the LEA overlap on the Immune System Process gene set (GO:0002682), a broad collection of 1709 genes associated with the immune system (**Figure 4.4E**). Iso-FUS and KD-FUS enriched 512 and 304 of these respectively, with 103 genes enriched by both. IL-1α was found in both LEAs and significantly upregulated across multiple contrasts while IL-1β was only found in the Iso-FUS LEA and indeed only significantly upregulated in Iso-only FUS contrasts. TNFα was found in both LEAs to be significantly upregulated by FUS under both anesthetics when compared to naïve controls, and trending upward in other FUS contrasts (Log2FC > 2, unadjusted p-value < 0.1 for Iso + MB + FUS vs Iso, Iso + MB + FUS vs Iso + MB, KD + MB + FUS vs KD, and KD + MB + FUS vs KD + MB contrasts). To narrow the scope of immune system-related LEA overlaps, we repeated this analysis on the Chemokine Activity gene set (GO:0008009) which only contains 34 genes (**Figure 4.4F**). Iso-FUS and KD-FUS enriched 16 and 12 chemokines respectively, 7 of which were shared. Iso-FUS induced the strongest Ccl2 upregulation regardless of the control condition. KD alone induced a comparable upregulation of Ccl2 with no additional effect due to FUS. Cxcl16 however was more strongly induced with KD-FUS than Iso-FUS when controlling for anesthetic. Ccl3 was upregulated by FUS under both anesthetics as well as KD alone. In summary, while FUS promotes phenotypes such as cell junction organization, inflammation, and chemokine activity independent of anesthetic, the nature of the transcripts mediating these effects are often anesthesia-dependent.

4.3.6 Anesthetics Differentially Affect Transcripts Associated with BBB Structure and Function

We next evaluated the effects of anesthesia, MB, and FUS on transcripts known to be associated with the BBB (208). Iso-FUS upregulated transcripts mediating leukocyte adhesion, including E-selectin, P-selectin, and Icam1 (**Figure 4.5A**). Icam1 was also upregulated by KD alone when compared to sham and by KD-FUS when compared to KD or KD + MB. With respect to BBB tight junction transcripts, FUS upregulated Cldn5 and Emp1 independent of anesthetic (**Figure 4.5B**). KD alone led to downregulation of Ocln and Tjp1. We next evaluated the effect of our experimental conditions on BBB transporter transcripts and observed heterogeneous effects (**Figure 4.5C**). In general, KD led to significantly more DGE in this category than Iso, with very few transcripts changing their expression due to FUS or MB on either anesthetic background. This trend was even more extreme when evaluating BBB transcripts involved in transcytosis and

other miscellaneous functions (**Figure 4.5D**); KD was the only variable significantly changing the expression of transcripts in this class.

4.3.7 Tissue Damage Elicited by FUS BBBD is Minimal and Not Affected by Anesthetic,

Given the anesthesia-dependence of BBBD and FUS-induced gene expression, we next tested whether anesthesia affected the extent of damage in the brain parenchyma after treatment with the same FUS pressure. We performed histological analysis of murine brains treated with combinations of Iso, KD, and FUS (**Figures 4.6A-D**). Brains treated at 0.8 MPa (twice the acoustic pressure of our standard BBBD protocol) were used as positive controls for damage. We scored multiple transverse sections from each condition for RBC extravasation and vacuolation (**Figure 4.6E**). With the exception of the 0.8 MPa positive control group, all conditions tested elicited minimal damage. Thus, BBBD using these conditions elicits little to no histological damage, independent of whether Iso or KD is used.

4.4 Discussion

BBBD mediated by FUS-activated MB has emerged as a promising technique for the image-guided and non-invasive delivery of therapeutics to the CNS. Though this procedure is safe, our understanding of cellular responses to FUS BBBD at the transcriptional level is still limited. This knowledge gap becomes especially significant when considering that pre-clinical BBBD studies have been performed on a multitude of different anesthetic backgrounds (**Table 4.S1**), a factor that could affect the interpretation of how experimental therapeutic outcomes will translate to human applications, wherein such anesthetics are not utilized. Our study systematically addressed how choice of general anesthetic shapes acute transcriptomic responses to FUS with respect to sterile inflammation, endothelial activity, metabolism, platelet activity, repair, molecular signaling, and BBB-associated genes. Ultimately, we conclude that the underlying transcriptomic response to FUS-mediated BBBD may be strongly influenced by the choice of anesthetic. Such responses may synergize and/or conflict with responses generated by the therapeutic approach itself. Thus, our results provide a framework for rational anesthesia selection for preclinical BBBD studies and will likely find utility when comparing clinical outcomes to pre-clinical results for FUS mediated BBBD drug and gene delivery approaches.

PCA and hierarchical clustering performed on variance-stabilizing transformed RNA-seq counts data revealed the relative contributions of Iso, KD, MB, and FUS to intersample variability with respect to CNS gene expression (**Figures 4.2A and 4.2B**). The most striking of these was KD, inducing DGE (p-adjusted <.05) of 3291 genes when compared to naïve controls (**Figure 4.3A**). Whether this profound change in gene expression is attributable to ketamine, dexmedetomidine, or both is unclear. Microarray studies of developing rat brain have shown a similar magnitude of acute differential gene expression from ketamine alone (288). More specifically, investigators reported 819 differentially expressed genes with fold change >1.4, p-adj < 0.05 compared to the 1182 meeting these criteria in our study at an identical timepoint. Though ketamine's mechanism of action is still unclear, recent studies into its rapid anti-depressant action suggest ketamine indirectly suppresses eukaryotic elongation factor 2 kinase (eEf2K), leading to increased protein translation (289). This mechanism is in agreement with our pathway level findings (**Figure 4.3C**). Though fewer transcriptomic level studies exist for dexmedetomidine, it is known to acutely augment transcriptional programs associated with inflammation and circadian rhythm (290, 291). In stark contrast to KD, we found Iso had a negligible impact on gene expression, only significantly altering the expression of 26 genes. This finding is in close agreement with existing acute transcriptomic studies of inhalable anesthetics in rats, which report between 0 and 20 differentially expressed genes (292, 293). Interestingly,

despite weak changes in expression magnitude, Iso changed regulation of significantly more pathways than KD (**Figure 4.2D**). We thus hypothesize that, while Iso influences more targeted transcriptional programs, the combination of ketamine and dexmedetomidine elicits wide-ranging, complex transcription thereby preventing GSEA from detecting discrete pathway enrichment.

We observed increases in inflammatory signatures elicited by both anesthetics (**Figure 4.3D**). Of the few genes upregulated by Iso alone, a surprising number were immune-associated. Some examples include upregulation of T-cell associated markers Ly6a and Ctla2a, upregulation of adhesion markers Pecam1 and CD93, and downregulation of Nfkbia, the protein product of which inhibits NF-κB. Indeed, activation of NF-κB has been proposed as a mechanism by which volatile anesthetics elicit neuroinflammation (294, 295). Several rodent studies have demonstrated volatile anesthetics can also acutely induce expression of IL-6, IL-1β, and activated caspase-3 (296–299). Under conditions of CNS stress, including ischemia or LPS exposure, volatile anesthetics attenuate inflammation, suggesting that these drugs may contribute to maintaining homeostasis in the brain, rather than being strictly pro- or anti- inflammatory (300–303). KD also induced signatures associated with inflammation, though to a lesser extent and with a less clear mechanism than Iso. At the chemokine level, for example, KD significantly upregulated Ccl17, Ccl2, Ccl3, and Ccl6 with minor but significant downregulation of Cxcl12 and Cx3cl1. These mixed effects may be caused by contrasting neuroinflammatory effects produced by ketamine and dexmedetomidine. Ketamine has been shown to be acutely inflammatory in naïve mice, increasing levels of IL-6, IL-1β, and TNF-α (304), while Dexmedetomidine tends to protect against neuroinflammation (305–308). The ability of each anesthetic to amplify or protect against SI induced by FUS may be an important experimental consideration for future preclinical FUS work.

SI caused by FUS-activated MB has raised concerns over its feasibility for repeated clinical application. SI can last for at least 24 h after a single sonication, and is dependent on MB dose and FUS pressure (119, 150–152). Proposed causes of SI include direct acoustic force damage, NVU injury caused by cavitation-induced shockwaves, ischemia reperfusion injury due to vasospasm, and leakage of blood into the parenchyma (119, 150–152). Our unbiased analyses suggest a confluence of these mechanisms that can be affected by choice of anesthetic (**Figure 4.4C**). Pathways enriched by both Iso-FUS and KD-FUS clearly indicate extensive cytokine production, possibly initiated by damage associated molecular pattern (DAMP) release and pattern recognition receptor (PRR) signaling. In general, Iso-FUS led to more extensive activation of the immune response compared to KD-FUS, enriching signatures associated with NF-κB signaling, consistent with previous studies (119, 151, 152). However even for pathways with

similar enrichment, LEA suggests anesthesia affects the quality of FUS-induced SI. The anesthesia dependent induction of IL-1β and IL-1α provides an example (**Figure 4.4E**). Though they bind to the same receptor, they have fundamentally different upstream triggers and downstream consequences. IL-1α is constitutively expressed. It possesses both intracellular activity as a proinflammatory transcription factor and extracellular activity as a DAMP (309, 310). IL-1β, however, is induced by NOD-, LRR- and pyrin domain-containing protein 3 (NLRP3) inflammasome activation (311). Importantly, these two cytokines recruit different populations of myeloid cells and represent distinct stages of the SI response (312). Thus, anesthesia may impact the temporal relationship between FUS application and SI. Enrichment of junctional assembly pathways, VEGF signaling, and angiogenesis supports FUS-induced activation of endothelial cells, leading to both recruitment of leukocytes and barrier repair, especially under Iso. Of note, we observed significant upregulation of claudin-5 transcript, whose tight junction protein product is essential to BBB integrity, in both FUS groups. This may indicate initiation of transcriptional programs to repair the disrupted barrier (**Figure 4.5B**). In contrast, a microarray study of brain microvessels did not detect significant differences in claudin-5 post-FUS(152). This discrepancy could be due to differences in species (i.e. mouse vs. rat), the source of the analyzed tissue in the brain, anesthesia protocol, and several focused ultrasound and microbubble parameters. Downregulation of multiple metabolic pathways in Iso-FUS contrasts further suggests Iso may prime the BBB for more significant alteration than KD.

Despite differential responses at the transcriptional level and in MRI signal enhancement (**Figure 4.1**), FUS applied under both anesthetics led to little to no generation of petechiae by H&E (**Figure 4.6**). With respect to coagulation signatures by RNA-seq, only Iso-FUS led to increased platelet activity despite no significant difference in RBC extravasation compared to KD-FUS (**Figure 4.4C**). While Iso has minimal effect on platelet activity (313–315), both ketamine and dexmedetomidine reduce coagulability (316–319). Thus, KD may minimize the inflammatory response resulting from blood products in the brain parenchyma compared to Iso upon FUS application.

Transient SI can provide beneficial effects in certain disease contexts with respect to clearance and regeneration (153). Indeed, this may be the primary mechanism by which FUS promotes Aβ plaque clearance in Alzheimer's disease (154). Similarly, neurogenesis observed after FUS may be attributable to tissue repair mechanisms preceded SI (156, 320). We observed activation of repair mechanisms by FUS, though to different extents depending on the anesthetic chosen. The observation that KD promotes stronger signatures of repair and weaker signatures

of inflammation, endothelial activation, coagulation, and metabolic alteration supports its use over Iso for pathologies where further CNS stress is undesirable.

Our investigation has some limitations. First, RNA-sequencing only provides transcript-level information. mRNA may not always correlate proportionally to protein expression (198–201). This risk is mitigated at the pathway level, where we present significant alteration of large families of genes consistently up or downregulated by FUS and/or anesthesia. Further, the high intragroup consistency along with the absolute magnitude of differential gene or pathway level changes make noise an unlikely driver of the diverse changes we observed. However, because RNA-seq was performed on bulk tissue, it is not easy to distinguish changes in transcription from changes in relative cell numbers. Next, whether transcriptional changes in Iso-FUS mice are a consequence of isoflurane's interaction with FUS or enhanced BBB permeability is unclear. Finally, not all experiments were performed on the same FUS-system. Though transducer frequencies and acoustic pressures were matched between systems, it is possible that differences in transducer geometries produced confounders in experimental endpoints.

4.5 Conclusions

We investigated how Iso and KD, the two most commonly used anesthetics in preclinical FUS BBBD studies, differentially affect CNS responses to FUS-activated MB. At the same acoustic pressure, FUS induced similar profiles of MB cavitation and measures of damage regardless of the anesthetic. RNA sequencing performed acutely after treatment with combinations of Iso, KD, MB, and FUS revealed distinct contributions from each. Specifically, while Iso alone produced transcriptomic profiles nearly identical to those of naïve mice, it also elicited stronger signatures of stress in the neurovascular unit when combined with FUS. KD, however, induced sweeping transcriptome changes alone, but blunted markers of SI while promoting gene sets associated with tissue repair upon FUS application compared to Iso-FUS. These results provide important context for previous preclinical FUS studies, and underscore anesthesia as an important experimental variable to consider for future work.

4.6 Materials and Methods

4.6.1 Animals

11 week old female C57BL/6 mice were purchased from Jackson and maintained on a 12/12 hour light/dark cycle. Mice weighed between 22 and 28 g and were given food and water *ad libitum*. All animal experiments were approved by the Animal Care and Use Committee at the University of Virginia and conformed to the National Institutes of Health regulations for the use of animals in research.

4.6.2 Anesthesia

Mice in groups designated “KD” received 50-70 mg/kg Ketamine and 0.25-0.5 mg/kg Dexmedetomidine via intraperitoneal injection with no additional maintenance or reversal drug given. Mice in groups designated as “Iso” or “Iso-MA” were placed in an induction chamber and received isoflurane delivered to effect in concentrations of 2.5% in medical air using a vaporizer. For isoflurane groups, anesthesia was maintained via nosecone for a total of 90 minutes.

4.6.3 MRgFUS mediated BBBD

An MRgFUS system was used for RNA-seq studies. Once mice were anesthetized, a tail vein catheter was inserted to permit intravenous injections of MBs and the MRI contrast agent. The heads of the mice were shaved and depilated, and the animals were then placed in a supine position over a degassed water bath coupled to an MR-compatible small animal FUS system (RK-100; FUS Instruments, Toronto, Canada). The entire system was then placed in a 3T MR scanner (Magnetom Prisma; Siemens Medical Solutions, Malvern, Pennsylvania). A 3.5 cm diameter receive RF coil, designed and built in-house, was placed around the head to maximize imaging SNR. Baseline three-dimensional T1-weighted MR images were acquired at 0.3 mm resolution using a short-TR spoiled gradient-echo pulse sequence and used to select 4 FUS target locations in and around the right or left striatum.

Mice received an injection of albumin-shelled MBs (1×10^5 MBs/g b.w.), formulated as previously described (115, 321, 322). Briefly, MBs consist of an albumin protein shell and an octofluoropropane gas core. While made in-house, these MBs are nearly identical to the clinical product Optison, which is commonly used for contrast enhancement with ultrasound. A Beckman Coulter counter was used to determine the MB concentration and size distribution. The mean diameter of the bubbles was 2.32 µm (SD = 1.41 µm), with 90% of the bubbles falling below 4.09 µm. The stock concentration was 2.6E9 MBs/mL, but the bubbles were diluted to a concentration of 1E5 MBs/g b.w. in 50 µL of saline just prior to injection. MBs were delivered via a single bolus

injection. Sonication began immediately after clearance of the catheter. Sonications (4 spots in a 2x2 grid) were performed at 0.4 MPa peak-negative pressure (PNP) using a 1.1 MHz single element focused transducer (FUS Instruments, Toronto, Canada) operating in 10 ms bursts, 0.5 Hz pulse repetition frequency and 2 minutes total duration. A voltage-pressure calibration is provided in **Supplemental Figure 4.2.** Immediately following the FUS treatment, mice received an intravenous injection of gadolinium-based contrast agent (0.05 ml of 105.8 mg/ml preparation; Multihance; Bracco Diagnostics), and contrast-enhanced images were acquired to assess BBBD using the same T1-weighted pulse sequence mentioned above.

4.6.4 Passive Cavitation Detection

Acoustic emissions were detected with a 2.5 mm wideband unfocused hydrophone mounted in the center of the transducer. Acoustic signal was captured using a scope card (ATS460, Alazar, Pointe-Claire, Canada) and processed using an in-house MATLAB (MathWorks) algorithm. Acoustic emissions at the fundamental frequency, harmonics (2f, 3f, 4f), sub harmonic (0.5f), and ultra-harmonics (1.5f, 2.5f, 3.5f) were assessed by first taking the root mean square of the peak spectral amplitude (Vrms) in each frequency band after applying a 200 Hz bandwidth filter, and then summing the product of Vrms and individual sonication duration over the entire treatment period. Broadband emissions were assessed by summing the product of Vrms and individual sonication duration for all remaining emissions over the entire treatment period.

4.6.5 Bulk RNA Sequencing and Analysis

6 hours after treatment, mice were euthanized via an overdose of pentobarbital sodium and phenytoin sodium. Immediately following euthanasia, the mouse brains were harvested and the anterior right quadrants (~100 mg) were excised (with the exception of 1 mouse, which had FUS treatment on the left). For FUS-treated mice, MRI contrast images were referenced to confirm extraction of the full volume of sonicated brain. A representative 3D image of the harvested tissue is provided in **Supplemental Figure 4.1.** Harvested tissue was placed in RNAlater (Qiagen), and stored at -80 °C. RNA extraction was performed using the RNeasy Mini Kit (Qiagen). mRNA was isolated using the NEBNext Poly(A) mRNA Magnetic Isolation Module (New England Biolabs, Ipswich, Massachusetts) followed by library preparation using the NEBNext Ultra II Directional RNA Library Prep Kit for Illumina (New England Biolabs). Sequencing was performed using a NextSeq 500 (Illumina, San Diego, California) at a target depth of 25 million 2 x 75 bp paired end reads per sample. Reads were quasi-mapped to the mouse genome

(mm10 assembly) and quantified at the transcript level using Salmon v0.11.2(202) followed by summary to the gene level using tximport v1.10.1(203). Differential gene expression was performed with DESeq2 v1.22.2 (204). Gene set enrichment analysis was performed with the GO Biological Processes(205, 206) gene sets from MSigDB(208) using FGSEA v1.8.0(209) run with 100,000 permutations. 4-group intersections were visualized with UpSetR plots (323). All other plots were generated in figures 2 – 5 were generated using ggplot2 unless otherwise specified (281).

4.6.6 Stereotactic FUS mediated BBBD

A stereotactic tabletop FUS system was used for histological studies. Sonications using the stereotactic frame were performed using a 1-MHz spherical-face single-element FUS transducer with a diameter of 4.5 cm (Olympus). FUS (0.4 MPa or 0.8 MPa; 120 s, 10-ms bursts, 0.5-Hz burst rate) was targeted to the right striatum. The 6-dB acoustic beamwidths along the axial and transverse directions are 15 mm and 4 mm, respectively. The waveform pulsing was driven by a waveform generator (AFG310; Tektronix) and amplified using a 55-dB RF power amplifier (ENI 3100LA; Electronic Navigation Industries). A voltage-pressure calibration is provided in **Supplemental Figure 4.2.**

Once anesthetized, a tail-vein catheter was inserted to permit i.v. injections of MBs and Evans Blue. The heads of the mice were shaved and depilated, and the animals were then positioned prone in a stereotactic frame (Stoelting). The mouse heads were ultrasonically coupled to the FUS transducer with ultrasound gel and degassed water and positioned such that the ultrasound focus was localized to the right striatum. Mice received an i.v. injection of the MBs (1 x 10^5 MBs/g b.w.) and Evans Blue, followed by 0.1 mL of 2% heparinized saline to clear the catheter. Sonication began immediately after clearance of the catheter. In contrast to the MR-guided experiments, which targeted four spots, only one location was targeted in these studies due to the increased focal region of the transducer (4 mm in the transverse direction, relative to 1 mm for the transducer in the MR-compatible system).

4.6.7 Histological Processing and Analysis

60 minutes after Evans Blue injection, mice were euthanized via an overdose of pentobarbital sodium and phenytoin sodium. A macroscopic image was taken immediately after whole brain harvest. Brains were then placed in 10% NBF, embedded in paraffin, and sectioned 400 µm apart. H&E stained sections were imaged with 4x and 20x objectives on an Axioskop light microscope (Zeiss, Germany) equipped with a PROGRES GRYPAX microscope camera

(Jenoptik, Germany). 10 20x images from the region of the right striatum with maximal Evans Blue extravasation were taken per section and 2 – 6 sections were imaged per brain. A researcher blinded to treatment condition assigned a semi-quantitative score of 0 (none – complete absence of RBC extravasation/vacuolation), 1 (mild – sparse small sites of RBC extravasation/vacuolation), 2 (moderate – singular large OR multiple small sites of RBC extravasation/vacuolation), or 3 (severe – multiple large sites of RBC extravasation/vacuolation) to each 20x image for RBC extravasation and vacuolation using a custom MATLAB (MathWorks) script.

4.6.8 Statistical Methods:

For contrast enhancement and acoustic emissions analyses, data are presented as mean ± SEM. Statistical significance was detected by Mann-Whitney test. For differential gene expression significance analysis, DESeq2[75] was used with default parameters. Briefly, DESeq2 pools expression information across all replicates and fits a negative binomial model to each gene followed by a Wald test. An independent filtering process combined with automatic outlier detection using Cook's distance maximize the number of significant genes remaining after FDR correction. Only genes with FDR adjusted p-values < 0.05 are presented as significant unless stated otherwise. For GSEA, the fgsea[80] tool was implemented with 100,000 permutations. Briefly, statistical significance for each pathway is evaluated with a permutation test followed by standard FDR correction. Only enrichment scores with FDR adjusted p-values < 0.05 are presented as significant unless stated otherwise. For histological analyses, data are presented as mean ± SEM. Statistical significance was detected by one-way ANOVA followed by comparison against naïve with Dunnett's multiple comparison test.

4.7 Acknowledgements

Supported by National Institutes of Health Grants R01EB020147, R01CA197111, R01NS111102, and R21EB024323 to R.J.P. and R01EB023055 to A.L.K. A.S.M. was supported by National Institutes of Health Training Grant T32LM012416. C.M.G. was supported by American Heart Association Fellowship 18PRE34030022 and a UVA School of Medicine Wagner Fellowship. N.D.S. was supported by a National Cancer Institute F99/K00 Predoctoral to Postdoctoral Fellow Transition Award (F99CA234954), NSF Graduate Research Fellowship, and a UVA School of Medicine Wagner Fellowship. We thank the UVa Genome and Technology Core for their assistance with sample processing.

4.8 Conflict of Interest

The authors declare no conflict of interest.

4.9 Data Availability

Bulk RNA sequencing data have been deposited in the Gene Expression Omnibus database (https://www.ncbi.nlm.nih.gov/geo/query/acc.cgi?acc=GSE152171). All remaining data generated or analyzed during this study are included in this article.

4.10 Author Contributions

Conceptualization - A.S.M., C.M.G., N.D.S., E.A.T., and R.J.P.; Methodology - A.S.M., C.M.G., N.D.S., E.A.T., W.J.G., A.L.K., G.W.M., and R.J.P.; Investigation - A.S.M., C.M.G., N.D.S., E.A.T., W.J.G., A.L.K., G.W.M., and R.J.P.; Formal Analysis - A.S.M., C.M.G., N.D.S., E.A.T., and R.J.P.; Writing – Original Draft Preparation, A.S.M. and R.J.P.; Writing – Review & Editing, A.S.M., C.M.G., N.D.S., E.A.T., W.J.G., A.L.K., G.W.M., and R.J.P.; Supervision, G.W.M. and R.J.P.; Funding Acquisition - A.S.M. and R.J.P.

4.11 Figures and Tables

Figure 4.1

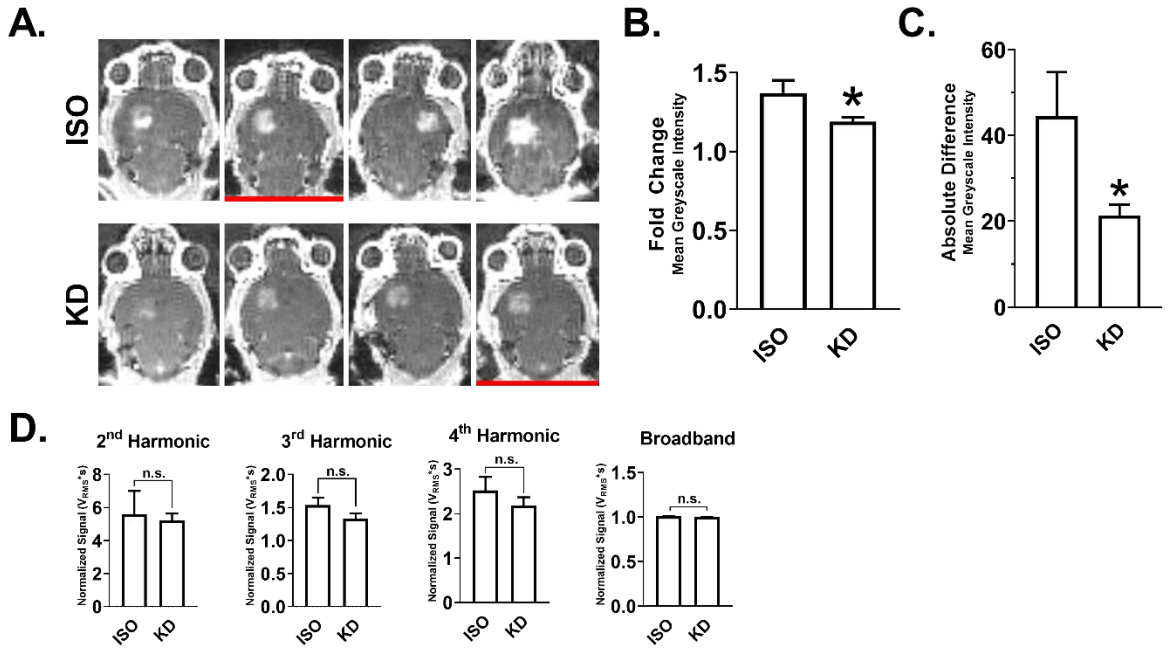

Figure 4.1: Characterization of FUS-Induced BBBD and Passive Cavitation Analysis. (A) T1-weighted contrast-enhanced 3T MRI images of naïve brains immediately following BBB disruption with FUS+MB (n = 4 per anesthetic). Red lines denote mice that were removed from RNA sequencing analysis due to low RNA integrity number (RIN). (B) Fold difference in mean grayscale signal intensity in contrast-enhanced images in FUS-treated hemisphere relative to contralateral hemisphere. Data are represented as mean with SEM. *p<0.05 (p = 0.0286) by Mann-Whitney test. n=4 mice per group. (C) Acoustic emissions signals (2nd, 3rd, 4th harmonics and broadband) at 0.4 MPa FUS + MB exposure, normalized to 0.005 MPa signal without MB. Data are represented as mean with SEM. No significance was detected by Mann-Whitney test. n=4 mice per group.

Figure 4.2

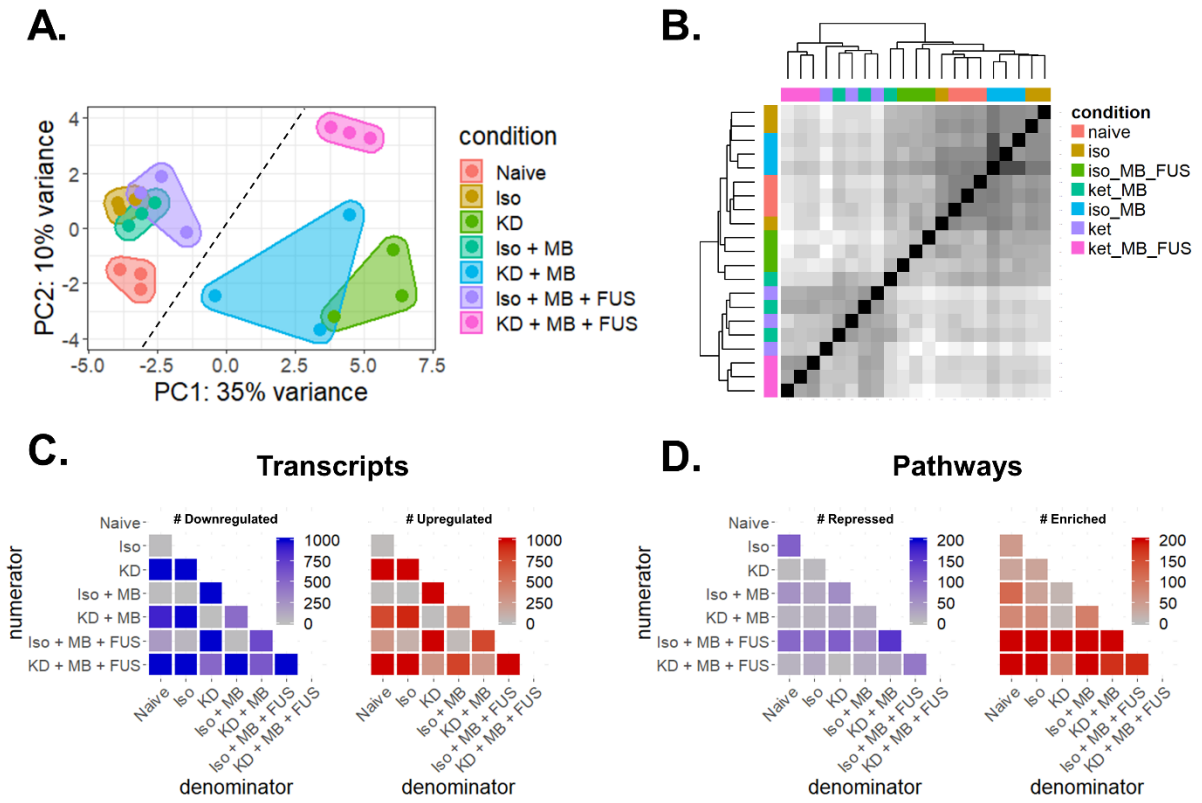

Figure 4.2: RNA sequencing overview. (A) Principal components analysis of RNA-seq transcript counts after variance stabilizing transformation. Each dot represents a single sample (n = 3 per group). The dashed line separates KD- samples (left of line) from KD+ samples (right of line). (B) Pairwise sample Euclidean distance matrix computed on transcript counts. Each row and column represents a single sample. Hierarchical clustering was performed using complete linkage. Darker shade corresponds to increasing transcriptome similarity. (C) Number of significantly downregulated (left) and upregulated genes (right) for all 21 contrasts of the 7 conditions tested. Each row represents a numerator condition and each column represents a denominator condition. (D) Magnitude of significantly repressed (left) and enriched pathways (right) for all 21 contrasts of the 7 conditions tested. Each row represents a numerator condition and each column represents a denominator condition. For all genes and pathways, significance is defined as p-adjusted < 0.05.

Figure 4.3:

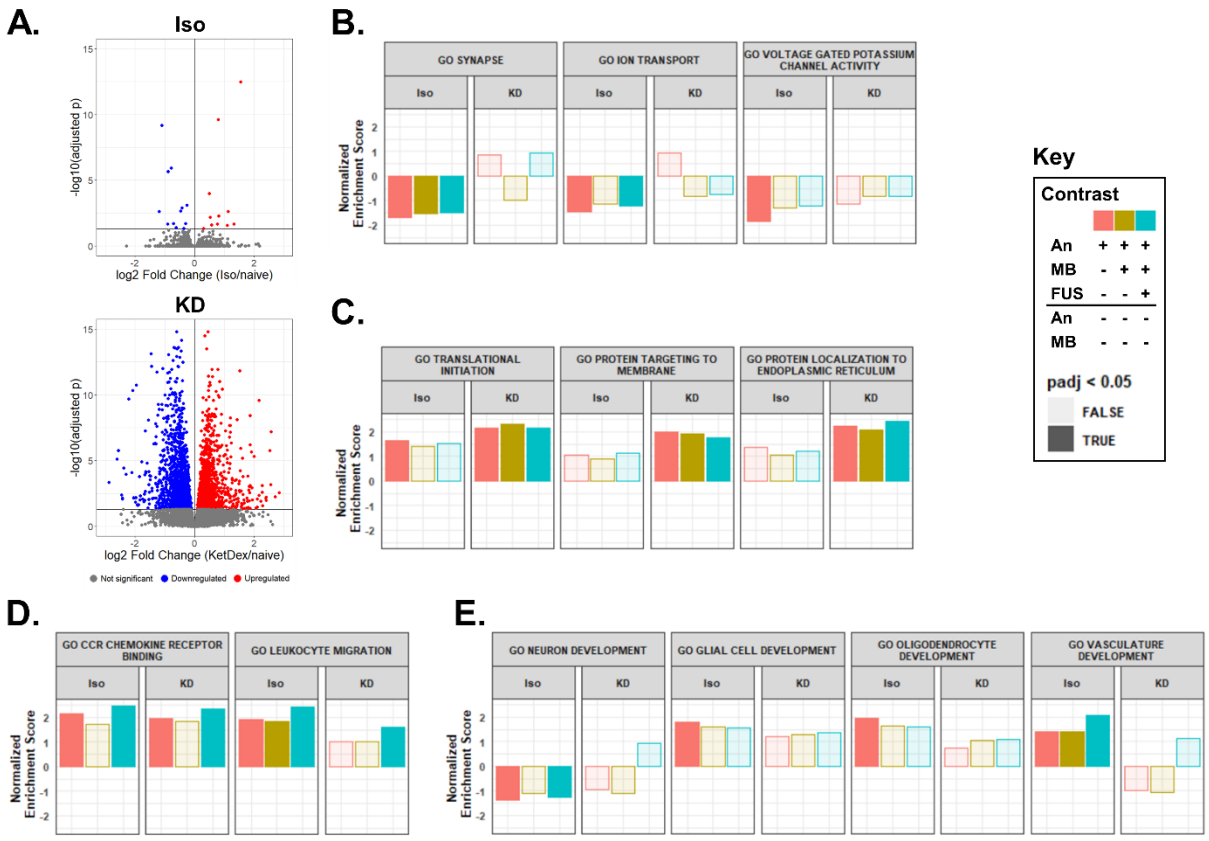

Figure 4.3: Anesthetics Differentially Affect the Transcriptome of Normal Brain Tissue. (A) Volcano plots of differentially regulated transcripts 6 h post anesthesia delivery with Iso (top) or KD (bottom) compared to naïve controls. (B-E) Normalized Enrichment scores (NES) for gene sets associated with (B) neuronal signaling, (C) protein synthesis, (D) inflammation, and (E) development. GSEA was computed based on ranked DGE from (An, red), An+MB (blue), and An+MB+FUS (gold) against naïve controls for Iso and KD. Opaque bars indicate an adjusted p-value < 0.05.

Figure 4.4

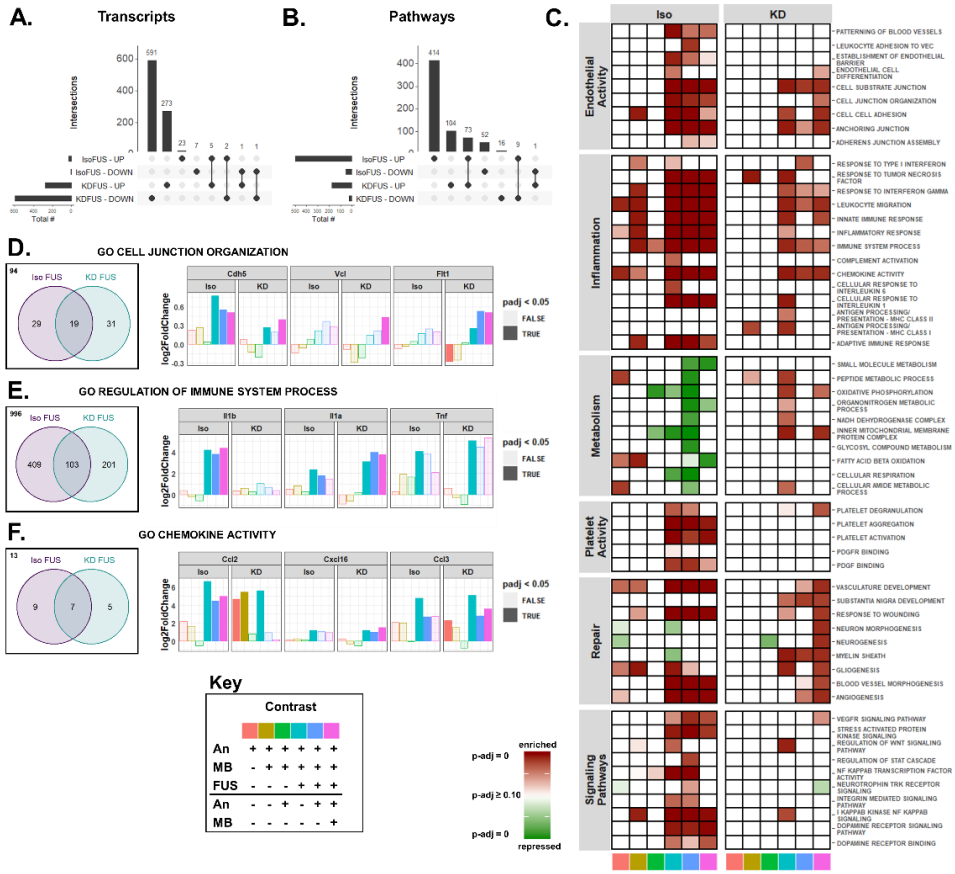

Figure 4.4: Anesthetics Differentially Affect the Transcriptomic of Brain Tissue Exposed to FUS BBBD. (A) UpSetR plots for evaluating intersections of upregulated and downregulated transcripts between IsoFUS and KDFUS, controlling for the effects of anesthesia and MB. (B) UpSetR plots for evaluating intersections of enriched and repressed pathways between IsoFUS and KDFUS, controlling for the effects of anesthesia and MB alone. (C) Heatmap showing significance of repression (green) or enrichment (red) of pathways (rows) associated with endothelial activity, inflammation, metabolism, platelet activity, repair, and signaling for multiple contrasts (columns), separated by anesthetic. Contrast identities are shown by the color at the bottom of the column, corresponding to the key. Full opacity corresponds to an adjusted-p-value of 0, while full transparency corresponds to an adjusted p-value ≥ 0.10. (D-F) Venn diagrams (left) of leading edge transcripts and selected leading edge transcript expression (right) for (D) Cell Junction Organization (GO:0034330), (E) Regulation of Immune Process (GO:0002682), and (F) Chemokine Activity (GO:0008009) gene sets, separated by anesthetic background. Bar color represents the contrast, corresponding to the key. Opaque bars indicate an adjusted p-value < 0.05. Each color in the key corresponds to a specific pairwise comparison of Anesthesia (An), An + MB, and An + MB + FUS for either Iso or KD, specifying the numerator (above the black line), and denominator (below the black line). For example, pink corresponds to the ratio of gene expression for mice treated with An + MB + FUS to those treated with just An + MB.

Figure 4.5

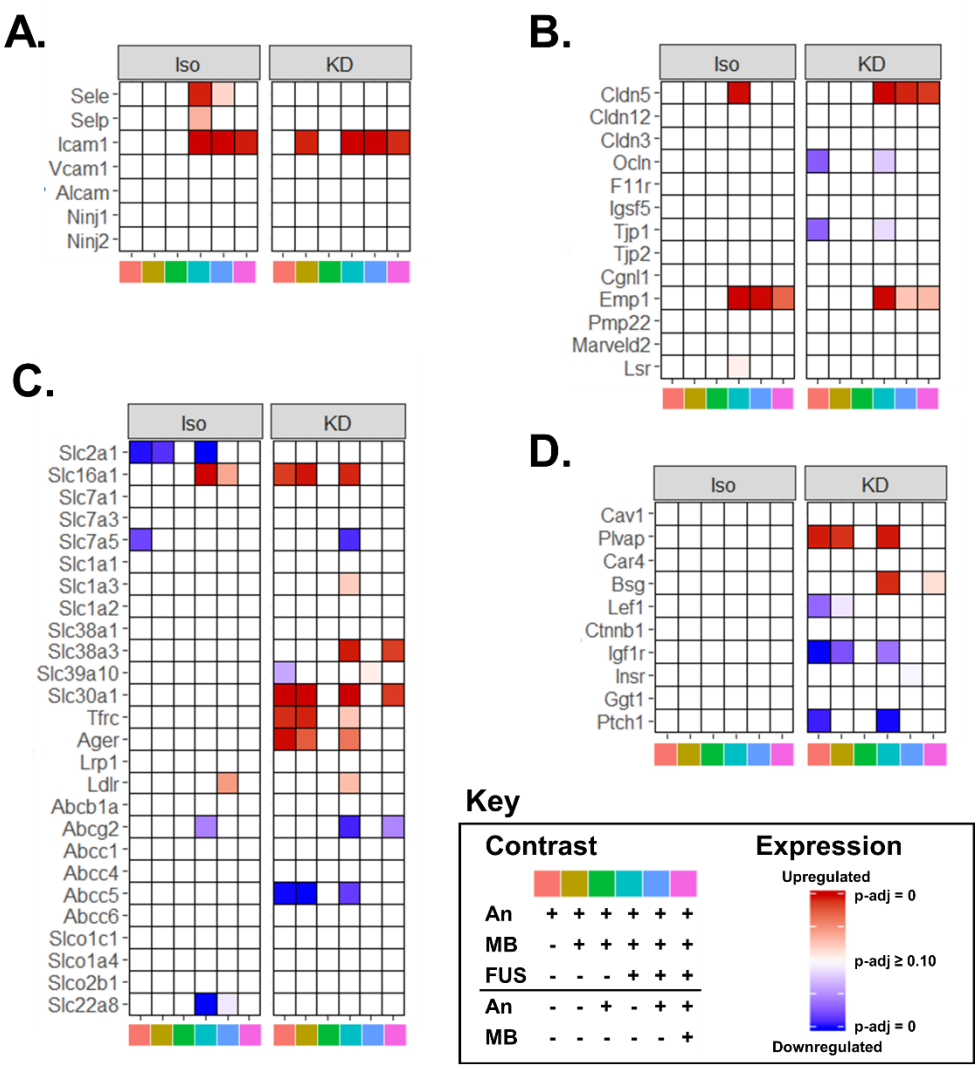

Figure 4.5: Anesthetics Differentially Affect Transcripts Associated with BBB Structure and Function. (A-D) Heatmaps of significance of upregulation (red) or downregulation (blue) for selected genes (rows) across multiple contrasts (columns), separated by anesthetic for transcripts associated with BBB structure and function. Selected categories include (A) leukocyte adhesion, (B) BBB tight junctions, (C) transporters, and (D) transcytosis/miscellaneous. Contrast identities are shown by the color at the bottom of the column, corresponding to the key. Full opacity corresponds to an adjusted-p-value of 0, while full transparency corresponds to an adjusted p-value ≥ 0.10. Each color in the key corresponds to a specific pairwise comparison of Anesthesia (An), An + MB, and An + MB + FUS for either Iso or KD, specifying the numerator (above the black line), and denominator (below the black line). For example, pink corresponds to the ratio of gene expression for mice treated with An + MB + FUS to those treated with just An + MB.

Figure 4.6

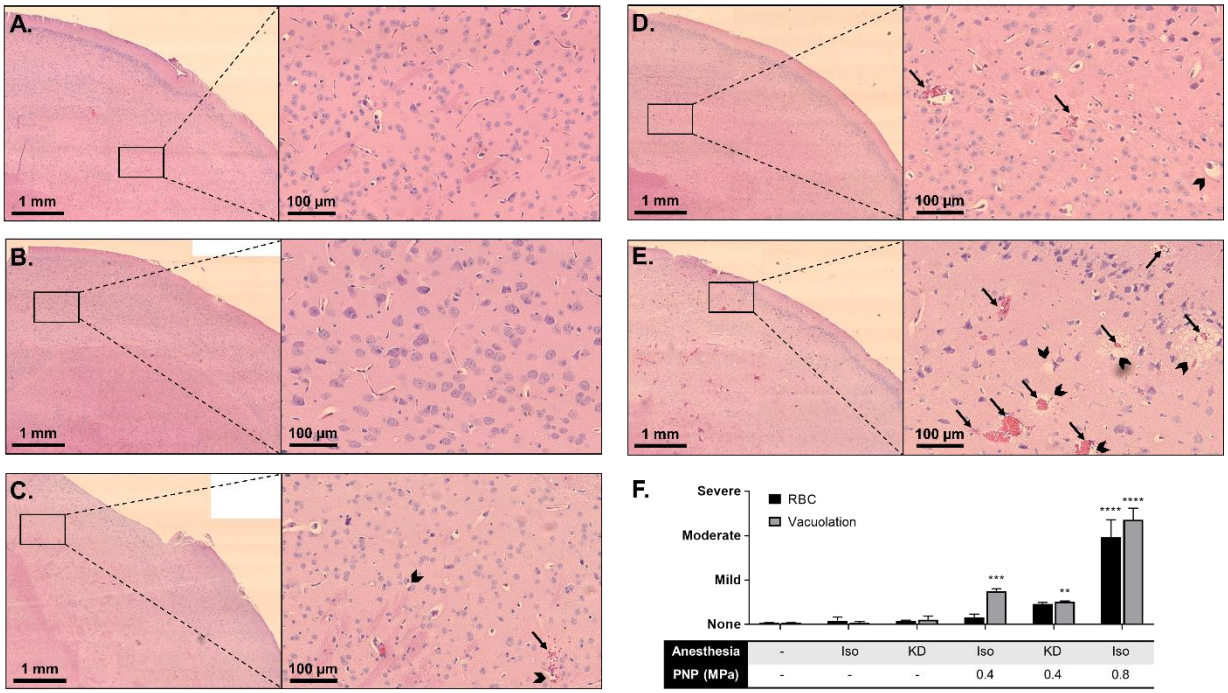

Figure 4.6: Tissue Damage Elicited by FUS BBBD is Minimal and Not Affected by Anesthetic. Representative 4x stitched (left) and 20x (right) H&E images of murine right striatum either (A) untreated or treated with (B) IsoMA-FUS at 0.4 MPa, (C) KD-FUS at 0.4 MPa, or (D) IsoMA-FUS at 0.8 MPa. Arrows indicate RBC extravasation, chevrons indicate vacuolation. (E) Scoring of RBC extravasation (black bars) and vacuolation (grey bars). Data are represented as mean ± SEM. **p < 0.01, **p 0 < 0.001, ****p < 0.00001 by one-way ANOVA followed by comparison against naïve with Dunnett's multiple comparison test. n = 2-3 per group.

Figure 4.S1

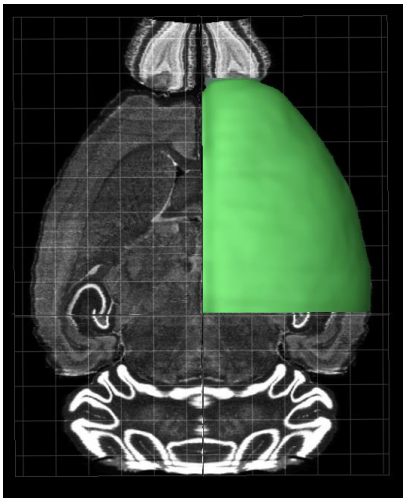

Figure 4.S1: Region of brain harvested for RNA-seq. Top-down view of a 3-D rendering of a representative region of brain (green) harvested for RNA-sequencing, overlaid with an axial mouse MRI. Harvested regions weighed approximately 100 mg. The right quadrant was harvested for all sequenced mice, with the exception of one Iso-FUS mouse, which was treated on the left side.

Figure 4.S2

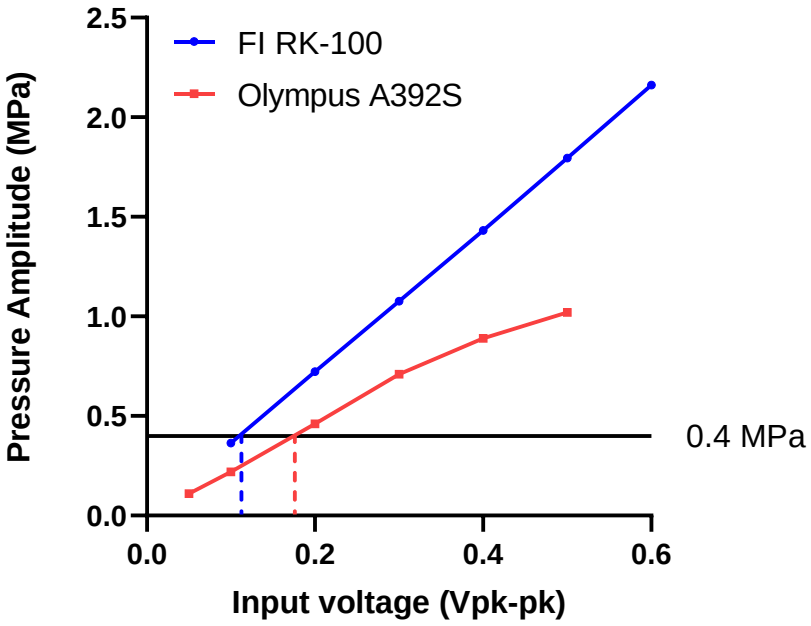

Figure 4.S2: Voltage-Pressure calibrations for FUS transducers. Voltage-Pressure calibrations for the two FUS systems used in this study. An MRIgFUS system (FUS Instruments RK-100, blue) was used for RNA-seq studies, while a tabletop system (Olympus A392S, red) was used for histological evaluation. Input voltages were determined for each system according to the calibration curve to achieve a matching output Peak-negative pressure (PNP) of 0.4 MPa (vertical dashed lines).

Table 4.S1.

	Reference	Disease model	Therapeutic	Anesthesia details
ISOFLURANE	1	Glioma	Polymeric nanoparticles	Isoflurane
	2	Naive	N/A	2-3% Isoflurane
	3	Naive	Dextrans	1.5% Isoflurane
	4	Naive	Dextrans	2-3% Isoflurane
	5	Alzheimer's disease	N/A	1-2% Isoflurane
	6	Naive	Nanoparticles	2-2.5% Isoflurane
	7	Huntington's disease	GDNF plasmid	2% Isoflurane
	8	Naive	N/A	2% Isoflurane (vol/vol) in MA
	9	Glioma	Carboplatin	2-3% Isoflurane in air
	10	Naive	Polymeric nanoparticles	Induction: 2% Isoflurane in 20% O2/78% MA, Maintenance: 2% Isoflurane in MA
	11	Naive	Gad-based nanoparticles	1.5-2% Isoflurane "in a mixture of air and oxygen"
	12	Naive	Alpha-synuclein gene	Induction: 3% Isoflurane in O2, Maintenance: 2% Isoflurane in MA
	13	Naive	NA	Induction: 5% Isoflurane (1 L/min) in O2, Maintenance: 1-2% Isoflurane (1 L/min) in MA
	14	Naive	rAAV	2% Isoflurane (vol/vol) in 50% O2/50% MA
	15	Naive	NA	1–3.5% Isoflurane (vol/vol) in O2
	16	GBM	Doxirubicin	Isoflurane in O2
	17	Naive	IP BRDU after FUS, nothing coinjected	1-3.5% Isoflurane (vol/vol) in O2
	18	Naive	Gold nanoclusters	1-2% Isoflurane (vol/vol) in O2
	19	Naive	N/A	2% Isoflurane (vol/vol) in O2
	20	Naive	N/A	Induction: 3% Isoflurane in O2, Maintenance: 2% Isoflurane in O2
	21	Naive	Polymeric nanoparticles	1.5-2% Isoflurane in O2
	22	Naive	N/A	2-3% Isoflurane in O2
	23	Naive	N/A	1.25% Isoflurane + 0.8 ppm O2
	24	GBM	IL-12	2% Isoflurane (0.8 L/min) in O2
	25	GBM	Gene and folate conjugated MB	1% Isoflurane (1 L/min) in O2
	26	Parkinson's disease	Intranasal BDNF	1-2% Isoflurane in O2
	27	Naive	N/A	Induction: 2% Isoflurane in O2, Maintenance: 0.5% Isoflurane in O2
	28	Naive	N/A	1-3.5% Isoflurane in O2
KETAMINE + α_2 AGONIST	29	Parkinson's disease	GDNF transgene	Ketamine (40 mg/kg) + Dexmedetomidine (0.2 mg/kg)
	30	Naive	Polymeric nanoparticles	Ketamine (40 mg/kg) + Dexmedetomidine (0.2 mg/kg)
	31	Glioma	Polymeric nanoparticles	Ketamine (40 mg/kg) + Dexmedetomidine (0.2 mg/kg)
	32	Naive	Polymeric nanoparticles	Ketamine (40 mg/kg) + Dexmedetomidine (0.2 mg/kg)
	33	Naive	Reporter gene nanoparticles	Ketamine (40 mg/kg) and Dexmedetomidine (0.2 mg/kg)
	34	Naive	Herceptin (trastuzumab)	Ketamine (70 mg/kg) + Xylazine(10 mg/kg)
	35	Alzheimer's disease	Endogenous IgG	Ketamine (150 mg/kg) + Xylazine (10 mg/kg)
	36	Naive	AAV for GFP	Ketamine (90 mg/kg) + Xylazine (4 mg/kg)
	37	Naive	Evans Blue	Ketamine (75 mg/kg) + Xylazine (4 mg/kg)
	38	Naive	N/A	Claims Ketamine (90 mg/kg) and Xylazine (10 mg/kg)
	39	Metastatic BrCa	Therapeutic antibodies	Ketamine (80 mg/kg) + Xylazine (10 mg/kg)
	40	Glioma	Liposomal Doxorubicin	Ketamine (80 ml/kg/h) + Xylazine (10 ml/kg/h)
	41	Metastatic BrCa	Trastuzumab	Ketamine (90 mg/kg) + Xylazine (10 mg/kg)
	42	Naive	N/A	Ketamine (40–50 mg/kg) + Xylazine (10 mg/kg)
	43	Alzheimer's disease	N/A	Ketamine (75 mg/kg) + Xylazine (4 mg/kg)
	44	Naive	Dually labeled liposomes	Ketamine (80 mg/kg/hr) + Xylazine (10 mg/kg/hr)
	45	Naive	N/A	Ketamine (80 mg/kg) + Xylazine (10 mg/kg)
	46	Alzeheimer's disease	Anti-tau antibody	Ketamine (100 mg/kg) + Xylazine (10 mg/kg)
MISCELLANEOUS	47	Naive	N/A	Induction: 3% Isoflurane (vol/vol) in MA, Maintenance: Dexmedetomidine (0.1 mg/kg)
	48	Naive	N/A	For sedate animals: Ketamine (10 mg/kg) + Atropine (0.02-0.04 mg/kg) to induce, 1-2% Isoflurane/O2 to maintain. For awake animals: Ketamine (5 mg/kg)
	49	Naive	N/A	Induction: Ketamine (50 mg/kg/h) + Xylazine (5 mg/kg/h), Maintenance: 1-3% Isoflurane (2 L/min) in MA
	50	Naive	N/A	Zoletil (25 mg/kg) and Rompun (4.6 mg/kg)
	51	Naive	N/A	Induction: Tiletamine (6 mg/kg) + Xylazine (2.2 mg/kg), Maintenance: Propofol (10 mg/kg/hr)
	52	Naive	GABA	Induction: Ketamine (3 mg/kg) + Dexmedetomidine (0.015 mg/kg), Maintenance: 1% Isoflurane in O2
	53	Naive	Doxorubicin	Zoletil (25 mg/kg) and Rompun (4.6 mg/kg) in saline
	54	Naive	N/A	Telazol (tiletamine and zolazepam): 2-4 mg/kg
	55	Metastatic melanoma	Polymeric nanoparticles	2:1:2:5 mixture of Fentanyl, Medetomidine, Midazolam, and water, (10 ul/g), subcutaneous injection
	56	GBM	Doxorubicin	gas anesthesia
	57	GBM	BCNU	Chlorohydrate (30 mg/kg)
	58	Naive	N/A	Chlorohydrate (30 mg/kg)
	59	GBM	TMZ	Chlorohydrate (30 mg/kg)

4.12 Chapter 4 Supplement References

1. R. J. Diaz, *et al.*, Focused ultrasound delivery of Raman nanoparticles across the blood-brain barrier: Potential for targeting experimental brain tumors. *Nanomedicine Nanotechnology, Biol. Med.* **10**, e1075–e1087 (2014).
2. B. Cheng, C. Bing, R. Chopra, The effect of transcranial focused ultrasound target location on the acoustic feedback control performance during blood-brain barrier opening with nanobubbles. *Sci. Rep.* **9**, 1–10 (2019).
3. M. A. Valdez, E. Fernandez, T. Matsunaga, R. P. Erickson, T. P. Trouard, Distribution and Diffusion of Macromolecule Delivery to the Brain via Focused Ultrasound using Magnetic Resonance and Multispectral Fluorescence Imaging. *Ultrasound Med. Biol.* **46**, 122–136 (2020).
4. D. Omata, *et al.*, Effects of encapsulated gas on stability of lipid-based microbubbles and ultrasound-triggered drug delivery. *J. Control. Release* **311**–**312**, 65–73 (2019).
5. M. E. Karakatsani, *et al.*, Unilateral focused ultrasound-induced blood-brain barrier opening reduces phosphorylated Tau from the rTg4510 mouse model. *Theranostics* **9**, 5396–5411 (2019).
6. J. Le Floc'h, *et al.*, Transcranial Photoacoustic Detection of Blood-Brain Barrier Disruption Following Focused Ultrasound-Mediated Nanoparticle Delivery. *Mol. Imaging Biol.* **22**, 324–334 (2019).
7. C. Y. Lin, *et al.*, Focused ultrasound-induced blood brain-barrier opening enhanced vascular permeability for GDNF delivery in Huntington's disease mouse model. *Brain Stimul.* **12**, 1143–1150 (2019).
8. S. J. Mooney, J. N. Nobrega, A. J. Levitt, K. Hynynen, Antidepressant effects of focused ultrasound induced blood-brain-barrier opening. *Behav. Brain Res.* **342**, 57–61 (2018).
9. N. McDannold, *et al.*, Acoustic feedback enables safe and reliable carboplatin delivery across the blood-brain barrier with a clinical focused ultrasound system and improves survival in a rat glioma model. *Theranostics* **9**, 6284–6299 (2019).
10. A. K. O. Åslund, *et al.*, Nanoparticle delivery to the brain - By focused ultrasound and self-assembled nanoparticle-stabilized microbubbles. *J. Control. Release* **220**, 287–294 (2015).
11. A. Conti, *et al.*, Empirical and Theoretical Characterization of the Diffusion Process of Different Gadolinium-Based Nanoparticles within the Brain Tissue after Ultrasound-Induced Permeabilization of the Blood-Brain Barrier. *Contrast Media & Mol. Imaging* **2019**, 6341545 (2019).
12. C. J. Lin, *et al.*, Microbubble-facilitated ultrasound pulsation promotes direct α-synuclein gene delivery. *Biochem. Biophys. Res. Commun.* **517**, 77–83 (2019).
13. D. McMahon, K. Hynynen, Acute inflammatory response following increased blood-brain barrier permeability induced by focused ultrasound is dependent on microbubble dose. *Theranostics* **7**, 3989–4000 (2017).
14. Z. Noroozian, *et al.*, "MRI-guided focused ultrasound for targeted delivery of rAAV to the brain" in *Methods in Molecular Biology*, (Humana Press Inc., 2019), pp. 177–197.
15. Z. I. Kovacs, *et al.*, Disrupting the blood–brain barrier by focused ultrasound induces sterile inflammation. *Proc. Natl. Acad. Sci.* **114**, E75–E84 (2017).
16. F. Y. Yang, *et al.*, Focused ultrasound and interleukin-4 receptor-targeted liposomal doxorubicin for enhanced targeted drug delivery and antitumor effect in glioblastoma multiforme. *J. Control. Release* **160**, 652–658 (2012).
17. Z. I. Kovacs, *et al.*, MRI and histological evaluation of pulsed focused ultrasound and microbubbles treatment effects in the brain. *Theranostics* **8**, 4837–4855 (2018).
18. D. Sultan, *et al.*, Focused Ultrasound Enabled Trans-Blood Brain Barrier Delivery of Gold Nanoclusters: Effect of Surface Charges and Quantification Using Positron Emission Tomography. *Small* **14**, 1703115 (2018).

19. G. Samiotaki, *et al.*, Pharmacokinetic analysis and drug delivery efficiency of the focused ultrasound-induced blood-brain barrier opening in non-human primates. *Magn. Reson. Imaging* **37**, 273–281 (2017).
20. P. C. Chu, *et al.*, Focused Ultrasound-Induced Blood-Brain Barrier Opening: Association with Mechanical Index and Cavitation Index Analyzed by Dynamic Contrast-Enhanced Magnetic-Resonance Imaging. *Sci. Rep.* **6**, 1–13 (2016).
21. D. S. Hersh, *et al.*, MR-guided transcranial focused ultrasound safely enhances interstitial dispersion of large polymeric nanoparticles in the living brain. *PLoS One* **13** (2018).
22. C. Bing, *et al.*, Characterization of different bubble formulations for blood-brain barrier opening using a focused ultrasound system with acoustic feedback control. *Sci. Rep.* **8**, 1–12 (2018).
23. O. O. Olumolade, S. Wang, G. Samiotaki, E. E. Konofagou, Longitudinal Motor and Behavioral Assessment of Blood–Brain Barrier Opening with Transcranial Focused Ultrasound. *Ultrasound Med. Biol.* **42**, 2270–2282 (2016).
24. P. Y. Chen, *et al.*, Focused ultrasound-induced blood-brain barrier opening to enhance interleukin-12 delivery for brain tumor immunotherapy: A preclinical feasibility study. *J. Transl. Med.* **13**, 93 (2015).
25. C. H. Fan, *et al.*, Folate-conjugated gene-carrying microbubbles with focused ultrasound for concurrent blood-brain barrier opening and local gene delivery. *Biomaterials* **106**, 46–57 (2016).
26. R. Ji, *et al.*, Focused ultrasound enhanced intranasal delivery of brain derived neurotrophic factor produces neurorestorative effects in a Parkinson's disease mouse model. *Sci. Rep.* **9** (2019).
27. Z. Cui, *et al.*, Enhanced neuronal activity in mouse motor cortex with microbubbles' oscillations by transcranial focused ultrasound stimulation. *Ultrason. Sonochem.* **59**, 104745 (2019).
28. S. Sinharay, *et al.*, In vivo imaging of sterile microglial activation in rat brain after disrupting the blood-brain barrier with pulsed focused ultrasound: [18F]DPA-714 PET study. *J. Neuroinflammation* **16**, 155 (2019).
29. B. P. Mead, *et al.*, Novel Focused Ultrasound Gene Therapy Approach Noninvasively Restores Dopaminergic Neuron Function in a Rat Parkinson's Disease Model. *Nano Lett.* **17**, 3533–3542 (2017).
30. E. Nance, *et al.*, Non-invasive delivery of stealth, brain-penetrating nanoparticles across the blood - Brain barrier using MRI-guided focused ultrasound. *J. Control. Release* **189**, 123–132 (2014).
31. K. F. Timbie, *et al.*, MR image-guided delivery of cisplatin-loaded brain-penetrating nanoparticles to invasive glioma with focused ultrasound. *J. Control. Release* **263**, 120–131 (2017).
32. B. P. Mead, *et al.*, Targeted gene transfer to the brain via the delivery of brain-penetrating DNA nanoparticles with focused ultrasound. *J. Control. Release* **223**, 109–117 (2016).
33. B. P. Mead, *et al.*, Focused Ultrasound Preconditioning for Augmented Nanoparticle Penetration and Efficacy in the Central Nervous System. *Small* **15**, 1903460 (2019).
34. M. Kinoshita, N. McDannold, F. A. Jolesz, K. Hynynen, Noninvasive localized delivery of Herceptin to the mouse brain by MRI-guided focused ultrasound-induced blood-brain barrier disruption. *Proc. Natl. Acad. Sci. U. S. A.* **103**, 11719–11723 (2006).
35. J. F. Jordão, *et al.*, Amyloid-β plaque reduction, endogenous antibody delivery and glial activation by brain-targeted, transcranial focused ultrasound. *Exp. Neurol.* **248**, 16–29 (2013).
36. M. Stavarache, N. Petersen, … E. J.-J. of, undefined 2018, Safe and stable noninvasive focal gene delivery to the mammalian brain following focused ultrasound. *thejns.org* (March 25, 2020).

37. J. Shin, *et al.*, Focused ultrasound-mediated noninvasive blood-brain barrier modulation: preclinical examination of efficacy and safety in various sonication parameters. *Neurosurg. Focus* **44**, E15 (2018).
38. N. McDannold, Y. Zhang, N. Vykhodtseva, Nonthermal ablation in the rat brain using focused ultrasound and an ultrasound contrast agent: long-term effects. *J. Neurosurg.* **125**, 1539–1548 (2016).
39. T. Kobus, I. K. Zervantonakis, Y. Zhang, N. J. McDannold, Growth inhibition in a brain metastasis model by antibody delivery using focused ultrasound-mediated blood-brain barrier disruption. *J. Control. Release* **238**, 281–288 (2016).
40. M. Aryal, N. Vykhodtseva, Y. Z. Zhang, J. Park, N. McDannold, Multiple treatments with liposomal doxorubicin and ultrasound-induced disruption of blood-tumor and blood-brain barriers improve outcomes in a rat glioma model. *J. Control. Release* **169**, 103–111 (2013).
41. E. J. Park, Y. Z. Zhang, N. Vykhodtseva, N. McDannold, Ultrasound-mediated blood-brain/blood-tumor barrier disruption improves outcomes with trastuzumab in a breast cancer brain metastasis model. *J. Control. Release* **163**, 277–284 (2012).
42. M. A. O'Reilly, K. Hynynen, Blood-brain barrier: Real-time feedback-controlled focused ultrasound disruption by using an acoustic emissions-based controller. *Radiology* **263**, 96–106 (2012).
43. J. Shin, *et al.*, Focused ultrasound-induced blood-brain barrier opening improves adult hippocampal neurogenesis and cognitive function in a cholinergic degeneration dementia rat model. *Alzheimer's Res. Ther.* **11**, 110 (2019).
44. M. Aryal, *et al.*, MRI Monitoring and Quantification of Ultrasound-Mediated Delivery of Liposomes Dually Labeled with Gadolinium and Fluorophore through the Blood-Brain Barrier. *Ultrasound Med. Biol.* **45**, 1733–1742 (2019).
45. N. Todd, Y. Zhang, M. Livingstone, D. Borsook, N. McDannold, The neurovascular response is attenuated by focused ultrasound-mediated disruption of the blood-brain barrier. *Neuroimage* **201**, 116010 (2019).
46. P. W. Janowicz, G. Leinenga, J. Götz, R. M. Nisbet, Ultrasound-mediated blood-brain barrier opening enhances delivery of therapeutically relevant formats of a tau-specific antibody. *Sci. Rep.* **9**, 1–9 (2019).
47. P. C. Chu, *et al.*, Neuromodulation accompanying focused ultrasound-induced blood-brain barrier opening. *Sci. Rep.* **5**, 1–12 (2015).
48. S. Y. Wu, *et al.*, Efficient blood-brain barrier opening in primates with neuronavigation-guided ultrasound and real-time acoustic mapping. *Sci. Rep.* **8**, 1–11 (2018).
49. R. M. Jones, *et al.*, Three-dimensional transcranial microbubble imaging for guiding volumetric ultrasound-mediated blood-brain barrier opening. *Theranostics* **8**, 2909–2926 (2018).
50. H. Choi, E.-H. Lee, M. Han, S.-H. An, J. Park, Diminished Expression of P-glycoprotein Using Focused Ultrasound Is Associated With JNK-Dependent Signaling Pathway in Cerebral Blood Vessels. *Front. Neurosci.* **13**, 1350 (2019).
51. F. Prada, *et al.*, In vitro and in vivo characterization of a cranial window prosthesis for diagnostic and therapeutic cerebral ultrasound. *J. Neurosurg. JNS*, 1–13 (2020).
52. C. Constans, *et al.*, Non-invasive ultrasonic modulation of visual evoked response by GABA delivery through the blood brain barrier. *J. Control. Release* **318**, 223–231 (2020).
53. B. Jung, H. Huh, E. hee Lee, M. Han, J. Park, An advanced focused ultrasound protocol improves the blood-brain barrier permeability and doxorubicin delivery into the rat brain. *J. Control. Release* **315**, 55–64 (2019).
54. K. Yoon, *et al.*, Localized Blood–Brain Barrier Opening in Ovine Model Using Image-Guided Transcranial Focused Ultrasound. *Ultrasound Med. Biol.* **45**, 2391–2404 (2019).
55. H. Baghirov, *et al.*, Ultrasound-mediated delivery and distribution of polymeric nanoparticles in the normal brain parenchyma of a metastatic brain tumour model. *PLoS*

One **13**, e0191102 (2018).
56. Z. Kovacs, *et al.*, Prolonged survival upon ultrasound-enhanced doxorubicin delivery in two syngenic glioblastoma mouse models. *J. Control. Release* **187**, 74–82 (2014).
57. H. L. Liu, *et al.*, Blood-brain barrier disruption with focused ultrasound enhances delivery of chemotherapeutic drugs for glioblastoma treatment. *Radiology* **255**, 415–425 (2010).
58. J. Xia, P. H. Tsui, H. L. Liu, Low-pressure burst-mode focused ultrasound wave reconstruction and mapping for blood-brain barrier opening: A preclinical examination. *Sci. Rep.* **6**, 1–11 (2016).
59. K. C. Wei, *et al.*, Focused Ultrasound-Induced Blood-Brain Barrier Opening to Enhance Temozolomide Delivery for Glioblastoma Treatment: A Preclinical Study. *PLoS One* **8** (2013).

Chapter 5: Single-Cell Mapping of Focused Ultrasound-Transfected Brain

Alexander S. Mathew, Catherine M. Gorick, and Richard J. Price

*This chapter is adapted from:

Mathew, A. S., C. M. Gorick, and R. J. Price. "Single-cell mapping of focused ultrasound-transfected brain." *Gene Therapy* (2021): 1-9.

5.1 Abstract

Gene delivery via focused ultrasound (FUS) mediated blood-brain barrier (BBB) opening is a disruptive therapeutic modality. Unlocking its full potential will require an understanding of how FUS parameters [e.g. peak-negative pressure (PNP)] affect transfected cell populations. Following plasmid (mRuby) delivery across the BBB with 1 MHz FUS, we used single cell RNA-sequencing to ascertain that distributions of transfected cell types were highly dependent on PNP. Cells of the BBB (i.e. endothelial cells, pericytes, and astrocytes) were enriched at 0.2 MPa PNP, while transfection of cells distal to the BBB (i.e. neurons, oligodendrocytes, and microglia) was augmented at 0.4 MPa PNP. PNP-dependent differential gene expression was observed for multiple cell types. Cell stress genes were upregulated proportional to PNP, independent of cell type. Our results underscore how FUS may be tuned to bias transfection toward specific brain cell types in-vivo and predict how those cells will respond to transfection.

5.2 Introduction

Despite increasing knowledge of the underlying mechanisms of many neurological diseases, safe and effective treatments are often lacking. Anatomical, physiological, and cellular obstacles make therapeutic intervention in the central nervous system (CNS) extremely challenging. High vascularity and limited regenerative capacity of the CNS, along with the thickness and nonuniformity of the skull, significantly enhance the risk profile of any surgical approach. The blood-brain barrier (BBB), an arrangement of endothelial cells, tight junctions, basement membrane, astrocytic endfeet, and transport proteins common to most CNS vasculature, limits the vast majority of systemically injected therapies from accessing the brain (102). Furthermore, current therapies for major neurological pathologies such as Alzheimer's Disease, Parkinson's Disease, and multiple sclerosis (MS), are transiently effective and/or only palliative. Thus, there exists a pressing need for the development of non-invasive, spatially-targeted, and durable treatment approaches across the spectrum of neurological disorders.

Focused ultrasound (FUS) mediated BBB disruption (BBBD) holds significant promise toward overcoming the aforementioned obstacles (103, 105, 118). In this modality, gas-filled microbubbles (MB) and therapeutic agents are injected intravenously. Under image guidance, an extracorporeal transducer then directs conforming acoustic waves toward a pathologic region of the brain. These waves pass harmlessly through the skull and converge on the targeted region, causing the circulating MB to oscillate. These oscillations impart mechanical forces on cerebrovascular endothelium, temporarily disrupting BBB integrity and allowing therapeutics into the brain parenchyma. FUS mediated BBBD is targeted, non-invasive, and repeatable and has facilitated successful delivery of chemotherapies (109–111), antibodies (106–108), and even neural stem cells (112, 113).

Importantly, FUS BBBD also enables the delivery of systemically circulating gene therapies to the CNS (114, 115, 324–327). Indeed, non-invasive gene delivery to the brain by FUS under precise image-guidance offers the prospect of curative therapies. However, translational hurdles still remain. First, knowledge of which brain-resident cell populations are most likely to be transfected after FUS-mediated BBBD and how transfection specificity depends on FUS parameters (e.g. PNP) are still unknown. Second, because the biophysical mechanisms through which gene delivery to the brain is achieved with FUS are complex, it is difficult to predict how FUS parameters like PNP will affect which cells are transfected and to what extent. Indeed, different brain cell types may exhibit markedly discrepant responses to FUS application and subsequent transfection. Recently, we used immunofluorescence analyses and single cell RNA sequencing (scRNA seq) to determine that the specificity of transfection of endothelial cells of the

BBB is inversely proportional to peak-negative pressure (PNP), a phenomenon we term “sonoselective” transfection (150). Herein, we extend these previous scRNAseq studies considerably to investigate how the distribution of transfected brain-resident cell populations and their transcriptomes are affected by FUS PNP.

5.3 Results

5.3.1 Focused Ultrasound BBBD and Brain Cell Transfection

Our experimental pipeline is shown in **Figure 5.1**. Briefly, we intravenously injected cationic MBs and mRuby plasmid followed by MRI-guided FUS (1.1 MHz) targeted to the right striatum at either 0 MPa, 0.2 MPa, or 0.4 MPa PNP (estimated to be effectively 0 MPa, 0.164 MPa, and 0.328 MPa after skull attenuation). As expected, both MRI contrast enhancement in the targeted region and harmonic acoustic emissions were significantly greater at 0.4 MPa compared to 0.2 MPa (**Figure 5.S1**). After allowing 48 hours for sufficient expression of mRuby by transfected cells, mouse brains were harvested and dissociated into single cell suspensions. We then isolated live mRuby-expressing cells by fluorescence activated cell sorting (FACS) and performed scRNA-seq. 12.4% of dissociated cells treated at 0.4 MPa were $mRuby^+$, compared to 2.3% treated at 0.2 MPa (**Figure 5.1**). However, it is important to emphasize that we harvested the entire quadrant of the brain to ensure maximum cellular yield. Thus, these percentages are not representative of overall transfection efficiency. Given the weight of the harvested brains, the average density of the murine brain, and the volume of the -6 dB focal region for our transducer (i.e. 10.7 mm^3), we estimate the true transfection efficiencies to be 28.5% and 5.4% at 0.4 MPa and 0.2 MPa, respectively. To establish the baseline proportions of brain-resident cell types and account for biases introduced in our dissociation protocol, cells from the 0 MPa treatment group were sequenced without mRuby FACS.

5.3.2 Focused Ultrasound-Transfected Cell-Type Distributions Depend on Peak-Negative Pressure

To assign cell identities to our dataset, we performed graph-based clustering followed by comparison of globally distinguishing genes within each cluster against scRNA-seq databases. After filtering ambiguous clusters and pooling those of the same class, we identified 6 distinct cell types, namely astrocytes, endothelial cells, microglia, neurons, oligodendrocytes, and pericytes (**Figure 5.2A**). The proportions of these mRuby+ cell types were dependent on PNP (**Figure 5.2B**). Specifically, 0.2 MPa FUS transfection led to marked enrichment of cells comprising and in contact with the BBB (i.e. endothelial cells, pericytes, and astrocytes) compared to control, while 0.4 MPa FUS led to a transfection distribution in between that of 0.2 MPa transfection and 0 MPa controls (**Figure 5.2C**). Thus, cells of the BBB (i.e. endothelial cells, pericytes, and astrocytes) are relatively enriched at lower FUS PNP while those farther from the BBB (neurons, oligodendrocytes, and microglia) are more efficiently transfected at higher FUS PNP.

5.3.3 Transcriptional Responses of Individual Focused Ultrasound-Transfected Cells

To assess cell-type specific transcriptional responses to FUS-mediated BBBD and transfection, we performed differential expression testing, comparing 0.2 MPa and 0.4 MPa transfected cells to matching populations from the 0 MPa control group across multiple cell types (**Figure 5.3A-D**). Transfected microglia exhibited massive differential gene expression (1630 significantly regulated transcripts) when compared to 0 MPa control cells, with 0.4 MPa PNP FUS exerting a much stronger effect than 0.2 MPa PNP FUS (Figure 3A and 3E). While neurons exhibited the same PNP-dependent response, far fewer differentially regulated transcripts were identified overall (Figure 3B and 3E). In contrast, neither oligodendrocytes (Figure 3C and 3E) nor astrocytes (Figure 3D and 3E) differentially expressed more transcripts at the higher PNP (i.e. 0.4 MPa). Overall, our results indicate that the absolute numbers and identities of significantly differentially expressed genes depended on cell type and FUS PNP (**Figure 5.3E**, **Supplemental Table 5.1**). Finally, despite the robust cell type-specific responses shown in Figure 3, we questioned whether there might exist sets of genes that are affected by FUS regardless of the cell type. Interestingly, a careful curation of our data set revealed that several genes associated with cellular stress and inflammation, including *CTSD, CTSB, LY86, CD68, LYZ2,* and *TYROBP,* are indeed significantly upregulated in multiple cell types as a function of increasing PNP (**Figure 5.4**). A complementary analysis revealed *CKB, DNAJA1, HBB-BS, HSPA8, JUN, JUND, and RPS27* were downregulated across multiple cell types with increasing PNP (**Figure 5.S2**).

5.4 Discussion

Conventional approaches for gene delivery to the CNS can be limited by their invasiveness, poor localization, systemic toxicity, or inefficient transit across the BBB. FUS activation of systemically administered MB surmounts all of these, as it is noninvasive, targeted, safe, and transiently disrupts the BBB (328). While we and others have established the potential of this technology for gene therapy (114, 115, 324–327), considerable knowledge gaps still exist. Indeed, we reason that acquiring a more comprehensive understanding of (i) how FUS parameters affect which cell types are transfected and (ii) how these cells respond to transfection at the transcriptional level will permit fine tuning of FUS-mediated transfection approaches for selected applications. Toward this end, we used scRNA-seq to quantify proportions of brain-resident cell types transfected by FUS, their transcriptional responses 48 h post treatment, and the relationship of these metrics to PNP. Both 0.2 MPa and 0.4 MPa FUS application elicited successful transfection of endothelial cells, astrocytes, pericytes, neurons, oligodendrocytes, and microglia. While 0.2 MPa PNP preferentially transfected BBB-associated cells (i.e. endothelial cells, astrocytes, and pericytes), 0.4 MPa PNP shifted transfected cell-type distributions to include more microglia, neurons, and oligodendrocytes. These data, in conjunction with prior histological studies demonstrating that 0.1 MPa PNP is highly selective for endothelial cell transfection (150), are consistent with the hypothesis that the probability of a cell being transfected by FUS is directly proportional to PNP and inversely proportional to distance from the microcirculation. Moreover, at least in the context of focused ultrasound transfection, our results suggest that any cell-type differences in transfection potential that may exist appear to be overridden by physical factors. While the extent and nature of significant differential gene expression were cell- and PNP-dependent, we identified several cellular stress-associated genes that were consistently upregulated independent of cell type and proportional to PNP. Together, these results provide high-resolution insight into the cellular implications of FUS mediated transfection that will ultimately refine preclinical design and accelerate clinical translation.

Our experimental and computational pipeline enabled unbiased identification of 6 brain-resident cell types in the neurovascular unit (NVU). We noted a bias toward transfection of cells closer to the microcirculation, such as endothelial cells, astrocytes, and pericytes, especially at lower FUS PNP. Neurons, oligodendrocytes, and microglia were enriched with higher PNP, presumably because of enhanced plasmid availability beyond the BBB. Microglial activation in the context of PNP-dependent sterile inflammation may also lead to chemotaxis to the BBB, thereby increasing microglial propensity for transfection. Overall, our results are in agreement with previous work from our group, wherein gene-bearing nanoparticles were delivered instead of

plasmid (329). In that study, we observed higher transfection of astrocytes compared to neurons by immunofluorescence. Our model is also consistent with work in which FUS mediated delivery of recombinant adeno-associated virus (rAAV) elicited transduction of significantly more astrocytes than neurons (330). However we note disagreement with another rAAV study, which transduced primarily neurons (114). This discrepancy could be attributed to differences in cellular uptake, expression stability for FUS-enhanced delivery of bacterial vs viral vectors, or FUS experimental parameters. Other studies of FUS-mediated viral gene delivery that demonstrate highly selective neuronal transgene expression utilize neuron-specific promoters (325). Indeed, the overall approach and results presented here may be especially useful for choosing FUS parameters that best synergize with gene therapy approaches that utilize cell-specific promoters by biasing plasmid delivery to the cell type(s) of interest. Furthermore, independent of the specific gene delivery vehicle that is chosen for focused ultrasound transfection, our study provides a framework for how scRNA seq can be used to inform and optimize the transfection of selected cell types in the brain.

Several genes associated with cellular stress and inflammation were upregulated across multiple cell types in proportion to PNP. While many studies have demonstrated that FUS-mediated BBBD results in minimal damage at the tissue level (104, 117, 118), impacts at the cellular and molecular levels are actively under investigation. Transcriptomic and proteomic profiling by multiple groups have found that, under certain FUS and MB conditions, FUS mediated BBBD may elicit a sterile inflammatory response in the brain parenchyma (150–152, 331). The precise mechanistic relationship between FUS-mediated BBBD and sterile inflammation remains unclear. Possible causes include direct acoustic damage to BBB, NVU injury caused by cavitation-induced shockwaves, ischemia reperfusion injury caused by transient vasospasm, and exposure of the brain parenchyma to blood products. Sonoporation, one of the mechanisms by which FUS is proposed to enhance gene delivery, has been shown to generate large irreversible pores, increase reactive oxygen species, reduce endoplasmic reticulum mass, increase apoptosis, and delay the cell cycle (332–334). It is probable that multiple interactions contribute to sterile inflammatory response induced by FUS. Given that we harvested tissue 48 h post-FUS to allow time for sufficient transgene expression, the differential gene expression profile we report is consistent with a landscape of resolving inflammation. We noted pressure dependent upregulation of *CTSD*, *CTSB, LY86*, *LYZ2, CD68,* and *TYROBP* across multiple cell types. Cathepsin D, the protein product of *CTSD*, is a protease expressed in the lysosome involved in antigen processing, apoptosis, and biomolecule degradation (335, 336). Studies of its role in Alzheimer's disease suggest it is upregulated during neuronal repair (337). Cathepsin B, another

lysosomal protease, is activated in response to diverse inflammatory stimuli in multiple brain cell types and contributes to programmed cell death (338, 339). The function of LY86 is not well understood, though it is thought to play a role in regulating inflammation and toll-like receptor (TLR) signaling (340, 341). CD68 is a lysosomal protein that is upregulated in actively phagocytosing microglia (342). While its expression was clearly the highest in microglia, we observed PNP dependent upregulation in all cell types. Non-myeloid expression of CD68 has been reported before as evidence of increased lysosomal activity (343). Further evidence of microglial activation is supported by the PNP-dependent upregulation of *LYZ2* (Lysozome 2), a powerful antimicrobial hydrolase. Increases in *LYZ2* across multiple cell types were also observed in a scRNA-study of Niemann-Pick disease, a neurodegenerative pathology characterized by inappropriate activation of innate immunity (344). Similarly, TYRO protein tyrosine kinase-binding protein (TYROBP, the protein product of *TYROBP*) is also primarily expressed in microglia. TYROBP has complex functions in microglia, having roles in increasing phagocytic activity and decreasing cytokine production (345). Non-myeloid expression of TYROBP has also been linked to neuroinflammation (346). Interestingly, many of the genes highlighted by our analysis exactly match those found in a gene cluster specific to resolution of neuroinflammation (347). Notably, we did not detect significant upregulation of classical markers of brain sterile inflammation such *AIF1* in microglia, *GFAP* in astrocytes, and *ICAM1* in endothelial cells. Thus, our differential expression analysis is consistent with a resolving PNP-dependent inflammatory response 48 h post-FUS.

There are some limitations of this investigation. The requirement for dissociation of treated tissue to viable single cell suspensions and myelin removal prior to scRNA-seq likely limited the yield of large complex cells such as neurons or oligodendrocytes. We corrected for this methodological limitation by making comparisons to sequences from non-transfected cells that were subject to the same isolation methods, including FACS. Nonetheless, while this approach does allow us to make relative comparisons, we are not able to accurately report the absolute extent of transfection on a per-cell-type basis without making significant assumptions. Further, the process of mechanical and enzymatic dissociation itself may have imparted transcriptional effects on the sequenced cells. Finally, due to the high processing complexity and cost of scRNA-seq, replicates were not sequenced separately. Instead, we pooled multiple biological replicates from each condition prior to FACS and scRNA-seq library preparation and subsequently ran all samples in the same sequencing run. This approach is common (348, 349) and has been shown to mitigate batch effects and improve statistical power (350, 351).

To summarize, we used single cell RNA-sequencing to study the effects of 0.2 MPa and 0.4 MPa FUS-mediated transfection on the brain. At 48 h post-treatment, we observed lower overall transfection at 0.2 MPa compared to 0.4 MPa, but higher selectivity for cells comprising the BBB, namely endothelial cells, astrocytes, and pericytes. Differential gene expression analysis highlighted PNP dependent, cell-type independent upregulation of genes associated with cellular stress. This work has significant implications for the design of future investigations leveraging FUS-mediated transfection. For applications where higher cell-type specificity and/or lower cellular stress are required, lower PNPs should be used. Inversely, for applications where higher general transfection is desired, and when a sterile inflammatory response is tolerable (or even desirable), higher PNPs may be recommended. Other FUS experimental parameters (such as frequency, pulsing interval, duty cycle, burst length, and MB dose) are also likely to affect transfection selectivity and efficiency and could be tested in future investigations.

5.5 Materials and Methods

The work presented herein is an extended analysis of a dataset generated in previous studies by our group (150), the details of which are provided below.

5.5.1 Single Cell RNA Sequencing and Analysis

After FACS, 0 MPa (unsorted), 0.2 MPa ($mRuby^+$), and 0.4 MPa ($mRuby^+$) single cell libraries were generated using the Chromium Controller (10X Genomics, Pleasanton, CA) with the Chromium Single Cell 3' GEM, Library & Gel Bead Kit v3 (10X Genomics) and Chromium Single Cell B Chip Kit (10X Genomics). An average of 1482 cells per condition were sequenced on a NextSeq 500 (Illumina) at an average depth of 92,409 reads per cell. The CellRanger v3.0.2 pipeline was implemented to first convert bcl2 reads to FASTQ files followed by alignment to the mm10 (Ensembl 84) mouse reference genome and filtering. All further single cell analysis was performed in R using Seurat v3.1.5(352) with default parameters unless otherwise specified. Cells with low read depth, low expression diversity, or high mitochondrial content were filtered out of the analysis. Cell clusters were computed by graph-based clustering and subsequently identified by comparing the top 20 globally distinguishing markers (i.e. those with p adjusted < 1E-240, average natural log fold change above all other cell types > 0.25, and expressed in at least 25% of that cell type) with those having high cell-type specificity scores in the PanglaoDB webserver(353). Clusters of the same cell type were merged. Cells of unclear significance in the context of FUS mediated transfection including, ependymal cells, choroid plexus cells, and peripheral leukocytes were removed from the analysis. Differential gene expression between endothelial subsets was performed using the MAST framework(354). PNP-dependent, cell-type independent genes were defined as those differentially regulated in at least 5/6 cell types at 0.4 MPa vs control with a p-value < 0.15.

5.6 Acknowledgements

We thank the UVa Genome Analysis and Technology Core for their assistance with sample processing.

5.7 Funding

Supported by National Institutes of Health Grants R01EB020147, R01NS111102, R01CA197111, and R21EB024323 to R.J.P. A.S.M. was supported by National Institutes of Health Training Grant T32LM012416 and Fellowship F30CA247254. C.M.G. was supported by American Heart Association Fellowship 18PRE34030022.

5.8 Conflict of Interest

The authors declare no conflict of interest.

5.9 Author Contributions

Conceptualization - A.S.M., C.M.G., and R.J.P.; Methodology - A.S.M., C.M.G., and R.J.P.; Investigation - A.S.M., C.M.G., and R.J.P.; Formal Analysis - A.S.M., C.M.G., and R.J.P.; Writing – Original Draft Preparation, A.S.M. and R.J.P.; Writing – Review & Editing, A.S.M., C.M.G., and R.J.P.; Supervision, R.J.P.; Funding Acquisition - A.S.M. and R.J.P.

5.10 Data Availability

scRNA-seq data have been deposited in the Gene Expression Omnibus database (https://www.ncbi.nlm.nih.gov/geo/query/acc.cgi?acc=GSE%20141922).

5.11 Figures

Figure 5.1

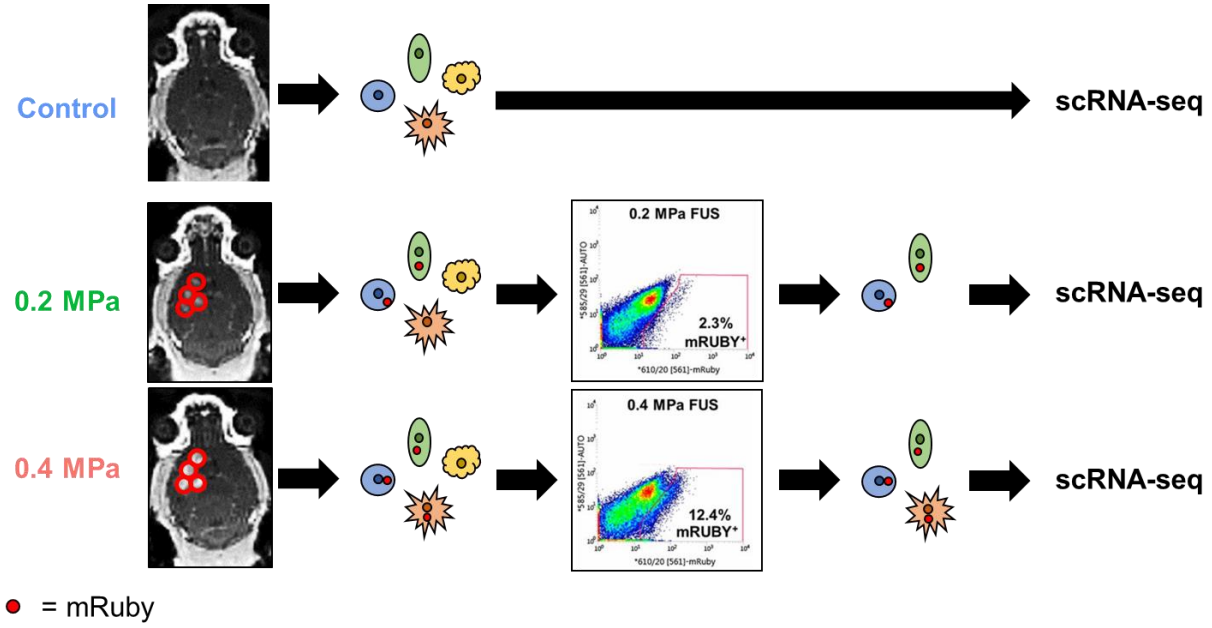

Figure 5.1: Overview of experimental methods. MR guided FUS was applied at either 0.2 MPa or 0.4 MPa to mouse striata following IV injection of mRuby plasmid conjugated to cationic MB. Brains were excised and dissociated, producing single cell suspensions containing both untransfected and transfected cells. Using cells from the control condition to define the mRuby gating strategy, mRuby+ cells were sorted from FUS-treated brains by FACS. Single cell RNA-sequencing was performed on untransfected, untreated cells from the control condition, mRuby+ cells from the 0.2 MPa condition, and mRuby+ cells from the 0.4 MPa condition.

Figure 5.2

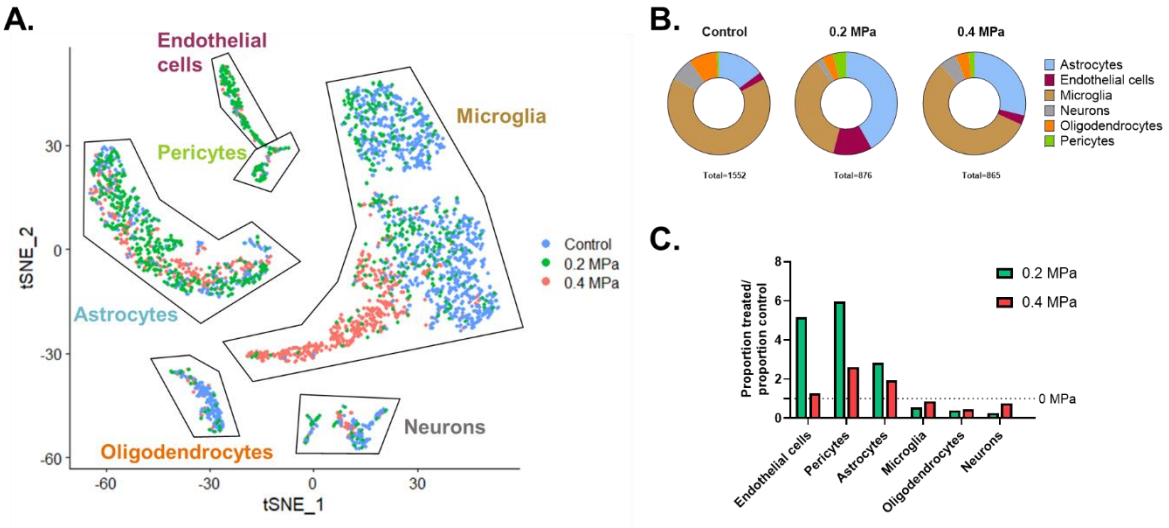

Figure 5.2: Identification of FUS-transfected cell types as a function of PNP. A) t-SNE plot showing all sequenced cells, colored according to their treatment condition. Labels on graph indicate cell populations identified by graph-based clustering followed by analysis of globally distinguishing transcripts within each cluster. B) Proportions of each of the 6 identified cell types for each condition. Total numbers of cells analyzed are shown below each chart. C) Bar graph illustrating the influence of FUS PNP on the distribution of transfected cells.

Figure 5.3

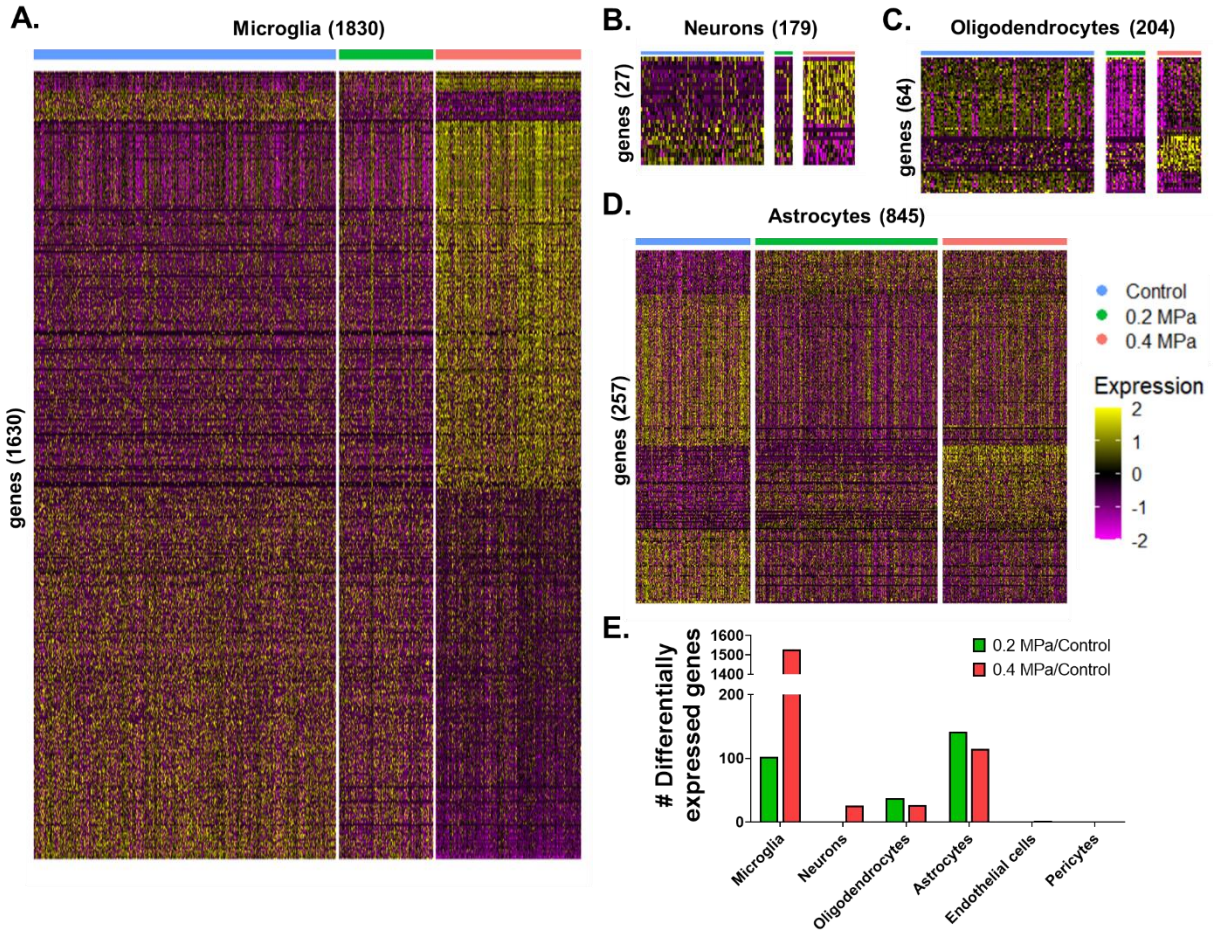

Figure 5.3: Transcriptional responses of individual focused ultrasound-transfected cells. A-D) Gene expression heatmaps for (A) microglia, (B) neurons, (C) oligodendrocytes, and (D) astrocytes. Each column represents a single cell and each row represents a gene of interest. Selected genes for each cell type are significantly (p-adjusted < 0.05) upregulated or downregulated at 0.2 MPa or 0.4 MPa compared to control. Expression levels are presented as row-normalized z-scores according to the key. Numbers in parenthesis indicate total number of cells (columns) or genes (rows) presented. E) Magnitude of significant (p adjusted < 0.05) differential gene expression (upregulated + downregulated) for each cell type at each pressure vs control cells.

Figure 5.4

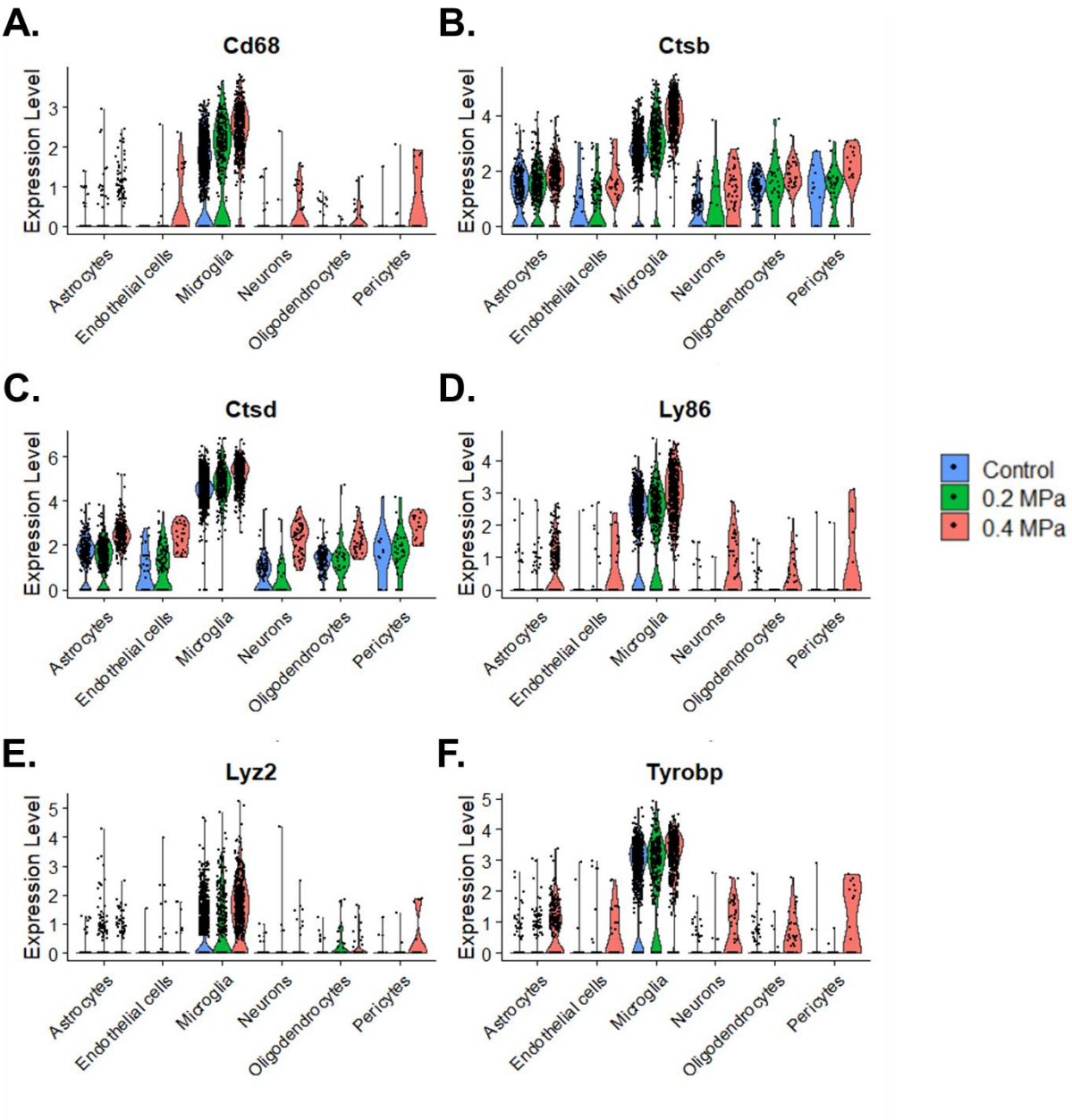

Figure 5.4: Genes associated with cell stress are upregulated across multiple cell types as a function of FUS PNP. A-F) Violin plots of normalized expression levels for selected transcripts. Each dot represents a single cell, grouped by cell type and treatment condition.

Figure 5.S1

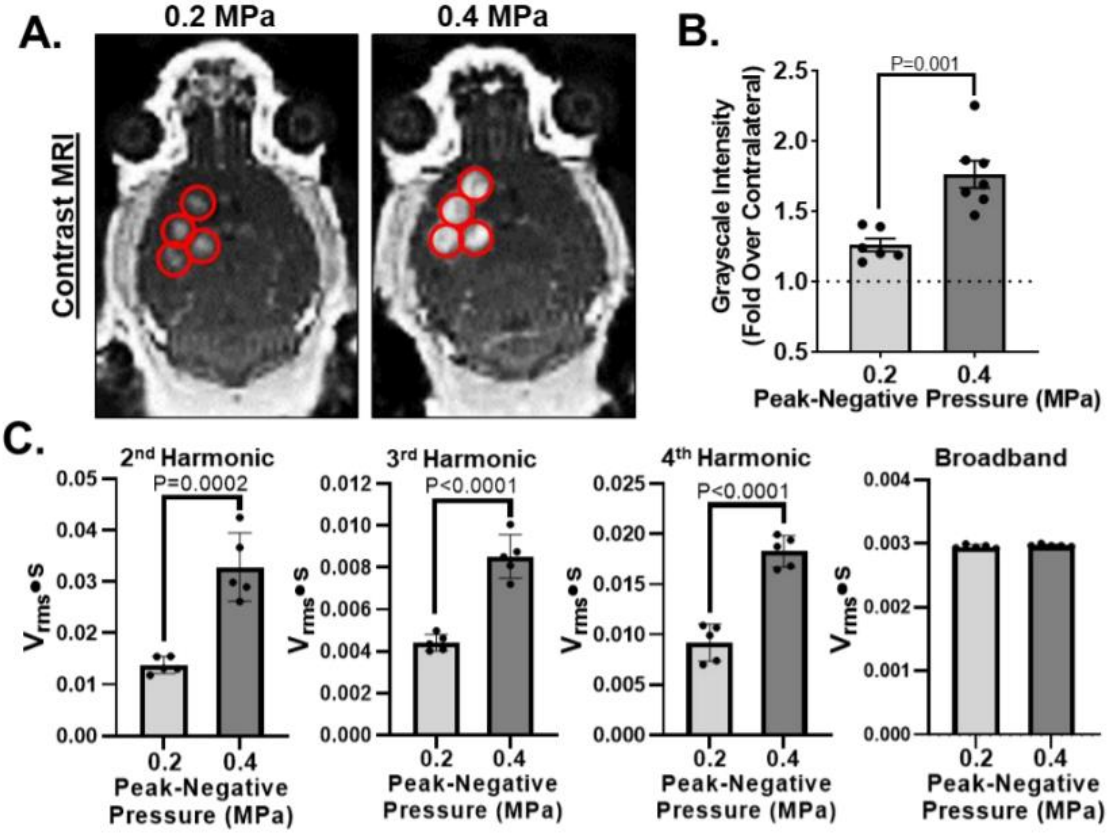

Figure 5.S1: Characterization of blood-brain barrier opening with focused ultrasound. A) Contrast MR images of mouse brains after application of pulsed FUS in the presence of systemically administered MBs. FUS was applied at peak-negative pressures of 0.2 and 0.4 MPa, with a 4-spot sonication pattern. Sonication sights are denoted with red circles. **B)** Bar graph of contrast enhancement over contralateral FUS^- control hemisphere as a function of pressure. **C**) Passive cavitation analyses for 2^{nd}, 3^{rd}, and 4^{th} harmonics, as well as broadband emissions. All statistical comparisons by unpaired t-tests. Adapted with permission from Gorick et al. (*Proc Nat Acad Sci.* 117(11):5644-5654).

Figure 5.S2

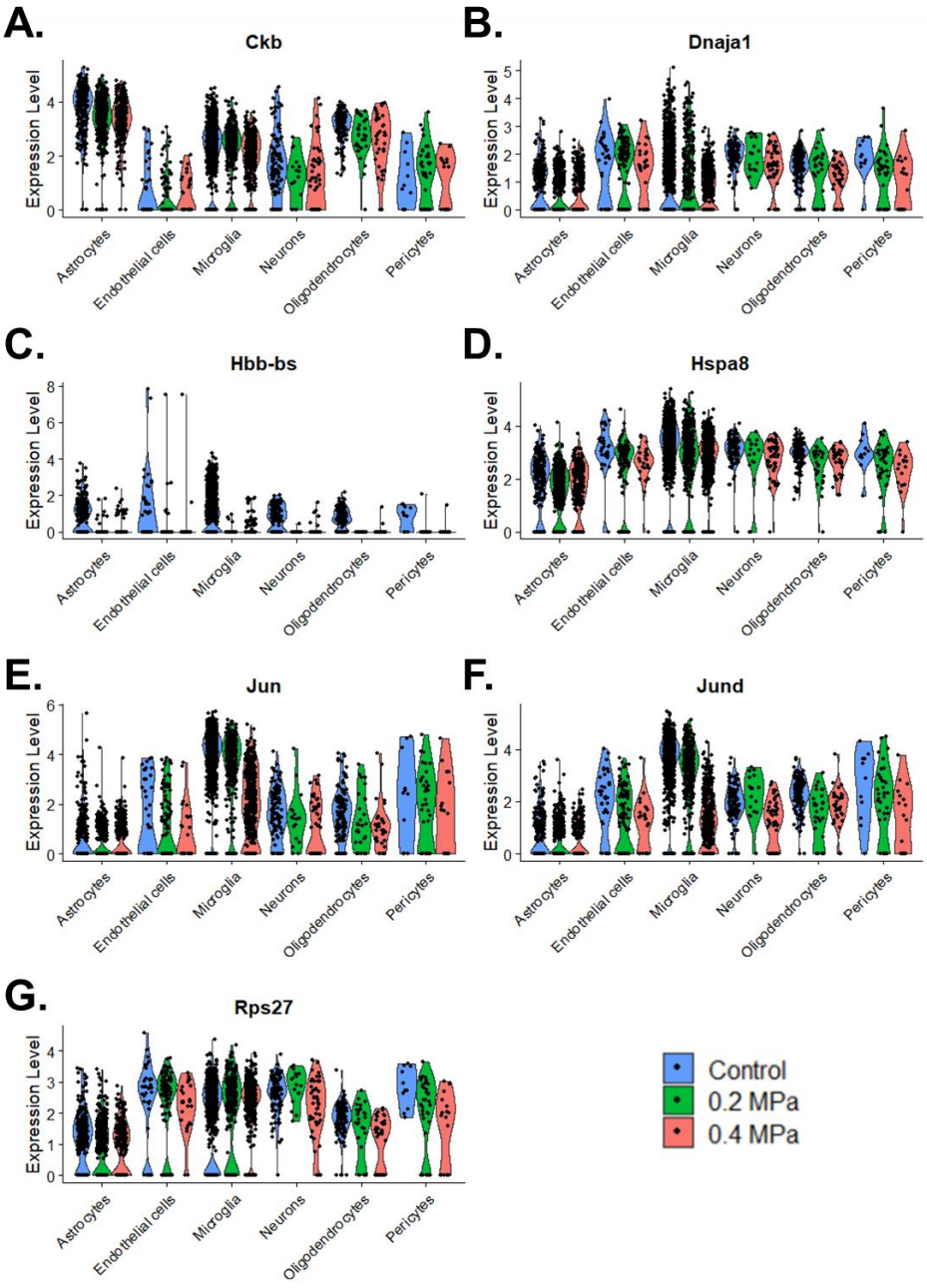

Figure 5.S2: Genes downregulated across multiple cell types as a function of FUS PNP. A-G) Violin plots of normalized expression levels for selected transcripts. Each dot represents a single cell, grouped by cell type and treatment condition.

Figure 5.S3

A.

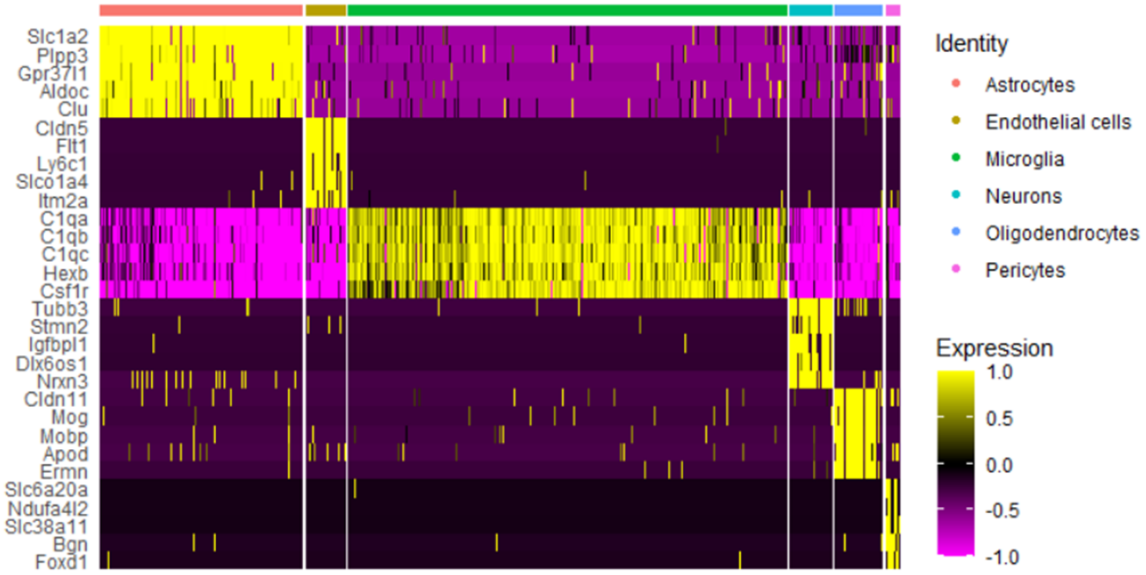

B.

Rank	Astrocytes	Endothelial cells	Microglia	Neurons	Oligodendrocytes	Pericytes
1	Slc1a2	Cldn5	C1qa	Tubb3	Cldn11	Slc6a20a
2	Plpp3	Flt1	C1qb	Stmn2	Mog	Ndufa4l2
3	Gpr37l1	Ly6c1	C1qc	Igfbpl1	Mobp	Slc38a11
4	Aldoc	Slco1a4	Hexb	Dlx6os1	Apod	Bgn
5	Clu	Itm2a	Csf1r	Nrxn3	Ermn	Foxd1
6	Atp1a2	Pltp	Ctss	Dcx	Enpp2	Mir143hg
7	Gja1	Ly6a	Ctsd	Dpysl3	Tspan2	Tbx18
8	Bcan	Spock2	Atf3	Stmn3	Stmn4	Ogn
9	Slc4a4	Cxcl12	Selplg	Dlx1	Opalin	Vtn
10	Mt3	Ptprb	Cx3cr1	Celf4	Ppp1r14a	Enpep
11	Htra1	Egfl7	Tmem119	Cd24a	Tubb4a	Pcolce
12	Cspg5	Abcb1a	Fcrls	Gad2	Ugt8a	Col3a1
13	Ttyh1	Igfbp7	Lgmn	6330403K07Rik	Pllp	Gpc3
14	Nrxn1	9430020K01Rik	Trem2	Bcl11a	Grb14	S1pr3
15	Sparcl1	Pglyrp1	P2ry12	Nsg1	Aspa	Ace2
16	Fjx1	Adgrf5	Tyrobp	Gad1	Sez6l2	Kcnj8
17	Ptprz1	Fn1	Junb	Sp9	Tmem151a	Higd1b
18	Slc6a11	Pcp4l1	Fcer1g	Bex2	Tmeff2	Twist1
19	Ndrg2	Adgrl4	Mafb	Dlx2	Edil3	Abcc9
20	Ntsr2	Sema3c	Laptm5	Nsg2	Efnb3	Aspn

Figure 5.S3: Globally distinguishing transcripts used to assign cell-types to clusters. A) Gene expression heatmap showing the top 5 globally distinguishing genes from each cluster. Each row represents a single gene and each column represents a single cell, with each element of the heatmap representing a row-normalized expression value. Cluster membership is represented by the bars above the heatmap. B) The top 20 globally distinguishing transcripts from each cell cluster, which were compared against the PanglaoDB webserver4 to assign cell type. Globally distinguishing transcripts were defined as very significantly (p adjusted < 1E-240) upregulated (average natural log fold change above all other cell types > 0.25) and expressed in at least 25% of that cell type.

Chapter 6: Multiple Regression Analysis of a Massive Transcriptomic Data Assembly Elucidates Novel Mechanically- and Biochemically-Driven Gene Sets in Response to Focused Ultrasound Blood-Brain Barrier Disruption

Alexander S. Mathew, Catherine M. Gorick, and Richard J. Price

6.1 Abstract

Focused ultrasound (FUS) mediated blood brain barrier disruption (BBBD) is a promising therapeutic strategy for the noninvasive, targeted, and repeatable delivery of drugs to the brain. FUS induces oscillations of circulating microbubbles (MBs), which effect intravascular mechanical forces that enhance BBB permeability. The relationship between the extent of BBB permeabilization and gene expression in the brain is incomplete. Further, the relative transcriptional impacts of the mechanical forces imparted by activated MBs vs the accumulation of blood plasma products in the brain parenchyma are currently unknown. Here, we aggregate 77 murine transcriptomes in a multiple regression framework to identify genes expressed in proportion to metrics of BBBD at multiple time points after treatment. Models were constructed to control for potential confounders, such as sex, anesthesia, and sequencing batch. We found microbubble activation (MBA) or contrast enhancement (CE) at the time of FUS treatment differentially predict expression patterns of 1,124 genes 6 h or 24 h later. While there existed considerable overlap in the transcripts correlated with MBA vs CE, MBA was principally predictive of genes associated with endothelial reactivity while CE chiefly predicted sterile inflammation gene sets. Additionally, over-representation analysis revealed that the magnitude of CE and MBA forecasted expression of transcripts involved in actin filament organization, blood coagulation, and vasculature development and wound repair. This study empowers MBA and CE for use not only as treatment readouts, but as independent predictors of transcriptional reactions in the CNS following FUS BBBD.

6.2 Introduction

The selection of therapeutic agents capable of accessing the central nervous system (CNS) via the vasculature is severely limited by the blood brain barrier (BBB) (102). Microbubble activation (MBA) with focused ultrasound (FUS) causes temporary BBB disruption (BBBD), and thus represents a promising method for significantly expanding the neuropharmacological arsenal (103–105). In this regimen, biologically inert MB are first administered systemically. Focused acoustic waves generated outside the skull are then applied to a region of interest, usually under MRI-guidance, causing the circulating MB to spherically oscillate. Theses oscillations impart mechanical forces on the BBB, transiently increasing its permeability. FUS-mediated BBBD is an attractive modality compared to surgery or global chemical BBBD methods, as it is non-invasive, targeted, and easily repeatable. This approach has enabled successful delivery of many large therapeutics to the CNS normally barred by the BBB, such as antibodies (106–108), genes (115, 116, 355), and neural stem cells (112, 113).

Unique to CNS microvasculature, the BBB represents the aggregate of continuous capillaries, basement membrane, tight junctions, pericytes, astrocytic endfeet, and transporters that collectively mediate homeostasis in the brain. Physiologic functions of the BBB include creating an optimal ionic microenvironment for neuronal signaling, permitting transport of nutrients for brain-resident cells, and preventing parenchymal exposure to bloodbourne pathogens and toxins. Dysregulation and/or deterioration of the BBB are consequences or even directly pathogenic for nearly all neurological diseases, including traumatic brain injury (356, 357), stroke (358, 359), multiple sclerosis (360, 361), Alzheimer's disease (362, 363), glioma (364), and bacterial meningitis (365, 366). Therefore, care must be taken when even transiently perturbing BBB integrity to facilitate drug transport, such as with FUS BBBD.

The benefits of temporally disrupting the BBB to deliver new therapies for chronic CNS pathologies are considered to significantly outweigh the risks. The safety of FUS-mediated BBBD has been asserted in several studies (104, 117, 118), and continues to be tested in clinical trials (NCT02986932, NCT03739905, NCT03119961, NCT03671889, NCT04118764). There now exists a growing interest in understanding the cellular and subcellular consequences of mechanical perturbation of the BBB. In addition to expanding the safety profile, understanding downstream effects of enhanced local BBB permeability may shed light on its potential to directly incite protective and therapeutic molecular mechanisms. Transcriptomic and proteomic profiling studies have demonstrated that FUS BBBD can elicit local sterile inflammation (SI) even in the absence of histological damage (331). While SI can be produce neuronal damage in some contexts, it may also be the trigger for increased amyloid β plaque clearance (367) and

neurogenesis c reported after FUS BBBD. Previously, we showed FUS BBBD enhances inflammatory gene signatures, antigen availability, and dendritic cell maturation in a model of metastatic melanoma (137).

Elucidating the precise relationship between barrier disruption and local signaling mechanisms is challenging, as FUS BBBD exists on a spectrum, varying widely with respect to experimental parameters, including peak-negative-pressure (PNP), pulsing scheme, and MB administration. Recent investigations have shown that SI is dependent on MB dose (151) and can be attenuated by administration of dexamethasone (282). In a recent study of FUS enhanced gene therapy, we observed expression of SI genes was significantly higher at PNPs capable of reliably disrupting the BBB as measured via gadolinium contrast enhancement (CE), compared to brains treated at lower PNPs with minimal or absent CE (150). In a separate investigation, where PNP was kept constant and anesthesia was varied, we noted stronger signatures of SI in groups of mice with more pronounced CE at the time of treatment (368).

Thus far, our understanding of the secondary effects of BBBD is built upon discrete snapshots from various studies with distinct parameter sets. Investigations have primarily focused on characterization of SI, with less attention paid to other, non-inflammatory consequences of FUS on the BBB. Further, relative contributions of the mechanical forces imparted by activated MBs vs the accumulation of plasma in the brain parenchyma are currently unknown. Toward establishment of quantitative relationships between the extent of FUS BBBD and CNS reactivity, we performed transcriptome-wide multiple regression analyses on 77 murine samples, controlling for variation due to sex and anesthesia. We identify genes whose expression levels at 6 h and 24 h covary with the magnitude of MBA or CE at the time of treatment, establishing generalizable FUS-responsive transcriptional programs. These data further demonstrate the distinct utility of MBA and CE to predict novel mechanisms mechanically- and biochemically-driven by BBBD.

6.3 Results

6.3.1 Data Processing Pipeline

Across multiple blood-brain barrier opening and gene delivery experiments from our lab (150, 368), paired MBA and CE data had been previously acquired from mice (**Table 6.S1**). Analyzing these data via a simple linear regression of MBA against CE revealed significant variability and a moderate correlation, with $R^2 = 0.59$ (**Figure 6.1A**). Some FUS-treated samples with high MBA had low CE, and vice versa (**Figure 6.1B**). Thus, we reasoned there could be sufficient divergence between MBA and CE to permit the identification of transcripts and gene sets uniquely correlated to either MBA or CE.

To this end, we established a multiple regression pipeline to test whether contrast enhancement (CE) or microbubble activation (MBA) measured at the time of FUS BBBD could predict gene expression 6 or 24 h after treatment (**Figure 6.2A**). Pooling previously published studies (GSE141728, GSE152171), our combined dataset contained 27 transcriptomes from FUS-treated mice with paired CE analyses, 18 of which also permitted analysis of MBA. Additionally, our dataset contained 50 transcriptomes obtained from FUS-negative male and female mice treated with distinct combinations of anesthesia and microbubbles (MB). Principle components analysis (PCA) of all 77 transcriptomes revealed recent treatment with ketamine + α_2 agonist (KA) followed by sex as the primary drivers of transcriptome-wide variability (**Figure 6.2B**).

Gene expression at 6 or 24 h was modeled as linear or exponential functions of CE or MBA, controlling for anesthesia, sex, and sequencing batch where possible, for a total of 8 models. Presence of MB was not included as a model variable as we have shown it has negligible effects on the murine transcriptome (368). Similarity between each linear and exponential model varied, with as much as 88% overlap in the case of the genes expressed 24 h post-treatment significantly (p adjusted < 0.05) linearly or exponentially correlated with CE, and as little as 45% for 6 h gene expression correlates of MBA (**Figure 6.S1**). We combined significant expression correlates from each pair of models for a total of 4 pools of genes (6 h genes predicted by CE, 6 h genes predicted by MBA, 24 h genes predicted by CE, and 24 h genes predicted by MBA).

6.3.2 CE and MBA Predict Expression of 1,124 Transcripts After FUS BBBD

In total, we identified 1,124 unique transcripts whose expression could be predicted at 6 or 24 h using CE or MBA. Multiple regression utilizing the continuous nature CE or MBA predicted gene expression with more sensitivity than the categorical contrast of FUS-positive vs FUS-negative (**Figure 6.S2**). The 3 most significant genes from each pool were *Tlr2, Tubb6*, and *Nfkb2*

correlated with CE at 6 h, *Nfkb2*, *Icam1,* and *Emp1* correlated with MBA at 6 h, *Ptx3*, *Tgm*, and *Cd44* correlated with CE at 24 h, and *Ptx3*, *Tgm*, and *Fat2* correlated with MBA at 24 h (**Figure 6.3A**). The top 15 positively correlated genes from each pool were similar, with many inflammatory transcripts such as *Icam1*, *Ccl12*, and *Ccl3*, present in at least 2 pools (**Figure 6.3B**). Of the 764 transcripts positively correlated with CE or MBA at 6 or 24 h, 463 were unique to a particular pool and 31 were common to all 4 (**Figure 6.3D**). Anti-correlated genes were less abundant but more distinct, with 302/360 transcripts unique to a particular pool and 0 transcripts common to all 4 (**Figure 6.3C and 6.3E**).

6.3.3 MBA and CE Predict Temporal Activation of Distinct Transcripts and Transcriptional Programs After FUS BBBD

Next, we focused our attention on whether CE or MBA could predict temporal expression of transcripts of interest related to BBB integrity, BBB function, and leukocyte adhesion. Among BBB tight junction transcripts, expression of *Emp1* was found to be correlated with both CE and MBA at both 6 and 24 h post-FUS (**Figure 6.4A**). *Cldn5* was also significantly correlated with both metrics 6 h post-FUS. Interestingly, *Tjp2* expression 24 h after BBBD was anti-correlated with MBA. We then interrogated the expression of leukocyte adhesion molecules (**Figure 6.4B**). *Icam1* expression 6 h post-FUS was positively correlated with both CE and MBA. *Sele* expression was also significantly correlated with CE 6 h post-FUS. CE and MBA predicted divergent effects on expression of BBB transporters (**Figure 6.4C**). At 6 h post-BBBD, CE was positively correlated with expression of *Slc16a1, Slc7a1, Slc38a3, Slc30a1,* and *Ldlr*. Meanwhile, *Abcb1a, Abcg2, Slco1a4, Slco2b1, and Slc22a8* were anti-correlated with CE 6 h post-FUS. Finally, we found expression of *Cav1* 24 h post-FUS was uniquely proportional to CE (**Figure 6.4D**).

To then test whether positively and negatively correlated BBBD gene sets from each pool were associated with broader biological processes, we performed over-representation analysis (ORA) using the Gene Ontology Biological Processes domain. We then examined the identities of the top 5 most significantly enriched pathways and their supporting transcripts for each correlate pool (**Figure 6.5**). All 4 pools were enriched for transcripts associated with leukocyte migration and/or activation. Genes expressed proportional to CE 6 h post-FUS were skewed toward acute sterile inflammatory responses such as toll-like receptor signaling (**Figure 6.5A**). Conversely, genes expressed 24 h post-FUS proportional to CE and MBA were more associated with subacute sterile inflammation, indicated by enriched interferon gamma signaling (**Figure 6.5C and 6.5D**). Interestingly, several of the top biological processes correlated with MBA 6 h

post-FUS were associated with vasculature repair and development rather than inflammation (**Figure 6.5B**).

Examination all significantly enriched pathways (p adjusted < 0.01) revealed consistent CE and MBA dependent enrichment of additional, non-inflammatory transcriptional programs. All 4 pools contained transcripts enriched for actin filament organization (**Figure 6.6**). Though we have previously confirmed that the FUS peak-negative pressure used for BBBD elicit at most mild RBC extravasation, we also observed consistent enrichment for transcripts associated with coagulation as a function of CE and MBA. Several of these transcripts associated with vasculature development and coagulation contributed to a broader functional enrichment of wound healing pathways. Notably, ORA performed on anti-correlated genes did produce any significant (p adjusted < 0.01) GO terms for any of the 4 gene pools.

6.4 Discussion

FUS mediated BBBD is an established approach for the targeted, non-invasive, and repeatable delivery of therapeutics from the bloodstream to the CNS, with several clinical trials now underway (NCT02986932, NCT03739905, NCT03119961, NCT03671889, NCT04118764). Recently, there has also been considerable interest in better understanding and therapeutically leveraging effects that occur secondary to FUS BBBD. These secondary effects include enhanced penetration of therapeutics (i.e. nanoparticles) through tissue (326, 327), activation of neurogenesis (320, 369), amyloid-β (367) and tau clearance (370), sterile inflammation (151, 331) , and suppression of neuronal signaling (371, 372). Insights into these mechanisms may prove useful in anticipating longer term consequences of repeated FUS BBBD. Nonetheless, achieving a comprehensive understanding of these consequences of FUS BBBD has been hampered due to variability across experimental parameters and lack of unbiased profiling approaches. Moreover, while separating the mechanical impact of FUS BBBD (i.e. MB oscillation in capillaries) from the biochemical impact of FUS BBBD (i.e. exposure of brain tissue to plasma constituents) could yield remarkable insight, no existing empirical approaches offer such a delineation. Here, to both extend our understanding of the impact of FUS BBBD on the brain transcriptome and potentially distinguish the relative impacts of mechanical and biochemical stimuli on these responses, we employed a data driven approach that combined CE and MBA measurements with 77 separate transcriptional data sets from mice exposed to FUS BBBD. CE and MBA served as independent predictors of gene expression 6 h and 24 h post-treatment to identify gene sets that covary with the extent of BBBD. By pooling datasets across experimental conditions and including these as model covariates, we extend the generalizability of our results to other experimental conditions and FUS parameters. We identified over 1000 distinct genes that are expressed 6 h or 24 h post FUS in proportion to the magnitude of CE or MBA, several of which were directly associated with BBB structure and function. Expression of a substantial number of genes was unique to a particular time point. Notably, many transcripts were also uniquely dependent on either MBA or CE, suggesting that both the mechanical and biochemical perturbations created by FUS BBBD can significantly and differentially affect transcriptional responses. Furthermore, consistent with the hypothesis that the mechanical component associated with FUS BBBD will preferentially affect the endothelium, gene sets expressed 6 h post-FUS in response to MBA specifically were most strongly associated with endothelial activity and repair. Importantly, common to all models was an enrichment for genes associated with actin filament organization, coagulation, and wound healing suggesting new mechanisms for BBB restoration.

The central concept of our investigation was enabled by the observation that, while CE and MBA are correlated during FUS BBBD, there may also be sufficient variability in their relationship to permit delineation of their relative contributions to FUS BBBD-driven transcriptional changes. Of note, this observation is in close agreement with previous studies. For example, a similar analysis of the linear correlation between contrast enhancement and 2nd harmonic emission returned an R value of 0.77 (R^2 = 0.59) (373), perfectly matching the value obtained here. While CE and MBA are both used to monitor FUS BBBD treatment, they are measuring fundamentally distinct processes. CE represents the accumulation of contrast agent in the brain parenchyma due to increased BBB permeability, and we argue it is a proxy for exposure of brain tissue to the biochemical milieu of plasma. On the other hand, MBA is a measure of the magnitude of MB oscillation in response to FUS, and we argue it is a proxy for mechanical perturbation of BBB endothelium. The fact that roughly 40% of the variance in CE could not be explained by variance in MBA led us to hypothesize that each metric may have unique predictive value for gene expression after FUS application. Indeed many of the transcripts whose expression was predicted by CE were not predicted by MBA, and vice versa. Interestingly, unique predictions were more marked for CE, with MBA predicting expression of fewer genes overall, most of which were also predicted by CE. Thus, based on this evidence, we postulate that biochemical stimuli (i.e. exposure of brain tissue to plasma) predominantly drive transcriptional responses to FUS BBBD.

One major advantage of the approach reported here is that it exhibits several statistical advantages compared to past studies of the transcriptional effects of FUS on the BBB. Integrating data from multiple experiments with variation in PNP, MB type, anesthesia, sex, and time point produced a large data set (77 transcriptomes). This allowed us to improve gene dispersion estimates and explicitly control for confounder variables in multiple regression models. We utilized established bioinformatics tools to construct multiple regressions in a negative binomial framework that appropriately models gene expression as a function of categorical and continuous experimental variables. Finally, our approach of leveraging the continuous nature of CE or MBA returned many fold more transcripts with higher confidence than simply testing the effect of FUS treatment as a categorical variable.

While several FUS parameters have been shown to influence the extent of SI responses after BBBD, we argue that these responses are ultimately attributable to impact these parameters have on barrier disruption, rather than the parameters themselves. In a study concluding SI is dependent on MB dose, the dosing schema leading to the most SI also elicited the strongest CE signatures, whether PNP was feedback-controlled or fixed (151). The authors noted this relationship, identifying significant correlations between 9 stress-related genes and CE using

linear least-squares regression. In a study from our group utilizing cationic microbubbles for gene therapy, we report 0.4 MPa FUS elicits significant upregulations of SI cytokines relative to 0.1 MPa or 0.2 MPa FUS (150). Roughly, PNPs of 0.1, 0.2 and 0.4 MPa FUS lead to increases in CE of 0%, 25%, and 75% respectively. Finally, in a separate study of the effect of anesthesia on BBBD, we observed isoflurane (Iso) predisposes the BBB to more marked CE compared to ketamine + α_2 agonist (KA) when PNP and MB dose were kept constant (368). Indeed while BBBD induced signatures of SI under both anesthetics, the responses were more marked when FUS was applied under Iso. A minor but important corollary of the studies from our group was that neither albumin nor cationic lipid shelled MB had any effect on the transcriptome in the absence of FUS. With these previous investigations in mind and the analyses presented here, we propose that MBA and CE are the unifying determinants of post-FUS gene expression.

Across all 4 models, we identified expression of 1,124 genes predicted by the magnitude of CE or MBA. Many positively correlated genes were associated with SI, such as *Nfkb2*, *Tnf, Tlr2, Ccl12, Cd14, Il1a, Il1b,* and *Ccl12*, consistent with previous studies (151, 331). ORA revealed that SI pathways, such as “Leukocyte Migration”, “Regulation to molecule of bacterial origin”, and “Positive Regulation of Cytokine Production” were the most consistently and strongly enriched among genes positively correlated with CE or MBA. SI is primarily considered to be an innate immune response. Interestingly, signatures of adaptive immunity also appeared to be predicted by CE or MBA, especially at 24 h post-treatment. *Cd44*, a glycoprotein found on the surface of lymphocytes that aids in adhesion to endothelial cells and commonly-used marker for T-cell activation, was one of the strongest correlates of both CE and MBA 24 h after treatment. “Cellular response to interferon-gamma” was one of the most enriched gene sets 24 h post-FUS, implicating multiple guanylate-binding proteins (GBPs), including *Gbp2, Gpb3,* and *Gbp6*. Thus, these analyses 1) demonstrate MBA and CE similarly predict SI, 2) highlight previously unreported families of pro-inflammatory transcripts induced by FUS BBBD, and 3) suggest that induced SI responses exist on a continuum, initiated by even minor perturbations of the BBB.

Interestingly, both CE and MBA predicted differential expression of certain genes directly involved with BBB function. *Emp1*, whose expression was strongly correlated across all 4 models, has been shown to mediate the assembly of the BBB (374). The positive correlations of the adhesion molecules *Icam1* and *Sele* are consistent with an inflamed endothelium, in agreement with previous results (150, 151, 331). A mixture of positive and negative correlations of transporters with BBBD has been reported previously (152), and could reflect mechanisms to reestablish ionic and metabolic homeostasis in the brain parenchyma. Interestingly, we also observed correlations between CE and expression of *Cav1* 24 hours later. Upregulation of

caveolin-1 expression after FUS BBBD has been shown to mediate transcellular transport across the BBB (149, 375), representing an alternative to the paracellular mechanism for how FUS enhances BBB permeability. Our data support both phenomena.

Beyond SI, we identified additional transcriptional programs that may be involved in barrier reactivity and repair after FUS. It is well known that FUS BBBD is transient, enhancing permeability on the order of hours before the BBB reseals. The mechanisms engaged during repair are still unclear, and knowledge of them would likely provide insight into how FUS disrupted the barrier originally. Among the top over-represented gene sets correlated with MBA were “Endothelium development”, “Regulation of vasculature development”, and “Regulation of angiogenesis”. Constituent, non-inflammatory genes contributing to these pathways’ enrichment code for proteins mediating tight junctions (*Cldn5, Cdh5*), VEGF signaling (*Flt1, Dll4, Hey1),* and basement membrane interaction (*Itga5, Adamts1, Lgals3, Vcl).* The fact that these pathways were most strongly associated with MBA specifically suggests that these may be the direct consequences of the mechanical forces MB impart on the vasculature.

A fascinating family of transcripts consistently overrepresented in gene sets correlated with both CE and MBA was “Actin filament organization”. The actin cytoskeleton has been proposed to be a crucial mediator of BBB permeability. Actin provides anchoring support to tight junction proteins critical to the BBB such as JAM-1 (376, 377) and ZO-1 (378–380). Additionally, temporospatial reorganization and dynamic expression alterations of actin have been shown modulate tight junction complexes, suggesting an active role of the cytoskeleton in modulating the structure of the BBB (381–384). Studies of CNS hypoxia, wherein BBB integrity is compromised, demonstrate redistributions of actin (385). Reoxygenation of hypoxic tissue then leads to rapid actin polymerization, thickening, and redistribution as barrier integrity is reestablished (386). Our data suggest a similar phenomenon may occur in response to FUS BBBD.

We also observed consistent increases in gene sets associated with tissue repair in proportion to both CE and MBA, including “Wound healing” and “Blood coagulation”. Notable FUS BBBD correlates supporting these enrichments include growth factors (*Tgfb1, Pdgfa, Hbegf*), matrix remodeling enzymes (*Mmp12, Timp1*), serine protease inhibitors (*Serpine1, Serpinf2, Serping1*), and platelet activity regulators (*Plek, Thbs1, Thbd)*. These processes are congruent with SI and barrier repair and may explain to some of neurogenic processes shown to be stimulated by FUS previously (320, 369).

There are some limitations to this study. We note that we had insufficient data coverage to model the effects of anesthesia and sex for all 8 models. Further, several mice in our data set

did not have corresponding MBA data, which could contribute to the larger number of gene correlates detected in the CE. While our approach of using common metrics like CE and MBA paired with blockage of the confounding effects (like anesthesia, sex, and sequencing batch) is intended to increase the generalizability of our results, we acknowledge that the numeric effect sizes will likely vary among other experimental systems due to variability in MRI, PCD setups, and FUS equipment. Finally, we acknowledge two primary limitations of RNA-seq data – that transcription does not always predict protein synthesis, and that it is impossible to distinguish differential transcription from changes in cell type proportions (198–201).

To our knowledge, this is the most comprehensive delineation of the implications of FUS-mediated contrast accumulation and MB oscillation on the CNS. Together, our results indicate initiation of a complex transcriptional program in response to FUS BBBD that facilitates SI, tissue repair, angiogenesis, coagulation, and actin filament reorganization, among others. Our multiple regression framework highlights that these processes occur on a continuum in proportion to BBBD, emphasizing the importance of careful parameter selection, real-time feedback monitoring during treatment, and investigation into the subclinical effects of FUS BBBD on the brain parenchyma. Further, the modest correlation between MBA and CE and the fact that they each predict expression of unique gene sets highlight that MBA is an imperfect measure of BBBD. Further investigation will be required to determine if FUS BBBD parameters can be tailored such that transcriptional programs are strategically avoided or therapeutically leveraged based the pathological microenvironment.

6.5 Materials and Methods

Murine transcriptomes were acquired and processed as previously described (150, 368). Modifications or additions to previously processed data are described below.

6.5.1 Passive Cavitation Detection

We sought to define a metric of harmonic acoustic emissions that could be applied across multiple previous experiments in our lab. To this end, previously collected acoustic emissions data were re-analyzed using an in-house MATLAB (MathWorks) program. For each FUS-treated mouse, a fast Fourier transform (FFT) was applied to appended waveforms collected from a 2.5 mm wideband unfocused hydrophone mounted in the center of the treatment transducer during each FUS pulse. MBA was then defined as the ratio of the average amplitude of the top 5 peaks in a 200 Hz band surrounding the second harmonic (2.22 MHz) to the average amplitude of the top 5 peaks in 200 Hz band in a broadband region in which our hydrophone is not sensitive.

6.5.2 Data Aggregation and Multiple Regression

Raw RNA-seq data were generated and summarized to transcript-level abundance estimates as previously described (150, 368). All subsequent analyses were performed in R v4.0.0. Transcriptomes from different FUS BBBD studies were aggregated with paired CE and MBA analyses. Samples which were not FUS-treated were assigned CE and MBA values of 1. Eight multiple regression models were then generated using DESeq2 v1.3.1 (204). Each one was a unique permutation of correlation type (linear vs exponential), continuous BBBD metric (MBA vs CE), and time point (6 h vs 24 h). Sex, anesthesia type, and sequencing batch were including as categorical covariates for each model permitting enough samples were available. Significantly correlated genes were defined as those with adjusted p values less than 0.05 when testing for the effect of CE or MBA. Significant genes from pairs of linear and exponential models were merged via union. Over representation analysis (ORA) was performed for positively and negatively correlated genes from each pool using clusterProfiler v3.18.1 (387) with the Gene Ontology: Biological Processes gene sets (205, 206). Gene concept networks were generated using clusterProfiler. For visualization of top functional enrichments, redundant pathways were removed via semantic similarity analysis. 4-group intersections were visualized with UpSetR v.1.4.0 (323).

6.6 Acknowledgements

We thank the UVa Genome Analysis and Technology Core for their assistance with sample processing.

6.7 Author Contributions

Conceptualization - A.S.M., C.M.G., and R.J.P.; Methodology - A.S.M., C.M.G., and R.J.P.; Investigation - A.S.M., C.M.G., and R.J.P.; Formal Analysis - A.S.M., C.M.G., and R.J.P.; Writing – Original Draft Preparation, A.S.M. and R.J.P.; Writing – Review & Editing, A.S.M., C.M.G., and R.J.P.; Supervision, R.J.P.; Funding Acquisition - A.S.M. and R.J.P.

6.8 Figures and Tables

Figure 6.1

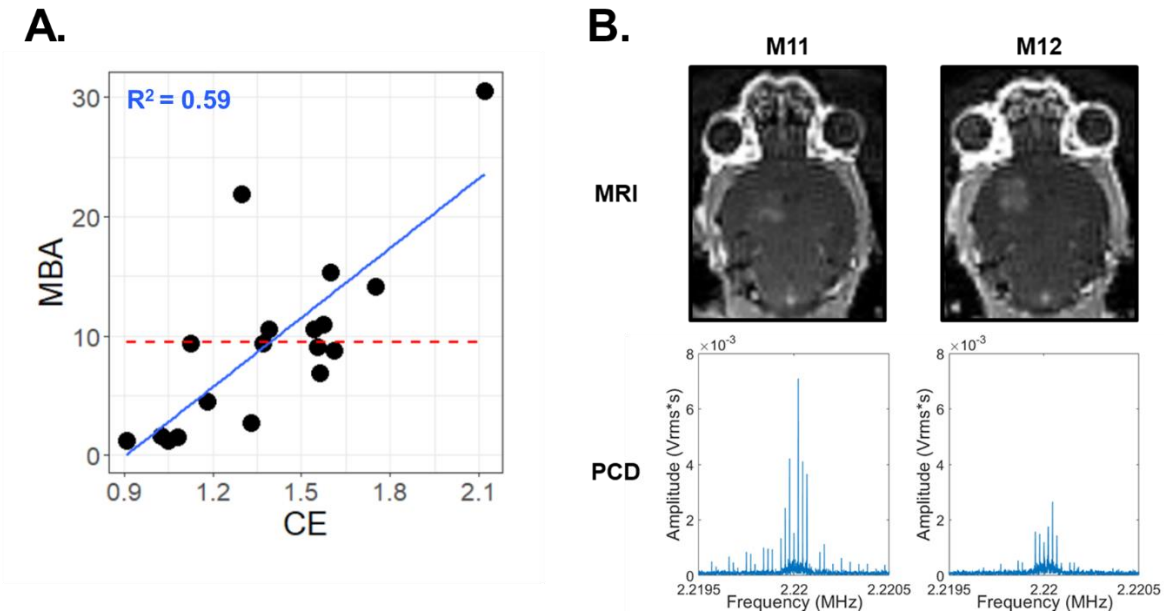

Figure 6.1: MBA and CE are correlated, but with substantial variability. (A) Scatter-plot for all samples with paired CE and MBA data. The solid blue line and text represent linear regression, while the dashed red line represents the MBA mean, simulating a null linear fit. (B) Paired T1-weighted contrast-enhanced 3T MRI images (top) and PCD traces in the Fourier domain around the 2nd harmonic (bottom) for 2 different mice (M11 and M12) during FUS BBBD treatment within a single experiment. Comparison of M11 and M12 illustrates that the relative magnitudes of MBA and CE can vary markedly from treatment to treatment.

Figure 6.2

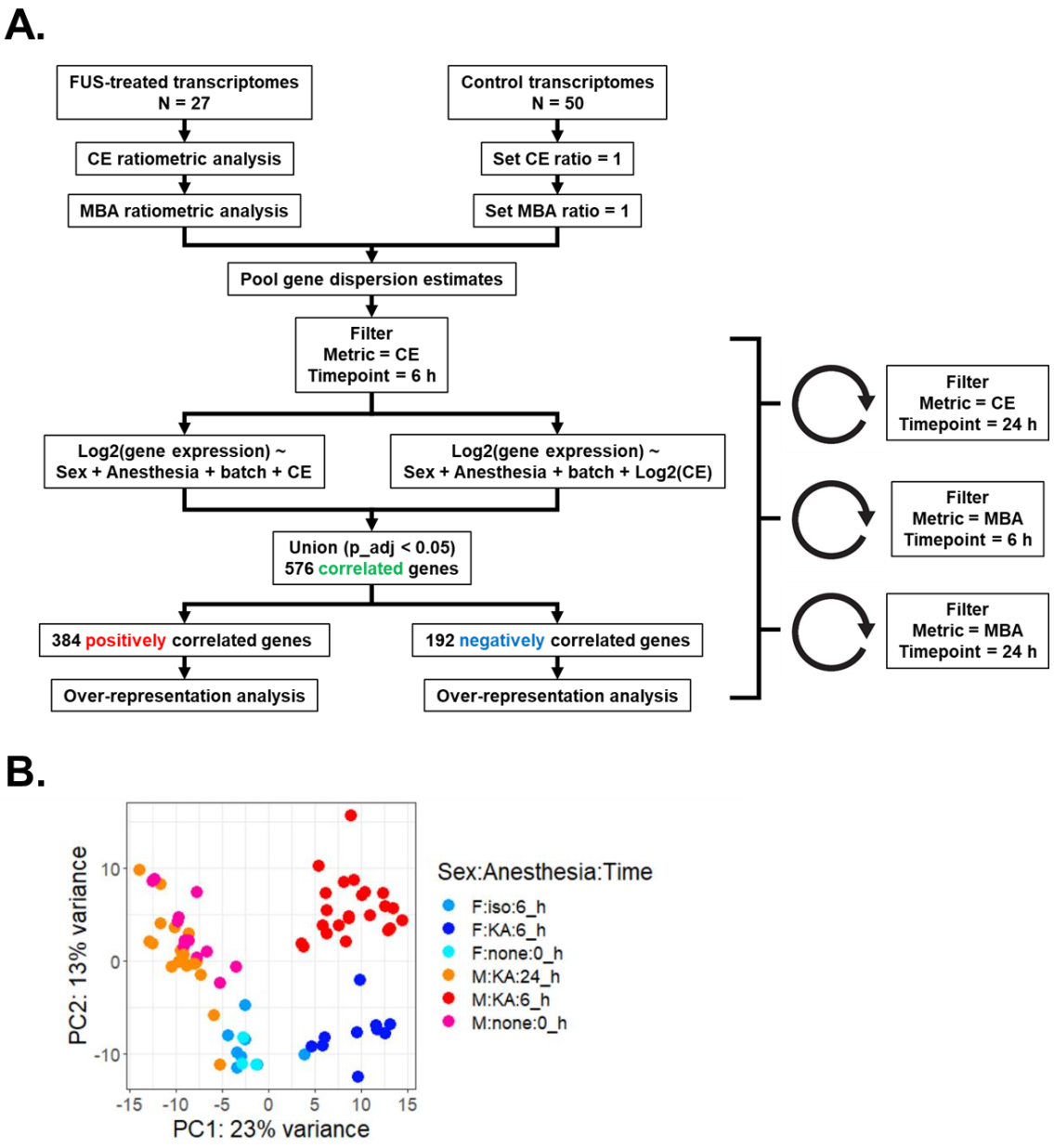

Figure 6.2: Overview of dataset processing and variability. (A) Flow chart describing computational processing pipeline. Untreated and FUS treated samples from multiple studies were pooled and analyzed for contrast enhancement (CE) and microbubble activation (MBA). Linear and exponential models were fit for each prediction metric (CE or MBA) and timepoint (6 h vs 24 h post treatment), followed by bioinformatics analyses. (B) Principle components analysis of RNA-seq transcript counts after variance stabilizing transformation. Each dot represents a single sample, color coded according to the sample characteristics including sex, anesthetic, and harvest timepoint.

Figure 6.3

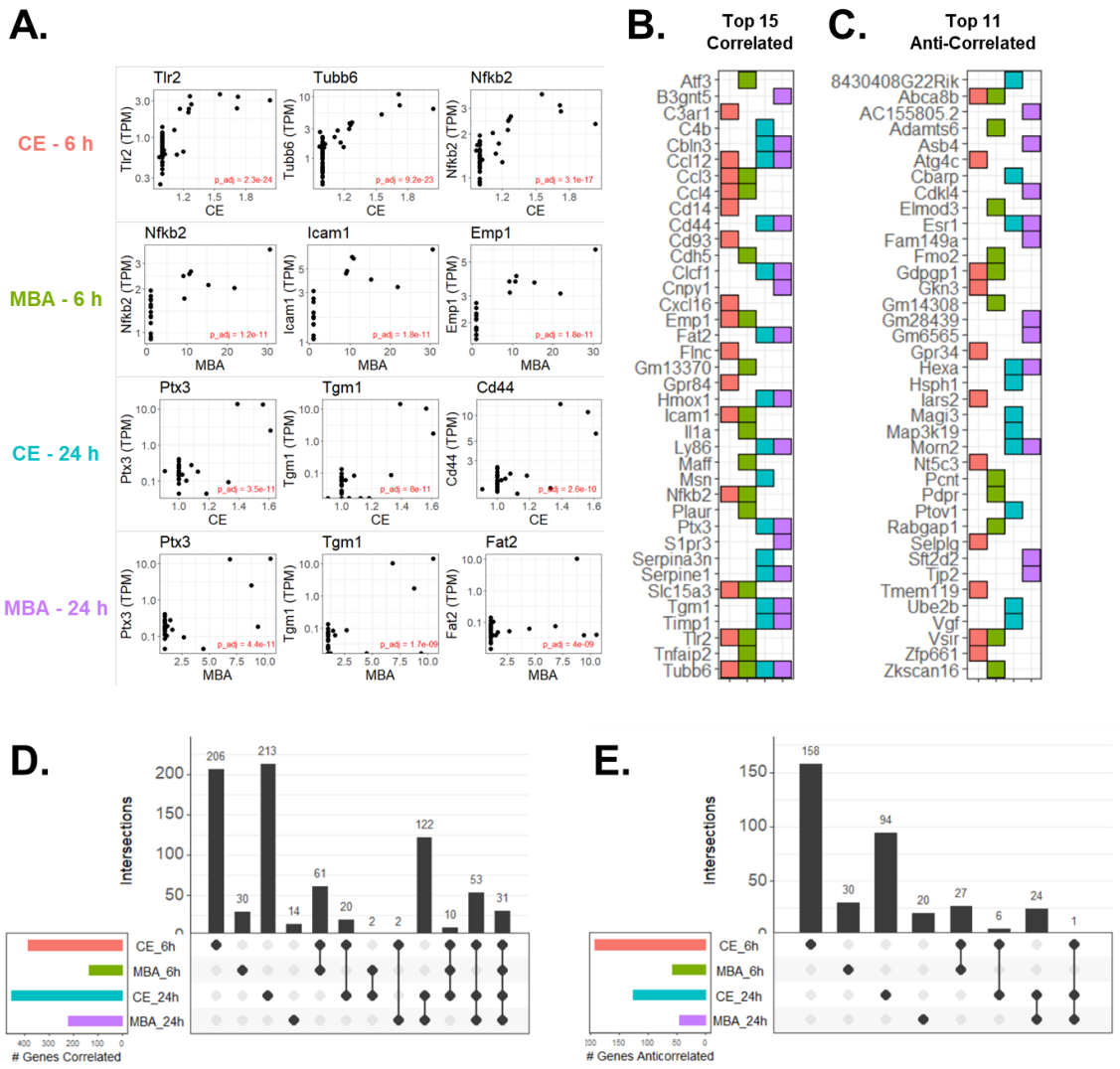

Figure 6.3 CE and MBA predict significant gene expression 6 h and 24 h after FUS BBBD. (A) Scatter-plots of TPM normalized expression for the top 3 genes predicted by CE or MBA at 6 h or 24 h after treatment. (B) Tile chart representing the top 15 genes predicted in each pool. Note that the absence of a tile for a particular pool-gene combination does not necessarily mean the gene is not significantly correlated, just that it is not in the top 15. (C) Tile chart representing the top 11 anti-correlated genes from each pool, with the same conditions as in B. (D) Upset plot indicating gene identity overlaps of positively correlated genes from each pool. (E) Upset plot indicate gene identity overlaps of anti-correlated genes from each pool.

Figure 6.4

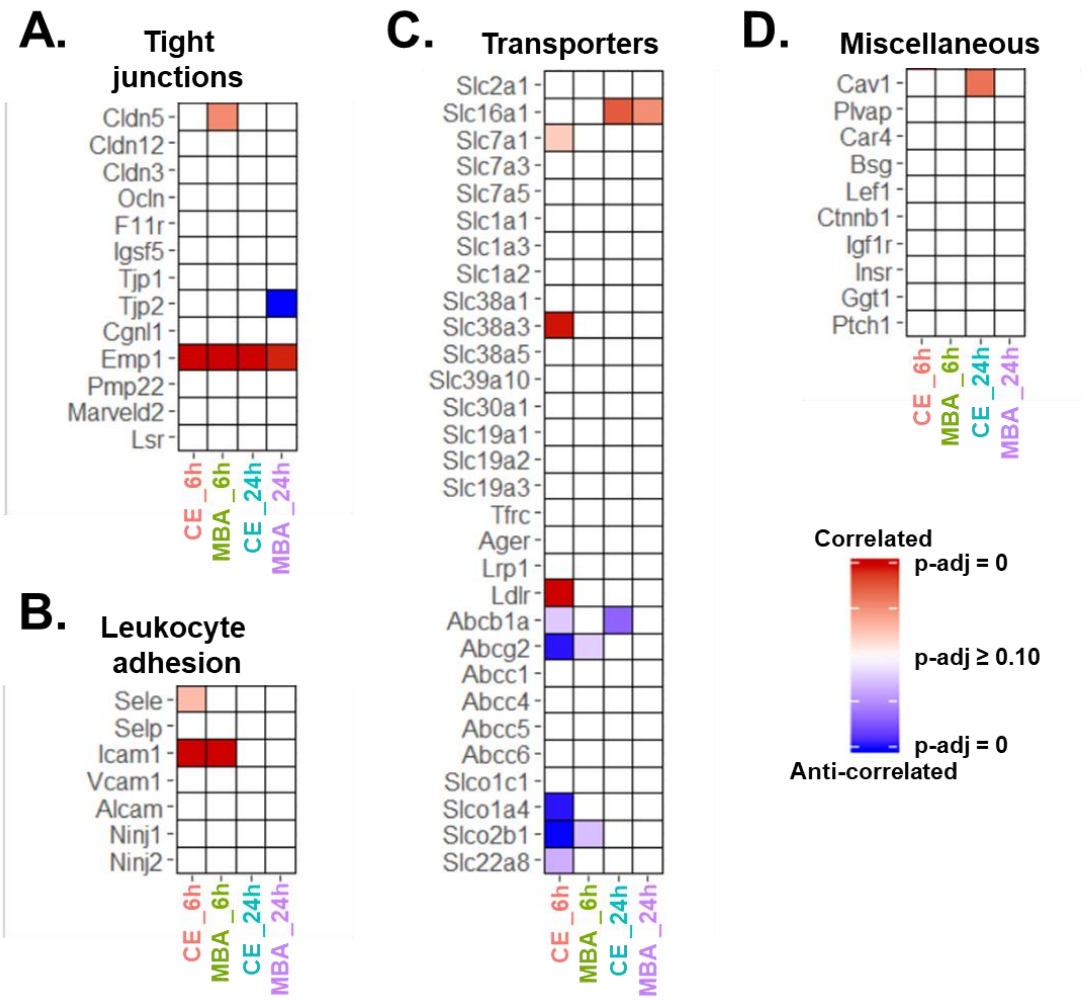

Figure 6.4: CE and MBA differentially predict expression of BBB associated transcripts. (A-D) Heatmaps of significance of correlation (red) or anti-correlation (blue) for selected BBB-associated genes predicted by CE or MBA at 6 or 24 h post-FUS (columns). Selected categories include (A) tight junctions, (B) leukocyte adhesion, (C) transporters, and (D) transcytosis/miscellaneous.

Figure 6.5

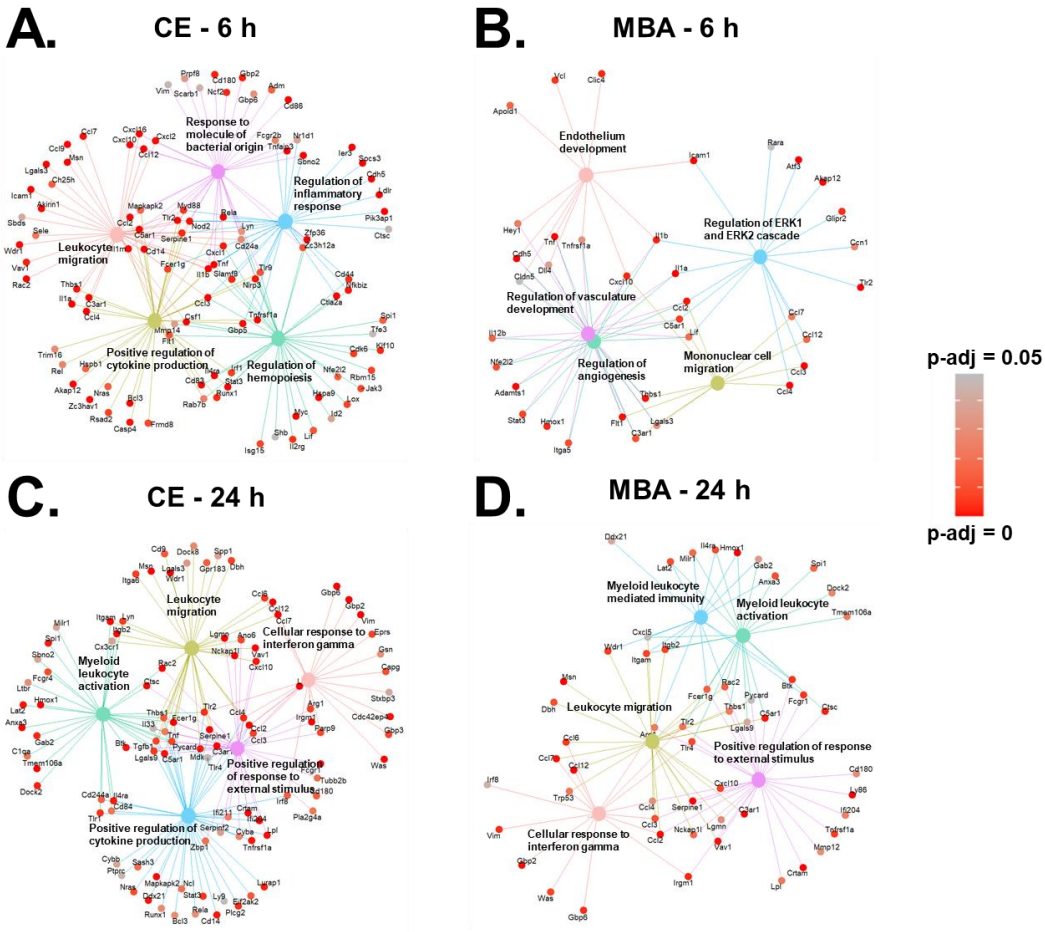

Figure 6.5 Overview of over-representation analysis. (A-D) Gene concept networks of the top 5 over-represented gene sets expressed 6 h after FUS proportional to CE (A), 6 h after FUS proportional to MBA (B), 24 h after FUS proportional to CE (C), and 24 h after FUS proportional to MBA (D). Redundant pathways were removed by semantic similarity analysis. Supporting genes within each network are colored in proportion to the significance of their correlation with the specified metric at the specific timepoint.

Figure 6.6

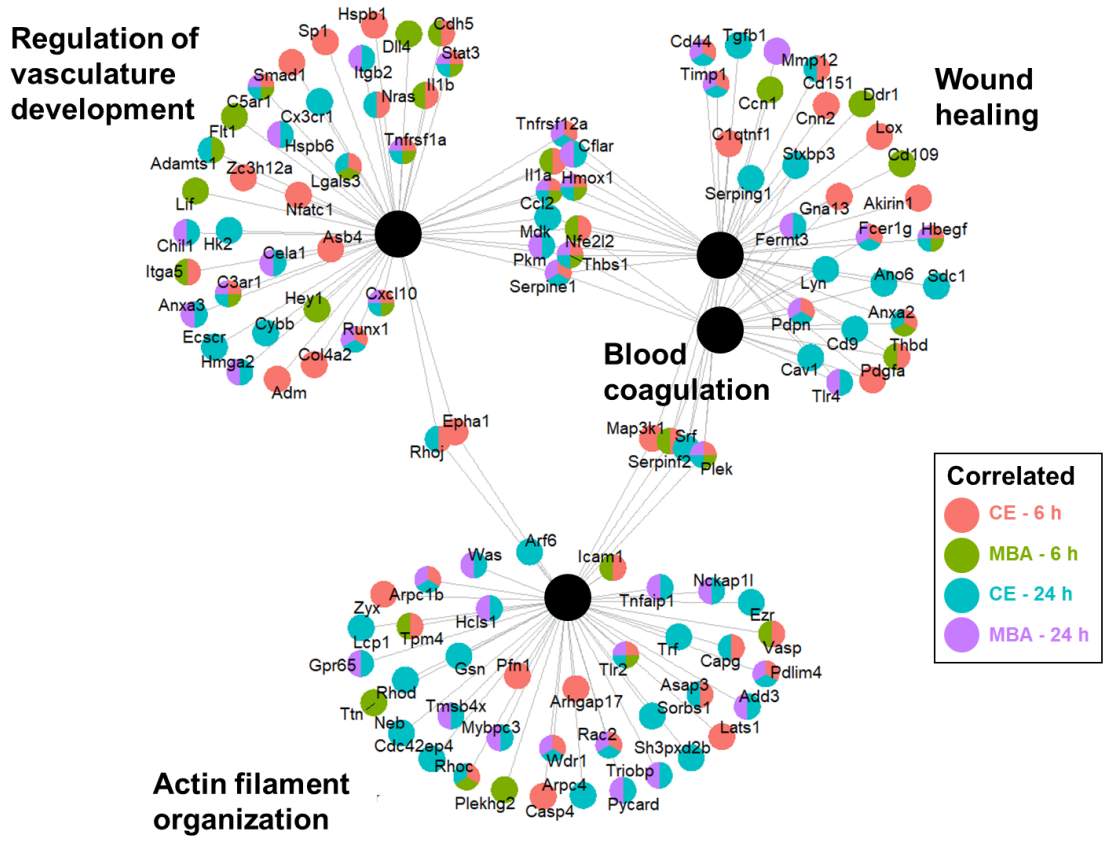

Figure 6.6: CE and MBA predict enrichment of genes associated with diverse repair mechanisms. Integrated gene concept network for 4 selected pathways significantly enriched across all 4 pools. Each dot, representing a contributing gene, is color coded as a pie-chart representing pools in which that gene is significantly correlated.

Figure 6.S1

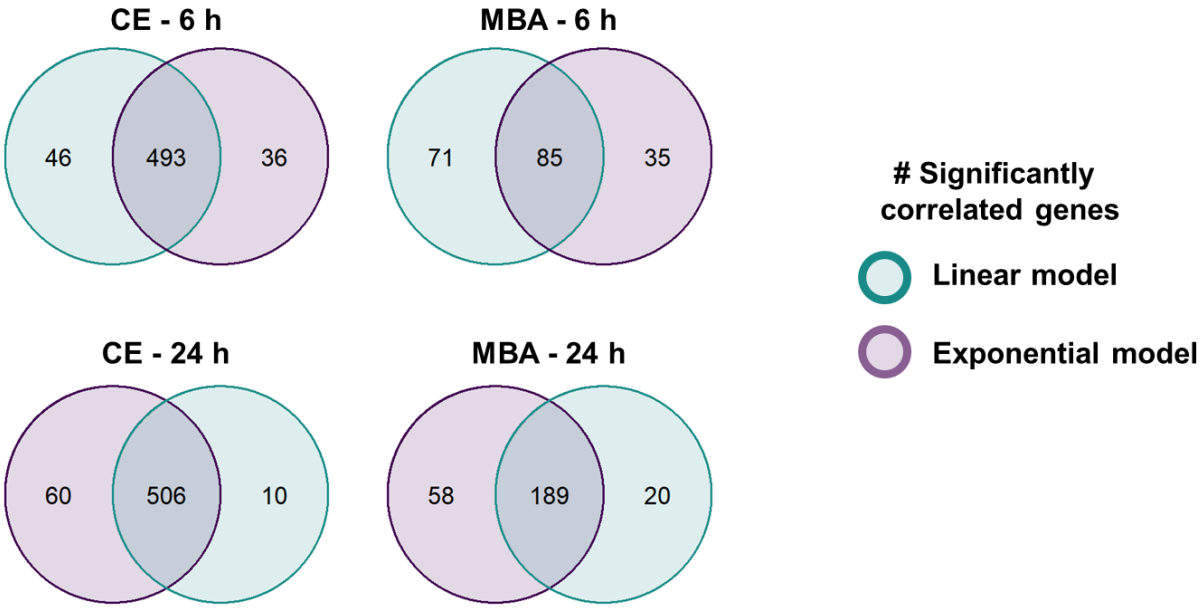

Figure 6.S1: Overlap between correlates identified by pairs of linear and exponential models. A linear model and an exponential model were constructed to identify genes expressed in proportion to CE or MBA at 6 h or 24 h post FUS. Overlaps between significantly (p adjusted < 0.05) correlated genes from each pair of models are shown.

Figure 6.S2

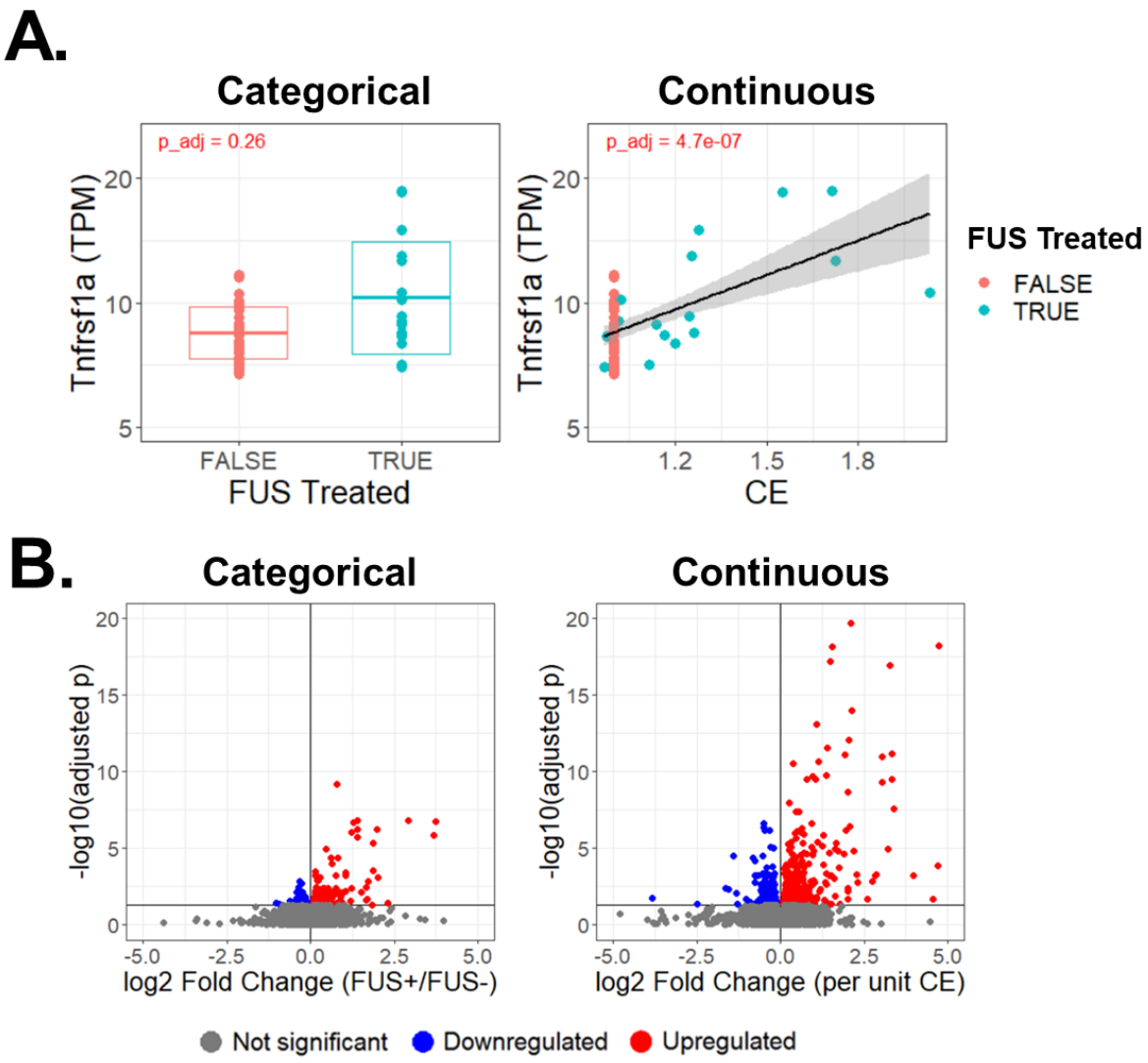

Figure 6.S2: Continuous metrics of BBBD predict gene expression with higher sensitivity than treatment status alone. (A) TPM normalized expression of Tnfrsf1a with data organized according to FUS treated or FUS untreated (left) or according to the extent of CE. Note that the error metrics, namely SEM shown in the categorical plot and the 95% confidence interval in the continuous plot are for visualization purposes only. The adjusted p values on each plot are derived from the Wald test after appropriate negative binomial regression of gene expression, and blockage of the effects of sex, anesthesia, and sequencing batch. (B) Volcano plots of differential gene expression when FUS is treated as a categorical variable (left) or a continuous variable according to CE (right) at 6 h post-treatment. Each dot represents a gene, color coded by the significance of its relative expression (left) or correlation (right).

Table 6.S1

Contingency table for 77 transcriptomes used in multiple regression analyses

Group	1	2	3	4	5	6	7	8	9	10	11	12	13	14	15	16	17	18	19	20
Anesthesia	-	KA	KA	KA	Iso	Iso	Iso	-	KA	KA	KA	KA	KA	KA	KA	KA	KA	KA	KA	KA
Bubbles	-	-	Alb	Alb	-	Alb	Alb	-	-	Cat	Cat	Cat	Cat	Cat	-	Cat	Cat	Cat	Cat	Cat
PNP (MPa)	-	-	-	0.4	-	-	0.4	-	-	-	0.1	0.1	0.2	0.4	-	-	0.1	0.1	0.2	0.4
Time (h)	-	6	6	6	6	6	6	-	6	6	6	6	6	6	24	24	24	24	24	24
Hemisphere (Ipsi v Contra)	I	I	I	I	I	I	I	I	I	I	I	C	I	I	I	I	I	C	I	I
n	3	3	3	4	3	3	4	12	6	4	4	3	3	3	3	3	4	3	3	3
Sex	F	F	F	F	F	F	F	M	M	M	M	M	M	M	M	M	M	M	M	M
Have MRI?	-	-	-	Y	-	-	Y	-	-	-	Y	Y	Y	Y	-	-	Y	Y	Y	Y
Have PCD?	-	-	-	Y	-	-	Y	-	-	-	N	N	N	N	-	-	Y	Y	Y	Y

Anesthesia Study

Sonoselective Study

Chapter 7: Considerations for the Next Generation of FUS Research in Tumors and the Brain

7.1 Conclusions and Future Directions for Tumor Immunomodulation with Focused Ultrasound Thermal Ablation

Focused ultrasound thermal ablation (FUSTA) is an attractive therapeutic technology for the sensitization of tumors to immune recognition. It is non-invasive, highly targetable, non-ionizing, and already positioned in multiple clinical settings worldwide for tumor debulking. Indeed using a single technology for simultaneous primary and systemic tumor growth control could rapidly shift therapeutic norms in multiple cancer types. Toward realizing this objective, we utilized high throughput methods to investigate immunomodulatory effects of FUSTA in aggressive murine melanoma models in Chapter 2, and human breast cancer in Chapter 3. Here, we summarize parallels between the two and discuss next steps for the field.

Despite structural differences between the studies carried out in Chapter 2 and Chapter 3 (species, tumor type, analysis time points, FUSTA delivery systems), we note striking similarities in TME responses to FUSTA. Both murine and human tumors exhibited signatures of sterile inflammation, including enhanced DAMP and cytokine transcription. Pro-tumor inflammation, characterized by increased myeloid representation, decreased lymphoid abundance, growth factor transcription, and matrix remodeling gene set enrichment were also observed in both studies. A novel sterile inflammatory finding reported in Chapter 2 was activation of the inflammasome after FUSTA in murine melanoma. Fascinatingly, this pathway was also significantly enriched in ablated and periablated regions of human breast cancer tumors in Chapter 3. Therefore pyroptosis may be a universal consequence of FUSTA, contributing to post-treatment immunosuppression in the TME.

The parallels between Chapter 2 and Chapter 3 likely speak to the high degree of evolutionary conservation of sterile inflammatory signaling. While the associated tissue repair phenotype represents a barrier to FUSTA immunogenicity, it could also be viewed as a reliable therapeutic target. If FUSTA perturbs a highly conserved pathway, we reason that pharmacological polarization could be immunologically favorable to cancer patients regardless of tumor type. Combining FUSTA with an immunoadjuvant could therefore impart a “tumor-normalization” force, combating the pervasive hurdle of inter-tumoral variability. Future studies should investigate the generalizability of this strategy to multiple tumor types with varying degrees and mechanisms of immune evasion. Additional mechanistic studies will be required to understand the extent to which pyroptosis drives pro-tumor inflammation, and if its blockade

leaves desirable adaptive immune responses intact. Finally, technical studies will be required to optimize induced intratumoral immunomodulation, including testing different FUSTA regimens alongside alternative FUS and non-FUS focal therapies.

7.2 Conclusions and Future Directions for Drug Delivery Across the BBB with FUS

In chapters 4, 5, and 6, we used bioinformatics approaches to describe novel relationships between experimental parameters and central nervous system (CNS) responses to FUS mediated blood brain barrier disruption (BBBD). A common theme shared across all 3 chapters was the sensitivity of the brain parenchyma to relatively minor perturbations. Short duration anesthesia alone in Chapter 4, low intensity FUS in Chapter 5, and marginal increases in contrast enhancement or microbubble activation in Chapter 6 all produced detectable elevations in markers of cellular stress and disruption of homeostasis. Together, these findings support the notion that, though FUS activation of MB is more targeted and reversible than other CNS drug delivery strategies, it still ultimately requires rupture of a physiologically protective structure. Our analyses also contradict claims that the cellular stress and sterile inflammatory responses engaged by FUS BBBD are binary, only occurring beyond a certain threshold. I propose these mechanisms should be considered a necessary consequence of BBBD, to be weighed against the benefit of enhanced therapeutic delivery. Finally, our analytic pipelines demonstrate that histological analyses are insufficiently sensitive to comprehensively assess the safety profile of BBBD. Even the maximally inflammatory parameters sets chosen across chapters 4, 5, and 6 did not produce any evidence of histological damage. We draw parallels to the recent investigations of mild traumatic brain injury (mTBI) experienced by soldiers and professional athletes, where accumulated sub-clinical or sub-cellular insults precipitate lasting neurological deficits (388–392).

Future investigations should thoroughly investigate the consequences of other FUS BBBD parameter sets (such as pulsing frequency, pulse duration, MB type) on sterile inflammatory responses in the brain. These studies should also be carried out in different disease models, in which BBB function and integrity are already altered at baseline. Molecular profiling and functional neurologic studies on brains treated with multiple sessions of FUS BBBD at both acute and chronic time points will contribute to the safety profile of therapy for wider clinical adoption.

7.3 Feasibility Considerations for FUS Research

In this dissertation, we examined two FUS regimens: FUSTA immunomodulation and FUS BBBD. As of May 2021, I have authored or coauthored 4 published manuscripts related to the

latter project compared to 0 related to the former. This difference in research productivity is despite significantly more time, research experience, and funding dedicated to the FUSTA projects. In this section, I reflect on potential explanatory factors to aid future investigators interested in FUS research.

The first consideration is selection of a disease model. The single largest barrier to the progression of the FUSTA projects was tumor heterogeneity. Cells expanded from a single parental line implanted into genetically identical mice with minimal experimental variation consistently produced highly variable tumors with respect to tumor growth dynamics, histology, and response to FUSTA. We believe this is attributable to the stochastic nature of highly proliferative, genomically instable tumor cells which leads to the rapid development of considerable intra- and inter tumor diversity. The B16F10 cell line was particularly challenging to work with, as it is among the most aggressive, leaving little room for detection of a therapeutic effect before tumors met euthanasia criteria. B16F10 is also poorly immunogenic, making it a useful comparator to certain human malignancies but also significantly raising the immunostimulatory threshold required to observe a systemic response. These challenges were mirrored in the human studies carried out in Chapter 3. Significant inter-tumor heterogeneity combined with an already-refractory patient population created a highly noisy baseline, limiting our ability and potential to detect therapy-specific effects. We contrast this to the FUS BBBD projects, all of which were carried out in young healthy mice. In these studies, the baseline biological variability was negligible, enabling acquisition of significant detail concerning the effects of FUSTA BBBD even though it is a much less disruptive modality than FUSTA.

A second important consideration is the administration of FUS. In our lab, FUSTA was applied under US guidance using a home-built system, while BBBD was performed under MRI guidance with a commercial system. The US guided treatments were faster and easier, but the lack of real-time treatment monitoring increased guess-work, lessening reproducibility between and within experiments. The MRI-guided system enabled real time monitoring via contrast enhancement and MBA, which facilitated treatment reproducibility, outlier detection, and comparison across multiple studies.

FUS research has a steep learning curve, requiring specialized knowledge of acoustics, imaging, and signal processing and their application in pathological contexts. To maximize research productivity, a reproducible model should be selected with a relatively low threshold for confirming or refuting the desired therapeutic effect. Similarly, a FUS delivery system should be implemented with as little variability as possible, ideally with the option of real-time treatment monitoring.

7.4 (Focused Ultra)Sound's a Bit Too Good to be True? Managing Expectations for a Rapidly Expanding Technology

A colleague and I jokingly liken FUS to "magic fairy dust", referencing its apparently mystical capacity to reverse any pathology. Supposedly, FUS can stimulate immunosuppressed microenvironments (79–86), yet quell inflammation in autoimmune diseases (393, 394). It can initiate wound healing responses after injury (177) but also inhibit fibrosis (395, 396). Neurons can be both excited and inhibited (397–402). Blood vessels can be compelled to constrict (403–405) or dilate (406–408), to grow via angiogenesis (409–412) or to become hemostatic (413–416). Cancer biomarkers can be "amplified" (413). Tumor cells can be released into circulation when needed for liquid biopsy (417–419), yet metastases can also be prevented (82, 83, 86, 92, 241, 245, 420). A non-FUS researcher attending a FUS conference may reasonably conclude that the technology can be applied to practically any disease with high likelihood of success.

While some of these claims are accurate, achieved by logical pairing of FUS regimens with amenable pathologies, or the assistance of drugs, others sound a bit too good to be true. Having designed a FUS system and applied the technology in multiple regimens and disease models, I am reminded that FUS is primarily a physical stimulus. There is nothing inherently therapeutic about acoustic energy. FUS does not provide a resource cells need. It does not target a dysregulated, pathogenic pathway. There is no evolutionarily conserved survival advantage conferred by cellular absorption of sound waves. FUS is a treatment, not a cure, and most of its therapeutic effects are elicited by cellular damage. This mechanistic simplicity is often avoided or overlooked, in favor of loftier claims that falsely assign a sort of "disease awareness" to the technology. Such overstatements ultimately obscure biomedically pertinent insights into FUS' interaction with tissue, delaying effective translation and potentially risking undue harm to patients. We identify two contributory factors.

The first is scientific in nature. Many of the therapeutic effects of FUS are stated without context, because the study was too limited in scope and/or not designed to detect anything negative. FUSTA may elicit a significant increase in intratumoral T cells, but what if they are 100% anergic or accompanied by a flood of suppressive myeloid cells? How useful is repeatedly opening the BBB to treat a neurodegenerative disease if the therapy itself is neurotoxic? The second contributory factor is cultural. We were surprised to be among the first to report therapeutically nuanced mechanisms of FUSTA immunomodulation and FUS BBBD, despite the wealth of preclinical research and progression to clinical trials for both regimens. This is likely in part attributable to challenges faced by all research communities – the "publish or perish" mindset, combined with desirability of positive over negative data. However these factors may be

particularly exacerbated in the FUS community, where the focus is on a new technology rather than a particular disease. Rapidly expanding adoption of the technology as well as well as commercialization pressures may produce a research community especially unreceptive to “unsightly” data that could hamper its momentum. Indeed the first major paper to report sterile inflammatory responses in the brain after FUS BBBD received significant pushback, and may have been ignored completely were it not associated with a well-respected investigator and published in a high impact journal.

In the introductory chapter of this thesis, I make the case that high throughput unbiased approaches to FUS research are required to sufficiently capture the biological dynamics of a complex perturbation in a complex microenvironment. A corollary of this research model is that the detection of hypothesized or desired therapeutic biological signatures is no more likely than the emergence of unintuitive, undesirable, or even pathogenic ones. A common thread throughout this dissertation is the reporting of double-edged responses to FUS. In Chapters 2 and 3, we describe how FUSTA does ignite several of the immunogenic mechanisms reported previously, but these are either outweighed or outlasted by tolerogenic and tissue repair mechanisms. FUSTA alone had limited potential to engage the adaptive immune compartment critical for the establishment of systemic anti-cancer immunity. In Chapter 4, we established that anesthesia differentially augments the sensitivity of the brain parenchyma to FUS BBB, revealing a potential confounding variable underlying many previous FUS BBBD studies. Chapters 4, 5, and 6 reveal FUS BBBD is inextricably linked with cellular and neuronal stress, even under conditions considered to be “safe”. These novel insights, though therapeutically ambiguous, ultimately validate our experimental approach and support its application in other FUS research contexts.

This is not to say our approaches are without bias; condensing massive transcriptomic datasets into meaningful, useful knowledge requires significant manual selection of certain signatures and exclusion of others. Nor is our objective to disparage the therapeutic potential of FUS. Our argument is motivated by our belief in the unprecedented potential of FUS to non-invasively perturb pathological microenvironments without the use of ionizing radiation. Bringing FUS to patient bedsides will require being realistic about both its therapeutic effects and potential consequences, so that they can be appropriately leveraged and mitigated respectively. Toward this end, we propose the incorporation of unbiased methods into more mechanistic FUS studies and a wider acceptance of mixed efficacy data in the FUS research community.

7.5 Integrating Lessons Learned to Prototype an Impactful FUS Research Project

In the preceding sections, we enumerated scientific, pragmatic, and forward-looking insights gained throughout this dissertation to aid the next generation of FUS investigators. In this final segment, we demonstrate how these conclusions can be leveraged by outlining a prospective research strategy we believe would bring FUS BBBD closer to clinical adoption.

FUS BBBD has obvious and far-reaching clinical implications, potentially unlocking a wealth of previously-ignored pharmacological tools for any neurological pathology. Given its well established therapeutic utility, the success of BBBD now hinges on two critical factors: safety and repeatability. Both have been evaluated at higher levels of biological organization (organism and tissue levels) (104, 117, 118), paving the way for early clinical trials (NCT02986932, NCT03739905, NCT03119961, NCT03671889, NCT04118764). However the recent molecular profiling studies performed by our group and others have generated new appreciation for secondary effects of BBBD, such as sterile inflammation, bringing the issues of safety and repeatability back into focus (150, 151, 368, 421). These have also generated hypotheses that repeated BBBD with FUS could itself be therapeutic, such as for the enhancement of plaque clearance in Alzheimer's disease (154). Therefore, we propose that a future impactful and achievable FUS BBBD research project should investigate the effects of repeated BBBD in healthy and disease models at clinically relevant scales and multiple levels of biological organization.

Most repeated studies of FUS BBBD assess safety at histological or functional levels after only a handful of FUS treatments (typically between 3 and 6). However, FUS BBBD is intended to treat chronic diseases, some of which could require years of repeated therapy. To more appropriately mirror clinically relevant courses, we propose studying brain tissue of mice treated after 1, 15, and 30 weekly rounds of FUS BBBD. Sham mice should be anesthetized with isoflurane during each session. CE and MBA should be assessed after each round of therapy, to evaluate the extent to which the BBB's permeability is dependent on past FUS exposure. Treated brains should be excised and cut in half. Bulk RNA-sequencing should be performed on the first halves after 1, 15, or 30 rounds of FUS BBBD, assessing for gene and pathway level changes relative to sham-treated mice. The second treated brain halves should be assessed by histology for fibrosis, apoptosis, RBC extravasation, and vacuolation. Finally, mice treated after 1, 15, or 30 rounds of FUS should be assessed for cognitive function, using tests like the Morris Water Maze (spatial memory), fear conditioning (contextual memory), or Y-maze (working memory) (422). We suggest all proposed experiments should be carried out in parallel in an Alzheimer's disease (AD) model, as AD is one of the most common pathologies hypothesized to benefit from the secondary

effects of FUS (372). Further, the BBB is known to be dysfunctional in AD (362, 363), potentially lowering the threshold for continual FUS BBBD to positively or negatively influence the brain parenchyma. AD treated brains could also be histologically assessed for relative changes in Aβ levels after each course of FUS BBBD.

Together, this combination of studies captures clinically relevant courses of FUS BBBD, includes unbiased high-throughput methods, accounts for baseline variation attributable to anesthesia and disease model, and spans a much wider range of biological organization compared to previous work. This proposal was structured around BBBD rather than FUSTA immunomodulation due to the practicality limitations of FUSTA immunomodulation research laid out in section 7.3. However it is our hope that the general design principles exemplified herein enhance the design of any future FUS investigation, regardless of the mechanism.

References

1. J. Curie, P. Curie, Development by pressure of polar electricity in hemihedral crystals with inclined faces. *Bull. soc. min. Fr.* **3**, 90 (1880).

2. G. Lippmann, Principe de la conservation de l'électricité, ou second principe de la théorie des phénomènes électriques. *J. Phys. Théorique Appliquée* **10**, 381–394 (1881).

3. J. Curie, P. Curie, Contractions et dilatations produites par des tensions électriques dans les cristaux hémièdres à faces inclinées. *Compt. Rend* **93**, 1137–1140 (1881).

4. J. Gruetzmacher, Piezoelektrischer Kristall mit Ultraschallkonvergenz. *Zeitschrift für Phys.* **96**, 342–349 (1935).

5. J. G. Lynn, R. L. Zwemer, A. J. Chick, A. E. Miller, "A NEW METHOD FOR THE GENERATION AND USE OF FOCUSED ULTRASOUND IN EXPERIMENTAL BIOLOGY" (April 4, 2021).

6. W. J. FRY, W. H. MOSBERG, J. W. BARNARD, F. J. FRY, Production of focal destructive lesions in the central nervous system with ultrasound. *J. Neurosurg.* **11**, 471–478 (1954).

7. R. MEYERS, *et al.*, Early experiences with ultrasonic irradiation of the pallidofugal and nigral complexes in hyperkinetic and hypertonic disorders. *J. Neurosurg.* **16**, 32–54 (1959).

8. W. J. FRY, R. MEYERS, Ultrasonic method of modifying brain st ructures. *Confin. Neurol.* **22**, 315–327 (1962).

9. F. J. FRY, Precision high intensity focusing ultrasonic machines for surgery. *Am. J. Phys. Med.* **37**, 152–156 (1958).

10. K. Hynynen, *et al.*, 500-Element ultrasound phased array system for noninvasive focal surgery of the brain: A preliminary rabbit study with ex vivo human skulls. *Magn. Reson. Med.* **52**, 100–107 (2004).

11. F. A. Jolesz, K. Hynynen, N. McDannold, C. Tempany, MR imaging-controlled focused ultrasound ablation: A noninvasive image-guided surgery. *Magn. Reson. Imaging Clin. N. Am.* **13**, 545–560 (2005).

12. P. C. Lauterbur, Image formation by induced local interactions: Examples employing nuclear magnetic resonance. *Nature* **242**, 190–191 (1973).

13. C. J. Diederich, K. Hynynen, The feasibility of using electrically focused ultrasound arrays

to induce deep hyperthermia via body cavities. *IEEE Trans. Ultrason. Ferroelectr. Freq. Control* **38**, 207–219 (1991).

14. K. Hynynen, *et al.*, A clinical, noninvasive, MR imaging-monitored ultrasound surgery method. *Radiographics* **16**, 185–195 (1996).

15. K. Hynynen, V. Colucci, A. Chung, F. Jolesz, Noninvasive arterial occlusion using MRI-guided focused ultrasound. *Ultrasound Med. Biol.* **22**, 1071–1077 (1996).

16. P. E. Huber, *et al.*, A new noninvasive approach in breast cancer therapy using magnetic resonance imaging-guided focused ultrasound surgery. *Cancer Res.* **61**, 8441–8447 (2001).

17. H. Furusawa, *et al.*, The evolving non-surgical ablation of breast cancer: MR guided focused ultrasound (MRgFUS). *Breast cancer* **14**, 55–58 (2007).

18. F. Wu, *et al.*, “Wide local ablation” of localized breast cancer using high intensity focused ultrasound. *J. Surg. Oncol.* **96**, 130–136 (2007).

19. H. Furusawa, *et al.*, Magnetic resonance–guided focused ultrasound surgery of breast cancer: reliability and effectiveness. *J. Am. Coll. Surg.* **203**, 54–63 (2006).

20. F. Wu, *et al.*, Extracorporeal high intensity focused ultrasound treatment for patients with breast cancer. *Breast Cancer Res. Treat.* **92**, 51–60 (2005).

21. D. B. Zippel, M. Z. Papa, The use of MR imaging guided focused ultrasound in breast cancer patients; a preliminary phase one study and review. *Breast cancer* **12**, 32–38 (2005).

22. F. Wu, *et al.*, A randomised clinical trial of high-intensity focused ultrasound ablation for the treatment of patients with localised breast cancer. *Br. J. Cancer* **89**, 2227–2233 (2003).

23. W. Hundt, C. E. O’Connell-Rodwell, M. D. Bednarski, S. Steinbach, S. Guccione, In vitro effect of focused ultrasound or thermal stress on HSP70 expression and cell viability in three tumor cell lines. *Acad. Radiol.* **14**, 859–870 (2007).

24. K. A. Skalina, S. Singh, C. G. Chavez, F. Macian, C. Guha, Low intensity focused ultrasound (LOFU)-mediated acoustic immune priming and ablative radiation therapy for in situ tumor vaccines. *Sci. Rep.* **9**, 1–12 (2019).

25. H. Grüll, S. Langereis, Hyperthermia-triggered drug delivery from temperature-sensitive

liposomes using MRI-guided high intensity focused ultrasound. *J. Control. Release* **161**, 317–327 (2012).

26. M. D. Gray, *et al.*, Focused ultrasound hyperthermia for targeted drug release from thermosensitive liposomes: results from a phase I trial. *Radiology* **291**, 232–238 (2019).

27. R. Staruch, R. Chopra, K. Hynynen, Localised drug release using MRI-controlled focused ultrasound hyperthermia. *Int. J. Hyperth.* **27**, 156–171 (2011).

28. A. D. Maxwell, *et al.*, Cavitation clouds created by shock scattering from bubbles during histotripsy. *J. Acoust. Soc. Am.* **130**, 1888–1898 (2011).

29. E. Vlaisavljevich, *et al.*, Histotripsy-induced cavitation cloud initiation thresholds in tissues of different mechanical properties. *IEEE Trans. Ultrason. Ferroelectr. Freq. Control* **61**, 341–352 (2014).

30. M. Fini, W. J. Tyler, Transcranial focused ultrasound: a new tool for non-invasive neuromodulation. *Int. Rev. Psychiatry* **29**, 168–177 (2017).

31. H. Kim, S. D. Lee, A. Chiu, S.-S. Yoo, S. Park, Estimation of the spatial profile of neuromodulation and the temporal latency in motor responses induced by focused ultrasound brain stimulation. *Neuroreport* **25**, 475 (2014).

32. E. Mehić, *et al.*, Increased anatomical specificity of neuromodulation via modulated focused ultrasound. *PLoS One* **9**, e86939 (2014).

33. D. P. Darrow, Focused ultrasound for neuromodulation. *Neurotherapeutics* **16**, 88–99 (2019).

34. H. A. S. Kamimura, *et al.*, Focused ultrasound neuromodulation of cortical and subcortical brain structures using 1.9 MHz. *Med. Phys.* **43**, 5730–5735 (2016).

35. N. D. Sheybani, R. J. Price, Perspectives on recent progress in focused ultrasound immunotherapy. *Theranostics* **9**, 7749 (2019).

36. C. T. Curley, N. D. Sheybani, T. N. Bullock, R. J. Price, Focused ultrasound immunotherapy for central nervous system pathologies: challenges and opportunities. *Theranostics* **7**, 3608 (2017).

37. R. J. E. van den Bijgaart, *et al.*, Thermal and mechanical high-intensity focused ultrasound: perspectives on tumor ablation, immune effects and combination strategies. *Cancer*

Immunol. Immunother. **66**, 247–258 (2017).

38. D. Hanahan, R. A. Weinberg, Hallmarks of cancer: the next generation. *Cell* **144**, 646–674 (2011).

39. D. Hanahan, R. A. Weinberg, The hallmarks of cancer. *Cell* **100**, 57–70 (2000).

40. I. Mellman, G. Coukos, G. Dranoff, Cancer immunotherapy comes of age. *Nature* **480**, 480–489 (2011).

41. G. P. Dunn, A. T. Bruce, H. Ikeda, L. J. Old, R. D. Schreiber, Cancer immunoediting: from immunosurveillance to tumor escape. *Nat. Immunol.* **3**, 991–998 (2002).

42. H. Raskov, A. Orhan, J. P. Christensen, I. Gögenur, Cytotoxic CD8+ T cells in cancer and cancer immunotherapy. *Br. J. Cancer* **124**, 359–367 (2021).

43. K. Wing, *et al.*, CTLA-4 control over Foxp3+ regulatory T cell function. *Science (80-.).* **322**, 271–275 (2008).

44. C. Stockmann, D. Schadendorf, R. Klose, I. Helfrich, The impact of the immune system on tumor: Angiogenesis and vascular remodeling. *Front. Oncol.* **4 APR**, 69 (2014).

45. I. Romero, F. Garrido, A. M. Garcia-Lora, Metastases in immune-mediated dormancy: A new opportunity for targeting cancer. *Cancer Res.* **74**, 6750–6757 (2014).

46. I. Romero, *et al.*, T lymphocytes restrain spontaneous metastases in permanent dormancy. *Cancer Res.* **74**, 1958–1968 (2014).

47. D. Mittal, M. M. Gubin, R. D. Schreiber, M. J. Smyth, New insights into cancer immunoediting and its three component phases-elimination, equilibrium and escape. *Curr. Opin. Immunol.* **27**, 16–25 (2014).

48. D. H. Kaplan, *et al.*, Demonstration of an interferon γ-dependent tumor surveillance system in immunocompetent mice. *Proc. Natl. Acad. Sci. U. S. A.* **95**, 7556–7561 (1998).

49. L. H. Wong, *et al.*, Interferon-resistant human melanoma cells are deficient in ISGF3 components, STAT1, STAT2, and p48-ISGF3γ. *J. Biol. Chem.* **272**, 28779–28785 (1997).

50. E. Contardi, *et al.*, CTLA-4 is constitutively expressed on tumor cells and can trigger apoptosis upon ligand interaction. *Int. J. Cancer* **117**, 538–550 (2005).

51. K. Garber, First Results for Agents Targeting Cancer-Related Inflammation. *JNCI J. Natl.*

Cancer Inst. **101**, 1110–1112 (2009).

52. P. H. Pandya, M. E. Murray, K. E. Pollok, J. L. Renbarger, The Immune System in Cancer Pathogenesis: Potential Therapeutic Approaches. *J. Immunol. Res.* **2016** (2016).

53. V. Kumar, S. Patel, E. Tcyganov, D. I. Gabrilovich, The Nature of Myeloid-Derived Suppressor Cells in the Tumor Microenvironment. *Trends Immunol.* **37**, 208–220 (2016).

54. A. Mantovani, S. Sozzani, M. Locati, P. Allavena, A. Sica, Macrophage polarization: Tumor-associated macrophages as a paradigm for polarized M2 mononuclear phagocytes. *Trends Immunol.* **23**, 549–555 (2002).

55. R. F. Gabitass, N. E. Annels, D. D. Stocken, H. A. Pandha, G. W. Middleton, Elevated myeloid-derived suppressor cells in pancreatic, esophageal and gastric cancer are an independent prognostic factor and are associated with significant elevation of the Th2 cytokine interleukin-13 https:/doi.org/10.1007/s00262-011-1028-0.

56. , Correlation between frequencies of blood monocytic myeloid-derived suppressor cells, regulatory T cells and negative prognostic markers in patients with castration-resistant metastatic prostate cancer Manja Idorn · Tania Køllgaard · Per Kongsted · Lisa Sengeløv · Per thor Straten https:/doi.org/10.1007/s00262-014-1591-2.

57. X. Li, *et al.*, Neutrophil count is associated with myeloid derived suppressor cell level and presents prognostic value of for hepatocellular carcinoma patients. *Oncotarget* **8**, 24380–24388 (2017).

58. L. Cao, *et al.*, M2 macrophage infiltration into tumor islets leads to poor prognosis in non-small-cell lung cancer. *Cancer Manag. Res.* **11**, 6125–6138 (2019).

59. S. Edin, *et al.*, The Distribution of Macrophages with a M1 or M2 Phenotype in Relation to Prognosis and the Molecular Characteristics of Colorectal Cancer. *PLoS One* **7**, e47045 (2012).

60. Y. Komohara, *et al.*, Macrophage infiltration and its prognostic relevance in clear cell renal cell carcinoma. *Cancer Sci.* **102**, 1424–1431 (2011).

61. K. S. Peggs, S. A. Quezada, C. A. Chambers, A. J. Korman, J. P. Allison, Blockade of CTLA-4 on both effector and regulatory T cell compartments contributes to the antitumor activity of anti-CTLA-4 antibodies. *J. Exp. Med.* **206**, 1717–1725 (2009).

62. C. Wang, *et al.*, In vitro characterization of the anti-PD-1 antibody nivolumab, BMS-936558, and in vivo toxicology in non-human primates. *Cancer Immunol. Res.* **2**, 846–856 (2014).

63. A. M. M. Eggermont, *et al.*, Adjuvant ipilimumab versus placebo after complete resection of high-risk stage III melanoma (EORTC 18071): A randomised, double-blind, phase 3 trial. *Lancet Oncol.* **16**, 522–530 (2015).

64. J. S. Weber, *et al.*, Nivolumab versus chemotherapy in patients with advanced melanoma who progressed after anti-CTLA-4 treatment (CheckMate 037): A randomised, controlled, open-label, phase 3 trial. *Lancet Oncol.* **16**, 375–384 (2015).

65. D. McDermott, J. Haanen, T. T. Chen, P. Lorigan, S. O'Day, Efficacy and safety of ipilimumab in metastatic melanoma patients surviving more than 2 years following treatment in a phase III trial (MDX010-20). *Ann. Oncol.* **24**, 2694–2698 (2013).

66. C. J. Langer, *et al.*, Carboplatin and pemetrexed with or without pembrolizumab for advanced, non-squamous non-small-cell lung cancer: a randomised, phase 2 cohort of the open-label KEYNOTE-021 study. *Lancet Oncol.* **17**, 1497–1508 (2016).

67. L. Horn, *et al.*, Nivolumab versus docetaxel in previously treated patients with advanced non-small-cell lung cancer: Two-year outcomes from two randomized, open-label, phase III Trials (CheckMate 017 and CheckMate 057). *J. Clin. Oncol.* **35**, 3924–3933 (2017).

68. D. T. Le, *et al.*, KEYNOTE-164: Pembrolizumab for patients with advanced microsatellite instability high (MSI-H) colorectal cancer. *J. Clin. Oncol.* **36**, 3514–3514 (2018).

69. M. J. Overman, *et al.*, Nivolumab in patients with metastatic DNA mismatch repair-deficient or microsatellite instability-high colorectal cancer (CheckMate 142): an open-label, multicentre, phase 2 study. *Lancet Oncol.* **18**, 1182–1191 (2017).

70. B. Escudier, *et al.*, CheckMate 025 Randomized Phase 3 Study: Outcomes by Key Baseline Factors and Prior Therapy for Nivolumab Versus Everolimus in Advanced Renal Cell Carcinoma [Figure presented]. *Eur. Urol.* **72**, 962–971 (2017).

71. F. S. Hodi, *et al.*, Overall survival in patients with advanced melanoma (MEL) who discontinued treatment with nivolumab (NIVO) plus ipilimumab (IPI) due to toxicity in a phase II trial (CheckMate 069). *J. Clin. Oncol.* **34**, 9518–9518 (2016).

72. J. Schachter, *et al.*, Pembrolizumab versus ipilimumab for advanced melanoma: final overall survival results of a multicentre, randomised, open-label phase 3 study (KEYNOTE-

006). *Lancet* **390**, 1853–1862 (2017).

73. M. Reck, *et al.*, Updated analysis of KEYNOTE-024: Pembrolizumab versus platinum-based chemotherapy for advanced non–small-cell lung cancer with PD-L1 tumor proportion score of 50% or greater. *J. Clin. Oncol.* **37**, 537–546 (2019).

74. R. S. Herbst, *et al.*, Pembrolizumab versus docetaxel for previously treated, PD-L1-positive, advanced non-small-cell lung cancer (KEYNOTE-010): A randomised controlled trial. *Lancet* **387**, 1540–1550 (2016).

75. I. Lugowska, P. Teterycz, P. Rutkowski, Immunotherapy of melanoma. *Wspolczesna Onkol.* **2**, 61–67 (2017).

76. R. P. Perez, *et al.*, Epacadostat plus nivolumab in patients with advanced solid tumors: Preliminary phase I/II results of ECHO-204. *J. Clin. Oncol.* **35**, 3003–3003 (2017).

77. R. Weber, *et al.*, Myeloid-derived suppressor cells hinder the anti-cancer activity of immune checkpoint inhibitors. *Front. Immunol.* **9**, 1 (2018).

78. K. H. Toomer, Z. Chen, Autoimmunity as a double agent in tumor killing and cancer promotion. *Front. Immunol.* **5**, 116 (2014).

79. Z. Hu, *et al.*, Investigation of HIFU-induced anti-tumor immunity in a murine tumor model. *J. Transl. Med.* **5**, 34 (2007).

80. Y. Xing, X. Lu, E. C. Pua, P. Zhong, The effect of high intensity focused ultrasound treatment on metastases in a murine melanoma model. *Biochem. Biophys. Res. Commun.* **375**, 645–650 (2008).

81. S. Chida, K. Okada, N. Suzuki, C. Komori, Y. Shimada, Infiltration by macrophages and lymphocytes in transplantable mouse sarcoma after irradiation with high-intensity focused ultrasound. *Anticancer Res.* **29**, 3877–3882 (2009).

82. X. Huang, *et al.*, M-HIFU inhibits tumor growth, suppresses STAT3 activity and enhances tumor specific immunity in a transplant tumor model of prostate cancer. *PLoS One* **7** (2012).

83. F. Liu, *et al.*, Boosting high-intensity focused ultrasound-induced anti-tumor immunity using a sparse-scan strategy that can more effectively promote dendritic cell maturation. *J. Transl. Med.* **8**, 7 (2010).

84. J. Z. Xia, *et al.*, High-Intensity Focused Ultrasound Tumor Ablation Activates Autologous

Tumor-Specific Cytotoxic T Lymphocytes. *Ultrasound Med. Biol.* **38**, 1363–1371 (2012).

85. M. T. Silvestrini, *et al.*, Priming is key to effective incorporation of image-guided thermal ablation into immunotherapy protocols. *JCI insight* **2**, e90521 (2017).

86. S. Bandyopadhyay, *et al.*, Low-Intensity Focused Ultrasound Induces Reversal of Tumor-Induced T Cell Tolerance and Prevents Immune Escape. *J. Immunol.* **196**, 1964–1976 (2016).

87. D. F. Rosberger, *et al.*, Immunomodulation in choroidal melanoma: Reversal of inverted CD4/CD8 ratios following treatment with ultrasonic hyperthermia. *Biotechnol. Ther.* **5**, 59–68 (1994).

88. X. Wang, J. Sun, High-intensity focused ultrasound in patients with late-stage pancreatic carcinoma. *Chin. Med. J. (Engl).* **115**, 1332–1335 (2002).

89. F. Wu, *et al.*, Changes in biologic characteristics of breast cancer treated with high-intensity focused ultrasound. *Ultrasound Med. Biol.* **29**, 1487–1492 (2003).

90. G. Kramer, *et al.*, Response to sublethal heat treatment of prostatic tumor cells and of prostatic tumor infiltrating T-cells. *Prostate* **58**, 109–120 (2004).

91. F. Wu, *et al.*, Activated anti-tumor immunity in cancer patients after high intensity focused ultrasound ablation. *Ultrasound Med. Biol.* **30**, 1217–1222 (2004).

92. Q. Zhou, *et al.*, Changes in Circulating Immunosuppressive Cytokine Levels of Cancer Patients After High Intensity Focused Ultrasound Treatment. *Ultrasound Med. Biol.* **34**, 81–87 (2008).

93. F. Wu, *et al.*, Expression of tumor antigens and heat-shock protein 70 in breast cancer cells after high-intensity focused ultrasound ablation. *Ann. Surg. Oncol.* **14**, 1237–1242 (2007).

94. P. Lu, *et al.*, Increased infiltration of activated tumor-infiltrating lymphocytes after high intensity focused ultrasound ablation of human breast cancer. *Surgery* **145**, 286–293 (2009).

95. X. Wang, *et al.*, The effect of high-intensity focused ultrasound treatment on immune function in patients with uterine fibroids. *Int. J. Hyperth.* **29**, 225–233 (2013).

96. Z. Hu, *et al.*, Release of endogenous danger signals from HIFU-treated tumor cells and their stimulatory effects on APCs. *Biochem. Biophys. Res. Commun.* **335**, 124–131 (2005).

97. D. E. Kruse, M. A. Mackanos, C. E. O'Connell-Rodwell, C. H. Contag, K. W. Ferrara, Short-duration-focused ultrasound stimulation of Hsp70 expression in vivo. *Phys. Med. Biol.* **53**, 3641—3660 (2008).

98. Z. Hu, *et al.*, Release of endogenous danger signals from HIFU-treated tumor cells and their stimulatory effects on APCs. *Biochem. Biophys. Res. Commun.* **335**, 124–131 (2005).

99. Y. Zhang, J. Deng, J. Feng, F. Wu, Enhancement of antitumor vaccine in ablated hepatocellular carcinoma by high-intensity focused ultrasound. *World J. Gastroenterol.* **16**, 3584–3591 (2010).

100. J. Deng, Y. Zhang, J. Feng, F. Wu, Dendritic Cells Loaded with Ultrasound-Ablated Tumour Induce in vivo Specific Antitumour Immune Responses. *Ultrasound Med. Biol.* **36**, 441–448 (2010).

101. A. Eranki, *et al.*, High-intensity focused ultrasound (hIFU) triggers immune sensitization of refractory murine neuroblastoma to checkpoint inhibitor therapy. *Clin. Cancer Res.* **26**, 1152–1161 (2020).

102. W. M. Pardridge, The blood-brain barrier: bottleneck in brain drug development. *NeuroRx* **2**, 3–14 (2005).

103. J. J. Choi, M. Pernot, S. A. Small, E. E. Konofagou, Noninvasive, transcranial and localized opening of the blood-brain barrier using focused ultrasound in mice. *Ultrasound Med. Biol.* **33**, 95–104 (2007).

104. K. Hynynen, N. McDannold, N. A. Sheikov, F. A. Jolesz, N. Vykhodtseva, Local and reversible blood-brain barrier disruption by noninvasive focused ultrasound at frequencies suitable for trans-skull sonications. *Neuroimage* **24**, 12–20 (2005).

105. K. Hynynen, N. McDannold, N. Vykhodtseva, F. A. Jolesz, Noninvasive MR Imaging–guided Focal Opening of the Blood-Brain Barrier in Rabbits. *Radiology* **220**, 640–646 (2001).

106. M. Kinoshita, N. McDannold, F. A. Jolesz, K. Hynynen, Noninvasive localized delivery of Herceptin to the mouse brain by MRI-guided focused ultrasound-induced blood-brain barrier disruption. *Proc. Natl. Acad. Sci. U. S. A.* **103**, 11719–11723 (2006).

107. E. J. Park, Y. Z. Zhang, N. Vykhodtseva, N. McDannold, Ultrasound-mediated blood-brain/blood-tumor barrier disruption improves outcomes with trastuzumab in a breast

cancer brain metastasis model. *J. Control. Release* **163**, 277–284 (2012).

108. P. W. Janowicz, G. Leinenga, J. Götz, R. M. Nisbet, Ultrasound-mediated blood-brain barrier opening enhances delivery of therapeutically relevant formats of a tau-specific antibody. *Sci. Rep.* **9**, 1–9 (2019).

109. N. McDannold, *et al.*, Acoustic feedback enables safe and reliable carboplatin delivery across the blood-brain barrier with a clinical focused ultrasound system and improves survival in a rat glioma model. *Theranostics* **9**, 6284–6299 (2019).

110. M. Aryal, N. Vykhodtseva, Y. Z. Zhang, J. Park, N. McDannold, Multiple treatments with liposomal doxorubicin and ultrasound-induced disruption of blood-tumor and blood-brain barriers improve outcomes in a rat glioma model. *J. Control. Release* **169**, 103–111 (2013).

111. H. L. Liu, *et al.*, Blood-brain barrier disruption with focused ultrasound enhances delivery of chemotherapeutic drugs for glioblastoma treatment. *Radiology* **255**, 415–425 (2010).

112. W.-B. Shen, *et al.*, Magnetic Enhancement of Stem Cell–Targeted Delivery into the Brain Following MR-Guided Focused Ultrasound for Opening the Blood–Brain Barrier. *Cell Transplant.* **26**, 1235–1246 (2017).

113. A. Burgess, *et al.*, Targeted Delivery of Neural Stem Cells to the Brain Using MRI-Guided Focused Ultrasound to Disrupt the Blood-Brain Barrier. *PLoS One* **6** (2011).

114. M. A. Stavarache, *et al.*, Safe and stable noninvasive focal gene delivery to the mammalian brain following focused ultrasound. *J. Neurosurg.* **130**, 989–998 (2019).

115. B. P. Mead, *et al.*, Novel Focused Ultrasound Gene Therapy Approach Noninvasively Restores Dopaminergic Neuron Function in a Rat Parkinson's Disease Model. *Nano Lett.* **17**, 3533–3542 (2017).

116. C. Y. C. J. Lin, *et al.*, Microbubble-facilitated ultrasound pulsation promotes direct α-synuclein gene delivery. *Biochem. Biophys. Res. Commun.* **517**, 77–83 (2019).

117. J. J. Choi, *et al.*, Noninvasive and localized blood-brain barrier disruption using focused ultrasound can be achieved at short pulse lengths and low pulse repetition frequencies. *J. Cereb. Blood Flow Metab.* **31**, 725–737 (2011).

118. N. McDannold, N. Vykhodtseva, S. Raymond, F. A. Jolesz, K. Hynynen, MRI-guided targeted blood-brain barrier disruption with focused ultrasound: Histological findings in

rabbits. *Ultrasound Med. Biol.* **31**, 1527–1537 (2005).

119. Z. I. Kovacs, *et al.*, Disrupting the blood–brain barrier by focused ultrasound induces sterile inflammation. *Proc. Natl. Acad. Sci.* **114**, E75–E84 (2017).

120. J. Silburt, N. Lipsman, I. Aubert, Disrupting the blood–brain barrier with focused ultrasound: Perspectives on inflammation and regeneration. *Proc. Natl. Acad. Sci. U. S. A.* **114**, E6735–E6736 (2017).

121. Z. I. Kovacs, S. R. Burks, J. A. Frank, Reply to Silburt et al.: Concerning sterile inflammation following focused ultrasound and microbubbles in the brain. *Proc. Natl. Acad. Sci. U. S. A.* **114**, E6737–E6738 (2017).

122. D. McMahon, K. Hynynen, Reply to Kovacs et al.: Concerning acute inflammatory response following focused ultrasound and microbubbles in the brain. *Theranostics* **8**, 2249–2250 (2018).

123. Z. I. Kovacs, S. R. Burks, J. A. Frank, Focused ultrasound with microbubbles induces sterile inflammatory response proportional to the blood brain barrier opening: Attention to experimental conditions. *Theranostics* **8**, 2245–2248 (2018).

124. P. S. Tofts, B. Berkowitz, M. D. Schnall, Quantitative Analysis of Dynamic Gd-DTPA Enhancement in Breast Tumors Using a Permeability Model. *Magn. Reson. Med.* **33**, 564–568 (1995).

125. C. Bing, *et al.*, Characterization of different bubble formulations for blood-brain barrier opening using a focused ultrasound system with acoustic feedback control. *Sci. Rep.* **8**, 1–12 (2018).

126. M. A. O'Reilly, K. Hynynen, Blood-brain barrier: Real-time feedback-controlled focused ultrasound disruption by using an acoustic emissions-based controller. *Radiology* **263**, 96–106 (2012).

127. M. Aryal, J. Park, N. Vykhodtseva, Y. Z. Zhang, N. McDannold, Enhancement in blood-tumor barrier permeability and delivery of liposomal doxorubicin using focused ultrasound and microbubbles: Evaluation during tumor progression in a rat glioma model. *Phys. Med. Biol.* **60**, 2511–2527 (2015).

128. M. Aryal, N. Vykhodtseva, Y. Z. Zhang, J. Park, N. McDannold, Multiple treatments with liposomal doxorubicin and ultrasound-induced disruption of blood-tumor and blood-brain

barriers improve outcomes in a rat glioma model. *J. Control. Release* **169**, 103–111 (2013).

129. L. H. Treat, N. McDannold, Y. Zhang, N. Vykhodtseva, K. Hynynen, Improved Anti-Tumor Effect of Liposomal Doxorubicin After Targeted Blood-Brain Barrier Disruption by MRI-Guided Focused Ultrasound in Rat Glioma. *Ultrasound Med. Biol.* **38**, 1716–1725 (2012).

130. A. Dréan, *et al.*, Temporary blood–brain barrier disruption by low intensity pulsed ultrasound increases carboplatin delivery and efficacy in preclinical models of glioblastoma. *J. Neurooncol.* **144**, 33–41 (2019).

131. N. McDannold, *et al.*, Acoustic feedback enables safe and reliable carboplatin delivery across the blood-brain barrier with a clinical focused ultrasound system and improves survival in a rat glioma model. *Theranostics* **9**, 6284–6299 (2019).

132. N. D. Sheybani, *et al.*, ImmunoPET-informed sequence for focused ultrasound-targeted mCD47 blockade controls glioma. *J. Control. Release* **331**, 19–29 (2021).

133. J. F. Jordão, *et al.*, Antibodies Targeted to the Brain with Image-Guided Focused Ultrasound Reduces Amyloid-β Plaque Load in the TgCRND8 Mouse Model of Alzheimer's Disease. *PLoS One* **5**, e10549 (2010).

134. S. Dubey, *et al.*, Clinically approved IVIg delivered to the hippocampus with focused ultrasound promotes neurogenesis in a model of Alzheimer's disease. *Proc. Natl. Acad. Sci. U. S. A.* **117**, 32691–32700 (2020).

135. B. P. Mead, *et al.*, Novel Focused Ultrasound Gene Therapy Approach Noninvasively Restores Dopaminergic Neuron Function in a Rat Parkinson's Disease Model. *Nano Lett.* **17**, 3533–3542 (2017).

136. C. Y. Lin, *et al.*, Non-invasive, neuron-specific gene therapy by focused ultrasound-induced blood-brain barrier opening in Parkinson's disease mouse model. *J. Control. Release* **235**, 72–81 (2016).

137. C. T. Curley, *et al.*, Immunomodulation of intracranial melanoma in response to blood-tumor barrier opening with focused ultrasound. *Theranostics* **10**, 8821–8833 (2020).

138. N. D. Sheybani, *et al.*, Combination of thermally ablative focused ultrasound with gemcitabine controls breast cancer via adaptive immunity. *J. Immunother. Cancer* **8** (2020).

139. J. Deng, Y. Zhang, J. Feng, F. Wu, Dendritic Cells Loaded with Ultrasound-Ablated Tumour Induce in vivo Specific Antitumour Immune Responses. *Ultrasound Med. Biol.* **36**, 441–448 (2010).

140. Z. L. Xu, *et al.*, Activation of Tumor-Infiltrating Antigen Presenting Cells by High Intensity Focused Ultrasound Ablation of Human Breast Cancer. *Ultrasound Med. Biol.* **35**, 50–57 (2009).

141. J. M. Lee, A. Bernstein, p53 Mutations increase resistance to ionizing radiation. *Proc. Natl. Acad. Sci. U. S. A.* **90**, 5742–5746 (1993).

142. Z. Ronai, *et al.*, ATF2 confers radiation resistance to human melanoma cells. *Oncogene* **16**, 523–531 (1998).

143. Z. H. Siddik, Cisplatin: Mode of cytotoxic action and molecular basis of resistance. *Oncogene* **22**, 7265–7279 (2003).

144. M. Garcia-Barros, *et al.*, Tumor response to radiotherapy regulated by endothelial cell apoptosis. *Science (80-.).* **300**, 1155–1159 (2003).

145. K. Ueda, C. Cardarelli, M. M. Gottesman, T. Pastan, Expression of a full-length cDNA for the human “MDR1” gene confers resistance to colchicine, doxorubicin, and vinblastine. *Proc. Natl. Acad. Sci. U. S. A.* **84**, 3004–3008 (1987).

146. J. M. Zaretsky, *et al.*, Mutations associated with acquired resistance to PD-1 blockade in melanoma. *N. Engl. J. Med.* **375**, 819–829 (2016).

147. N. P. Restifo, *et al.*, Loss of Functional Beta 2 -Microglobulin in Metastatic Melanomas From Five Patients Receiving Immunotherapy . *JNCI J. Natl. Cancer Inst.* **88**, 100–108 (1996).

148. J. Deng, *et al.*, The role of caveolin-1 in blood-brain barrier disruption induced by focused ultrasound combined with microbubbles. *J. Mol. Neurosci.* **46**, 677–687 (2012).

149. R. Pandit, *et al.*, Role for caveolin-mediated transcytosis in facilitating transport of large cargoes into the brain via ultrasound. *J. Control. Release* **327**, 667–675 (2020).

150. C. M. Gorick, *et al.*, Sonoselective transfection of cerebral vasculature without blood–brain barrier disruption. *Proc. Natl. Acad. Sci.* **117**, 5644–5654 (2020).

151. D. McMahon, K. Hynynen, Acute inflammatory response following increased blood-brain

barrier permeability induced by focused ultrasound is dependent on microbubble dose. *Theranostics* **7**, 3989–4000 (2017).

152. D. Mcmahon, R. Bendayan, K. Hynynen, Acute effects of focused ultrasound-induced increases in blood-brain barrier permeability on rat microvascular transcriptome. *Sci. Rep.* **7**, 1–15 (2017).

153. Y. K. Kim, K. S. Na, A. M. Myint, B. E. Leonard, The role of pro-inflammatory cytokines in neuroinflammation, neurogenesis and the neuroendocrine system in major depression. *Prog. Neuro-Psychopharmacology Biol. Psychiatry* **64**, 277–284 (2016).

154. G. Leinenga, J. Götz, Scanning ultrasound removes amyloid-b and restores memory in an Alzheimer's disease mouse model. *Sci. Transl. Med.* **7**, 278ra33-278ra33 (2015).

155. T. Scarcelli, *et al.*, Stimulation of hippocampal neurogenesis by transcranial focused ultrasound and microbubbles in adult mice. *Brain Stimul.* **7**, 304–307 (2014).

156. S. J. Mooney, *et al.*, Focused ultrasound-induced neurogenesis requires an increase in blood-brain barrier permeability. *PLoS One* **11** (2016).

157. B. A. Kohler, *et al.*, Annual report to the nation on the status of cancer, 1975-2011, featuring incidence of breast cancer subtypes by race/ethnicity, poverty, and state. *J. Natl. Cancer Inst.* **107** (2015).

158. A. Sandru, S. Voinea, E. Panaitescu, A. Blidaru, Survival rates of patients with metastatic malignant melanoma. *J. Med. Life* **7**, 572–576 (2014).

159. H. Sadozai, T. Gruber, R. E. Hunger, M. Schenk, Recent successes and future directions in immunotherapy of cutaneous melanoma. *Front. Immunol.* **8**, 1 (2017).

160. O. Hamid, *et al.*, Safety and Tumor Responses with Lambrolizumab (Anti–PD-1) in Melanoma. *N. Engl. J. Med.* **369**, 134–144 (2013).

161. M. A. Curran, W. Montalvo, H. Yagita, J. P. Allison, PD-1 and CTLA-4 combination blockade expands infiltrating T cells and reduces regulatory T and myeloid cells within B16 melanoma tumors. *Proc. Natl. Acad. Sci. U. S. A.* **107**, 4275–4280 (2010).

162. M. Khunger, *et al.*, Programmed Cell Death 1 (PD-1) Ligand (PD-L1) Expression in Solid Tumors As a Predictive Biomarker of Benefit From PD-1/PD-L1 Axis Inhibitors: A Systematic Review and Meta-Analysis. *JCO Precis. Oncol.*, 1–15 (2017).

163. P. C. Tumeh, *et al.*, PD-1 blockade induces responses by inhibiting adaptive immune resistance. *Nature* **515**, 568–571 (2014).

164. A. Snyder, *et al.*, Genetic Basis for Clinical Response to CTLA-4 Blockade in Melanoma. *N. Engl. J. Med.* **371**, 2189–2199 (2014).

165. S. Valpione, *et al.*, Personalised medicine: Development and external validation of a prognostic model for metastatic melanoma patients treated with ipilimumab. *Eur. J. Cancer* **51**, 2086–2094 (2015).

166. P. C. Rodriguez, *et al.*, Arginase I production in the tumor microenvironment by mature myeloid cells inhibits T-cell receptor expression and antigen-specific T-cell responses. *Cancer Res.* **64**, 5839–5849 (2004).

167. D. Massi, *et al.*, Baseline β-catenin, programmed death-ligand 1 expression and tumour-infiltrating lymphocytes predict response and poor prognosis in BRAF inhibitor-treated melanoma patients. *Eur. J. Cancer* **78**, 70–81 (2017).

168. B. Chen, M. S. Khodadoust, C. L. Liu, A. M. Newman, A. A. Alizadeh, “Profiling tumor infiltrating immune cells with CIBERSORT” in *Methods in Molecular Biology*, (Humana Press Inc., 2018), pp. 243–259.

169. R. C. Coll, *et al.*, A small-molecule inhibitor of the NLRP3 inflammasome for the treatment of inflammatory diseases. *Nat. Med.* **21**, 248–257 (2015).

170. E. Krüger, U. Kuckelkorn, A. Sijts, P. M. Kloetzel, The components of the proteasome system and their role in MHC class I antigen processing. *Rev. Physiol. Biochem. Pharmacol.* **148**, 81–104 (2003).

171. K. L. Singel, B. H. Segal, Neutrophils in the tumor microenvironment: trying to heal the wound that cannot heal. *Immunol. Rev.* **273**, 329–343 (2016).

172. S. Taniguchi, *et al.*, Tumor-initiating cells establish an IL-33–TGF-b niche signaling loop to promote cancer progression. *Science (80-.).* **369** (2020).

173. Y. Zhang, *et al.*, IL-33 promotes growth and liver metastasis of colorectal cancer in mice by remodeling the tumor microenvironment and inducing angiogenesis. *Mol. Carcinog.* **56**, 272–287 (2017).

174. M. H. Wasmer, P. Krebs, The role of IL-33-dependent inflammation in the tumor

microenvironment. *Front. Immunol.* **7**, 1 (2017).

175. M. S. Tsai, W. C. Chen, C. H. Lu, M. F. Chen, The prognosis of head and neck squamous cell carcinoma related to immunosuppressive tumor microenvironment regulated by IL-6 signaling. *Oral Oncol.* **91**, 47–55 (2019).

176. S. Hegde, J. Pahne, S. Smola-Hess, Novel immunosuppressive properties of interleukin-6 in dendritic cells: inhibition of NF-κB binding activity and CCR7 expression. *FASEB J.* **18**, 1439–1441 (2004).

177. B. Z. Fite, *et al.*, Immune modulation resulting from MR-guided high intensity focused ultrasound in a model of murine breast cancer. *Sci. Rep.* **11**, 927 (2021).

178. K. M. Fong, Y. Kida, P. V Zimmerman, P. J. Smith, TIMP1 and adverse prognosis in non-small cell lung cancer. *Clin. Cancer Res.* **2** (1996).

179. Y. Gong, *et al.*, TIMP-1 Promotes Accumulation of Cancer Associated Fibroblasts and Cancer Progression. *PLoS One* **8**, 77366 (2013).

180. S. Ylisirniö, M. Höyhtyä, T. Turpeenniemi-Hujanen, Serum matrix metalloproteinases -2, -9 and tissue inhibitors of metalloproteinases -1, -2 in lung cancer - TIMP-1 as a prognostic marker. *Anticancer Res.* **20**, 1311–1316 (2000).

181. F. Garrido, N. Aptsiauri, E. M. Doorduijn, A. M. Garcia Lora, T. van Hall, The urgent need to recover MHC class I in cancers for effective immunotherapy. *Curr. Opin. Immunol.* **39**, 44–51 (2016).

182. A. M. Cornel, I. L. Mimpen, S. Nierkens, MHC class I downregulation in cancer: Underlying mechanisms and potential targets for cancer immunotherapy. *Cancers (Basel).* **12**, 1–33 (2020).

183. N. F. S. Watson, *et al.*, Immunosurveillance is active in colorectal cancer as downregulation but not complete loss of MHC class I expression correlates with a poor prognosis. *Int. J. Cancer* **118**, 6–10 (2006).

184. D. C. Strachan, *et al.*, CSF1R inhibition delays cervical and mammary tumor growth in murine models by attenuating the turnover of tumor-associated macrophages and enhancing infiltration by CD8+ T cells. *Oncoimmunology* **2** (2013).

185. Y. Zhu, *et al.*, CSF1/CSF1R blockade reprograms tumor-infiltrating macrophages and

improves response to T-cell checkpoint immunotherapy in pancreatic cancer models. *Cancer Res.* **74**, 5057–5069 (2014).

186. M. A. Cannarile, *et al.*, Colony-stimulating factor 1 receptor (CSF1R) inhibitors in cancer therapy. *J. Immunother. Cancer* **5**, 1–13 (2017).

187. K. S. Peggs, S. A. Quezada, C. A. Chambers, A. J. Korman, J. P. Allison, Blockade of CTLA-4 on both effector and regulatory T cell compartments contributes to the antitumor activity of anti-CTLA-4 antibodies. *J. Exp. Med.* **206**, 1717–1725 (2009).

188. V. Kumar, *et al.*, Cancer-Associated Fibroblasts Neutralize the Anti-tumor Effect of CSF1 Receptor Blockade by Inducing PMN-MDSC Infiltration of Tumors. *Cancer Cell* **32**, 654-668.e5 (2017).

189. E. Ahern, *et al.*, Co-administration of RANKL and CTLA4 Antibodies Enhances Lymphocyte-Mediated Antitumor Immunity in Mice. *Clin Cancer Res* **23**.

190. Y. G. Liu, *et al.*, NLRP3 inflammasome activation mediates radiation-induced pyroptosis in bone marrow-derived macrophages. *Cell Death Dis.* **8**, e2579–e2579 (2017).

191. S. Son, D. W. Shim, I. Hwang, J. H. Park, J. W. Yu, Chemotherapeutic agent paclitaxel mediates priming of NLRP3 inflammasome activation. *Front. Immunol.* **10**, 1108 (2019).

192. Q. Lian, *et al.*, Chemotherapy-induced intestinal inflammatory responses are mediated by exosome secretion of double-strand DNA via AIM2 inflammasome activation. *Cell Res.* **27**, 784–800 (2017).

193. M. Bruchard, *et al.*, Chemotherapy-triggered cathepsin B release in myeloid-derived suppressor cells activates the Nlrp3 inflammasome and promotes tumor growth. *Nat. Med.* **19**, 57–64 (2013).

194. Y. Huang, *et al.*, Myeloid PTEN promotes chemotherapy-induced NLRP3-inflammasome activation and antitumour immunity https:/doi.org/10.1038/s41556-020-0510-3 (May 7, 2021).

195. C. Tulotta, *et al.*, Endogenous production of IL1B by breast cancer cells drives metastasis and colonization of the bone microenvironment. *Clin. Cancer Res.* **25**, 2769–2782 (2019).

196. S. Mitsunaga, *et al.*, Serum levels of IL-6 and IL-1β can predict the efficacy of gemcitabine in patients with advanced pancreatic cancer. *Br. J. Cancer* **108**, 2063–2069 (2013).

197. L. Chen, *et al.*, Blockage of the NLRP3 inflammasome by MCC950 improves anti-tumor immune responses in head and neck squamous cell carcinoma. *Cell. Mol. Life Sci.* **75**, 2045–2058 (2018).

198. L. Nie, G. Wu, W. Zhang, Correlation between mRNA and protein abundance in Desulfovibrio vulgaris: A multiple regression to identify sources of variations. *Biochem. Biophys. Res. Commun.* **339**, 603–610 (2006).

199. S. P. Gygi, Y. Rochon, B. R. Franza, R. Aebersold, Correlation between Protein and mRNA Abundance in Yeast. *Mol. Cell. Biol.* **19**, 1720–1730 (1999).

200. G. Chen, *et al.*, Discordant protein and mRNA expression in lung adenocarcinomas. *Mol. Cell. Proteomics* **1**, 304–313 (2002).

201. T. Maier, M. Güell, L. Serrano, Correlation of mRNA and protein in complex biological samples. *FEBS Lett.* **583**, 3966–3973 (2009).

202. R. Patro, G. Duggal, M. I. Love, R. A. Irizarry, C. Kingsford, Salmon provides fast and bias-aware quantification of transcript expression. *Nat. Methods* **14**, 417–419 (2017).

203. C. Soneson, M. I. Love, M. D. Robinson, Differential analyses for RNA-seq: Transcript-level estimates improve gene-level inferences [version 2; referees: 2 approved]. *F1000Research* **4** (2016).

204. M. I. Love, W. Huber, S. Anders, Moderated estimation of fold change and dispersion for RNA-seq data with DESeq2. *Genome Biol.* **15**, 1–21 (2014).

205. The Gene Ontology Consortium, The Gene Ontology Resource: 20 years and still GOing strong. *Nucleic Acids Res.* **47**, D330–D338 (2018).

206. M. Ashburner, *et al.*, Gene ontology: Tool for the unification of biology. *Nat. Genet.* **25**, 25–29 (2000).

207. A. Fabregat, *et al.*, The Reactome Pathway Knowledgebase. *Nucleic Acids Res.* **46**, D649–D655 (2018).

208. A. Liberzon, *et al.*, Molecular signatures database (MSigDB) 3.0. *Bioinformatics* **27**, 1739–1740 (2011).

209. A. A. Sergushichev, An algorithm for fast preranked gene set enrichment analysis using cumulative statistic calculation. *bioRxiv*, 060012 (2016).

210. G. P. Dunn, A. T. Bruce, H. Ikeda, L. J. Old, R. D. Schreiber, Cancer immunoediting: From immunosurveillance to tumor escape. *Nat. Immunol.* **3**, 991–998 (2002).

211. B. Seliger, Strategies of tumor immune evasion. *BioDrugs* **19**, 347–354 (2005).

212. C. G. Drake, E. Jaffee, D. M. Pardoll, Mechanisms of Immune Evasion by Tumors. *Adv. Immunol.* **90**, 51–81 (2006).

213. H. Sumimoto, F. Imabayashi, T. Iwata, Y. Kawakami, The BRAF-MAPK signaling pathway is essential for cancer-immune evasion in human melanoma cells. *J. Exp. Med.* **203**, 1651–1656 (2006).

214. A. Esteva, *et al.*, Dermatologist-level classification of skin cancer with deep neural networks. *Nature* **542**, 115–118 (2017).

215. T. Vos, *et al.*, Global, regional, and national incidence, prevalence, and years lived with disability for 328 diseases and injuries for 195 countries, 1990-2016: A systematic analysis for the Global Burden of Disease Study 2016. *Lancet* **390**, 1211–1259 (2017).

216. O. Hamid, *et al.*, Safety and tumor responses with lambrolizumab (anti-PD-1) in melanoma. *N. Engl. J. Med.* **369**, 134–144 (2013).

217. M. A. Curran, W. Montalvo, H. Yagita, J. P. Allison, PD-1 and CTLA-4 combination blockade expands infiltrating T cells and reduces regulatory T and myeloid cells within B16 melanoma tumors. *Proc. Natl. Acad. Sci. U. S. A.* **107**, 4275–4280 (2010).

218. S. L. Topalian, *et al.*, Safety, activity, and immune correlates of anti-PD-1 antibody in cancer. *N. Engl. J. Med.* **366**, 2443–2454 (2012).

219. J. J. Luke, P. A. Ott, PD-1 pathway inhibitors: The next generation of immunotherapy for advanced melanoma. *Oncotarget* **6**, 3479–3492 (2015).

220. F. Stephen Hodi, *et al.*, Improved Survival with Ipilimumab in Patients with Metastatic Melanoma A bs tr ac t. *n engl j med* **8**, 711–734 (2010).

221. J. Larkin, *et al.*, Combined Nivolumab and Ipilimumab or Monotherapy in Untreated Melanoma. *N. Engl. J. Med.* **373**, 23–34 (2015).

222. J. D. Wolchok, *et al.*, Nivolumab plus Ipilimumab in Advanced Melanoma. *N Engl J Med* **369**, 122–155 (2013).

223. P. A. Ott, *et al.*, Pembrolizumab (MK-3475) in patients (pts) with extensive-stage small cell

lung cancer (SCLC): Preliminary safety and efficacy results from KEYNOTE-028. *J. Clin. Oncol.* **33**, 7502–7502 (2015).

224. R. Cirincione, *et al.*, High-Intensity Focused Ultrasound– and Radiation Therapy–Induced Immuno-Modulation: Comparison and Potential Opportunities. *Ultrasound Med. Biol.* **43**, 398–411 (2017).

225. T. Savage, S. Pandey, C. Guha, Postablation modulation after single high-dose radiation therapy improves tumor control via enhanced immunomodulation. *Clin. Cancer Res.* **26**, 910–921 (2020).

226. S. Kanagavelu, *et al.*, In vivo effects of lattice radiation therapy on local and distant lung cancer: Potential role of immunomodulation. *Radiat. Res.* **182**, 149–162 (2014).

227. J. Zhu, *et al.*, Enhanced antitumor efficacy through microwave ablation in combination with immune checkpoints blockade in breast cancer: A pre-clinical study in a murine model. *Diagn. Interv. Imaging* **99**, 135–142 (2018).

228. H. Zhang, X. Hou, H. Cai, X. Zhuang, Effects of microwave ablation on T-cell subsets and cytokines of patients with hepatocellular carcinoma. *Minim. Invasive Ther. Allied Technol.* **26**, 207–211 (2017).

229. L. Li, *et al.*, Microwave ablation combined with OK-432 induces Th1-type response and specific antitumor immunity in a murine model of breast cancer. *J. Transl. Med.* **15**, 23 (2017).

230. E. Reginato, Immune response after photodynamic therapy increases anti-cancer and anti-bacterial effects. *World J. Immunol.* **4**, 1 (2014).

231. H. S. Hwang, H. Shin, J. Han, K. Na, Combination of photodynamic therapy (PDT) and anti-tumor immunity in cancer therapy. *J. Pharm. Investig.* **48**, 143–151 (2018).

232. M. Korbelik, Induction of tumor immunity by photodynamic therapy. *J. Clin. Laser Med. Surg.* **14**, 329–334 (1996).

233. T. G. St. Denis, *et al.*, Combination approaches to potentiate immune response after photodynamic therapy for cancer. *Photochem. Photobiol. Sci.* **10**, 792–801 (2011).

234. T. Kato, *et al.*, Characterization of the cryoablation-induced immune response in kidney cancer patients. *Oncoimmunology* **6** (2017).

235. M. S. Sabel, *et al.*, Immunologic response to cryoablation of breast cancer. *Breast Cancer Res. Treat.* **90**, 97–104 (2005).

236. H. L. McArthur, *et al.*, A pilot study of preoperative single-dose ipilimumab and/or cryoablation in women with early-stage breast cancer with comprehensive immune profiling. *Clin. Cancer Res.* **22**, 5729–5737 (2016).

237. T. Schneider, *et al.*, Immune Response After Radiofrequency Ablation and Surgical Resection in Nonsmall Cell Lung Cancer. *Semin. Thorac. Cardiovasc. Surg.* **28**, 585–592 (2016).

238. L. Shi, *et al.*, PD-1 blockade boosts radiofrequency ablation-elicited adaptive immune responses against tumor. *Clin. Cancer Res.* **22**, 1173–1184 (2016).

239. A. Giardino, *et al.*, Immunomodulation after radiofrequency ablation of locally advanced pancreatic cancer by monitoring the immune response in 10 patients. *Pancreatology* **17**, 962–966 (2017).

240. S. Demaria, *et al.*, Ionizing radiation inhibition of distant untreated tumors (abscopal effect) is immune mediated. *Int. J. Radiat. Oncol. Biol. Phys.* **58**, 862–870 (2004).

241. S. Qu, *et al.*, Non-thermal histotripsy tumor ablation promotes abscopal immune responses that enhance cancer immunotherapy. *J. Immunother. Cancer* **8** (2020).

242. J. Abdo, D. L. Cornell, S. K. Mittal, D. K. Agrawal, Immunotherapy plus cryotherapy: Potential augmented abscopal effect for advanced cancers. *Front. Oncol.* **8**, 1 (2018).

243. Z. Chen, *et al.*, Bioinspired hybrid protein oxygen nanocarrier amplified photodynamic therapy for eliciting anti-tumor immunity and abscopal effect. *ACS Nano* **12**, 8633–8645 (2018).

244. S. R. Gameiro, *et al.*, Radiation-induced immunogenic modulation of tumor enhances antigen processing and calreticulin exposure, resulting in enhanced T-cell killign. *Oncotarget* **5**, 403–416 (2014).

245. R. J. E. van den Bijgaart, *et al.*, Thermal and mechanical high-intensity focused ultrasound: perspectives on tumor ablation, immune effects and combination strategies. *Cancer Immunol. Immunother.* **66**, 247–258 (2017).

246. J. H. Newman, N. Bhardwaj, Uncloaking Breast Tumor Neoantigens with Radiation. *Trends*

Immunol. **42**, 277–279 (2021).

247. C. Lhuillier, N. P. Rudqvist, O. Elemento, S. C. Formenti, S. Demaria, Radiation therapy and anti-tumor immunity: Exposing immunogenic mutations to the immune system. *Genome Med.* **11**, 1–10 (2019).

248. J. S. Yu, *et al.*, Vaccination with tumor lysate-pulsed dendritic cells elicits antigen-specific, cytotoxic T-cells in patients with malignant glioma. *Cancer Res.* **64**, 4973–4979 (2004).

249. , Radiation-inducible Immunotherapy for Cancer: Senescent Tumor Cells as a Cancer Vaccine - ScienceDirect (May 8, 2021).

250. A. Gupta, *et al.*, Radiotherapy Promotes Tumor-Specific Effector CD8+ T Cells via Dendritic Cell Activation. *J. Immunol.* **189**, 558–566 (2012).

251. S. Demaria, *et al.*, Immune-Mediated Inhibition of Metastases after Treatment with Local Radiation and CTLA-4 Blockade in a Mouse Model of Breast Cancer. *Clin. Cancer Res.* **11**, 728 LP – 734 (2005).

252. J. Zeng, *et al.*, Anti-PD-1 blockade and stereotactic radiation produce long-term survival in mice with intracranial gliomas. *Int. J. Radiat. Oncol. Biol. Phys.* **86**, 343–349 (2013).

253. J. E. Kim, *et al.*, Combination therapy with anti-PD-1, anti-TIM-3, and focal radiation results in regression of murine gliomas. *Clin. Cancer Res.* **23**, 124–136 (2017).

254. C. Vanpouille-Box, K. A. Pilones, E. Wennerberg, S. C. Formenti, S. Demaria, In situ vaccination by radiotherapy to improve responses to anti-CTLA-4 treatment. *Vaccine* **33**, 7415–7422 (2015).

255. E. C. Ko, S. C. Formenti, Radiotherapy and checkpoint inhibitors: a winning new combination? *Ther. Adv. Med. Oncol.* **10**, 1758835918768240 (2018).

256. J. Wei, *et al.*, Sequence of αPD-1 relative to local tumor irradiation determines the induction of abscopal antitumor immune responses. *Sci. Immunol.* **6**, eabg0117 (2021).

257. S. G. Swisher, *et al.*, Induction of p53-regulated Genes and Tumor Regression in Lung Cancer Patients after Intratumoral Delivery of Adenoviral p53 (INGN 201) and Radiation Therapy. *Clin. Cancer Res.* **9**, 93 LP – 101 (2003).

258. N. Zou, *et al.*, DDB2 increases radioresistance of NSCLC cells by enhancing DNA damage responses. *Tumor Biol.* **37**, 14183–14191 (2016).

259. T. Ohno, T. Nakano, Y. Niibe, H. Tsujii, K. Oka, “Bax Protein Expression Correlates with Radiation-Induced Apoptosis in Radiation Therapy for Cervical Carcinoma” (1998) https:/doi.org/10.1002/(SICI)1097-0142(19980701)83:1.

260. K. Esbona, *et al.*, The Presence of Cyclooxygenase 2, Tumor-Associated Macrophages, and Collagen Alignment as Prognostic Markers for Invasive Breast Carcinoma Patients. *Am. J. Pathol.* **188**, 559–573 (2018).

261. H. R. Park, S. K. Jo, U. Jung, Ionizing Radiation Promotes Epithelial-to-Mesenchymal Transition in Lung Epithelial Cells by TGF-β-producing M2 Macrophages. *In Vivo (Brooklyn).* **33**, 1773–1784 (2019).

262. L. Meziani, *et al.*, CSF1R inhibition prevents radiation pulmonary fibrosis by depletion of interstitial macrophages. *Eur Respir J* **51**, 1702120 (2018).

263. M. Piper, A. C. Mueller, S. D. Karam, The interplay between cancer associated fibroblasts and immune cells in the context of radiation therapy. *Mol. Carcinog.* **59**, 754–765 (2020).

264. M. De Palma, C. E. Lewis, Macrophage regulation of tumor responses to anticancer therapies. *Cancer Cell* **23**, 277–286 (2013).

265. J. B. Katz, A. J. Muller, G. C. Prendergast, Indoleamine 2,3-dioxygenase in T-cell tolerance and tumoral immune escape. *Immunol. Rev.* **222**, 206–221 (2008).

266. J. J. Wu, L. Zhao, H. G. Hu, W. H. Li, Y. M. Li, Agonists and inhibitors of the STING pathway: Potential agents for immunotherapy. *Med. Res. Rev.* **40**, 1117–1141 (2020).

267. T. Robson, *et al.*, A novel human stress response-related gene with a potential role in induced radioresistance. *Radiat. Res.* **152**, 451–461 (1999).

268. T. Robson, *et al.*, Increased repair and cell survival in cells treated with DIR1 antisense oligonucleotides: Implications for induced radioresistance. *Int. J. Radiat. Biol.* **76**, 617–623 (2000).

269. M. Hoogenboom, *et al.*, In vivo MR guided boiling histotripsy in a mouse tumor model evaluated by MRI and histopathology. *NMR Biomed.* **29**, 721–731 (2016).

270. C. S. Chiang, *et al.*, Irradiation promotes an M2 macrophage phenotype in tumor hypoxia. *Front. Oncol.* **2 AUG**, 89 (2012).

271. L. Deloch, *et al.*, Low-Dose Irradiation Differentially Impacts Macrophage Phenotype in

Dependence of Fibroblast-Like Synoviocytes and Radiation Dose. *J. Immunol. Res.* **2019**, 3161750 (2019).

272. L. Seifert, *et al.*, Radiation Therapy Induces Macrophages to Suppress T-Cell Responses Against Pancreatic Tumors in Mice. *Gastroenterology* **150**, 1659-1672.e5 (2016).

273. H. Zheng, J. Wang, M. Hauer-Jensen, Role of mast cells in early and delayed radiation injury in rat intestine. *Radiat. Res.* **153**, 533–539 (2000).

274. F. Aldenborg, K. Nilsson, B. Jarlshammar, L. Bjermer, L. Enerbäck, Mast cells and biogenic amines in radiation-induced pulmonary fibrosis. *Am. J. Respir. Cell Mol. Biol.* **8**, 112–117 (1993).

275. R. Reikki, I. T. Harvima, A. Jukkola, J. Ristile, A. Oikarinen, The production of collagen and the activity of mast-cell chymase increase in human skin after irradiation therapy. *Exp. Dermatol.* **13**, 364–371 (2004).

276. J. T. Leek, J. D. Storey, Capturing heterogeneity in gene expression studies by surrogate variable analysis. *PLoS Genet.* **3**, 1724–1735 (2007).

277. T. M. Therneau, P. M. Grambsch, “The Cox Model” in (Springer, New York, NY, 2000), pp. 39–77.

278. A. Kassambara, M. Kosinski, P. Biecek, S. Fabian, Package ‘survminer.’ *Draw. Surviv. Curves using ‘ggplot2’.(R Packag. version 0.3. 1.)* (2017).

279. K. Blighe, S. Gurudas, J. Lasky-Su, RegParallel: Standard regression functions in R enabled for parallel processing over large data-frames (2020).

280. D. A. Bolotin, *et al.*, MiXCR: Software for comprehensive adaptive immunity profiling. *Nat. Methods* **12**, 380–381 (2015).

281. H. Wickham, *ggplot2: Elegant Graphics for Data Analysis* (Springer-Verlag New York, 2016).

282. D. McMahon, W. Oakden, K. Hynynen, Investigating the effects of dexamethasone on blood-brain barrier permeability and inflammatory response following focused ultrasound and microbubble exposure. *Theranostics* **10**, 1604–1618 (2020).

283. N. McDannold, Y. Zhang, N. Vykhodtseva, Blood-Brain Barrier Disruption and Vascular Damage Induced by Ultrasound Bursts Combined with Microbubbles can be Influenced by

Choice of Anesthesia Protocol. *Ultrasound Med. Biol.* **37**, 1259–1270 (2011).

284. L. Mullin, *et al.*, Effect of anesthesia carrier gas on in vivo circulation times of ultrasound microbubble contrast agents in rats. *Contrast Media Mol. Imaging* **6**, 126–131 (2011).

285. S. Velayudha Reddy, Effect of general anesthetics on the developing brain. *J. Anaesthesiol. Clin. Pharmacol.* **28**, 6–10 (2012).

286. G. K. Istaphanous, A. W. Loepke, General anesthetics and the developing brain. *Curr. Opin. Anaesthesiol.* **22**, 368–373 (2009).

287. A. W. Loepke, S. G. Soriano, An Assessment of the Effects of General Anesthetics on Developing Brain Structure and Neurocognitive Function. *Anesth. Analg.* **106**, 1681–1707 (2008).

288. F. Liu, M. G. Paule, S. Ali, C. Wang, Ketamine-Induced Neurotoxicity and Changes in Gene Expression in the Developing Rat Brain. *Curr. Neuropharmacol.* **9**, 256–261 (2011).

289. L. M. Monteggia, E. Gideons, E. T. Kavalali, The role of eukaryotic elongation factor 2 kinase in rapid antidepressant action of ketamine. *Biol. Psychiatry* **73**, 1199–1203 (2013).

290. M. Wittner, J. Sivenius, J. Koistinaho, α2-Adrenoreceptor agonist, dexmedetomidine, alters acute gene expression after global ischemia in gerbils. *Neurosci. Lett.* **232**, 75–78 (1997).

291. Y. Yoshida, K. Nakazato, K. Takemori, K. Kobayashi, A. Sakamoto, The influences of propofol and dexmedetomidine on circadian gene expression in rat brain. *Brain Res. Bull.* **79**, 441–444 (2009).

292. A. Sakamoto, *et al.*, Influence of inhalation anesthesia assessed by comprehensive gene expression profiling. *Gene* **356**, 39–48 (2005).

293. J. Z. Pan, *et al.*, Rat brain DNA transcript profile of halothane and isoflurane exposure. *Pharmacogenet. Genomics* **16**, 171–182 (2006).

294. Z. Li, *et al.*, Calcineurin/nuclear factor-κB signaling mediates isoflurane-induced hippocampal neuroinflammation and subsequent cognitive impairment in aged rats. *Mol. Med. Rep.* **15**, 201–209 (2017).

295. L. Zhang, *et al.*, Isoflurane and sevoflurane increase interleukin-6 levels through the nuclear factor-kappa B pathway in neuroglioma cells. *BJA Br. J. Anaesth.* **110**, i82–i91 (2013).

296. X. Wu, *et al.*, The inhalation anesthetic isoflurane increases levels of proinflammatory TNF-α, IL-6, and IL-1β. *Neurobiol. Aging* **33**, 1364–1378 (2012).

297. Z. Xie, *et al.*, The common inhalation anesthetic isoflurane induces caspase activation and increases amyloid β-protein level in vivo. *Ann. Neurol.* **64**, 618–627 (2008).

298. L. Cao, L. Li, D. Lin, Z. Zuo, Isoflurane Induces Learning Impairment That Is Mediated by Interleukin 1β in Rodents. *PLoS One* **7** (2012).

299. D. Lin, *et al.*, Lidocaine attenuates cognitive impairment after isoflurane anesthesia in old rats. *Behav. Brain Res.* **228**, 319–327 (2012).

300. R. V. Plachinta, J. K. Hayes, L. A. Cerilli, G. F. Rich, Isoflurane Pretreatment Inhibits Lipopolysaccharide-induced Inflammation in Rats. *Anesthesiology* **98**, 89–95 (2003).

301. I. S. Chung, *et al.*, Reactive Oxygen Species by Isoflurane Mediates Inhibition of Nuclear Factor κB Activation in Lipopolysaccharide-Induced Acute Inflammation of the Lung. *Anesth. Analg.* **116**, 327–335 (2013).

302. H. Li, *et al.*, Isoflurane postconditioning reduces ischemia-induced nuclear factor-κB activation and interleukin 1β production to provide neuroprotection in rats and mice. *Neurobiol. Dis.* **54**, 216–224 (2013).

303. F. E. Blum, Z. Zuo, Volatile anesthetics-induced neuroinflammatory and anti-inflammatory responses. *Med. Gas Res.* **3**, 16 (2013).

304. Y. Li, *et al.*, Effects of Ketamine on Levels of Inflammatory Cytokines IL-6, IL-1β, and TNF-α in the Hippocampus of Mice Following Acute or Chronic Administration. *Front. Pharmacol.* **8**, 139 (2017).

305. C.-H. Yeh, *et al.*, Dexmedetomidine reduces lipopolysaccharide induced neuroinflammation, sickness behavior, and anhedonia (2018) https:/doi.org/10.1371/journal.pone.0191070 (March 25, 2020).

306. C. Huang, *et al.*, Differential effects of propofol and dexmedetomidine on neuroinflammation induced by systemic endotoxin lipopolysaccharides in adult mice. *Neurosci. Lett.* **707**, 134309 (2019).

307. M. Peng, Y. L. Wang, C. Y. Wang, C. Chen, Dexmedetomidine attenuates lipopolysaccharide-induced proinflammatory response in primary microglia. *J. Surg. Res.*

179, e219–e225 (2013).

308. Y. J. Zhu, K. Peng, X. W. Meng, F. H. Ji, Attenuation of neuroinflammation by dexmedetomidine is associated with activation of a cholinergic anti-inflammatory pathway in a rat tibial fracture model. *Brain Res.* **1644**, 1–8 (2016).

309. I. Cohen, *et al.*, Differential release of chromatin-bound IL-1α discriminates between necrotic and apoptotic cell death by the ability to induce sterile inflammation. *Proc. Natl. Acad. Sci. U. S. A.* **107**, 2574–2579 (2010).

310. A. Werman, *et al.*, The precursor form of IL-1α is an intracrine proinflammatory activator of transcription. *Proc. Natl. Acad. Sci. U. S. A.* **101**, 2434–2439 (2004).

311. C. A. Dinarello, Overview of the IL-1 family in innate inflammation and acquired immunity. *Immunol. Rev.* **281**, 8–27 (2018).

312. P. Rider, *et al.*, IL-1α and IL-1β Recruit Different Myeloid Cells and Promote Different Stages of Sterile Inflammation. *J. Immunol.* **187**, 4835–4843 (2011).

313. I. V. Dogan, E. Ovali, Z. Eti, A. Yayci, F. Y. Gogus, The In Vitro Effects of Isoflurane, Sevoflurane, and Propofol on Platelet Aggregation. *Anesth. Analg.* **88**, 432–436 (1999).

314. H. Hirakata, *et al.*, Platelet aggregation is impaired during anaesthesia with sevoflurane but not with isoflurane. *Can. J. Anaesth.* **44**, 1157–1161 (1997).

315. N. L. Law, K. F. J. Ng, M. G. Irwin, J. S. F. Man, Comparison of coagulation and blood loss during anaesthesia with inhaled isoflurane or intravenous propofol. *BJA Br. J. Anaesth.* **86**, 94–98 (2001).

316. P. M. Atkinson, D. I. Taylor, N. Chetty, Inhibition of platelet aggregation by ketamine hydrochloride. *Thromb. Res.* **40**, 227–234 (1985).

317. A. Undar, *et al.*, Anesthetic Induction With Ketamine Inhibits Platelet Activation Before, During, and After Cardiopulmonary Bypass in Baboons. *Artif. Organs* **28**, 959–962 (2004).

318. T. Nakagawa, *et al.*, “Ketamine Suppresses Platelet Aggregation Possibly by Suppressed Inositol Triphosphate Formation and Subsequent Suppression of Cytosolic Calcium Increase” (2002).

319. Z. Chen, *et al.*, Effect of dexmedetomidine on blood coagulation in patients undergoing radical gastrectomy under general anesthesia. *Med. (United States)* **97** (2018).

320. T. Scarcelli, *et al.*, Stimulation of hippocampal neurogenesis by transcranial focused ultrasound and microbubbles in adult mice. *Brain Stimul.* **7**, 304–307 (2014).

321. E. Nance, *et al.*, Non-invasive delivery of stealth, brain-penetrating nanoparticles across the blood - Brain barrier using MRI-guided focused ultrasound. *J. Control. Release* **189**, 123–132 (2014).

322. B. P. Mead, *et al.*, Targeted gene transfer to the brain via the delivery of brain-penetrating DNA nanoparticles with focused ultrasound. *J. Control. Release* **223**, 109–117 (2016).

323. J. R. Conway, A. Lex, N. Gehlenborg, UpSetR: an R package for the visualization of intersecting sets and their properties. *Bioinformatics* **33**, 2938–2940 (2017).

324. C. H. Fan, *et al.*, Noninvasive, Targeted, and Non-Viral Ultrasound-Mediated GDNF-Plasmid Delivery for Treatment of Parkinson's Disease. *Sci. Rep.* **6**, 1–11 (2016).

325. S. Wang, O. O. Olumolade, T. Sun, G. Samiotaki, E. E. Konofagou, Noninvasive, neuron-specific gene therapy can be facilitated by focused ultrasound and recombinant adeno-associated virus. *Gene Ther.* **22**, 104–110 (2015).

326. C. T. Curley, *et al.*, Augmentation of brain tumor interstitial flow via focused ultrasound promotes brain-penetrating nanoparticle dispersion and transfection. *Sci. Adv.* **6**, eaay1344 (2020).

327. B. P. Mead, *et al.*, Focused Ultrasound Preconditioning for Augmented Nanoparticle Penetration and Efficacy in the Central Nervous System. *Small* **15**, 1903460 (2019).

328. F. Wu, *et al.*, A randomised clinical trial of high-intensity focused ultrasound ablation for the treatment of patients with localised breast cancer. *Br. J. Cancer* **89**, 2227–2233 (2003).

329. B. P. Mead, *et al.*, Targeted gene transfer to the brain via the delivery of brain-penetrating DNA nanoparticles with focused ultrasound. *J. Control. Release* **223**, 109–117 (2016).

330. P.-H. Hsu, *et al.*, Noninvasive and Targeted Gene Delivery into the Brain Using Microbubble-Facilitated Focused Ultrasound. *PLoS One* **8**, e57682 (2013).

331. Z. I. Kovacs, *et al.*, Disrupting the blood–brain barrier by focused ultrasound induces sterile inflammation. *Proc. Natl. Acad. Sci.* **114**, E75–E84 (2017).

332. Y. Hu, J. M. F. Wan, A. C. H. Yu, Membrane Perforation and Recovery Dynamics in Microbubble-Mediated Sonoporation. *Ultrasound Med. Biol.* **39**, 2393–2405 (2013).

333. C. Jia, *et al.*, Generation of Reactive Oxygen Species in Heterogeneously Sonoporated Cells by Microbubbles with Single-Pulse Ultrasound. *Ultrasound Med. Biol.* **44**, 1074–1085 (2018).

334. W. Zhong, W. H. Sit, J. M. F. Wan, A. C. H. Yu, Sonoporation induces apoptosis and cell cycle arrest in human promyelocytic leukemia cells. *Ultrasound Med. Biol.* **37**, 2149–2159 (2011).

335. A. Bańkowska, M. Gacko, E. Chyczewska, A. Worowska, Biological and diagnostic role of cathepsin D. *Rocz. Akad. Med. Bialymst.* **42 Suppl 1**, 79–85 (1997).

336. P. Benes, V. Vetvicka, M. Fusek, Cathepsin D-Many functions of one aspartic protease. *Crit. Rev. Oncol. Hematol.* **68**, 12–28 (2008).

337. A. M. Cataldo, *et al.*, Gene expression and cellular content of cathepsin D in Alzheimer's disease brain: Evidence for early up-regulation of the endosomal-lysosomal system. *Neuron* **14**, 671–680 (1995).

338. G. R. Hook, *et al.*, The cysteine protease cathepsin B is a key drug target and cysteine protease inhibitors are potential therapeutics for traumatic brain injury. *J. Neurotrauma* **31**, 515–529 (2014).

339. C.-L. Luo, *et al.*, Cathepsin B contributes to traumatic brain injury-induced cell death through a mitochondria-mediated apoptotic pathway. *J. Neurosci. Res.* **88**, n/a-n/a (2010).

340. S. Su, *et al.*, DNA methylation of the LY86 gene is associated with obesity, insulin resistance, and inflammation. *Twin Res. Hum. Genet.* **17**, 183–191 (2014).

341. S. Divanovic, *et al.*, Inhibition of TLR-4/MD-2 signaling by RP105/MD-1. *J. Endotoxin Res.* **11**, 363–368 (2005).

342. C. Perego, S. Fumagalli, M. G. De Simoni, Temporal pattern of expression and colocalization of microglia/macrophage phenotype markers following brain ischemic injury in mice. *J. Neuroinflammation* **8**, 174 (2011).

343. D. A. Chistiakov, M. C. Killingsworth, V. A. Myasoedova, A. N. Orekhov, Y. V. Bobryshev, CD68/macrosialin: Not just a histochemical marker. *Lab. Investig.* **97**, 4–13 (2017).

344. A. Cougnoux, *et al.*, Toll-like receptor mediated lysozyme expression in Niemann-pick disease, type C1. *Mol. Genet. Metab.* (2020) https:/doi.org/10.1016/j.ymgme.2020.10.009.

345. J. Ma, T. Jiang, L. Tan, J. T. Yu, TYROBP in Alzheimer's Disease. *Mol. Neurobiol.* **51**, 820–826 (2015).

346. C. Cunningham, A. Dunne, A. B. Lopez-Rodriguez, Astrocytes: Heterogeneous and Dynamic Phenotypes in Neurodegeneration and Innate Immunity. *Neuroscientist* **25**, 455–474 (2019).

347. C. L. Davies, A. Patir, B. W. McColl, Myeloid Cell and Transcriptome Signatures Associated With Inflammation Resolution in a Model of Self-Limiting Acute Brain Inflammation. *Front. Immunol.* **10**, 1048 (2019).

348. C.-M. Lee, *et al.*, Single-cell RNA-seq analysis revealed long-lasting adverse effects of tamoxifen on neurogenesis in prenatal and adult brains https:/doi.org/10.1073/pnas.1918883117/-/DCSupplemental (August 13, 2020).

349. J. Peng, *et al.*, Single-cell RNA-seq highlights intra-tumoral heterogeneity and malignant progression in pancreatic ductal adenocarcinoma. *Cell Res.* **29**, 725–738 (2019).

350. P. Y. Tung, *et al.*, Batch effects and the effective design of single-cell gene expression studies. *Sci. Rep.* **7**, 1–15 (2017).

351. S. C. Hicks, F. W. Townes, M. Teng, R. A. Irizarry, Missing data and technical variability in single-cell RNA-sequencing experiments. *Biostatistics* **19**, 562–578 (2018).

352. A. Butler, P. Hoffman, P. Smibert, E. Papalexi, R. Satija, Integrating single-cell transcriptomic data across different conditions, technologies, and species. *Nat. Biotechnol.* **36**, 411–420 (2018).

353. O. Franzén, L. M. Gan, J. L. M. Björkegren, PanglaoDB: A web server for exploration of mouse and human single-cell RNA sequencing data. *Database* **2019**, 46 (2019).

354. G. Finak, *et al.*, MAST: A flexible statistical framework for assessing transcriptional changes and characterizing heterogeneity in single-cell RNA sequencing data. *Genome Biol.* **16**, 278 (2015).

355. M. A. Stavarache, *et al.*, Safe and stable noninvasive focal gene delivery to the mammalian brain following focused ultrasound. *J. Neurosurg.* **130**, 989–998 (2019).

356. A. Chodobski, B. J. Zink, J. Szmydynger-Chodobska, Blood-Brain Barrier Pathophysiology in Traumatic Brain Injury. *Transl. Stroke Res.* **2**, 492–516 (2011).

357. D. Shlosberg, M. Benifla, D. Kaufer, A. Friedman, Blood-brain barrier breakdown as a therapeutic target in traumatic brain injury. *Nat. Rev. Neurol.* **6**, 393–403 (2010).

358. K. E. Sandoval, K. A. Witt, Blood-brain barrier tight junction permeability and ischemic stroke. *Neurobiol. Dis.* **32**, 200–219 (2008).

359. C. Yang, K. E. Hawkins, S. Doré, E. Candelario-Jalil, Neuroinflammatory mechanisms of blood-brain barrier damage in ischemic stroke. *Am. J. Physiol. - Cell Physiol.* **316**, C135–C153 (2019).

360. A. Minagar, J. S. Alexander, Blood-brain barrier disruption in multiple sclerosis. *Mult. Scler.* **9**, 540–549 (2003).

361. D. W. Holman, R. S. Klein, R. M. Ransohoff, The blood-brain barrier, chemokines and multiple sclerosis. *Biochim. Biophys. Acta - Mol. Basis Dis.* **1812**, 220–230 (2011).

362. R. D. Bell, B. V. Zlokovic, Neurovascular mechanisms and blood-brain barrier disorder in Alzheimer's disease. *Acta Neuropathol.* **118**, 103–113 (2009).

363. R. Deane, B. Zlokovic, Role of the Blood-Brain Barrier in the Pathogenesis of Alzheimers Disease. *Curr. Alzheimer Res.* **4**, 191–197 (2007).

364. S. Watkins, *et al.*, Disruption of astrocyte-vascular coupling and the blood-brain barrier by invading glioma cells. *Nat. Commun.* **5**, 1–15 (2014).

365. R. Paul, *et al.*, Matrix metalloproteinases contribute to the blood-brain barrier disruption during bacterial meningitis. *Ann. Neurol.* **44**, 592–600 (1998).

366. S. H. Huang, M. F. Stins, K. S. Kim, Bacterial penetration across the blood-brain barrier during the development of neonatal meningitis. *Microbes Infect.* **2**, 1237–1244 (2000).

367. J. F. Jordão, *et al.*, Amyloid-β plaque reduction, endogenous antibody delivery and glial activation by brain-targeted, transcranial focused ultrasound. *Exp. Neurol.* **248**, 16–29 (2013).

368. A. S. Mathew, *et al.*, Transcriptomic response of brain tissue to focused ultrasound-mediated blood–brain barrier disruption depends strongly on anesthesia. *Bioeng. Transl. Med.*, e10198 (2020).

369. S. J. Mooney, *et al.*, Focused ultrasound-induced neurogenesis requires an increase in blood-brain barrier permeability. *PLoS One* **11**, e0159892 (2016).

370. M. E. Karakatsani, *et al.*, Unilateral focused ultrasound-induced blood-brain barrier opening reduces phosphorylated Tau from the rTg4510 mouse model. *Theranostics* **9**, 5396–5411 (2019).

371. P. C. Chu, *et al.*, Neuromodulation accompanying focused ultrasound-induced blood-brain barrier opening. *Sci. Rep.* **5**, 1–12 (2015).

372. N. Todd, *et al.*, Secondary effects on brain physiology caused by focused ultrasound-mediated disruption of the blood–brain barrier. *J. Control. Release* **324**, 450–459 (2020).

373. N. McDannold, N. Vykhodtseva, K. Hynynen, Targeted disruption of the blood-brain barrier with focused ultrasound: Association with cavitation activity. *Phys. Med. Biol.* **51**, 793–807 (2006).

374. T. Bangsow, *et al.*, The epithelial membrane protein 1 is a novel tight junction protein of the blood-brain barrier. *J. Cereb. Blood Flow Metab.* **28**, 1249–1260 (2008).

375. J. Deng, *et al.*, The role of caveolin-1 in blood-brain barrier disruption induced by focused ultrasound combined with microbubbles. *J. Mol. Neurosci.* **46**, 677–687 (2012).

376. Y. Liu, *et al.*, Human junction adhesion molecule regulates tight junction resealing in epithelia. *J. Cell Sci.* **113**, 2363–2374 (2000).

377. I. Martìn-Padura, *et al.*, Junctional adhesion molecule, a novel member of the immunoglobulin superfamily that distributes at intercellular junctions and modulates monocyte transmigration. *J. Cell Biol.* **142**, 117–127 (1998).

378. J. Haskins, L. Gu, E. S. Wittchen, J. Hibbard, B. R. Stevenson, ZO-3, a novel member of the MAGUK protein family found at the tight junction, interacts with ZO-1 and occludin. *J. Cell Biol.* **141**, 199–208 (1998).

379. M. Itoh, *et al.*, Direct binding of three tight junction-associated MAGUKs, ZO-1, ZO-2, and ZO-3, with the COOH termini of claudins. *J. Cell Biol.* **147**, 1351–1363 (1999).

380. G. Bazzoni, *et al.*, Interaction of junctional adhesion molecule with the tight junction components ZO-1, cingulin, and occludin. *J. Biol. Chem.* **275**, 20520–20526 (2000).

381. P. Florian, T. Schöneberg, J. D. Schulzke, M. Fromm, A. H. Gitter, Single-cell epithelial defects close rapidly by an actinomyosin purse string mechanism with functional tight junctions. *J. Physiol.* **545**, 485–499 (2002).

382. J. L. Madara, Intestinal absorptive cell tight junctions are linked to cytoskeleton. *Am. J. Physiol. - Cell Physiol.* **253** (1987).

383. J. L. Madara, J. Stafford, Interferon-γ directly affects barrier function of cultured intestinal epithelial monolayers. *J. Clin. Invest.* **83**, 724–727 (1989).

384. D. E. Ingber, D. Prusty, Z. Sun, H. Betensky, N. Wang, Cell shape, cytoskeletal mechanics, and cell cycle control in angiogenesis. *J. Biomech.* **28**, 1471–1484 (1995).

385. K. S. Mark, T. P. Davis, Cerebral microvascular changes in permeability and tight junctions induced by hypoxia-reoxygenation. *Am. J. Physiol. - Hear. Circ. Physiol.* **282** (2002).

386. L. E. Crawford, *et al.*, Superoxide-mediated actin response in post-hypoxic endothelial cells. *J. Biol. Chem.* **271**, 26863–26867 (1996).

387. G. Yu, L. G. Wang, Y. Han, Q. Y. He, ClusterProfiler: An R package for comparing biological themes among gene clusters. *Omi. A J. Integr. Biol.* **16**, 284–287 (2012).

388. M. J. Kane, *et al.*, A mouse model of human repetitive mild traumatic brain injury. *J. Neurosci. Methods* **203**, 41–49 (2012).

389. Y. Yoshiyama, *et al.*, Enhanced neurofibrillary tangle formation, cerebral atrophy, and cognitive deficits induced by repetitive mild brain injury in a transgenic tauopathy mouse model. *J. Neurotrauma* **22**, 1134–1141 (2005).

390. C. E. Creeley, D. F. Wozniak, P. V. Bayly, J. W. Olney, L. M. Lewis, Multiple episodes of mild traumatic brain injury result in impaired cognitive performance in mice. *Acad. Emerg. Med.* **11**, 809–819 (2004).

391. S. M. DeFord, *et al.*, Repeated mild brain injuries result in cognitive impairment in B6C3F1 mice. *J. Neurotrauma* **19**, 427–438 (2002).

392. B. Mouzon, *et al.*, Repetitive mild traumatic brain injury in a mouse model produces learning and memory deficits accompanied by histological changes. *J. Neurotrauma* **29**, 2761–2773 (2012).

393. M. Ullah, D. D. Liu, S. Rai, W. Concepcion, A. S. Thakor, HSP70-mediated NLRP3 inflammasome suppression underlies reversal of acute kidney injury following extracellular vesicle and focused ultrasound combination therapy. *Int. J. Mol. Sci.* **21**, 1–13 (2020).

394. D. P. Zachs, *et al.*, Noninvasive ultrasound stimulation of the spleen to treat inflammatory

arthritis. *Nat. Commun.* **10**, 1–10 (2019).

395. M. Rauch, M. Marinova, H. H. Schild, H. Strunk, High intensity focused ultrasound for the treatment of advanced liver cancer. *Dig. Liver Dis.* **47**, 989–990 (2015).

396. C. Huang, H. Zhang, R. Bai, Advances in ultrasound-targeted microbubble-mediated gene therapy for liver fibrosis. *Acta Pharm. Sin. B* **7**, 447–452 (2017).

397. S. S. Yoo, H. Kim, B. K. Min, E. Franck, S. Park, Transcranial focused ultrasound to the thalamus alters anesthesia time in rats. *Neuroreport* **22**, 783–787 (2011).

398. Y. Tufail, A. Yoshihiro, S. Pati, M. M. Li, W. J. Tyler, Ultrasonic neuromodulation by brain stimulation with transcranial ultrasound. *Nat. Protoc.* **6**, 1453–1470 (2011).

399. Y. Younan, *et al.*, Influence of the pressure field distribution in transcranial ultrasonic neurostimulation. *Med. Phys.* **40** (2013).

400. T. Deffieux, *et al.*, Low-intensity focused ultrasound modulates monkey visuomotor behavior. *Curr. Biol.* **23**, 2430–2433 (2013).

401. W. J. Tyler, *et al.*, Remote excitation of neuronal circuits using low-intensity, low-frequency ultrasound. *PLoS One* **3** (2008).

402. R. A. Wahab, *et al.*, Mechanical bioeffects of pulsed high intensity focused ultrasound on a simple neural model. *Med. Phys.* **39**, 4274–4283 (2012).

403. D. E. Goertz, An overview of the influence of therapeutic ultrasound exposures on the vasculature: High intensity ultrasound and microbubble-mediated bioeffects. *Int. J. Hyperth.* **31**, 134–144 (2015).

404. S. Pichardo, R. Milleret, L. Curiel, O. Pichot, J. Y. Chapelon, In vitro experimental study on the treatment of superficial venous insufficiency with high-intensity focused ultrasound. *Ultrasound Med. Biol.* **32**, 883–891 (2006).

405. K. Hynynen, A. H. Chung, V. Colucci, F. A. Jolesz, Potential adverse effects of high-intensity focused ultrasound exposure on blood vessels in vivo. *Ultrasound Med. Biol.* **22**, 193–201 (1996).

406. S. Wang, V. Zderic, V. Frenkel, Extracorporeal, low-energy focused ultrasound for noninvasive and nondestructive targeted hyperthermia. *Futur. Oncol.* **6**, 1497–1511 (2010).

407. F. Y. Yang, W. H. Chiu, S. H. Liu, G. L. Lin, F. M. Ho, Functional changes in arteries induced

by pulsed high-intensity focused ultrasound. *IEEE Trans. Ultrason. Ferroelectr. Freq. Control* **56**, 2643–2649 (2009).

408. A. Maruo, *et al.*, Nitric oxide and prostacyclin in ultrasonic vasodilatation of the canine internal mammary artery. *Ann. Thorac. Surg.* **77**, 126–132 (2004).

409. S. Barzelai, *et al.*, Low-intensity ultrasound induces angiogenesis in rat hind-limb ischemia. *Ultrasound Med. Biol.* **32**, 139–145 (2006).

410. K. Hanawa, *et al.*, Low-intensity pulsed ultrasound induces angiogenesis and ameliorates left ventricular dysfunction in a porcine model of chronic myocardial ischemia. *PLoS One* **9** (2014).

411. P. Reher, N. Doan, B. Bradnock, S. Meghji, M. Harris, Effect of ultrasound on the production of IL-8, basic FGF and VEGF. *Cytokine* **11**, 416–423 (1999).

412. N. Mizrahi, D. Seliktar, E. Kimmel, Ultrasound-Induced Angiogenic Response in Endothelial Cells. *Ultrasound Med. Biol.* **33**, 1818–1829 (2007).

413. S. Vaezy, *et al.*, Hemostasis of punctured blood vessels using high-intensity focused ultrasound. *Ultrasound Med. Biol.* **24**, 903–910 (1998).

414. S. Vaezy, *et al.*, Liver hemostasis using high-intensity focused ultrasound. *Ultrasound Med. Biol.* **23**, 1413–1420 (1997).

415. V. Zderic, *et al.*, Hemorrhage control in arteries using high-intensity focused ultrasound: A survival study. *Ultrasonics* **44**, 46–53 (2006).

416. J. H. Hwang, Y. Zhou, C. Warren, A. A. Brayman, L. A. Crum, Targeted venous occlusion using pulsed high-intensity focused ultrasound. *IEEE Trans. Biomed. Eng.* **57**, 37–40 (2010).

417. Y. Meng, *et al.*, MR-guided focused ultrasound liquid biopsy enriches circulating biomarkers in patients with brain tumors. *Neuro. Oncol.* (2021) https:/doi.org/10.1093/neuonc/noab057 (June 3, 2021).

418. C. P. Pacia, *et al.*, Feasibility and safety of focused ultrasound-enabled liquid biopsy in the brain of a porcine model. *Sci. Rep.* **10**, 1–9 (2020).

419. L. Zhu, *et al.*, Focused Ultrasound-enabled Brain Tumor Liquid Biopsy. *Sci. Rep.* **8**, 1–9 (2018).

420. R. J. E. van den Bijgaart, *et al.*, Thermal and mechanical high-intensity focused ultrasound: perspectives on tumor ablation, immune effects and combination strategies. *Cancer Immunol. Immunother.* **66**, 247–258 (2017).

421. Z. I. Kovacs, *et al.*, Disrupting the blood-brain barrier by focused ultrasound induces sterile inflammation. *Proc. Natl. Acad. Sci. U. S. A.* **114**, E75–E84 (2017).

422. K. J. Bryan, H. Lee, G. Perry, M. A. Smith, G. Casadesus, *Transgenic Mouse Models of Alzheimer's Disease: Behavioral Testing and Considerations* (CRC Press/Taylor & Francis, 2009) (June 3, 2021).